JPL Publication 96-4, Vol. 1

Summaries of the Sixth Annual JPL Airborne Earth Science Workshop March 4–8, 1996

Volume 1. AVIRIS Workshop

Robert O. Green
Editor

March 4, 1996

National Aeronautics and
Space Administration

Jet Propulsion Laboratory
California Institute of Technology
Pasadena, California

JPL Publication 96-4, Vol. 1

Summaries of the Sixth Annual JPL Airborne Earth Science Workshop March 4–8, 1996

Volume 1. AVIRIS Workshop

Robert O. Green
Editor

March 4, 1996

National Aeronautics and
Space Administration

Jet Propulsion Laboratory
California Institute of Technology
Pasadena, California

This publication was prepared by the Jet Propulsion Laboratory, California Institute of Technology, under a contract with the National Aeronautics and Space Administration.

ABSTRACT

This publication contains the summaries for the Sixth Annual JPL Airborne Earth Science Workshop, held in Pasadena, California, on March 4–8, 1996. The main workshop is divided into two smaller workshops as follows:

- The Airborne Visible/Infrared Imaging Spectrometer (AVIRIS) workshop, on March 4–6. The summaries for this workshop appear in Volume 1.

- The Airborne Synthetic Aperture Radar (AIRSAR) workshop, on March 6–8. The summaries for this workshop appear in Volume 2.

Page intentionally left blank

TABLE OF CONTENTS

TABLE OF CONTENTS (continued)

TABLE OF CONTENTS (continued)

TABLE OF CONTENTS (continued)

MODTRAN CLOUD AND MULTIPLE SCATTERING UPGRADES WITH APPLICATION TO AVIRIS

A. Berk, L. S. Bernstein, D. C. Robertson, and P. K. Acharya
Spectral Sciences, Inc., 99 South Bedford St.,
Burlington, MA 01803

G. P. Anderson and J. H. Chetwynd
Phillips Laboratory, Geophysics Directorate
Hanscom AFB, MA 01731

1. INTRODUCTION

Characterization of surface properties from AVIRIS measurements is hampered by atmospheric attenuation and path radiances. MODTRAN (Berk et al., 1989), the Air Force PL/Geophysics Directorate moderate spectral resolution (2 cm^{-1}) background radiance and transmission model, is often used to account for the atmospherics in AVIRIS measurements. It rapidly predicts the molecular and aerosol/cloud emissive and scattered contributions to observed radiances along with the atmospheric attenuation. MODTRAN has been extensively validated against both measurements and the high spectral resolution FASCODE (Clough et al., 1988) model.

MODTRAN4, currently under development, contains two new features which greatly improve predictive capabilities under cloudy and/or heavy aerosol loading conditions. It allows a user to explicitly define water and ice cloud vertical profiles and spectral data either by scaling the default model clouds or by defining a new model cloud. MODTRAN4 also introduces a Correlated-*k* (CK) capability which significantly improves the accuracy of the multiple scattering radiance calculations. In the following sections, a discussion of the MODTRAN4 upgrades and an initial validation by comparison to airborne measurements of a solar illuminated cumulus cloud top are presented. Finally, the effect of the CK approach for two AVIRIS scenarios is demonstrated.

2. MODTRAN CLOUD/RAIN MODELS UPGRADE

The MODTRAN cloud/rain models have been upgraded (Berk, 1995) and now allow for generalized specification of layering and optical and physical properties as well as the presence of multiple overlapping and non-overlapping clouds. The cloud models affected are all of the cumulus and stratus type clouds, both with and without rain. This includes MODTRAN cloud/rain models 1 through 10. The cirrus models 17-19 only required improved layering. The cloud model upgrades include:

- adjustable cloud parameters,
  - thickness, altitude, vertical extinction, column amounts, humidity, and scattering phase functions,
- decoupling of the clouds from aerosols,
- introduction of ice particles,
- user-defined water droplet, ice particle and rain rate profiles,
- user-defined cloud spectral properties, and
- output of cloud/rain profiles and spectral data to tape6 (NOPRT = -1).

The decoupling of the cloud and aerosol models has a number of implications. Clouds and aerosols can co-exist at a single altitude, or clouds can be modeled with no aerosol profiles included. When clouds and aerosols co-exist, the cloud water droplets, cloud ice particles and aerosol particles may all have different scattering phase functions. The single scatter solar contribution of each component is properly combined. However, for multiple scattering a single effective phase function is defined based on a scattering optical depth weighted Henyey-Greenstein asymmetry factor; this is the same approach that is used to combine the aerosol and molecular scattering contributions.

Cloud profiles are merged with the other atmospheric profiles (pressure, temperature, molecular constituent and aerosol) by combining and/or adding new layer boundaries. Any cloud layer boundary within half a meter of an atmospheric boundary layer is translated to make the layer altitudes coincide; new atmospheric layer boundaries are defined to accommodate the additional cloud layer boundaries.

3. ADDITION OF A CORRELATED-*k* CAPABILITY TO MODTRAN

Addition of a CK capability to MODTRAN (Bernstein et al., 1995) provides an accurate and fast means for evaluation of the effects of clouds and heavy aerosol loading on retrievals (both surface properties and species concentration profiles) and on atmospheric radiative heating/cooling calculations. These radiative transfer computations require coupling the effects of gaseous molecular absorption due primarily to water vapor, carbon dioxide, and ozone, with particulate multiple scattering due to volcanic aerosols, ice crystals, and water droplets. The molecular absorption band model used in MODTRAN is not suitable for interfacing with standard multiple scattering algorithms. This is because the scattering models require a monochromatic representation of the molecular transmission (i.e., Beer's law), whereas molecular band models which represent the transmission for a finite spectral interval do not follow Beer's law. In order to adapt a band model approach for use in scattering calculations it is necessary to express the band model transmission function in terms of a weighted sum of Beer's law exponential terms. Thus, a method for determining the weighing factors and monochromatic absorption coefficients for the MODTRAN band model is required. An abbreviated discussion of the CK approach as tailored for integration into MODTRAN is given below; for a more complete discussion of the CK method the reader is referred to Lacis and Oinas (1991).

For simplicity, consider the problem of determining the average transmittance, as defined by Beer's law, for a homogeneous path over a finite spectral interval. The generalization to inhomogeneous paths is straightforward and is also described below. The path transmittance can be exactly determined through evaluation of

$$T(u) = \frac{1}{\omega_2 - \omega_1} \int_{\omega_1}^{\omega_2} d\omega \, \exp(-k(\omega)u) \quad , \tag{1}$$

where ω is frequency, $k(\omega)$ is the monochromatic absorption coefficient, and u is absorber column density. The basis of the CK approach is that evaluation of T(u) by integration over frequency can be replaced by an equivalent integration over the distribution of absorption coefficient values f(k) in the spectral interval

$$T(u) = \int_0^{\infty} dk \, f(k) \, \exp(-ku) \quad . \tag{2}$$

The difficulty in evaluation of T(u) via Equation (2) is the necessity of first determining f(k); the advantage is that $k(\omega)$ is typically a highly repetitive function of ω (i.e., there are many nearly equivalent values of a given k in a spectral interval) and thus numerical evaluation of Equation (2) requires far fewer grid points than Equation

(1). Note that f(k) = 0 above the maximum k_{max} and below the minimum k_{min} absorption coefficients in the spectral interval. The probability distribution f(k) can be determined directly from k(ω) by binning the k's into selected Δk sub-intervals.

The distribution function f(k) is not smooth or monotonic; it generally consists of a series of sharp spikes which reflects the sharp line structure of k(ω). It then becomes more computationally convenient to work with the smooth and monotonic cumulative probability distribution function

$$g(k) = \int_0^k dk' f(k') \quad . \tag{3}$$

Physically, g(k) is the fraction of absorption coefficients below k within the finite spectral interval ω_1 to ω_2. It assumes the values g = 0 at $k = k_{min}$ and g = 1 at $k = k_{max}$. The transmittance is related to g by

$$T(u) = \int_0^1 dg \exp(-k(g)u) \quad , \tag{4}$$

where k(g) is given by the inverse of g(k), $k(g) = g^{-1}(k)$. In practice, the evaluation of Equation (4) proceeds via summation according to

$$T(u) = \sum_{i=1}^{imax} \Delta g_i \exp(-\overline{k}_i u) \quad , \tag{5}$$

where the Δg_i's and $\overline{k}_i$'s are the sub-interval weighting factors and effective absorption coefficients necessary for the MODTRAN band model. The maximum number of intervals i_{max} and the specific selection of Δg_i interval boundaries (g_i, g_{i+1}) are chosen based on consideration of a number of factors including computational speed and accuracy, and the altitude and spectral ranges of interest. For multi-layer paths it is assumed that there is perfect spectral correlation among the sub-intervals of each layer, resulting in a total path transmittance given by

$$T(u) = \sum_{i=1}^{imax} \Delta g_i \sum_{j=1}^{jmax} \exp(-\overline{k}_{ij} u) \quad , \tag{6}$$

where j denotes the sum over layers.

The MODTRAN band model for a single species (multiple species are discussed later) is based on four parameters: (1) the integrated line strength S in a spectral interval Δω ($\Delta\omega = 1$ cm^{-1} in MODTRAN), (2) the effective number of equivalent lines n (non-integer values of n are acceptable) in the interval, (3) the average pressure broadening Lorentz line width γ_L, and (4) the Doppler line width γ_D. These parameters are determined directly from the 1992 HITRAN parameter line compilation (Rothman et al., 1992). The molecular transmittance model is given by

$$T(u) = \left(1 - \frac{W(S_{sl} u, \gamma_L, \gamma_D)}{\Delta\omega}\right)^n \quad , \tag{7}$$

where S_{sl} = S/n is the strength for a single effective line, and W is the Voigt equivalent width of the line taking into consideration only the portion of the line shape which falls within the 1 cm^{-1} MODTRAN spectral interval. This functional form for the band model transmittance derives from the assumption that all the lines in the spectral interval are positionally uncorrelated and thus accounts for line overlap in a statistically average sense. The transmittance contribution due to the tails of lines which originate from outside the spectral interval are included as a single multiplicative Beer's law term. Detailed formulas for the equivalent width W can be found in Berk et al. (1989). As discussed elsewhere (Bernstein et al., 1995), the k-distribution g(k) for the band model can be determined from line-by-line (LBL) simulations which are physically constrained by the same assumptions used to derive Equation (7). The use of real time LBL simulation to derive g(k) during a MODTRAN run is much too slow to be of practical value; however, the approach adopted in MODTRAN4 is to use LBL simulation off-line to pre-compute a table of k-distributions which can be rapidly accessed and interpolated during a run.

4. INITIAL VALIDATION OF MODTRAN4 MULTIPLE SCATTER SOLAR

Development of MODTRAN4 was necessary because MODTRAN3 predictions of multiple scatter solar radiances in spectral regions where non-continuum molecular absorption is important are inaccurate. Unfortunately, this scenario cannot be validated by comparisons to FASCODE because FASCODE does not calculate solar path scattered contributions. Thus, initial validation of MODTRAN4 multiple scatter solar calculations were made directly to measurements.

Figure 1 illustrates a comparison of calculated radiance predictions to airborne measurements (Malherbe et al., 1995) performed by ONERA and CELAR using SICAP, a circular variable filter cryogenic spectrometer (1500 - 5500 nm, 2% spectral resolution). The aircraft altitude was 3.0 km, the cloud top was 2.5 km, the sensor line-of-sight (LOS) zenith angle was 104°, and the solar zenith and relative azimuth angles were 48° and 137°, respectively. Three sets of calculations are shown: (1) results from NAULUM (Malherbe et al., 1995), a new radiative transport model developed at ONERA, (2) MODTRAN calculations performed without the CK approach (labeled MODTRAN3), and (3) MODTRAN calculations performed with the CK approach (labeled MODTRAN4). The MODTRAN4 cloud model upgrade enabled the cloud profile and spectral data to be explicitly entered for both the MODTRAN3 and MODTRAN4 calculations. The cumulus cloud was modeled with a homogeneous liquid water droplet density of 0.68 g/m^3 from 0.1 to 2.5 km altitude. Water droplet single scattering albedos (Hansen et al., 1970) for a mean spherical particle radius of 8μm were entered at a 0.05μm spectral resolution. Both MODTRAN calculations were performed using a simpler two-stream multiple scattering model (Isaacs et al., 1987); the discrete ordinate model in MODTRAN, DISORT (Stamnes et al., 1988), was run with 8-streams over a limited spectral sub-region and produced similar results. Differences between MODTRAN3 (no CK) and MODTRAN4 are small because extinction is dominated by continuum sources.

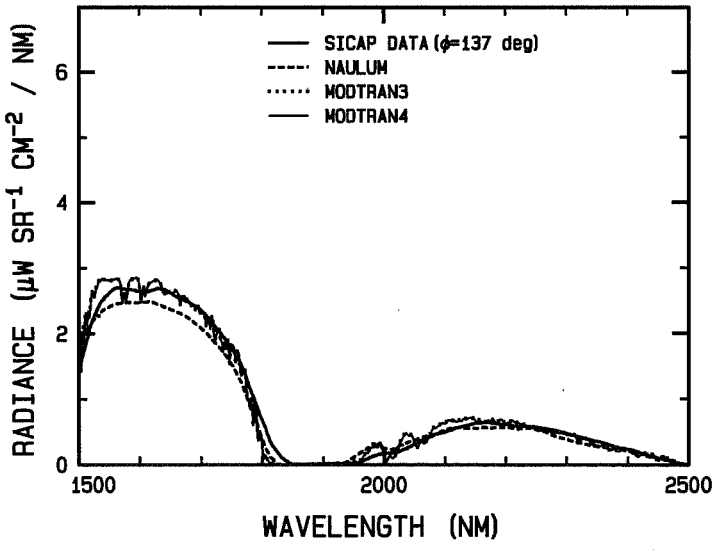

Figure 1. A Comparison Between SICAP Measurements (Malherbe et al., 1995) and Model Predictions for a Solar Illuminated Cumulus Cloud Top with a 137° Relative Solar Azimuth Angle.

Figure 2 illustrates an additional comparison of calculated radiances to SICAP, but with a LOS zenith angle of 95° and, more importantly, with a solar relative azimuth angle of 11°. In this forward scattering case, MODTRAN4 underpredicts the measurements by a factor of 2 because the multiple scattering model averages over the azimuthal dependence (MODTRAN does properly account for the relative azimuth angle in calculation of single scatter solar but single scatter solar is less than 20% of the total radiance in this example). The NAULUM calculation is an improvement over MODTRAN4 because it models the azimuthal distribution of radiation in its discrete ordinate multiple scattering calculation. A new version of DISORT has been developed which also models this azimuthal dependence, but this upgrade has not yet been ported to MODTRAN. For the nadir viewing geometries, such as AVIRIS, the neglect of the azimuthal dependence of the multiply scattered photons in DISORT is a reasonable approximation; similarly, the two-stream Isaac's model is also expected to yield good results.

5. APPLICATION OF MODTRAN4 TO AVIRIS

The primary focus of AVIRIS is the characterization of the Earth's terrestrial surface. For many applications, the upgrade from MODTRAN3 to MODTRAN4 will have only a minor effect on the analysis of AVIRIS data. Under clear sky or thin cirrus conditions, differences between MODTRAN3 and MODTRAN4 down-looking radiances from 20 km in the 400 to 2500 nm spectral region are generally small. This will be true whenever multiple scattering is only a small fraction of the total radiance, or whenever spectral variation of molecular absorption is small. However, these conditions are not always satisfied. Figure 3 illustrates differences between the down-looking radiances predicted by MODTRAN3 and MODTRAN4 in the center of the 1.9μm H_2O band. These calculations were performed with a 1km thick cirrus cloud at 10 km altitude (0.14 vertical extinction at 550 nm), a solar zenith angle of 75°, and using the MODTRAN grass surface reflectances (Mustard, 1991). Within the 1.9μm band region, MODTRAN3 radiances are too high by 0 to 10%.

For measurements of solar illuminated optically opaque clouds, MODTRAN4 upgrades are more critical. In Figure 4, MODTRAN3 and MODTRAN4 mid-IR and near-IR radiances are compared for a nadir view of the MODTRAN model altostratus cloud (ICLD = 2). The observer is at 20 km altitude and the solar zenith was again set to 75°. The cloud/rain model upgrade was used to introduce finer layering near the cloud top (12 layers were placed between 3.0 and 3.5 km altitude). Inaccurate fluxes result from the multiple scattering algorithms if the original coarse layering is used. Even with the fine layering, MODTRAN3 overpredicts MODTRAN4 by approximately 0 to 20% in the center and on the wings of the H_2O molecular bands. This example demonstrates the importance of using MODTRAN4 when analyzing AVIRIS measurements of solar scatter off clouds.

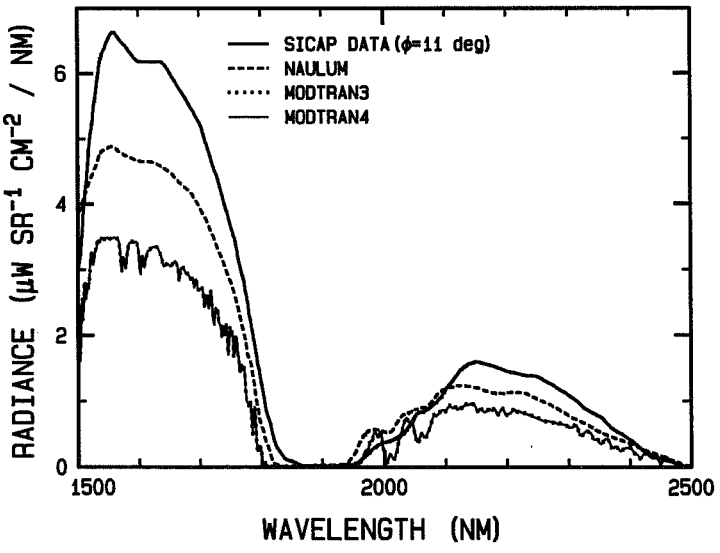

Figure 2. A Comparison Between SICAP Measurements (Malherbe et al., 1995) and Model Predictions for a Solar Illuminated Cumulus Cloud Top with a 11° Relative Solar Azimuth Angle.

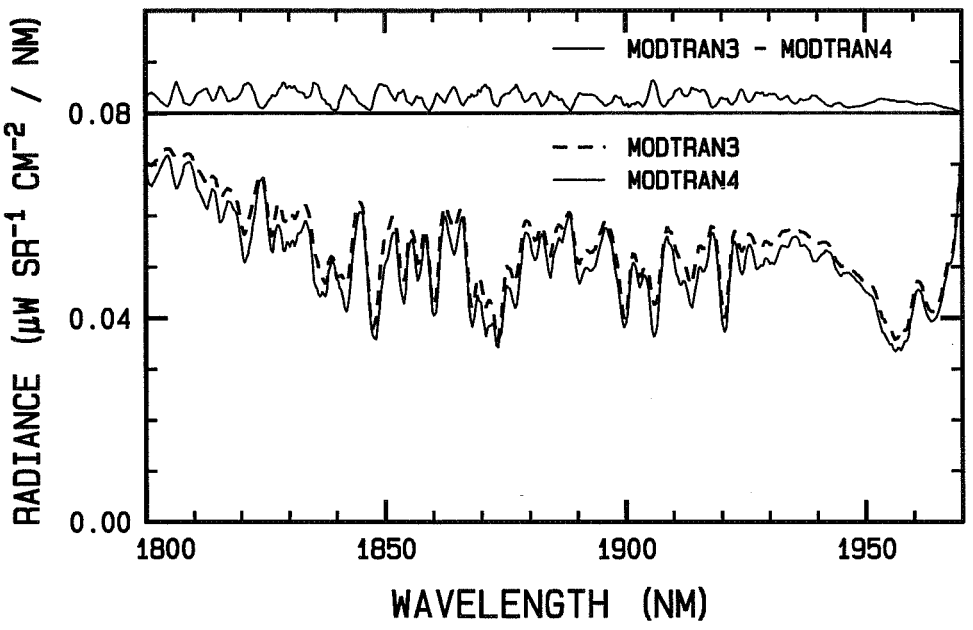

Figure 3. A Comparison Between MODTRAN3 and MODTRAN4 Radiances for Nadir Viewing of the Earth Through a Cirrus Cloud with a 75° Solar Zenith Angle. The differences Between MODTRAN3 and MODTRAN4 Are Offset by 0.08μW sr^{-1} cm^{-2} / nm.

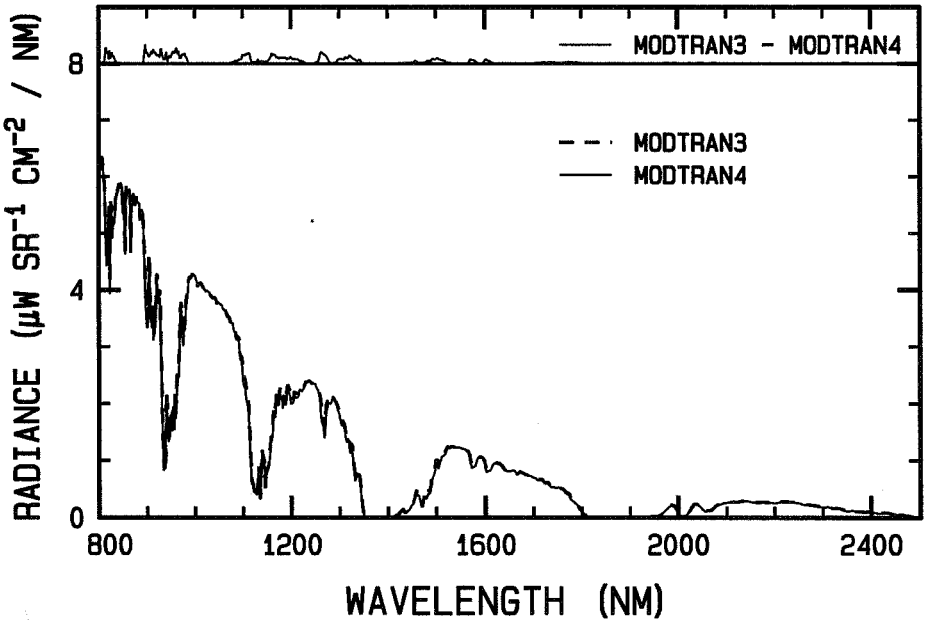

Figure 4. A Comparison Between MODTRAN3 and MODTRAN4 Radiances for Nadir Viewing of the MODTRAN Model Altostratus Cloud with a 75° Solar Zenith Angle. The differences Between MODTRAN3 and MODTRAN4 Are Offset by 8μW sr^{-1} cm^{-2} / nm.

6. SUMMARY

Major MODTRAN upgrades have been introduced which lead to significant improvements in the calculation of solar and thermal scattering from clouds and aerosols. The could/aerosol models now allow for generalized layering and specification of physical and optical properties. The new CK radiative transfer model leads to more accurate multiple scattering calculations, particularly in spectral regions containing strong molecular line absorption. It was shown that multiple scattering contributions can be important even for an optically thin solar illuminated cirrus cloud in the NIR-VIS spectral region; thus, these MODTRAN upgrades will lead to improved data analyses and atmospheric/surface property retrievals from down-looking sensors, such as AVIRIS, whose data are often "contaminated" by sub-visual clouds.

7. ACKNOWLEDGEMENTS

This work has been sponsored by the DOD/DOE/EPA interagency Strategic Environmental Research Program (SERDP) and funded through Air Force contracts F19628-93-C-0049 and F19628-91-C-0083 to Phillips Laboratory, Hanscom AFB, Bedford, Massachusetts. The authors express their appreciation to S. Miller (Geophysics Directorate, Phillips Laboratory) for technical and administrative oversight of this effort, to W. Cornette (Photon Research Associates) for insightful technical discussions, and to P. Simoneau (Office National d'Etudes et de Recherches Aerospatiales) for providing an advance copy of the Malherbe, et al., 1995 manuscript and for permission to include their measurements and calculations in this paper.

8. REFERENCES

Berk, A., 1995, "Upgrades to the MODTRAN Layer Cloud/Rain Models," Rpt. No. SSI-SR-56, Spectral Sciences, Inc., 99 S. Bedford St., Burlington, MA.

Berk, A., L. S. Bernstein, and D. C. Robertson, 1989, "MODTRAN: A Moderate Resolution Model for LOWTRAN7," Rep. GL-TR-89-0122, Air Force Geophys. Lab., Bedford, MA.

Bernstein, L. S., A. Berk, D. C. Robertson, P. K. Acharya, G. P. Anderson, and J. H. Chetwynd, 1996, "Addition of a Correlated-*k* Capability to MODTRAN," Proceeding of the 1996 IRIS Targets, Backgrounds, and Discrimination Mtg.

Clough, S. A., F. X. Kneizys, G. T. Anderson, E. P. Shettle, J. H. Chetwynd, L. W. Abreu, and L. A. Hall, 1988, "FASCODE3 Spectral Simulation" Proceedings of the International Radiation Symposium, Lenoble and Geleyn, Deepak Publishing.

Hansen, J. E. and J. B. Pollack, 1970, "Near-Infrared Light Scattering by Terrestrial Clouds," J. Atmos. Sci., *27*, 265 - 281.

Isaacs, R. G., W. C. Wang, R. D. Worsham, and S. Goldenberg, 1987, "Multiple Scattering LOWTRAN and FASCODE Models," Applied Optics, 26, 1272-1281.

Lacis, A. A., and V. Oinas, 1991, "A description of the Correlated K Distribution Method for Modeling Nongray Gaseous Absorption, Thermal Emission, and Multiple Scattering in Vertically in Homogeneous Atmospheres," J. Geophys. Res., 96, 9027 - 9063.

Malherbe, C., P. Simoneau, A. Boischot, G. Durand, J. Deschamps, and G. Gregoire, 1995, "Radiative Transfer Model in a Cloudy Atmosphere: A Comparison with Airborne Cumulus Measurement," Proceedings of the SPIE Conference on Passive IR Remote Sensing of Clouds and the Atmosphere III.

Mustard, J. F., 1991, "Distributions of Soil, Rock, and Grass in the Western Foothills of the Sierra Nevada," Proceedings of the Third Airborne Visible/Infrared Spectrometer (AVIRIS) Workshop, JPL Publication 91 - 28, 14 - 18.

Rothman, L. S. et al., 1992, "The HITRAN Molecular Database: Editions of 1991 and 1992," J. Quant. Spectrosc. Radiat. Transfer, 48, 469 - 507.

Stamnes, K., S. C. Tsay, W. J. Wiscombe, and K. Jayaweera, 1988, "Numerically Stable Algorithm for Discrete-Ordinate-Method Radiative Transfer in Multiple Scattering and Emitting Layered Media," Applied Optics, 27, 2502-2509.

Page intentionally left blank

52-43
046072
317309
4p.

MINERAL MAPPING WITH 1995 AVIRIS DATA

Joseph W. Boardman[1] and Jonathan F. Huntington[2]

1 Analytical Imaging and Geophysics, L.L.C.
Boulder, Colorado, USA

2 Division of Exploration and Mining
Commonwealth Scientific and Industrial Research Organisation
Sydney, New South Wales, Australia

1. INTRODUCTION

This extended abstract outlines preliminary mineral mapping results obtained using 1995 AVIRIS data acquired over the Oatman area of northwestern Arizona. The data were acquired in the summer of 1995 as a part of a "group-shoot" organized by Analytical Imaging and Geophysics and CSIRO. The results reported here, in the workshop presentation and in the full manuscript demonstrate the dramatic improvement in AVIRIS data quality, analysis tools and the associated advancement of quantitative spectral remote sensing. The improved signal to noise of the AVIRIS data, complemented by new data reduction and processing techniques, permits unambiguous mineral identification and spectral unmixing of subpixel targets. Subtle spectral differences observed and enhanced in the data include: calcite/chlorite discrimination; spectral shifting of muscovite absorption features as a result of cation substitution in mineral chemistry; hematite/goethite discrimination and the unraveling of spectral mixtures of alunite, muscovite and kaolinte.

2. DATA PROCESSING

The processing and analysis are briefly outlined here. There are three main phases in the analysis: preprocessing; reduction to apparent reflectance; and partial unmixing for mineral mapping. More detailed descriptions of these methods will be included in the workshop presentation and full manuscript.

2.1 Noise Characterization and Data Quality Assessment

Noise level estimations were made using the spectral radiance data, and the associated dark current imagery. The signal to noise ratios are very high, and coincide with the predictions of AVIRIS performance after the recent numerous improvements. For a fifty percent reflectance target, the apparent reflectance signal to noise ratio is greater than 1000 in the A spectrometer, and more importantly for geological studies, greater than 400:1 in portions of the D spectrometer. We believe these dramatic improvements in instrument capabilities permit new applications of imaging spectrometry for subtle and detailed surficial composition mapping that have been previously infeasible.

While the overall quality of the data is much improved, several small problems were identified. Channels 13 and 35 exhibit apparent spatial misregistrations. These two spectral channels were dropped from all of our subsequent analyses. A small number of pixels exhibit spectral "spikes" caused by dropped bits in the data. These pixels were identified and dropped from subsequent processing.

2.2 Reduction of AVIRIS Radiance to Apparent Surface Reflectance

The stability and precision of the AVIRIS instrument now exceed the accuracy of radiative transfer models such as MODTRAN and 6S. We believe inherent uncertainty in solar irradiance models, atmospheric transmission calculations and instrument calibration techniques limit the ultimately accuracy of theory-based data

reduction schemes. To circumvent this limitation, we have developed a two stage data reduction scheme combining the best aspects of theory-based and ground target-based methods.

First the data are reduced to apparent surface reflectance using a traditional theory-based approach, for example the ATREM program available from the University of Colorado. This first step models and removes the gross effects of solar irradiance and atmospheric scattering and absorption. However, the ATREM-produced spectral exhibit systematic band-to-band errors. These errors appear as "saw-tooth" noise and give the spectra an unnaturally rough or noisy appearance. We suggest these coherent errors are cumulative gain errors, combining errors in the instrument calibration and the atmospheric and solar modeling.

The second stage of the processing employs an empirical method to estimate these cumulative gain errors and to remove them. Drawing on the ideas of ground target-based reduction methods, we seek to identify a set of pixels and to calculate a best-fit gain function that minimizes the RMS error between their spectra and our model of their desired spectral reflectance curves. However, we use only the AVIRIS data for this process, removing the onerous requirement of *a priori* knowledge of ground target reflectance. Using this method, pairs of observed and modeled spectra are developed for thousands of pixels, permitting a very accurate derivation of the ideal gain function that removes the cumulative calibration and model errors. The method is based wholly on the remotely sensed data and requires no ground spectra. After removal of the calculated gain errors the true fidelity of the 1995 AVIRIS data is revealed. The efficacy of analysis methods based upon direct comparison to spectral libraries is greatly improved. Subtle spectral features that were buried in the systematic errors are made visible.

2.3 Partial Unmixing for Mineral Mapping

Identification and mapping of mineral species and other scene components, such as vegetation, was done in two steps. First, the data were compared to reference, or library, spectra of the desired target materials. This comparison was done both manually, using visual spectral interpretation, and automatically, using comparison metrics including correlation coefficients and spectral angles. This first step resulted in sets of image pixels that best match the desired target spectra. The mean spectra of these best-match pixel sets were used as seeds for the second stage of mineral mapping, an iterative partial unmixing process.

Partial unmixing seeks to accurately map the apparent abundance of a known target material in the presence of a background composed of many unknown, and spatially varying, components. The method is related to matched filtering, but extends that technique by incorporating useful attributes of the mixed pixel model. In this application the partial unmixing was performed in an iterative fashion, with convergence to a final solution after two or three iterations. The final result of the process is an optimal spectral signature for the desired material and an apparent spectral abundance image, mapping the spatial distribution of the target material. Combining the results for various materials permits an examination of the mixing characteristics of the scene components and an improved understanding of the surface geology and processes.

3. GEOLOGICAL RESULTS

The data were processed in two spectral ranges: visible and near infrared (0.4 to 1.0 micrometers) and short wave infrared (2.0 to 2.5 micrometers). Highlights of the results for each spectral region are outlined in this section. A post-analysis field trip is planned for February, 1995. Results of the field verification will be presented at the workshop and in the final manuscript.

3.1 0.4 to 1.0 Micrometer Spectral Range

Hematite, goethite, as well as dry and green vegetation, were mapped using the 0.4 to 1.0 micrometer spectral range. Partial unmixing results for each of these image endmembers were calculated independently using the methods described above. Initial comparison of the AVIRIS-derived mineral maps indicate agreement between the remotely sensed results and spectral measurement of previously acquired field samples. Verification and validation of these results, using field spectrometry and analysis of field samples, are planned for the February field trip.

3.2 2.0 to 2.5 Micrometer Spectral Range

The dramatically increased signal to noise ratio in the D spectrometer of the 1995 data permits an unambiguous discrimination between calcite and chlorite. Both minerals have strong absorption features near 2.35 micrometers, and past AVIRIS studies have had difficulty separating these two similar minerals. In the 1995 data, a secondary feature, an absorption present in chlorite spectra at 2.26 micrometers, is clearly visible. With these high fidelity data, the spatial distributions of chlorite and calcite were independently mapped. The calcite occurs mainly in a vein system, important for mineral exploration in the area. We believe that subpixel-width calcite veins have been detected and will field check these results in February.

The distributions of three types of hydroxyl-bearing minerals (kaolinite, alunite and muscovite) were mapped. Furthermore, excellent examples of mixed pixels were discovered. Evidence for the accurate unraveling of these mixed pixels is found in the scatterplots of the partial unmixing results, color composite imagery of the apparent abundance images and the spectral signatures of the mixed pixels. The high quality of the 1995 data permits both visual and numerical assessment of the spectral mixing on a pixel-by-pixel basis. Field studies planned for February will investigate areas of relative purity as well as highly mixed areas, for validation of the remotely sensed results.

Within the muscovite results, significant spectra shifting of the main 2.2 micrometer spectral feature is apparent. Pixels dominated by muscovite were identified and examined for spectral feature shifting. The position of the muscovite absorption feature was determined by a nonlinear fitting procedure on each of the muscovite-dominated spectra. The spectral position of the feature ranges from 2.190 to 2.210. The spatial position of the shifted spectra shows a coherent pattern. Initial studies of previously collected field samples indicate a correlation of band position with cation chemistry of the phyllosilicates. Further field and laboratory studies are planned to confirm the chemistry controls and to understand the geological significance.

4. CONCLUSIONS

The improvements made to the AVIRIS instrument have dramatically increased its capabilities as a tool for quantitative surface composition mapping. The high quality of the data demands new and innovative data reduction and analysis techniques. Subtle surface chemistry effects are now easily mapped. Subpixel targets are detected and identified. Complex spectrally mixed pixels are recognized and unraveled. The investment in improvement of the instrument capabilities has resulted in a dramatic and measurable advancement in the ability of AVIRIS to perform quantitative surface composition, chemistry and mineralogy studies. The incremental improvement in the D spectrometer appears to have crossed some threshold of data quality for mineral mapping uses, opening a wide range of previously infeasible applications.

5. ACKNOWLEDGMENTS

We would like to thank Robert Green and all the JPL and NASA team members that were involved in improving AVIRIS and facilitation this first "group-shoot" data acquisition.

Page intentionally left blank

ATMOSPHERIC PRE-CORRECTED DIFFERENTIAL ABSORPTION TECHNIQUES TO RETRIEVE COLUMNAR WATER VAPOR: THEORY AND SIMULATIONS

Christoph C. Borel and Daniel Schläpfer [1]
Astrophysics and Radiation Measurements Group, NIS-2, MS C323,
Los Alamos National Laboratory
Los Alamos, New Mexico 87545, USA
cborel@lanl.gov

1 Introduction

Two different approaches exist to retrieve columnar water vapor from imaging spectrometer data:

1. Differential absorption techniques based on:
   (a) Narrow-Wide (N/W) ratio between overlapping spectrally wide and narrow channels (Frouin et al, 1990)
   (b) Continuum Interpolated Band Ratio (CIBR) between a measurement channel and the weighted sum of two reference channels (Green et al, 1989, Bruegge et al, 1990, Gao and Goetz, 1990a, and Carrére and Conel, 1993)
2. Non-linear fitting techniques which are based on spectral radiative transfer calculations (Gao and Goetz, 1990b, Green et al, 1993).

The advantage of the first approach is computational speed and of the second, improved retrieval accuracy. Our goal was to improve the accuracy of the first technique using physics based on radiative transfer. Using a modified version of the Duntley equation (Middleton, 1952, p.68) we derived an "Atmospheric Pre-corrected Differential Absorption" (APDA) technique and described an iterative scheme to retrieve water vapor on a pixel-by-pixel basis (section 2). Next we compared both, the CIBR and the APDA using the Duntley equation for MODTRAN3 computed irradiances, transmissions and path radiance (using the DISORT option). This simulation showed that the CIBR is very sensitive to reflectance effects and that the APDA performs much better (section 3). An extensive data set was created with the radiative transfer code 6S (Vermote et al, 1994) over 379 different ground reflectance spectra. The calculated relative water vapor error was reduced significantly for the APDA. The APDA technique had about 8% (vs. over 35% for the CIBR) of the 379 spectra with a relative water vapor error of greater than $\pm 5\%$ (section 4). The APDA has been applied to 1991 and 1995 AVIRIS scenes which visually demonstrate the improvement over the CIBR technique (see paper in these proceedings: Schläpfer et al, 1996).

2 Derivation of the Atmospheric Pre-Corrected Differential Absorption Technique

Duntley in 1948 expressed the radiance L measured in channel i by a sensor as:

$$L_i = \rho_{g,i} E_i T_i + L_{h,i}(1 - T_i^*) = L_{g,i} T_{0,i} T_i(PW) + L_{p,i}(PW), \quad (1)$$

[1] Permanent Address: Dept. of Geography, RSL, Univ. of Zürich, CH-8057 Zürich, Switzerland, dschlapf@rsl.geogr.unizh.ch

where $\rho_{g,i}$ is the ground reflectance, E_i is the solar irradiance, T_i is the total transmission and $L_{h,i}$ is the radiance one would measure in a plane parallel atmosphere in horizontal direction and T_i^* is a special transmission term (Duntley assumes: $T_i = T_i^*$). The precipitable water vapor PW in $[g/cm^2]$ causes additional atmospheric transmission $T_i(PW)$. The transmission without any water vapor is $T_{0,i}$ and depends on aerosols and gas absorptions. To simplify the notation we define: $L_{g,i} = \rho_{g,i} E_i$. The path radiance $L_{p,i}$ is the sum of the atmospherically scattered radiance L_{atm} and the adjacency scattered radiance L_{adj}.

Using this equation we first write the radiances in three channels $i = m$, $r1$ and $r2$ where m is a measurement channel in an absorption region, e.g. the 940 nm water vapor absorption, and $r1$ and $r2$ are two reference channels. The transmission $T_i(PW)$ is a function of water vapor for channel m but not for the reference channels $r1$ and $r2$. Assuming a small difference between the central wavelengths λ_{r1} and λ_{r2} of the reference channels and $\lambda_{r1} < \lambda_m < \lambda_{r2}$ the radiance $L_m(PW)$ can be approximated by a linear interpolation as:

$$L_m = [w_{r1} L_{g,r1} T_{0,r1} + w_{r2} L_{g,r2} T_{0,r2}] T_m(PW) + L_{p,m}(PW), \tag{2}$$

where

$$w_{r1} = \frac{\lambda_{r2} - \lambda_m}{\lambda_{r2} - \lambda_{r1}} \quad \text{and} \quad w_{r2} = \frac{\lambda_m - \lambda_{r1}}{\lambda_{r2} - \lambda_{r1}}. \tag{3}$$

Note that we assume the reference channels have no water vapor absorption or $T_{r1}(PW) = 1.$ and $T_{r2}(PW) = 1.$. Solving equation (2) for the transmission in the water vapor channel $T_m(PW)$ and substituting $L_{g,r1}$ and $L_{g,r2}$ from equation (1) we find an equation similar to the CIBR (see equation (7)) but with atmospheric pre-correction terms for the path radiances $L_{p,i}$:

$$T_m(PW) = \frac{L_m - L_{p,m}(PW)}{w_{r1}(L_{r1} - L_{p,r1}) + w_{r2}(L_{r2} - L_{p,r2})} \tag{4}$$

Note however that $L_{p,m}$ is also a function of water vapor which can be expressed using a polynomial of second (or higher) order:

$$L_{p,m}(PW) = aPW^2 + bPW + c + L_{\mathrm{adj,m}}, \tag{5}$$

where we neglect the adjacency path radiance $L_{\mathrm{adj,m}}$ for now. In future work we plan to incorporate the adjacency effect in the retrieval over small dark targets and shadow regions where the adjacency effect dominates. The polynomial coefficients a, b and c are fitted to the total radiance over a zero ground reflectance computed by a radiative transfer code such as MODTRAN3 (Abreu et al, 1995) or 6S for the given observation geometry and assumed atmospheric conditions.

$$R_{APDA}(PW) = \frac{L_m - (aPW^2 + bPW + c)}{w_{r1}(L_{r1} - L_{p,r1}) + w_{r2}(L_{r2} - L_{p,r2})}. \tag{6}$$

The following iterative procedure can be used to compute the water vapor $PW(j,k)$ for pixel (j,k):

1. Use a radiative transfer code (6S or MODTRAN 3) to compute the path radiance $L_{p,m}$ for an average reflectance background (e.g. $\rho_{g,i} = 0.4$) as a function of water content and fit a polynomial (eq.(5)) to $L_{p,r1}$ and $L_{p,r2}$ for a zero reflectance backgrounds. Note that the path radiances $L_{p,r1}$ and $L_{p,r2}$ are assumed to be independent of PW.

2. Use a spectral radiative transfer code (6S or MODTRAN 3) to compute the total radiance over a zero reflectance background as a function of water vapor PW. Since the ratio $R_{APDA}(PW)$ decreases monotonically with increasing water vapor a spline interpolation is used to go from a given ratio to columnar water vapor.

3. Assume as a starting value an average water vapor $\overline{PW}_1$ for the whole scene.

4. Compute $R_{APDA}(j,k)$ for each pixel (j,k) using equation (6) and use the cubic spline interpolation to get a second estimate $PW_2(j,k)$ for the columnar water vapor.

5. Substitute $PW_2(j,k)$ for PW the right side of equation (6) to get a better atmospheric pre-corrected differential absorption ratio $R_{APDA}(j,k)$.

6. Determine from the second ratio $R_{APDA}(j,k)$ a third water vapor amount $PW_3(j,k)$ using the cubic spline interpolation.

7. Repeat steps 5 and 6 a few times or until $|PW_i(j,k) - PW_{i-1}(j,k)| \leq 10^{-4}$.

We have compared this iterative technique with the optimum solution where we assume the water vapor is known exactly and the iterative solution performs within a 0.5% of the optimal solution for the 6S generated data set (see section 4).

The continuum interpolated band ratio (CIBR) by contrast is defined as:

$$R_{CIBR} = \frac{L_m}{w_{r1}L_{r1} + w_{r2}L_{r2}} \tag{7}$$

If we assume that the ground reflectances $\rho_{g,i}$ are very low, equation (7) reduces to:

$$R_{CIBR}(\rho_{g,i} \approx 0.) \approx \frac{L_{p,m}(PW)}{w_{r1}L_{p,r1} + w_{r2}L_{p,r2}}. \tag{8}$$

Since $L_{p,r1}$ and $L_{p,r2}$ are constant, the CIBR is then proportional to the water vapor dependent path radiance $L_{p,m}(PW) = L_{h,m}[1 - T_m^*(PW)]$ which is no longer proportional to $T_m(PW)$. When the background reflectance is high, equation (7) reduces to:

$$R_{CIBR}(\rho_{g,i} \approx 1.) \approx Const\ T_m(PW). \tag{9}$$

Thus only for high background reflectances is the CIBR proportional to $T_m(PW)$ and thus can be used to retrieve water vapor.

3 Comparisons of the CIBR and APDA Ratios for a Fixed Water Vapor Amount

To test equations (6) and (7) we computed irradiances, transmissions and path radiance (with MODTRAN3 using the DISORT option). The atmospheric state was mid-latitude summer, visibility of 23 km and the columnar water vapor was fixed at 2.4 g/cm^2. The target height was at 0.4 km, the Sun at 40 degrees with approximately 1 nm spacing. The ground reflectances $\rho_{g,1}$ and $\rho_{g,2}$ was changed from 0.05 to 1. in steps of 0.05 on both sides of the spectral range $(\lambda_{min(r1)}, \lambda_{max(r2)})$ which is defined as the minimum and maximum wavelengths of channels r1 and r2. The following formula is used to create the various reflectance background spectra:

$$\rho_g(\lambda) = \rho_{g,1} + \frac{\rho_{g,2} - \rho_{g,1}}{\lambda_{max(r2)} - \lambda_{min(r1)}}\lambda - \lambda_{min(r1)}. \tag{10}$$

The selected optimum AVIRIS bands (55, 62 and 68) for 1995 data have the following full-width-half-maximum $r1$: 0.869-0.879 μm, m: 0.936-0.946 μm and $r2$: 0.994-1.004 μm (see paper in these proceedings: Schläpfer et al, 1996). From figure 1 it seems that the APDA is less sensitive to reflectance variations than the CIBR for both spectral cases.

Using broader bands, e.g. in a future multispectral sensor such as MODIS, the simulation shows similar results. The selected bands are $r1$: 0.86-0.89 μm, m: 0.91-0.97 μm and $r2$: 0.99-1.04 μm. In figure 1 we show a scatterplot of all computed CIBR and APDA ratios as a function of the band-averaged reflectance in channel 2. Note the large range for the CIBR compared with the APDA techniques. Also the CIBR maps low reflectances ($\rho_{g,m} < 0.2$) to higher ratios, whereas the APDA maps all reflectances to an almost constant ratio. There is still a residual effect visible from reflectance slopes (markers forming lines with

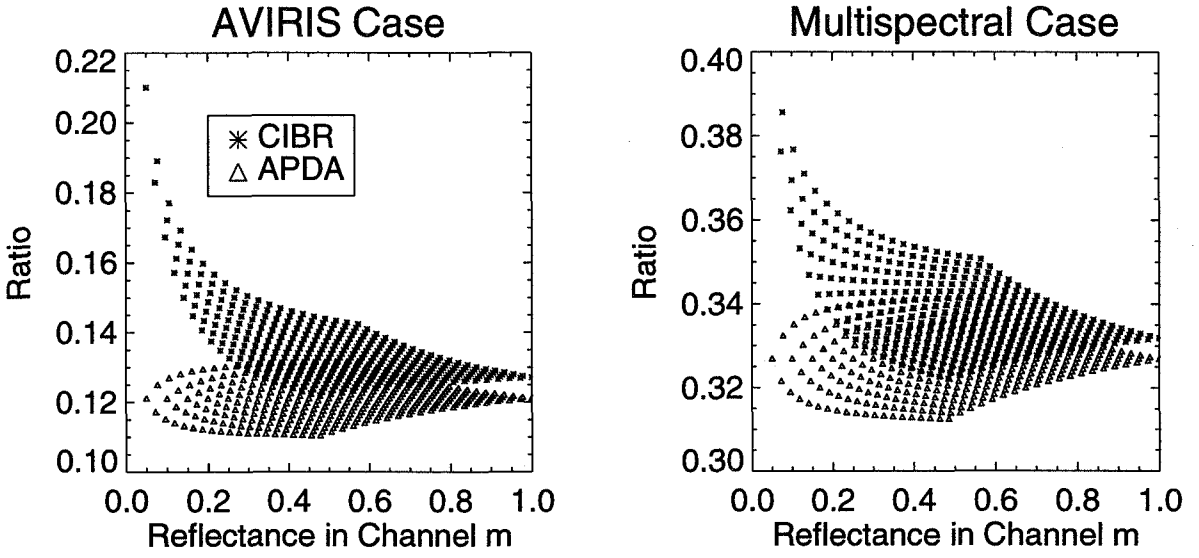

Figure 1: Water vapor ratios as a function of band-averaged ground reflectance of channel 2 for a 10 nm bandwidth instrument (AVIRIS) and a multispectral instrument using Duntley's model.

positive slopes) which could be corrected as well. The influence of reflectance slopes is similar for the CIBR and the APDA. The ratios or quasi water vapor transmittances for the AVIRIS case are much lower than for the multispectral case because the AVIRIS channel selected lies in a deep water absorption feature. Note that we have not yet investigated how the APDA technique depends on atmospheric conditions (aerosol loading, etc), calibration errors and radiative transfer code uncertainties.

4 Comparisons of the CIBR and APDA Ratios for Variable Water Vapor and 379 Reflectance Spectra

To test the behavior of CIBR and APDA techniques over spectrally varying backgrounds we performed a simulation. Existing reflectance spectral data bases for 165 (Grove et al, 1992) and 25 (Kruse et al, 1992) minerals and 64 other spectra of natural and man-made materials were used as background. Since leaves contain significant amounts of water, a data base for 125 simulated leaf reflectance and transmittance spectra with variable leaf water content (0.0046 to 0.0405 cm) was created using the PROSPECT REDUX (Jacquemoud et al, 1995). The radiosity method was then used to compute canopy spectra of a 20-layer canopy with a total leaf area index (LAI) of 5. (Borel et al, 1990).

All 379 reflectance spectra were resampled at 2.5 nm spacings. The radiative transfer code 6S (Vermote et al, 1994) was used to compute the TOA radiance over the water vapor band centered on 940 nm. The water vapor amounts ranged from 0.05 to 5 g/cm^2 in 12 steps. The atmosphere had a constant visibility of 20 km with continental aerosols. The target height was set at sea level and the sensor located above the atmosphere. Only the data for water vapor amounts ≥ 1 g/cm^2 was used in the following analysis. Figure 2 shows the RMS relative error in percent:

$$\varepsilon(PW_j) = 100\sqrt{\frac{1}{N}\sum_{i=1}^{N}[\frac{(PW_{j,true} - PW_{i,est})}{PW_{j,true}}]^2}$$

in water vapor for all N =379 reflectance spectra as a function of water vapor. The four different techniques are:

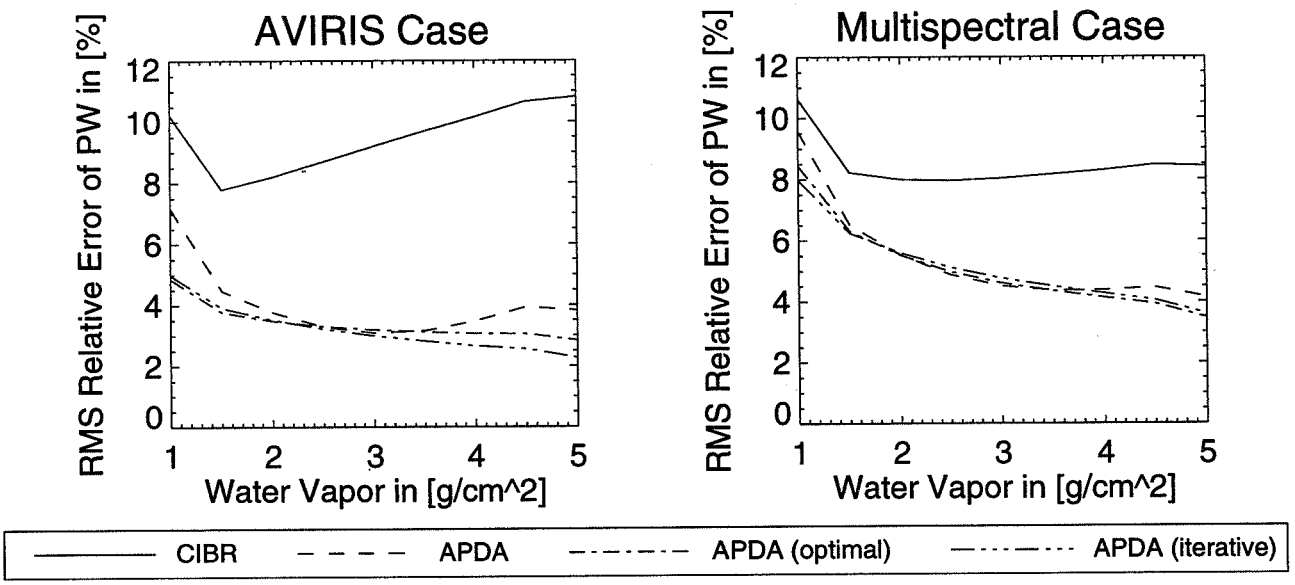

Figure 2: RMS relative error $\varepsilon(PW_j)$ in % in water vapor for all 379 reflectance spectra as a function of water vapor for four different water vapor retrieval techniques.

1. **CIBR**: Original CIBR equation (7).
2. **APDA**: Regular APDA equation (6) using a fixed water vapor amount of 3 g/cm^2 to compute the path radiance $L_{p,m}$.
3. **APDA (optimal)**: Equation (6) with computed water vapor dependent path radiance $L_{p,m}(PW)$.
4. **APDA (iterative)**: Equation (6) with the iterative scheme (5 iterations) described in section 2.

To compare the various water vapor retrieval techniques we defined a measure similar to a quasi signal to noise ratio (SNR):

$$SNR(R_x(PW)) = \frac{\overline{R}_x(PW_{min})) - \overline{R}_x(PW_{max})}{\sigma(R_x(PW))}, \text{ where } x = \{\text{CIBR, APDA, APDA(optimal), APDA(iterative)}\}, \tag{11}$$

where $PW_{min} = 1\ g/cm^2$ and $PW_{max} = 5\ g/cm^2$ are the minimum and maximum water vapor contents, $\overline{R_x(PW)}$ denotes the average over $R_x(PW)$, $\sigma(R_x(PW))$ denotes the standard deviation over $R_x(PW)$. Table 1 shows the minimum and maximum SNR for four retrieval techniques.

Table 1: SNR comparison

Case:	AVIRIS			Multispectral		
Retrieval Technique	Range of R	$\overline{\sigma(R)}$	$SNR_{min/max}$	Range of R	$\overline{\sigma(R)}$	$SNR_{min/max}$
CIBR	0.243	0.01607	14.7-15.8	0.267	0.01511	16.7-17.9
APDA	0.253	0.00604	21.5-58.7	0.277	0.00870	18.4-42.1
APDA (optimal)	0.245	0.00496	30.5-66.8	0.267	0.00789	20.7-50.2
APDA (iterative)	0.246	0.00497	30.5-66.6	0.270	0.00796	21.2-49.7

Next we compare the retrieval methods by setting thresholds at $\pm 5\%$ and $\pm 10\%$ RMS relative water vapor and counting the number of spectra which indicates how robust the retrievals are over many different backgrounds. Table 2 summarizes the results obtained for all 379 background spectra using the four above described techniques:

Table 2: Percentage of reflectance spectra above 5% and 10% RMS Relative Water Vapor Error				
Retrieval Technique	AVIRIS 5%	Multispectral 5%	AVIRIS 10%	Multispectral 10%
CIBR	35.3562	32.9815	9.49868	13.1926
APDA	8.17942	21.1082	1.84697	3.16623
APDA (optimal)	8.70712	20.3166	2.37467	3.43008
APDA (iterative)	7.91557	20.3166	1.84697	3.16623

Figure 3 shows a scatterplot of the relative water vapor errors over 379 backgrounds as a function of band-averaged ground reflectance. The result is that the CIBR has large water vapor errors for low ground reflectance and the regular and iterative APDA work better at low reflectance levels. The AVIRIS case has fewer reflectance spectra above the $\pm$ 10% limit than the multispectral approach, as is also evident from table 2. In both scatterplots the simulated vegetation spectra show up as two clustered sets of points along two lines between reflectances 0.55 and 0.66. The water vapor error is negative because vegetation has a water absorption feature which increases the apparent water vapor in the atmosphere causing a negative error in the estimated atmospheric water vapor. This feature could potentially be exploited to estimate canopy water content (Gao and Goetz, 1990b). Some of the materials which the iterative APDA had relative water vapor errors of more than $\pm$ 10% are listed below in Tables 3 and 4.

Table 3: Materials with RMS Relative Water Vapor Errors > 10% (AVIRIS Case)	
CUMMINGTONITE-IN-6A (sloped) (non-linear)	ENSTATITE-IN-10B (sloped) (non-linear)
FAYALITE-NS-1A (dark) (sloped) (non-linear)	HEMATITE-FE2602 (sloped) (non-linear)
MOLYBDENITE-S-11A (sloped)	SIDERITE-COS2002 (sloped) (non-linear)
TRIPHYLITE-P-4A (sloped)	

Table 4: Materials with RMS Relative Water Vapor Errors > 10% (Multispectral Case)	
ANTHOPHYLLITE-IN-8A (non-linear)	ANTLERITE-SO-11A (sloped) (non-linear)
BUDDINGTONITE-NHB2301	CUMMINGTONITE-IN-6A (sloped) (non-linear)
DICKITE-PS-3A (dark) (sloped) (non-linear)	ENSTATITE-IN-10B (sloped) (non-linear)
FAYALITE-NS-1A (dark) (sloped) (non-linear)	HEMATITE-FE2602 (sloped) (non-linear)
MOLYBDENITE-S-11A (sloped)	SIDERITE-COS2002 (sloped) (non-linear)
TOURMALINE-DRAVITE-S-CS-1A (dark) (sloped) (non-linear)	
TRIPHYLITE-P-4A (sloped)	

A spectrum was classified as 'dark' if the average reflectance in channel m was below 0.1. A spectrum was considered 'sloped' if the absolute of the normalized difference:

$$R_{slope} = \frac{|\overline{\rho_{g,r1}} - \overline{\rho_{g,r2}}|}{\overline{\rho_{g,r1}} + \overline{\rho_{g,r2}}}.$$

between the channel averaged reflectances of channels $r1$ and $r2$ exceeded 0.05. A spectrum was considered 'non-linear' if the ratio:

$$R_{non-linear} = \frac{\overline{\rho_{g,m}}}{w_{r1}\overline{\rho_{g,r1}} + w_{r2}\overline{\rho_{g,r2}}}$$

was less than 0.95 or greater than 1.05.

5 Conclusions

An efficient technique to determine the amount of columnar water vapor has been derived from a modified radiative transfer equation. The technique seems to work much better than the current CIBR techniques which neglect the effects of path radiance. We show how the CIBR and APDA behave over dark, bright and

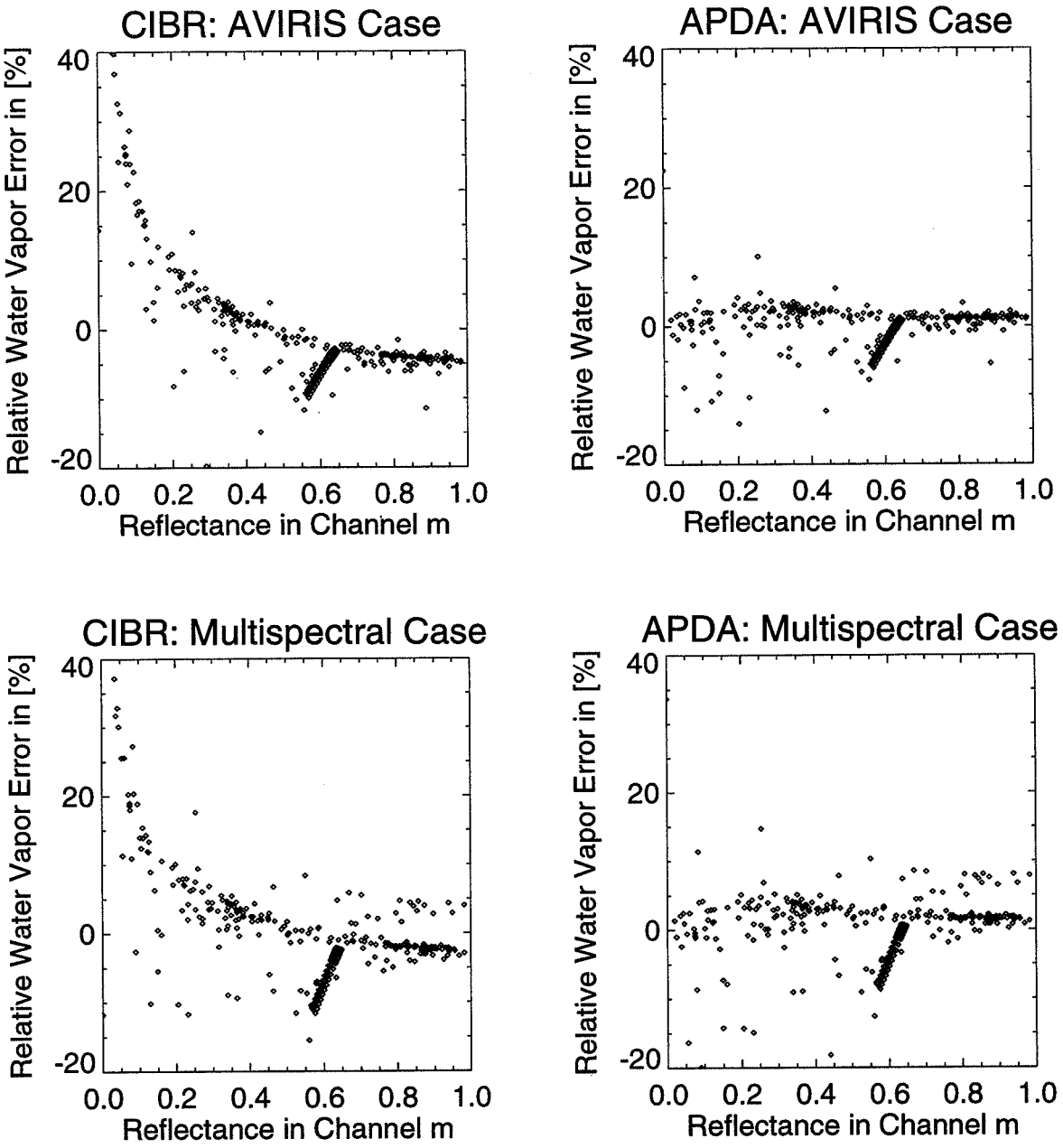

Figure 3: Relative water vapor errors over 379 backgrounds as a function of band-averaged ground reflectance for a 10 nm bandwidth instrument (AVIRIS) and a multispectral instrument. Note the lined up points near 0.6 reflectance are from canopy spectra.

spectrally variable backgrounds. A large number of mineral, man-made and simulated vegetation spectra were used and the relative water vapor error lies within $\pm 5\%$ for most reflectance spectra. We think this accuracy is sufficient for current applications since sensor calibration and modeling errors are estimated to have similar relative errors. A challenge remains to determine water vapor over dark surfaces such as water since the path radiance is now the only quantity containing information about the water vapor. More work is also needed to retrieve water vapor in rough terrain. The presented techniques may also be useful to retrieve other gases such as CO_2 and O_2.

6 Acknowledgments

This work has been funded by NASA HQ's Remote Sensing Science Program and the Department of Energy. The principal author acknowledges many fruitful technical discussions with and work done by Veronique Carrére (ISPRA, Italy), Jennifer Johnson (summer student at LANL in 1995) and Bill Clodius (LANL). James Theiler (LANL) reviewed the paper very carefully.

7 References

Abreu L.W., Chetwynd J.H, Anderson G.P. and Kimball L.M., 1995, MODTRAN 3 Scientific Report. Draft Preprint, Geophysics Laboratory, Air Force Command, US Air Force, Hanscom AFB, Ma, USA.

C.C. Borel and Gerstl S.A.W., Non-linear Spectral Mixing Models for Vegetative and Soil Surfaces, 1994, Remote Sens. of the Environment, 47:403-416.

Bruegge C.J., Conel J.E., Margolis J.S., Green R.O., Toon G., Carrére V., Holm R.G. and Hoover G., 1990, In-situ Atmospheric Water-Vapor Retrieval in Support of AVIRIS Validation., SPIE Vol. 1298 Imaging Spectroscopy of the Terrestrial Environment, pp 150 - 163.

Carrére V. and Conel J. E.,1993, Recovery of Atmospheric Water Vapor Total Column Abundance from Imaging Spectrometer Data around 940 nm - Sensitivity Analysis and Application to Airborne Visible/ Infrared Imaging Spectrometer (AVIRIS) Data. Remote Sensing of Environment, Nr. 44 , pp 179 - 204.

Frouin R., Deschamps P.-Y and Lecomte P., 1990, Determination from Space of Atmospheric Total Water Vapor Amounts by Differential Absorption Near 940 nm: Theory and Airborne Verification. Journal of Applied Meteorology, Vol. 29, American Meteorological Society, pp 448 - 459.

Gao B.-C. and Goetz A.F.H.,1990a, Determination of Total Column Water Vapor in the Atmosphere At High Spatial Resolution from AVIRIS Data Using Spectral Curve Fitting and Band Ratioing Techniques, SPIE Vol. 1298, Imaging Spectroscopy of the Terrestrial Environment, pp 138 - 149.

Gao B.-C. and Goetz A.F.H.,1990b, Column Atmospheric Water Vapor and Vegetation Liquid Water Retrievals from Airborne Imaging Spectrometer Data, Journal of Geophysical Research, Vol. 95, No. D4, pp 3549 - 3564.

Green, R.O., Carrére V. and Conel J.E., 1989, Measurement of Atmospheric Water Vapor Using the Airborne Visible/Infrared Imaging Spectrometer, Am. Soc. Photogram. and Remote Sensing, Workshop Image Processing, Sparkes, Nevada, 23-26 May.

Grove C.I., Hook S.J. and Paylor E.D., 1992, Spectral Reflectance of Minerals 0.4 to 2.5 Micrometes, JPL Publication 92-2.

Jacquemoud S., Ustin S.L., Verdebout J., Schmuck G., Andreoli G. and Hosgood B. , PROSPECT REDUX, 1995, Proceedings AVIRIS Workshop, Pasadena, January.

Kruse F.A., 1992, unpublished data. IUGS Special Publication.

Middleton, W.E.K., 1952, "Vision Through the Atmosphere," University of Toronto Press.

Schläpfer D., Borel C.C., Keller J. and Itten K., 1996, Atmospheric Pre-Corrected Differential Absorption Techniques to Retrieve Columnar Water Vapor: Application to AVIRIS 91/95 Data, Proceedings AVIRIS Workshop, Pasadena, March.

Vermote E., Tanré D., Deuzé J.L., Herman M. and Morcette J.J., 1994, Second Simulation of the Satellite Signal in the Solar Spectrum. , 6S User Guide Version 0, NASA-Goddard Space Flight Center, Greenbelt, USA, P 182.

Page intentionally left blank

Discrimination of Low Levels of Green Vegetation Cover Using a High Spectral Resolution Vegetation Index

Zhikang Chen
Commercial Remote Sensing Program, Lockheed Martin Engineering & Sciences Co.
Stennis Space Center, MS 39529

Christopher D. Elvidge
Biological Sciences Center, Desert Research Institute
University of Nevada System
Reno, NV 89506

David P. Groeneveld
Resource Management
Telluride, CO 81435

1. Introduction

Vegetation vigor or cover status is currently monitored globally using broad-band vegetation indices (e.g. NDVI, PVI, RVI, and SAVI etc). These red versus near-infrared (NIR) vegetation indices operate by contrasting the chlorophyll pigment absorption in the red with the high reflectance of green leaves in the NIR. Under conditions of low (≤30%) green canopy cover, background rock, soil, and litter materials produce a range of vegetation index values, dramatically degrading the accuracy of broad band vegetation indices. Broad-band data are unable to distinguish slope variations from the red to NIR in background materials from the red versus NIR signal of green leaves at green vegetation cover levels of typical arid and semi-arid regions. Our previous field experiment, conducted by high spectral-resolution ASD's PS-2 reflectance data with bandwidth of 4 nm, showed that the narrow-band conventional vegetation indices (DVI, NDVI, PVI, RVI, SAVI, $SAVI_2$, and TSAVI) have higher accuracy than the corresponding simulated broad-band vegetation indices on quantifying vegetation cover, especially the low (≤30% green cover) and very low (≤10% green cover) green cover conditions. However, derivative-based green vegetation indices (DGVI) derived from continuous PS-2 reflectance spectra proved to be the best among all of the tested broad- and narrow-band vegetation indices. DGVI was up to several times better than broad-band NDVI and RVI in prediction accuracy. The highest prediction accuracy of low green cover levels by DGVI is due to DGVI's optimally minimizing background impacts (brightness and red-NIR slope effects) on green vegetation signals centered at the chlorophyll red-edge. DGVI is defined as the integration of 1st/2nd order derivative spectra across chlorophyll red-edge spectral range in reference to a local or zero baseline and focuses on measuring the amplitude of the chlorophyll red-edge. Our previous study with AVIRIS data also revealed that the chlorophyll red-edge feature of Monterey pines can be readily detected in the high spectral resolution AVIRIS reflectance spectra for green cover levels ≥4.8%. Therefore, introduction of DGVI to AVIRIS data could lead to mapping low cover levels

of green vegetation with higher accuracy at larger scale.

2. Methods

Radiometrically calibrated AVIRIS data, which were acquired on October 3 of 1990 over a commercially operated Monterey pine plantation in Jasper Ridge, California, were used for this study. The Monterey pine plantation had nearly identical background soil and single Monterey pine species (*Pinus radiata*). Due to periodic cultivation, understory weeds were basically removed. Field check found only a little dry grass present in the plantation. Low altitude aerial photography of the plantation was acquired before the AVIRIS flight and used in assisting determination of locations and percent green cover levels of 22 sampling sites (Figure 1).

Entire AVIRIS scene of the study area was converted to 1st and 2nd order DGVI values on the pixel by pixel basis. Raw DN spectrum of each AVIRIS pixel was calibrated to ground reflectance in the full AVIRIS spectral range using a series of calibration targets ranging from dark to bright in brightness. The reflectance spectrum of each pixel was subsequently smoothed by a low pass filter to remove high frequency noise. Using equations (1) and (2), the 1st and 2nd order derivative reflectance spectra were then generated separately. Finally, the 1st order DGVI with local baseline correction (1DL_DGVI) and 2nd order DGVI using zero baseline (2DZ_DGVI) values of the pine plantation were calculated using equations (3) and (4). No local baseline correction is necessary for calculating 2DZ_DGVI.

$$\rho'(\lambda_i) = \frac{\rho(\lambda_{i+1}) - \rho(\lambda_{i-1})}{\lambda_{i+1} - \lambda_{i-1}} \qquad (1)$$

$$\rho''(\lambda_i) = \frac{\rho'(\lambda_{i+1}) - \rho'(\lambda_{i-1})}{\lambda_{i+1} - \lambda_{i-1}} \qquad (2)$$

$$1DL\_DGVI = \sum_{\lambda_1}^{\lambda_n} |\rho'(\lambda_i) - \rho'(\lambda_1)| \Delta\lambda_i \qquad (3)$$

$$2DZ\_DGVI = \sum_{\lambda_1}^{\lambda_n} |\rho''(\lambda_i)| \Delta\lambda_i \qquad (4)$$

In equations (1) to (4), i represents band number and λ_i represents center wavelength at the ith band. λ_1=626.1 nm (band 24) and λ_n=795.8 nm (band 45). The ρ, ρ', and ρ'' represent reflectance, 1st and 2nd order derivative reflectance, respectively.

3. Results

Vegetation signals centered at chlorophyll red-edge were enhanced in both 1st and 2nd

order derivative reflectance spectra. The red-edge feature for the site with 2% green cover level was more recognizable in its derivative reflectance than in the reflectance spectra. Higher linear regression coefficients (r^2 values) were acquired for percent green cover levels of the 22 sampling sites with corresponding 1DL_DGVI and 2DZ_DGVI values (Figure 2).

Both 1DL_DGVI and 2DZ_DGVI maps quantitatively delineated spatial variations of green cover conditions of the plantation and adjacent areas. Based on the existing strong linear relationship between the DGVI values and green cover densities of 22 sample sites from the pine plantation, the percent green cover levels of entire Monterey pine plantation were inversely estimated, including the areas with ≤1% cover level. The two percent green cover maps generated from 1DL_DGVI and 2DZ_DGVI showed very similar green distribution patterns. Visual examination of these two percent green cover maps showed that all of the 22 sample sites fall in the correct range of green cover (Figure 3).

4. Conclusion

Monitoring of green vegetation in arid and semi-arid lands will be substantially improved using imaging spectrometer data (e.g. AVIRIS data) with a continuous series of narrow bands across the chlorophyll red-edge region. Detection limit of low green cover levels can be further enhanced in derivative reflectance spectra of AVIRIS data. DGVI, which is developed on the basis of minimizing the linearly mixed background impacts on green vegetation signals, is a very effective and practical way to observe variations in green vegetation cover in arid and semi-arid regions.

5. Acknowledgements

This research was done at the Desert Research Institute in Reno, Nevada. The research was supported in part by the U.S. Environmental Protection Agency through Cooperative Agreement CR-816826.

Airborne Visible/Infrared Imaging Spectrometer (AVIRIS)
(Jasper Ridge Biological Preserve, CA; October 3, 1990)

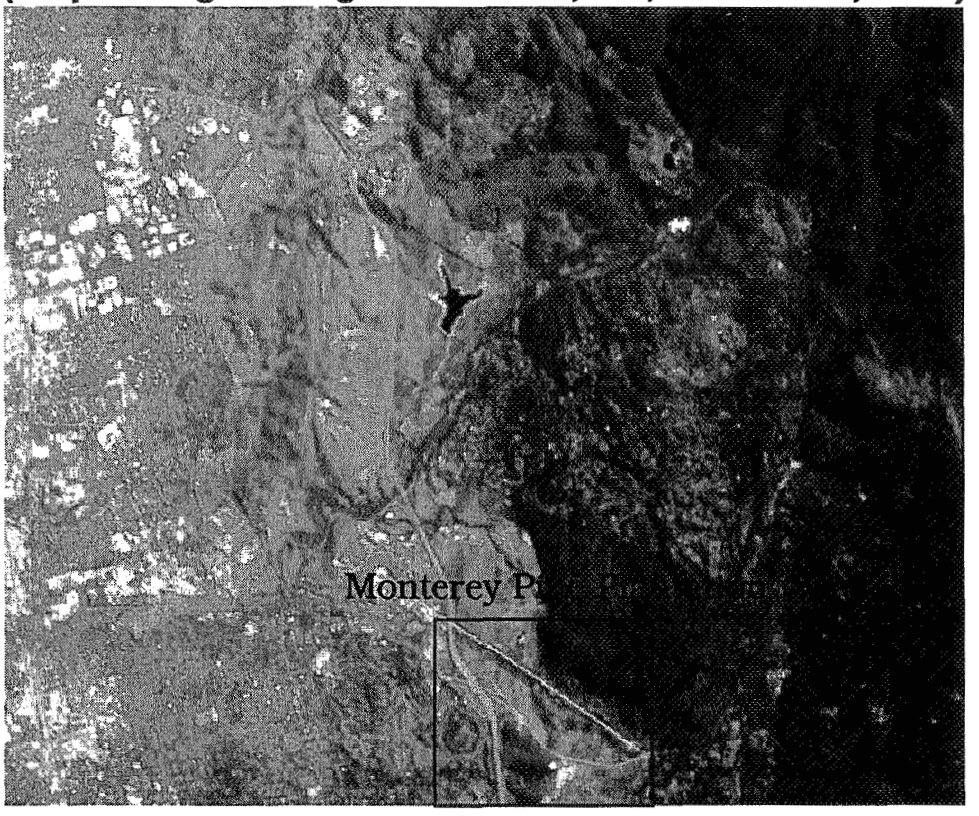

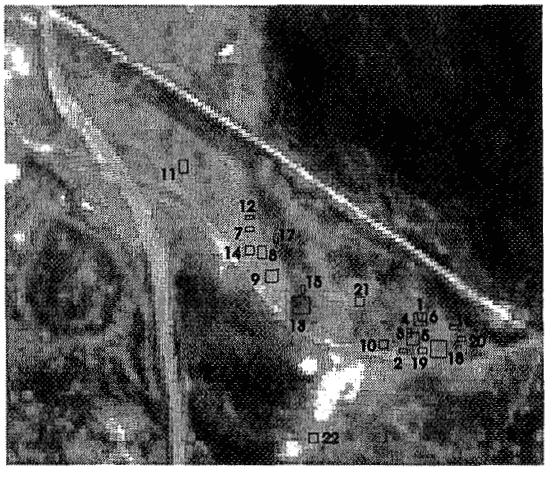

Red: 805.4 nm (CH. 46)
Green: 557.4 nm (CH. 17)
Blue: 449.5 nm (CH. 6)

desert research institute

Figure 1. AVIRIS 3-band false color composite of Jasper Ridge Biological Preserve, CA. The bottom image contains the Monterey pine plantation with 21 sample stands inside. The no. 22 stand is outside the plantation.

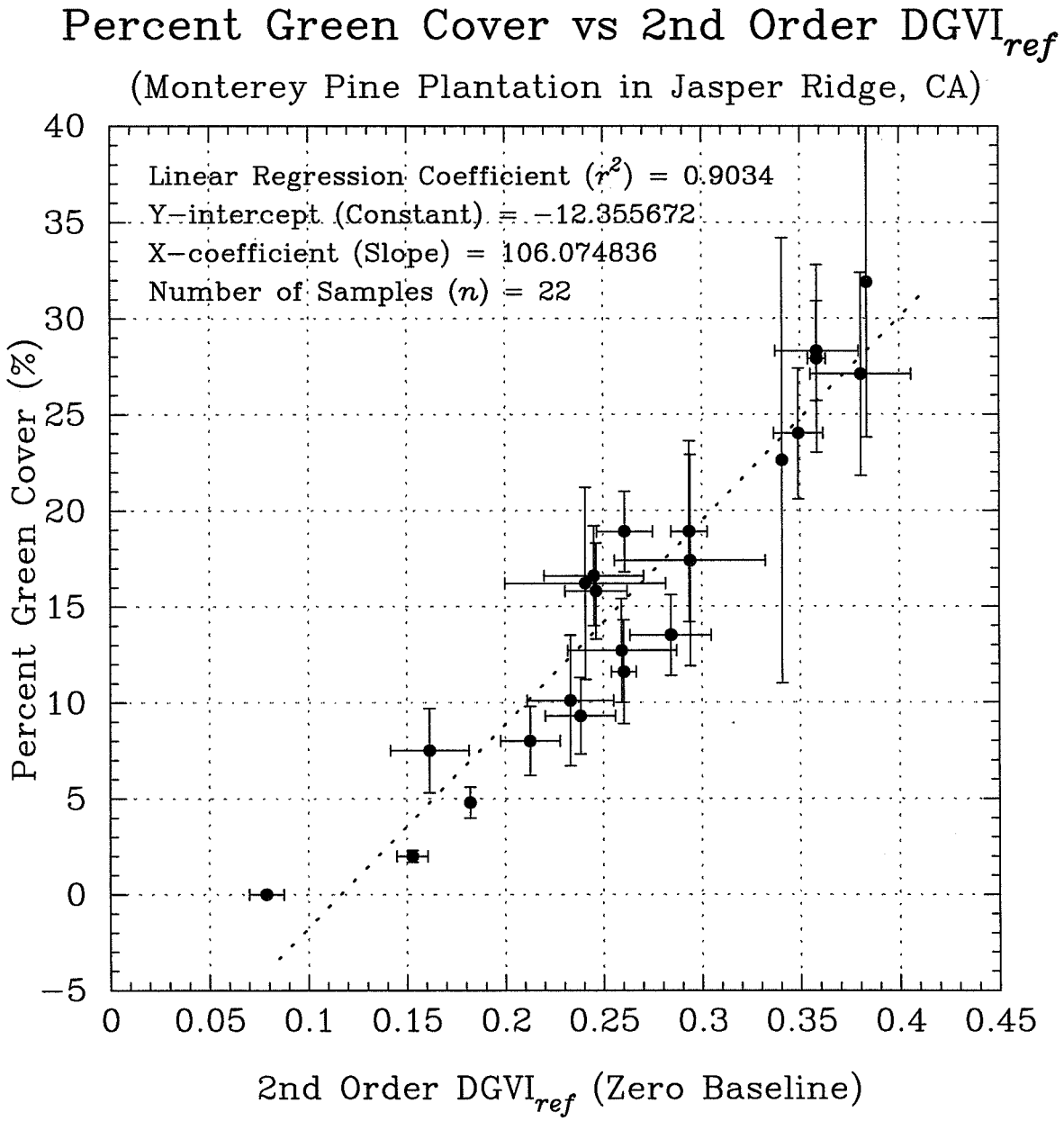

Figure 2. Percent green cover levels of 22 sampling sites versus 2nd order DGVI calculated from AVIRIS reflectance in reference to zero baseline (2DZ_DGVI). Horizontal and vertical bars represent standard deviations of the 2DZ_DGVI and percent green cover data.

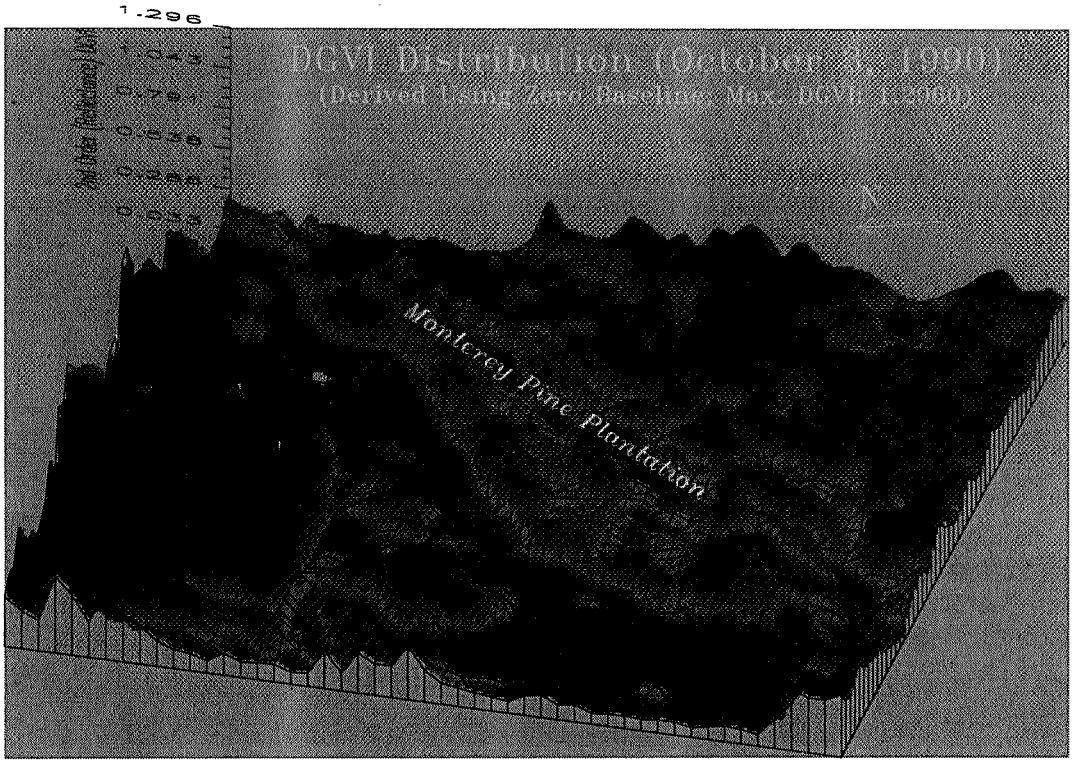

2nd Order DGVI Distribution
(Derived From Reflectance Spectra Using Zero Baseline)

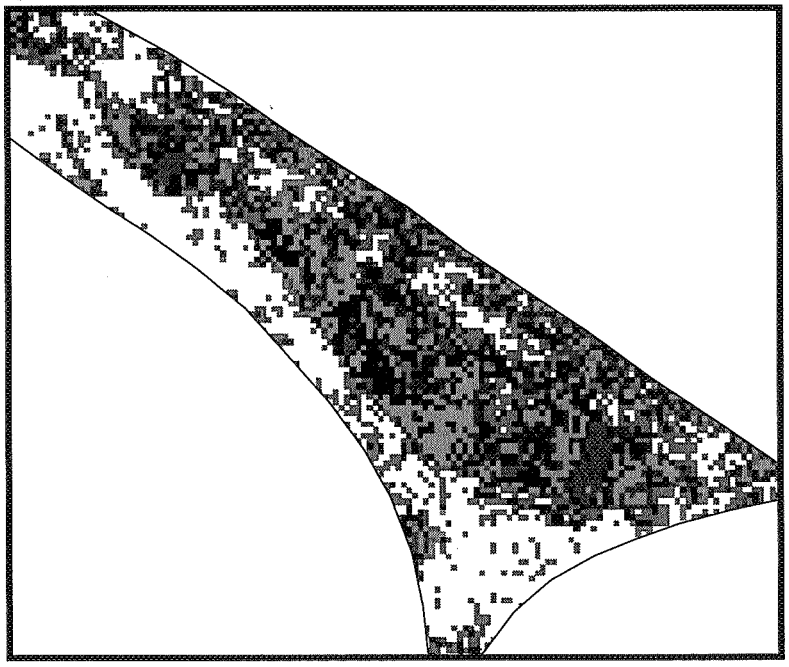

Green Cover Level
(%)

White:	< 1
Cyan:	1 - 4
Blue:	4 - 7
Green:	7 - 10
Light Green:	10 - 15
Red:	15 - 20
Orange:	20 - 30
Yellow:	> 30

desert research institute

Figure 3. Top: 2DZ_DGVI (2nd order derivative-based green vegetation index derived using zero baseline) distribution pattern of Monterey pine plantation and adjacent areas in Jasper Ridge, CA; Bottom: Percent green cover of Monterey pine plantation estimated from the 2DZ_DGVI values.

S5-43
046075

Monitoring Seasonal Dynamics of Arid Land Vegetation Using AVIRIS Data 10P.

Zhikang Chen*, Christopher D. Elvidge#, David P. Groeneveld+ 317345

* - Commercial Remote Sensing Program/Lockheed Martin Engineering & Sciences Co., Stennis Space Center, MS 39529; # - Biological Sciences Center/Desert Research Institute, University of Nevada System, Reno, NV 89506; + - Resource Management, Telluride, CO 81435

1. Introduction

The study of land vegetation cover conditions represents a major part of earth system science whether one is considering energy, water, carbon and nutrient cycles. Vegetation vigor, cover status and seasonal dynamics can affect many hydrologic factors on the regional to global scale, such as surface albedo, surface sensible and latent heat exchanges, rainfall infiltration , runoff and erosion. Thus plants have a major impact on inputs to ground water and surface hydrology, water, energy and cycling of the nutrients through the entire hydrologic cycle. Morever, vegetation cover is also a sensitive indicator of carbon status (storage and release). Change in the carbon status of plant communities may result in potential of insect outbreak and influence amount of carbon available to atmosphere. As one of the "forcing agents", concentration of carbon (e.g. CO_2) and its change in atmosphere play an important role on "greenhouse" effects. Therefore accurate estimation of land vegetation cover conditions and seasonal dynamics will improve the hydrologic modelling quality for surface hydrologic processes, evapotranspiration (ET) and other hydrologic variables as well as the estimation of carbon flux between the land surface and the atmosphere. Approximately 1/3 of land surface on the earth is arid and semi-arid areas. Due to limited water supply, vegetation in these areas are more sensitive to climate change and have rapid response to human induced impacts. As earlier study indicated, the expansion and contraction of the Saharan desert can be detected by vegetation monitoring using AVHRR data. So accurate mapping of vegetation cover density and seasonal dynamics in arid lands will certainly benefit the understanding and modelling of global change.

Our previous study with AVIRIS data of a Monterey pine plantation in Jasper Ridge Biological Preserve, CA has shown that derivative approach is very effective at minimizing background material's impacts and enhancing weak vegetation signals centered at chlorophyll red-edge. The derivative-based green vegetation index (DGVI) derived from AVIRIS reflectance of the plantation accurately quantified the spatial cover variations of the pines ranging from 1% to 32%. But this Monterey pine plantation has relatively uniform background and only a single plant species - Monterey pine (*Pinus radiata*). Thus reliability and robustness of the DGVI for quantifying low cover levels of green vegetation need to be further tested with AVIRIS data in an area with more complicated background materials and mixed vegetation communities.

2. Study Area

Mono Lake region was selected as the study area for the project. The Mono Lake area has a wide variation in rock and soil characteristics including colors, components, and spectral signatures. This area is a semi-arid region with different vegetation density levels. Major

vegetation types in the area include shrubs (e.g. bitterbrush, sagebrush and rabbitbrush), salt grass, and pine forest.

3. Data Acquisition and Analysis

A total of ten sampling stands were selected in the study area. One stand is located in a pumice surfaced area with no vegetation cover. Nine others are bitterbrush (*Purshia tridentata*), which was selected as a reference species for monitoring DGVI's performance. The ten sampling stands were measured of the leaf area index (LAI) in field during AVIRIS data acquisition. The LAI was defined in this study as the ratio of leaf area over projected area of canopy on the ground.

Two AVIRIS datasets of Mono Lake area were separately collected on August 20 and October 7 of 1992. The two images acquired at different seasons were registered to each other by linear transform warping. Both images covers same series of pre-selected calibration targets. Using gains and offsets derived from the calibration targets, the two images were calibrated to ground reflectance in the full AVIRIS spectral range by empirical line method. Although the green cover levels were low, the red-edge feature was well recognizable in the August AVIRIS reflectance spectra of the bitterbrush stands. After weather became colder in October, the red-edge magnitudes decreased and became subtle due to loss of green leaves.

Before applying derivative, a low pass filter called Blackman window was used to smooth the reflectance spectra of the ten sample stands. The first and second order derivative reflectance spectra were then calculated using spectral distance between every other band as derivative interval. Using equations (1) and (2), both 1DL_DGVI (1st order DGVI derived using local baseline) and 2DZ_DGVI (2nd order DGVI derived using zero baseline) were generated.

$$1DL\_DGVI = \sum_{\lambda_1}^{\lambda_n} |\rho'(\lambda_i) - \rho'(\lambda_1)| \Delta\lambda_i \qquad (1)$$

$$2DZ\_DGVI = \sum_{\lambda_1}^{\lambda_n} |\rho''(\lambda_i)| \Delta\lambda_i \qquad (2)$$

In equations (1) and (2), i represents band number and λ_i represents center wavelength at the ith band. λ_1=626.9 nm (band 25) and λ_n=792.9 nm (band 45). The ρ, ρ', and ρ'' represent reflectance, 1st and 2nd order derivative reflectance, respectively.

Linear regression results exhibited strong linear relationship between the 2DZ_DGVI and LAI values of the ten sampling stands, having r^2 values greater than 0.93 for both AVIRIS datasets. However, the linearity between the 1DL_DGVI and LAI values appeared very poor due to contribution from negative derivatives of gravel materials in the barren areas to the calculation of the 1DL_DGVI. To correct the errors introduced by the negative derivatives of the gravel materials, the definition for the 1DL_DGVI was modified. The modified 1DL_DGVI (i.e. 1DL_MDGVI) is expressed in equation (3).

$$1DL\_MDGVI = \sum_{\lambda_1}^{\lambda_n} [\rho'(\lambda_i) - \rho'(\lambda_1)]\Delta\lambda_i;\ if\ \rho'(\lambda_i) - \rho'(\lambda_1) \geq 0 \qquad (3)$$

By linear regression, the 1DL_MDGVI demonstrated strong linear correlation with the LAI values of the ten sample stands. High r^2 values (≥0.92) were acquired for both AVIRIS datasets collected in August and October of 1992.

4. Results

On the pixel by pixel conversion basis, equations (2) and (3) were applied to entire scene of the two AVIRIS images. Comparing two green cover maps developed from the 1DL_MDGVI and 2DZ_DGVI using August AVIRIS data, similar distribution patterns appear in the maps. Similarity of the green vegetation distribution patterns also exists in the green cover maps derived from the October's 1DL_MDGVI and 2DZ_DGVI. But the overall green vegetation cover levels of the study area decreased in October.

Seasonal changes in green cover density can be quantitatively analyzed by differencing DGVI values acquired for different seasons. The difference DGVI was calculated from following equation:

$$Difference\ DGVI = October's\ DGVI - August's\ DGVI \qquad (4)$$

In general, herbaceous species (e.g. salt grass) responded more sensitively to seasonal changes in the study area and had bigger drop in green cover density from August to October. Shrubs including bitterbrush and sagebrush changed less. The seasonal cover changes of shrubs were basically due to losing green leaves. The least change in cover density between the two dates happened in regions covered by Ponderosa pines (*Pinus ponderosa*).

5. Conclusion

Although background materials are more complex at Mono Lake, derivative approach still proved optimal in reducing background impacts on green vegetation signals across the red-edge region. The relative cover variations and vegetation health status of low vegetated regions with mixed plant species can be quantified by 2DZ_DGVI and 1DL_MDGVI with high accuracy. The cover change intensity due to change of seasons can also be easily derived from difference DGVI maps. Thus, DGVI could provide a practical and more accurate way for operational monitoring ecosystems in arid and semi-arid lands.

It has to be emphasized that analysis of hyperspectral data (e.g. AVIRIS) and development of DGVI should be based on ground reflectance spectra as opposed to the radiance spectra. Radiance spectra have instrument effects removed, but still contain solar irradiance and atmospheric effects which would impair the operation of any vegetation index. This has also been evaluated in this project.

6. Acknowledgements

This research was done at the Desert Research Institute in Reno, Nevada. The project was supported in part by the U.S. Environmental Protection Agency through Cooperative Agreement CR-816826.

Table 1 LAI Values of 10 Bitterbrush Sample Sites

Sample Site	Sept. 4-5, 1992		Oct. 3-4, 1992	
	LAI	Std Dev	LAI	Std Dev
Site 1	0.000	0.000	0.000	0.000
Site 2	0.289	0.125	0.236	0.080
Site 3	0.526	0.208	0.431	0.124
Site 4	0.473	0.195	0.387	0.121
Site 5	0.496	0.210	0.406	0.132
Site 6	0.661	0.259	0.541	0.153
Site 7	0.318	0.128	0.261	0.078
Site 8	0.381	0.148	0.312	0.087
Site 9	0.426	0.174	0.349	0.106
Site 10	0.326	0.149	0.267	0.098

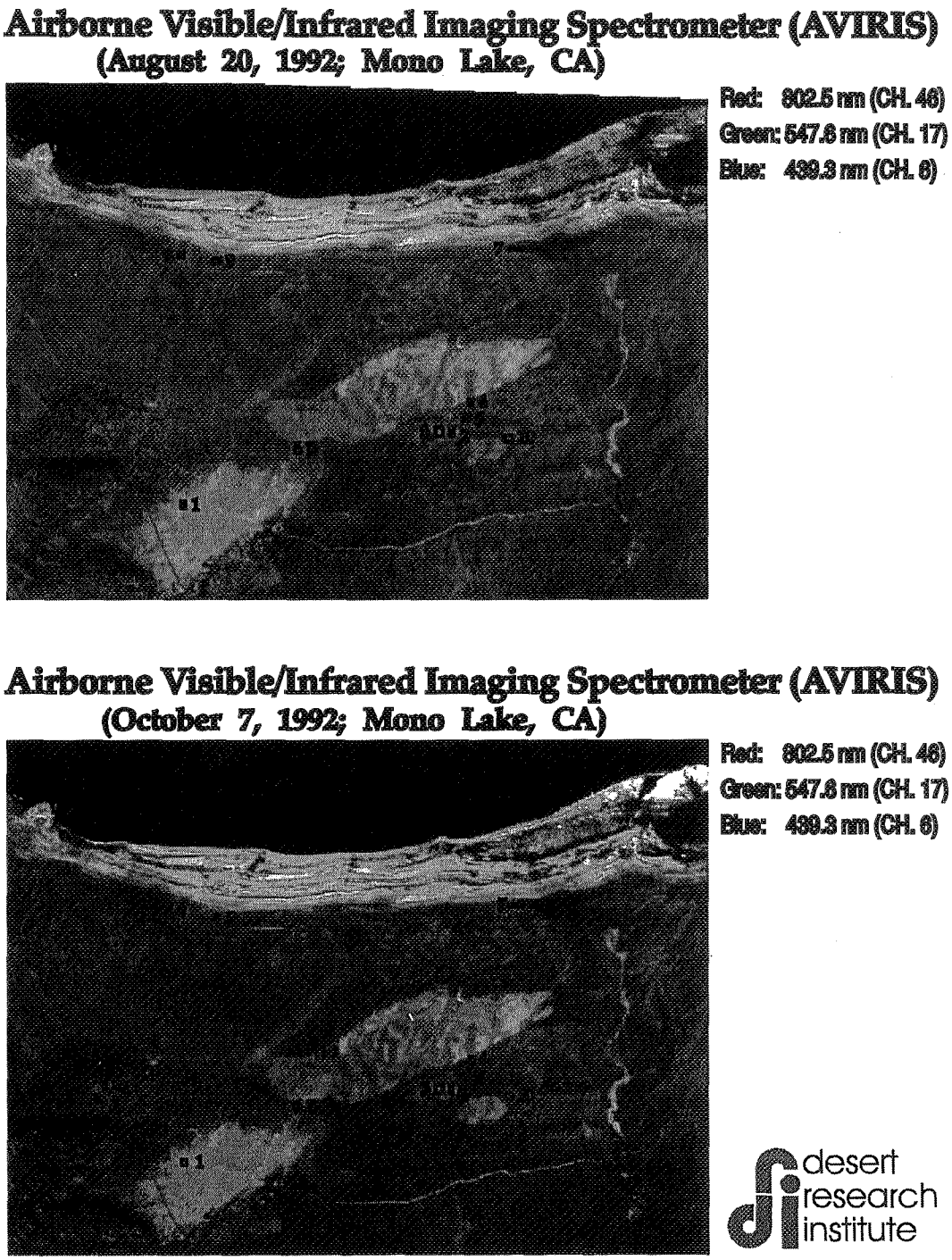

Figure 1. AVIRIS 3-band false color composite of the Mono Basin, CA. The top image was taken on August 20, 1992. The bottom image was acquired on October 7, 1992. Nine bitterbrush sample stands and a grey-colored pumice gravel stand (no.1) are displayed in both images.

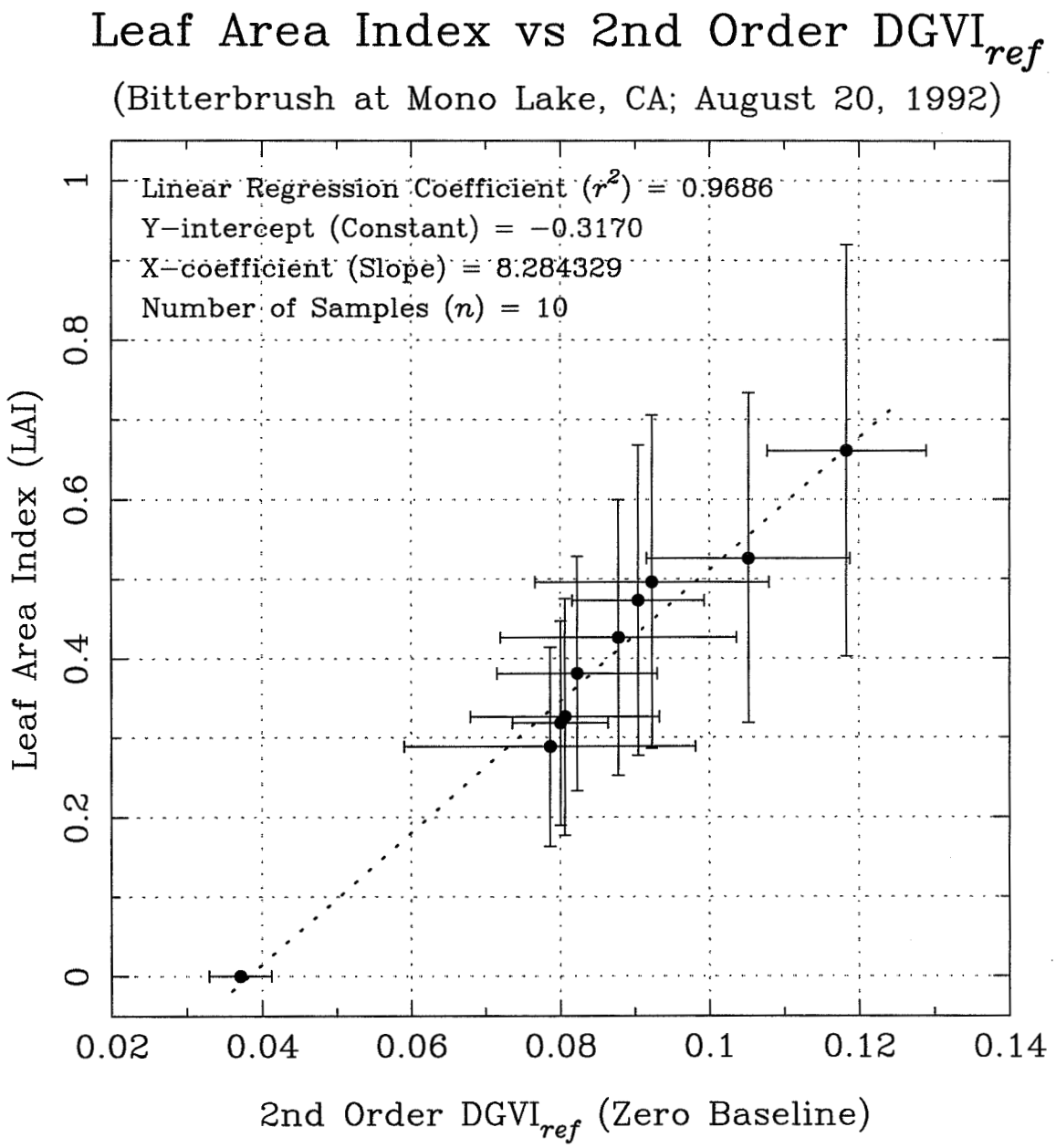

Figure 2. LAI values versus 2nd order DGVI calculated from 2nd order derivative reflectance of August 20, 1992 AVIRIS in reference to zero baseline (2DZ_DGVI). Horizontal and vertical bars represent standard deviations of the 2DZ_DGVI and LAI data.

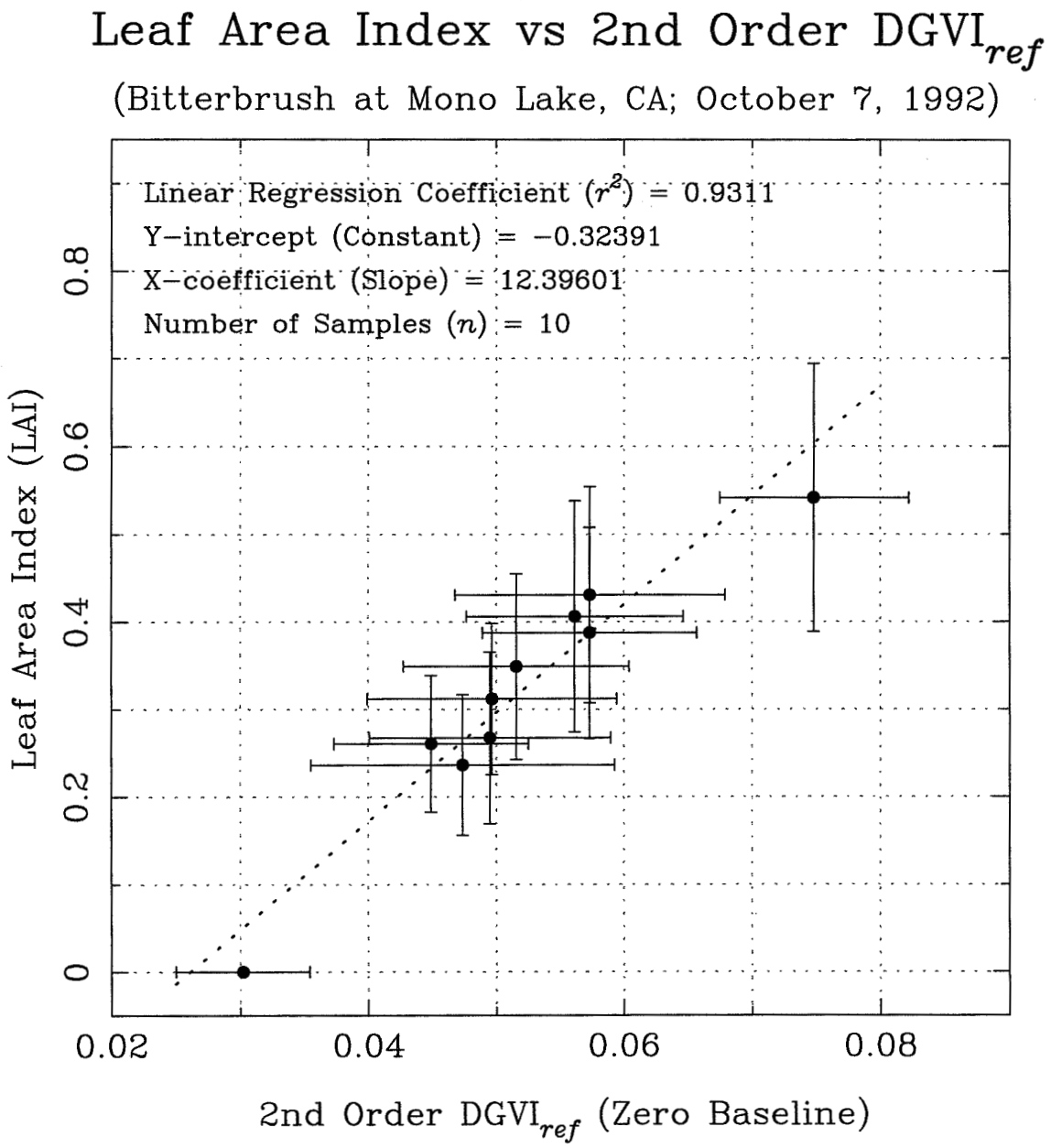

Figure 3. LAI values versus 2nd order DGVI calculated from 2nd order derivative reflectance of October 7, 1992 AVIRIS in reference to zero baseline (2DZ_DGVI). Horizontal and vertical bars represent standard deviations of the 2DZ_DGVI and LAI data.

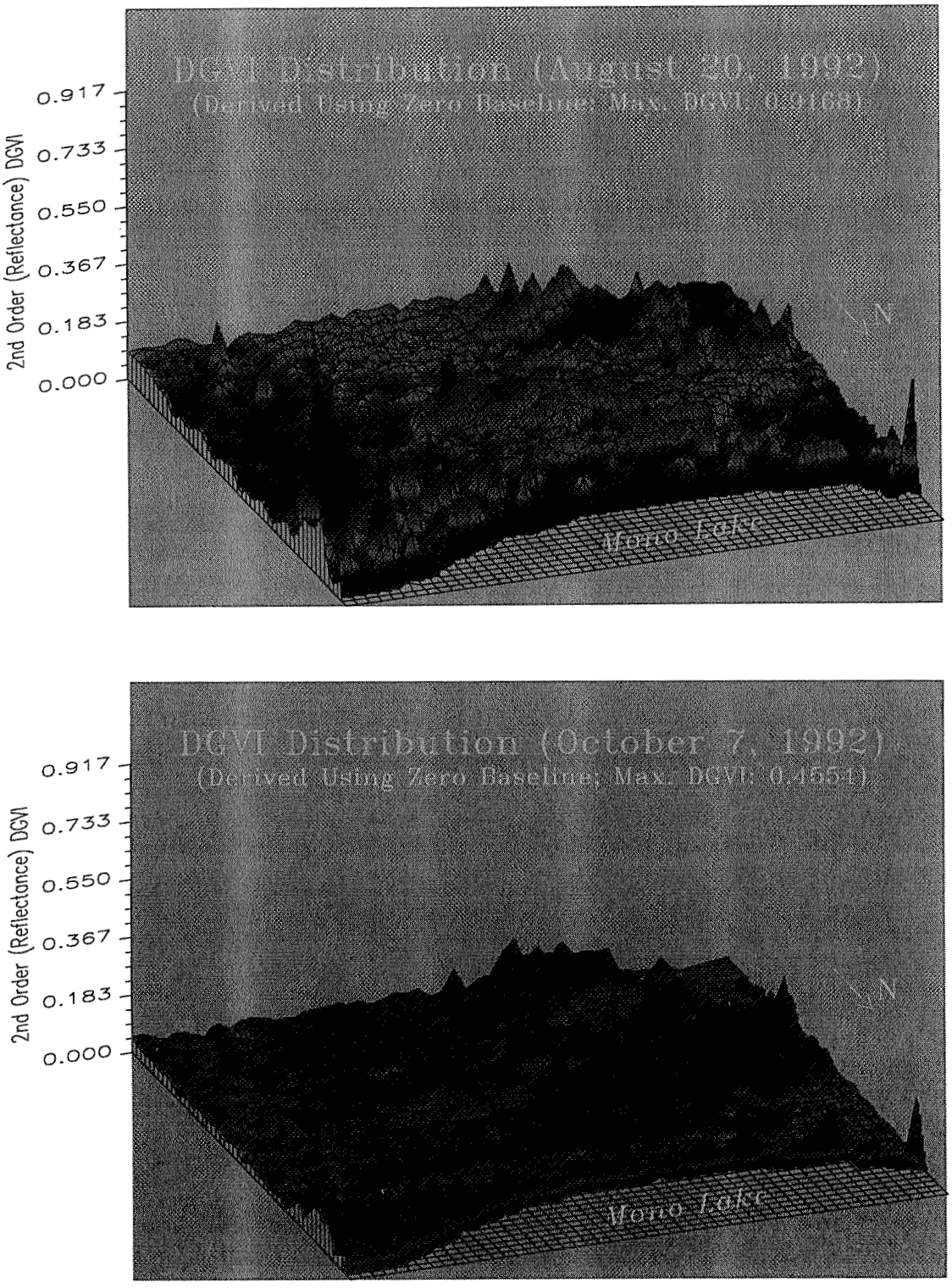

Figure 4. 3-D display of 2DZ_DGVI. Top map shows vegetation cover status on August 20, 1992. Bottom map displays vegetation cover status on October 7, 1992.

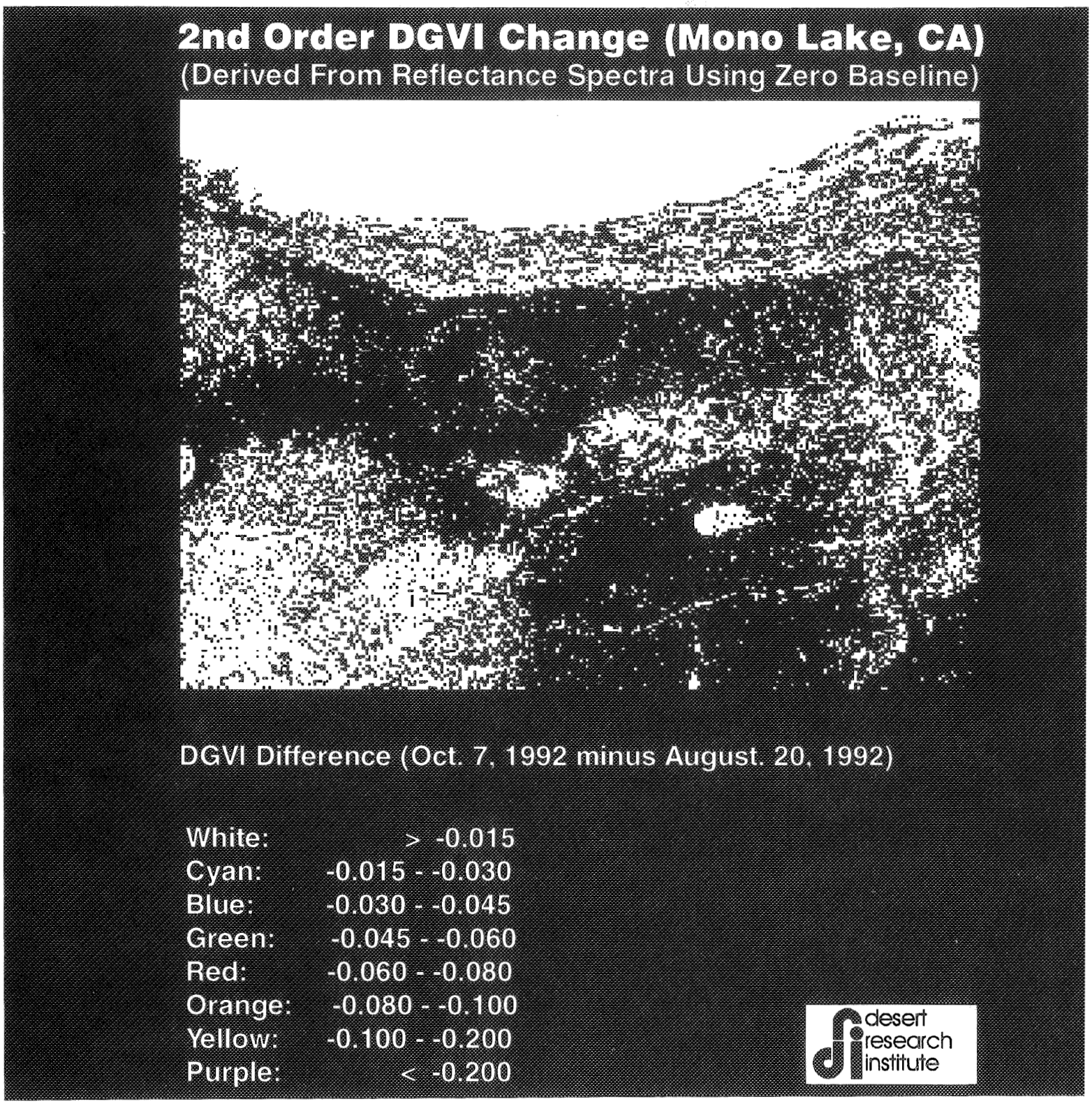

Figure 5. 2-D display of the difference 2DZ_DGVI distribution status. Seasonal change (decrease) in green vegetation cover of the study area is exhibited.

Page intentionally left blank

Calibration of the Airborne Visible/Infrared Imaging Spectrometer in the Laboratory

Thomas G. Chrien, Robert O. Green, Christopher J. Chovit,
Michael L. Eastwood, and Charles M. Sarture

Jet Propulsion Laboratory, California Institute of Technology, Pasadena, CA 91109

1.0 Introduction

Imaging spectrometry data must be spectrally, radiometrically and geometrically calibrated in order to 1) derive physical parameters from measured spectral radiance, 2) compare data acquired from different regions and at different times, 3) compare and analyze the imaging spectrometry data with data acquired from other calibrated sensors, and 4) compare and analyze data with results from computer models. The calibration of AVIRIS data is the process by which laboratory characterization data are applied to raw instrument data (digitized number versus spectral channels) to produce quantitative spectra (radiance versus wavelength) for each image pixel in units of spectral radiance. The AVIRIS sensor and calibration process are described by Vane (Vane et al., 1993) and the application of the calibration data to the raw digital data is described by Green (Green et al., 1991). This calibration process is validated for in-flight performance of the sensor using a rigorous ground-truth campaign (Green et al. 1996).

This workshop paper reviews the laboratory characterization data set that is used in the AVIRIS calibration process. The laboratory measurements used to acquire the calibration data are divided into three classes: 1) spectral calibration, 2) radiometric calibration, and 3) spatial calibration.

2.0 Spectral Calibration

The collection of spectral calibration data for AVIRIS was first described by Vane (Vane et al., 1987) and then updated by Chrien (Chrien et al., 1990). The spectral calibration requirement for AVIRIS is 0.1 nm accuracy in channel center wavelength and channel full width at half maximum (FWHM) (Green, 1995a) based on a sensitivity to the ubiquitous narrow solar and atmospheric absorptions in the upwelling spectral radiance. The method is to measure the response of each of the 224 AVIRIS channels to narrow bandwidth light (~1 nm FWHM) as the light is scanned in wavelength across the spectral response of the channel. A monochromator and collimator, as shown in Figure 1a, are used to measure the spectral response. Figure 1b shows a typical example of the Gaussian function fit to a channel spectral response from which the center wavelength and FWHM channel width are derived. The wavelength calibration of the monochromator is traced to mercury vapor, neon and krypton emission lamps.

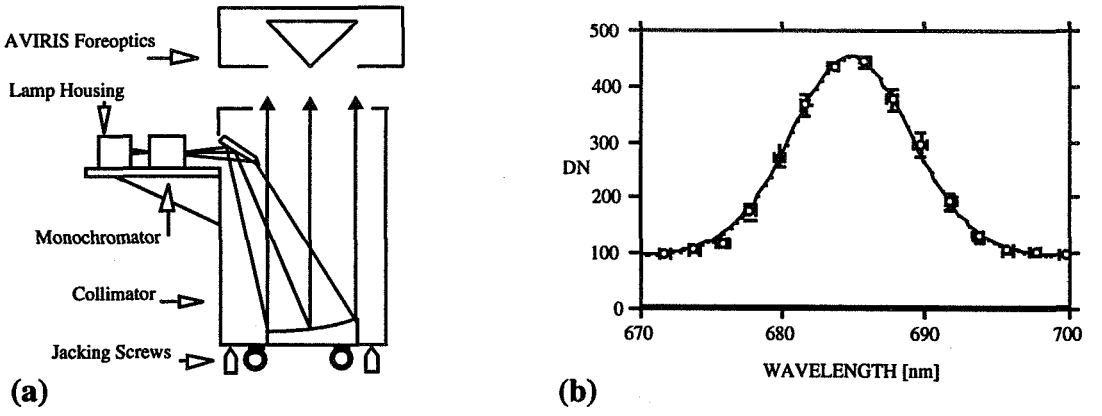

FIGURE 1. a) Laboratory spectral calibration setup. b) Typical spectral response function with error bars and best-fit Gaussian curve from which center wavelength, FWHM bandwidth, and uncertainties are derived.

The spectral response data are collected for each of the 224 spectral channels as the monochromator wavelength increments through the AVIRIS spectral range. The center wavelength and FWHM width for each channel are determined, with uncertainties, from a Gaussian fit to the raw response curve for that channel. The center wavelength for each of the 224 spectral channels' fit is shown in Figure 2 (bold line), where discontinuity in the line denotes the spectral overlap between the four AVIRIS spectrometers. The associated uncertainty in the determination of center wavelength is shown on the same plot by reading the right axis.

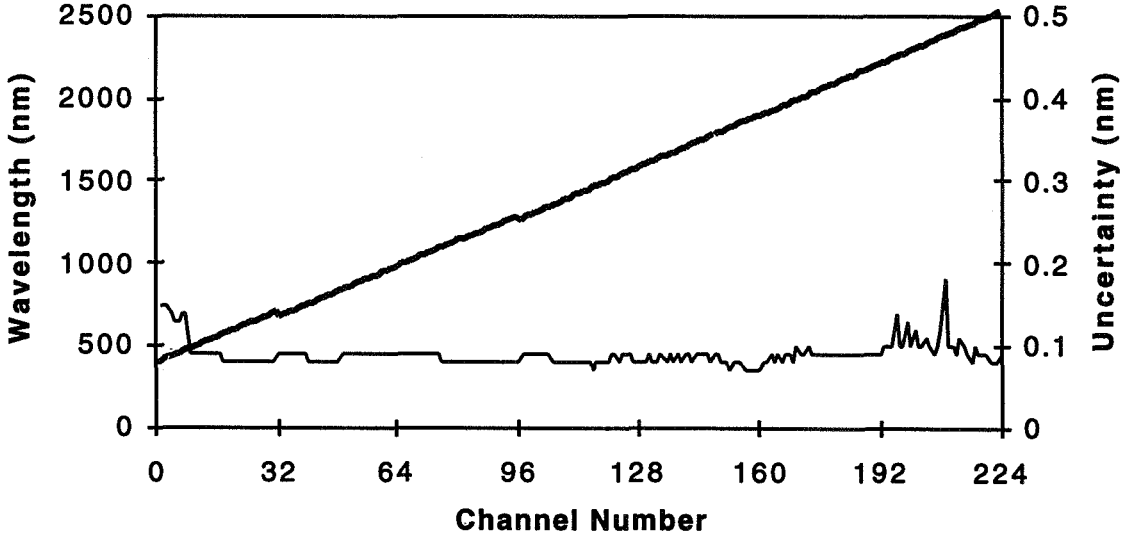

FIGURE 2. Derived center wavelengths for each AVIRIS channel (bold line), read from left axis, and associated uncertainty in center wavelength knowledge (normal line), read from right axis.

The best-fit Gaussian FWHM bandwidth for each of the 224 spectral channels is shown in Figure 3 (bold line). The associated uncertainty in the determination of FWHM bandwidth

is shown on the same plot by reading the right axis. A majority of the channels meet the calibration uncertainty goal of less than 0.1 nm in absolute knowledge of center wavelength and FWHM channel width.

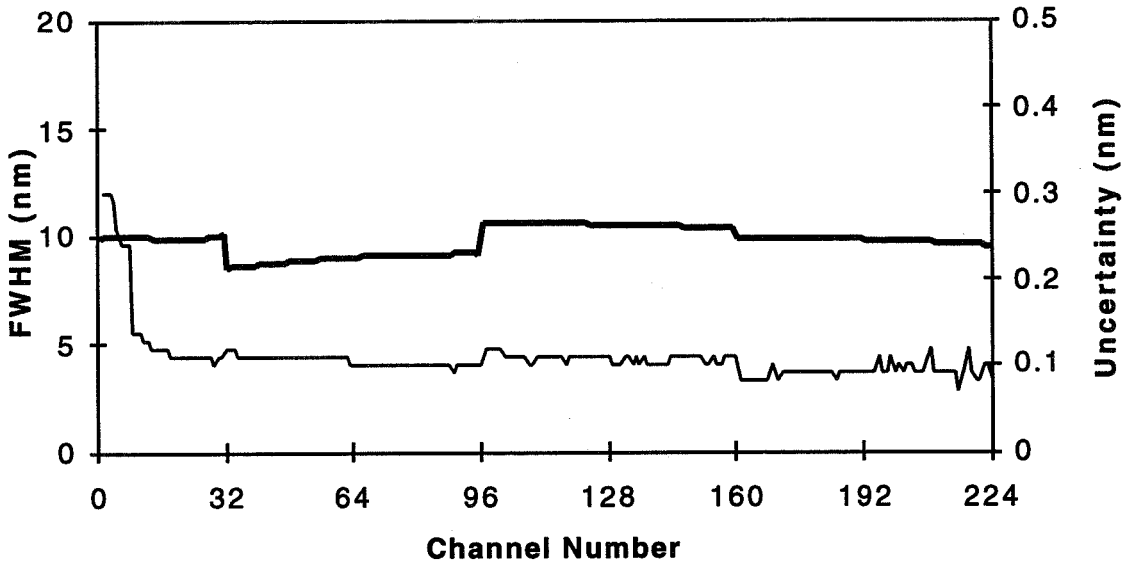

FIGURE 3. Derived FWHM bandwidth for each AVIRIS channel (bold line), read from left axis, and associated bandwidth uncertainty (normal line), read from right axis.

The in-flight calibration of the spectral response has been validated using a least-squares curve fit to atmospheric features over carefully characterized field targets such as Lunar Lake, Nevada, and Rogers Dry Lake, California (Green, 1995b; Green et al., 1993). The AVIRIS onboard calibration system can also be used to monitor minute changes in the spectral response by computing the transmittance of the spectrally feature-full filters and observing shifts with respect to filter data acquired at the time of the laboratory calibration (Chrien et al., 1995).

3.0 Radiometric Calibration

The absolute radiometric calibration of the AVIRIS sensor is determined by measuring the radiometric response of the sensor to a standard of known spectral radiance. The standard is constructed from an irradiance standard lamp and a reflectance standard panel as shown in Figure 4. The standards are purchased with calibrations traceable to the National Institute of Standards and Technology (NIST). The spectral radiance of the standard, $L(\lambda)$, is computed using EQ 1:

$$L(\lambda) = \frac{E(\lambda)R(\lambda)}{\pi} \qquad \text{(EQ 1)}$$

where $E(\lambda)$ is the lamp irradiance at a distance of 50 cm from a panel and $R(\lambda)$ is the Bidirectional reflectance factor (BRF) as measured in the 0°, 45° configuration. The spectral radiance of the standard is shown in Figure 5 along with the associated percent uncertainty

as computed using the error propagation in Equation 1. The AVIRIS sensor views the standard directly. The AVIRIS response is computed as the mean of 1000 digital number (dn) samples per spectral channel. The standard deviation of the 1000 samples divided by the mean is the percent uncertainty in the response. The mean and percent uncertainty in the response are shown in Figure 6.

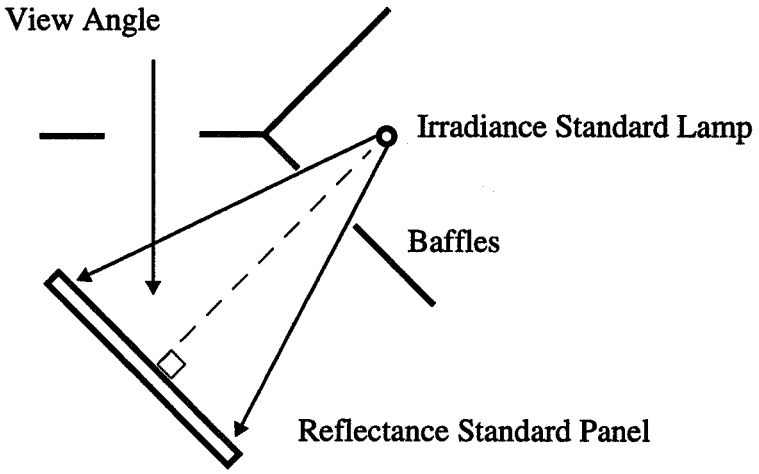

FIGURE 4. Viewing geometry for NIST-traceable radiance standard.

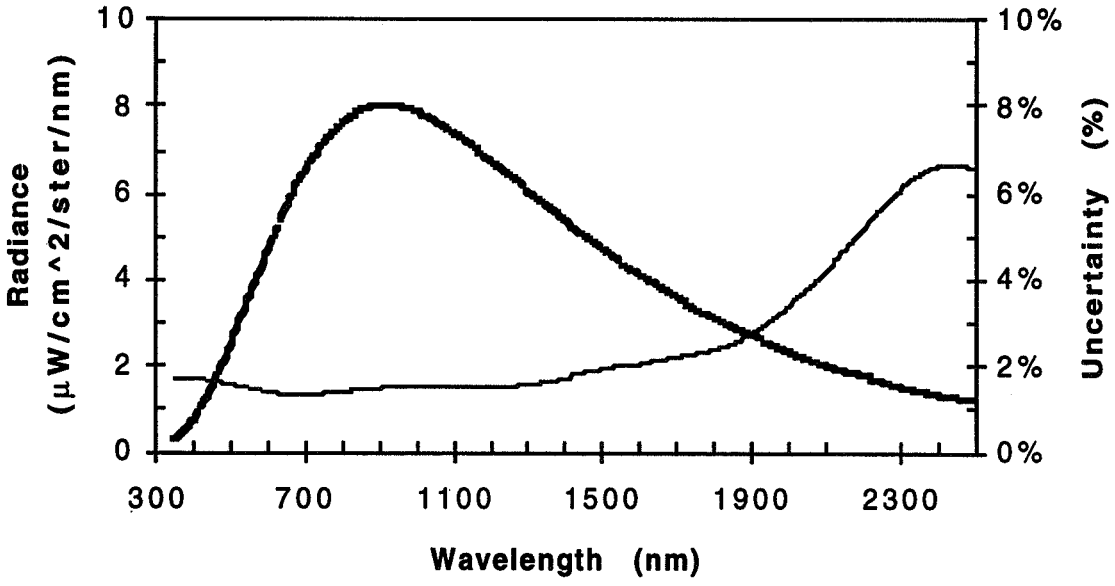

FIGURE 5. NIST traceable radiance standard target radiance (bold line), read from left axis, and percent radiometric uncertainty (normal line), read from right axis.

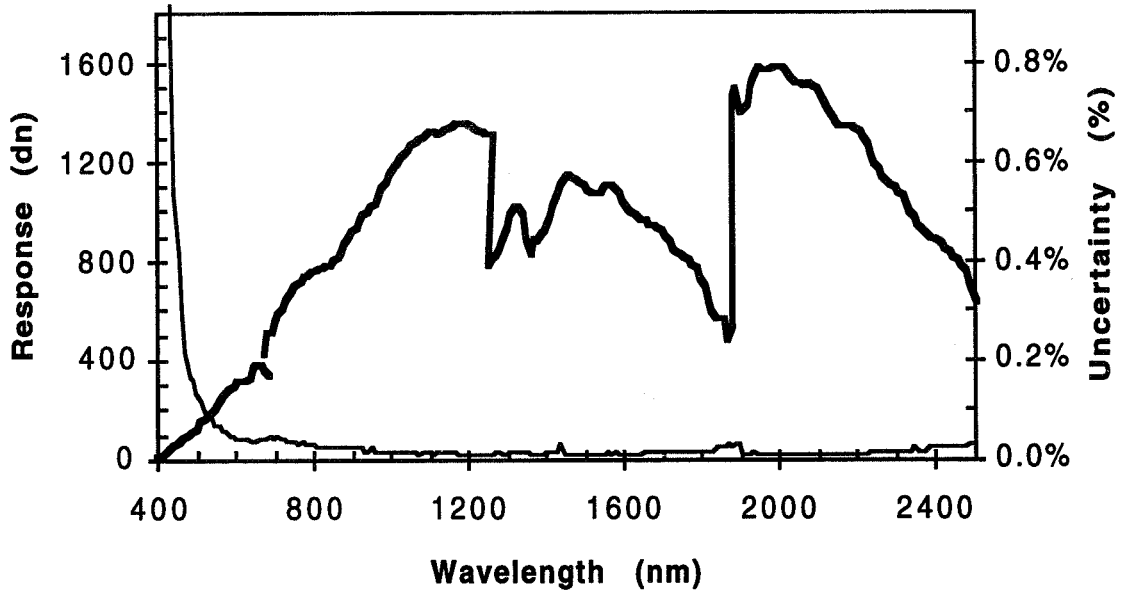

FIGURE 6. AVIRIS digital number (dn) response to NIST-traceable radiance standard (bold line), read from left axis, and percent uncertainty of response due to measurement noise (normal line), read from right axis.

Radiometric calibration coefficients are computed by dividing the standard radiance by the sensor dn response. The results are shown in Figure 7 along with the root-sum-square (RSS) uncertainty of standard radiance and sensor response.

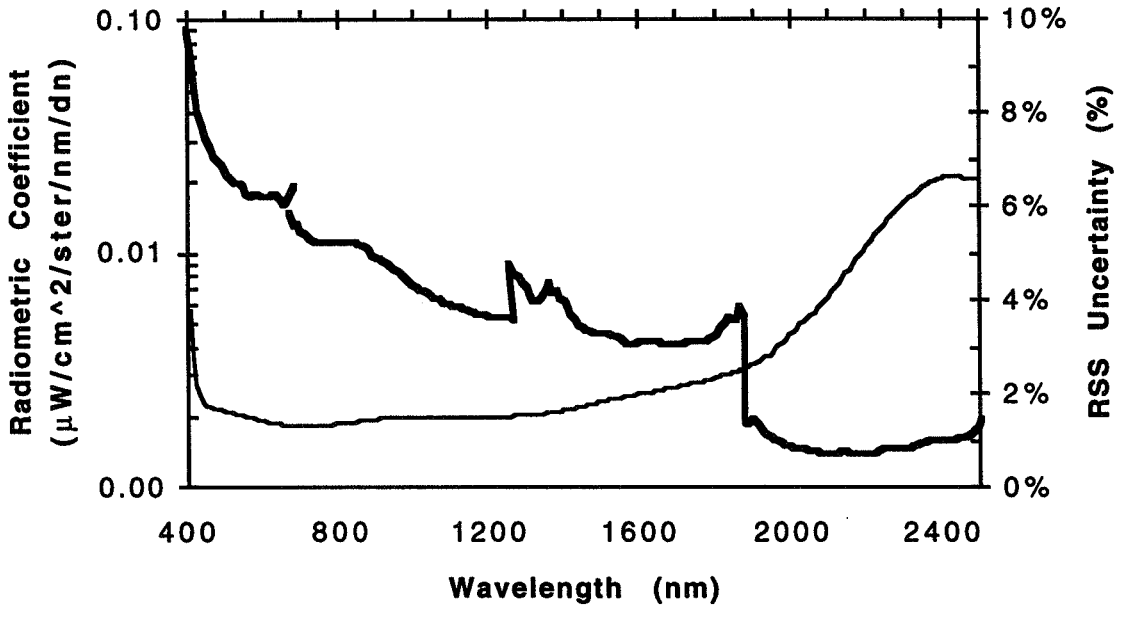

FIGURE 7. Radiometric calibration coefficients derived by dividing the NIST-traceable standard radiance by the AVIRIS radiometric response to the same standard (bold line), read from left axis, and root sum square (RSS) percent uncertainty (normal line), read from right axis.

The RSS uncertainty is dominated by the radiance standard uncertainty, except at wavelengths below 430 nm where the sensor response uncertainty becomes significant. These radiometric gain coefficients are applied to inflight image data to produce calibrated image radiance. An additional onboard calibrator correction factor may be applied to compensate for minor drifts in spectrometer response (Green, 1993).

The radiometric gain coefficients are validated in-flight using a series of calibration experiments scheduled for the start, middle, and end of the flight season (Green et al., 1996; Green et al., 1993). The field experiment predicts the upwelling radiance at the AVIRIS sensor via an independent calibration path that relies on measurements of playa reflectance, atmospheric optical depth, and the MODTRAN3 radiative transfer code (Anderson et al., 1995). Figure 8 shows the percent difference (dotted line) between the inflight calibration experiment predicted radiance and the AVIRIS measured, laboratory calibrated radiance. The percent uncertainty of the measurement (bold line) derived as the RSS of calibration uncertainty (normal line) and the inverse of the signal-to-noise ratio of the playa target spectra are shown for comparison. This indicates that the radiometric calibration uncertainty is approximately the right magnitude. The actual difference from the prediction is influenced by factors including errors in the MODTRAN3 line list and algorithm, errors in the AVIRIS spectral calibration, and instabilities in the field spectrometer used in the playa reflectance measurements. The point to note is that in spite of the many unknowns in the comparison, the level of agreement is better than the error analysis derived uncertainty in many parts of the spectrum. This suggests that the NIST calibration uncertainty may be overstated, especially in the 2100 to 2450 nm spectral region.

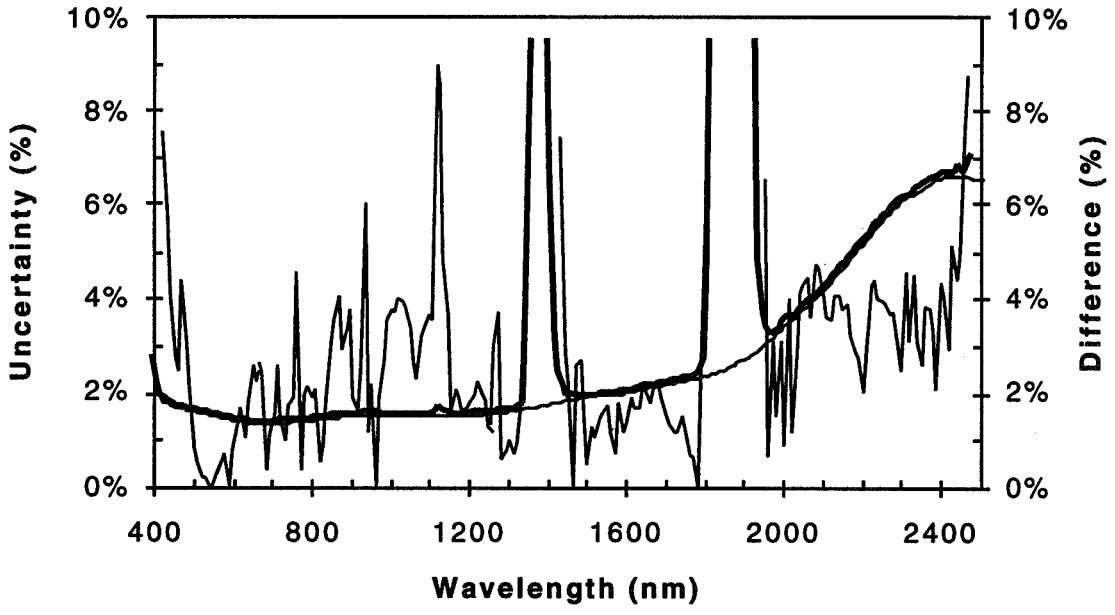

FIGURE 8. Measurement uncertainty (bold line), read from left axis, derived as the RSS of calibration uncertainty (normal line), read from right axis, and the percent variation in the measured spectrum due to instrument noise, atmospheric, and playa variability compared to the percentage difference between the laboratory calibrated spectra and the MODTRAN3 constrained independent prediction of radiance.

4.0 Spatial Calibration

The spatial calibration of AVIRIS describes the spatial sampling and geometric response function (GRF) of the sensor (Chrien and Green, 1993). Response data are collected while translating an illuminated narrow slit across the instantaneous field-of-view (IFOV) of a group of adjacent spatial samples. The slit consists of a 100 μm wide gap etched in a metalized coating on a glass slide and is illuminated by a lamp through a ground-glass diffuser. The entire slit-illuminator assembly is mounted on a computer-controlled translation stage such that the translation is perpendicular to the slit and located in the focal plane of the collimator. The setup, shown in Figure 9a, is aligned with and centered on the AVIRIS entrance aperture. The slit translation rate is measured using a microscope, dial gauges, and a stopwatch and converted to an angular rate using the focal length of the collimator. Figure 9b shows a typical GRF with a FWHM of 1.12 mrad and a sampling interval of 0.85 mrad.

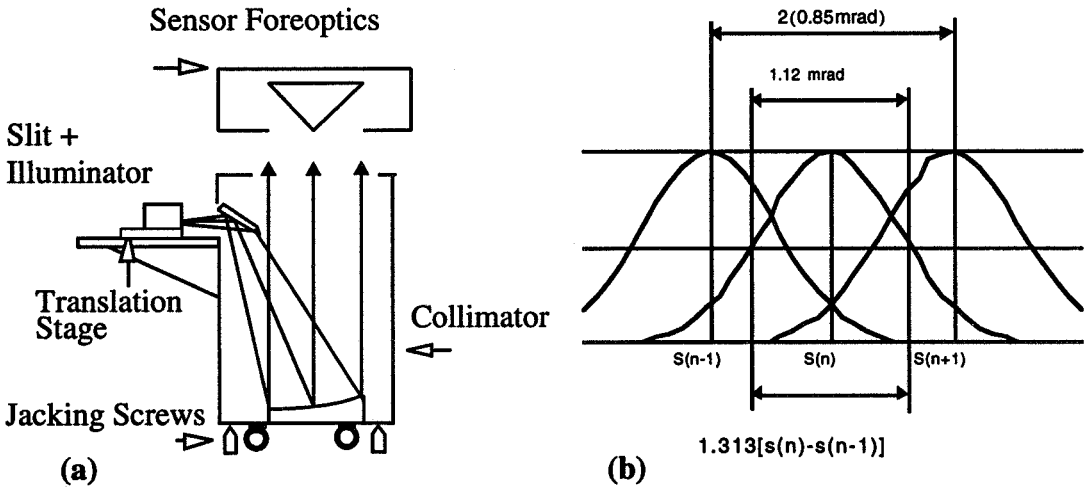

FIGURE 9. (a) Setup for measuring spatial response and sampling, (b) geometric response functions for three adjacent channels.

Data analysis is straightforward. Each along-track line of the response data observes the illuminated slit with a slight shift in angle. The GRF is interpreted as the normalized signal response versus along-track line for a given sample. Lines are calibrated to units of angle equal to slit scan rate [0.4 mrad/s] times AVIRIS scan period [1/12 s]. This moves the slit 1 sample to the right in about 25 along-track scan lines. As the image of the slit moves out of one sample it translates into the adjacent sample. Figure 10 shows the response of sample 270 and sample 271 (2 out of the 614 cross-track samples in the AVIRIS data). This data has been smoothed with a boxcar average to remove line-to-line scan jitter noise related to the GRF measurement technique. The slight asymmetry in the GRF is the result of a detector lag anomaly present in the 1995 and 1996 AVIRIS data. The lag affects both the width and the bore sight of the GRF and appears to be a function of channel brightness and change in channel brightness.

The scan jitter does not affect the shape of the GRF on any line but it does add a random element to line-to-line pointing variation. The smoothed response is shown in Figure 11 along with the raw (unsmoothed) data. A simulated normally distributed line-to-line scan jitter with a standard deviation of 0.07 milliradian closely matches the observed data.

The cross-track field of view of the AVIRIS sensor is determined by the 614 cross-track samples and the 0.85 milliradian sampling and is 30 degrees in extent. Table 1 summarizes the spatial calibration measurements made on 26 April 1996 just prior to the 1995 flight season.

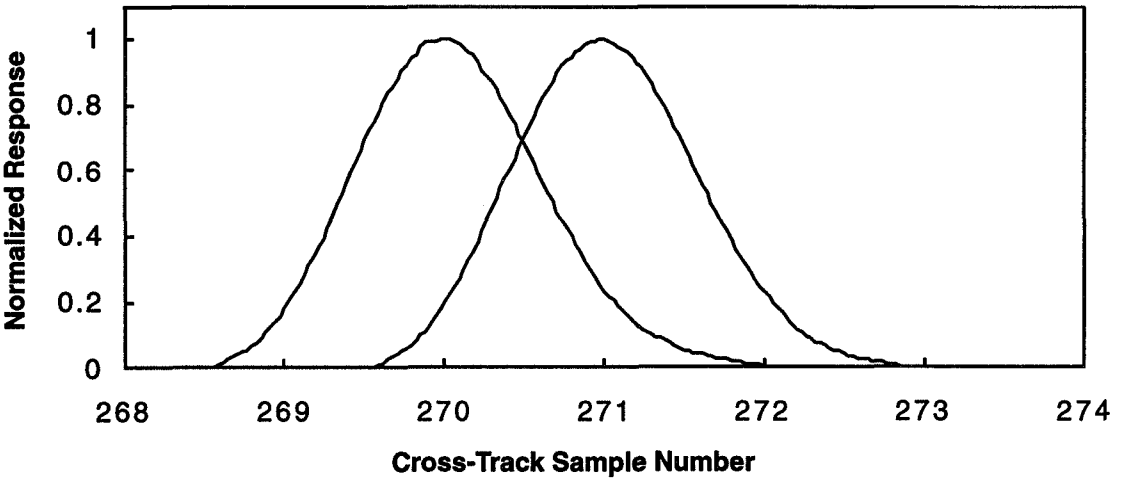

FIGURE 10. Dynamic (scanner-on) cross-track normalized response: Sampling interval is 0.85*FWHM. Asymmetry is the result of residual detector lag present in 1995 AVIRIS data.

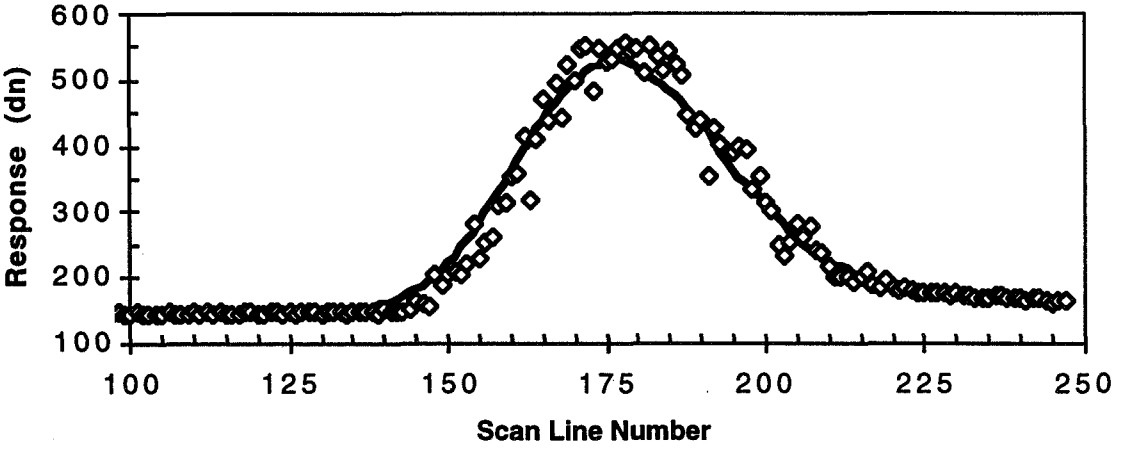

FIGURE 11. Box-car averaged (bold line) and raw (diamonds) dynamic slit response data used to estimate the line-to-line RMS scan jitter.

TABLE 1. Spatial calibration analysis results from 950426 data set. Variation in IFOV and channel alignment between spectrometers is due to a residual detector lag present in the 1995 AVIRIS data.

Spectrometer	A	B	C	D
Dynamic cross-track IFOV	1.12 mrad	1.22 mrad	1.16 mrad	1.25 mrad
Line-to-line RMS jitter	0.07 mrad	0.07 mrad	0.07 mrad	0.07 mrad
Cross-track sampling interval	0.85 mrad	0.85 mrad	0.85 mrad	0.85 mrad
Relative channel alignment to A	-	0.11 mrad	0.09 mrad	0.18 mrad
Static along-track IFOV	1.0 mrad	1.0 mrad	1.0 mrad	1.0 mrad
Static cross-track IFOV	1.0 mrad	1.0 mrad	1.0 mrad	1.0 mrad

5.0 Conclusions

The AVIRIS sensor appears to be meeting the spectral calibration goals of absolute center wavelength knowledge (0.1 nm) and FWHM bandwidth knowledge (0.1 nm) across the spectrum. This accuracy holds in-flight as independently validated using solar and atmospheric absorption features. The onboard calibrator spectral filter data (contained in the pre-cal and post-cal files included with every distributed science data set) may be used to sense wavelength calibration changes (due to inadvertent mechanical shock and residual spectrometer instability) with a 0.1 nm sensitivity.

The laboratory determined radiometric calibration coefficients have been shown to be valid under actual flight conditions when corrected using the signal from the onboard calibrator. An independently determined radiance based upon the MODTRAN3 code and in situ measurements agrees with the laboratory calibrated AVIRIS data to better than the calibration uncertainty. These results may indicate that NIST overestimates the radiometric uncertainty of irradiance standard lamps. Laboratory calibrated AVIRIS data appear to be limited by atmospheric correction errors rather than instrumental signal-to-noise ratio, instrument response instability, or laboratory calibration inaccuracies.

Techniques for measuring the AVIRIS spatial characteristics are presented along with a set of results from a recent spatial calibration. A detector lag anomaly present in the 1995 and 1996 data has an impact on both the GRF width and inter-channel bore sight.

6.0 Acknowledgments

This research was carried out by the Jet Propulsion Laboratory, California Institute of Technology, under contract with the National Aeronautics and Space Administration.

7.0 References

Anderson, G. P., J. Wang, and J. H. Chetwynd, "MODTRAN3: An update and recent validations against airborne high resolution interferometer measurements," Summaries of the Fifth Annual JPL Airborne Earth Science Workshop, JPL Publication 95-1, Vol. 1, Jet Propulsion Laboratory, Pasadena, California, pp. 5-8, 1995.

Chrien, T. G., M. Eastwood, R. O. Green, C. Sarture, H. Johnson, C. Chovit, and P. Hajek, "Airborne Visible/ Infrared Imaging Spectrometer (AVIRIS) onboard calibration system," Summaries of the Fifth Annual JPL Airborne Earth Science Workshop, JPL Publication 95-1, Vol. 1, Jet Propulsion Laboratory, Pasadena, California, pp. 31-32, 1995.

Chrien, T. G., and R. O. Green, "Instantaneous field of view and spatial sampling of the Airborne Visible/ Infrared Imaging Spectrometer (AVIRIS)," Summaries of the Fourth Annual JPL Airborne Geoscience Workshop, JPL Publication 93-26, Vol. 1, Jet Propulsion Laboratory, Pasadena, California, pp. 23-26, 1993.

Chrien, T. G., R. O. Green, M. L. Eastwood, "Accuracy of the spectral and radiometric laboratory calibration of the Airborne Visible/Infrared Imaging Spectrometer (AVIRIS)," SPIE Vol. 1298, Imaging Spectroscopy of the Terrestrial Environment, pp. 37-49, 1990.

Green, R. O., J. E. Conel, J. Margolis, C. Chovit, J. Faust, 1996, "In-flight calibration and validation of the Airborne Visible/Infrared Imaging Spectrometer (AVIRIS)," Summaries of the Sixth Annual JPL Airborne Earth Science Workshop, JPL Publication 96-20, Vol. 1, Jet Propulsion Laboratory, Pasadena, California, 1996 (this volume).

Green, R. O., "An Improved spectral calibration requirement for AVIRIS," Summaries of the Fifth Annual JPL Airborne Earth Science Workshop, JPL Publication 95-1, Vol. 1, Jet Propulsion Laboratory, Pasadena, California, pp. 75-78, 1995a.

Green, R. O., "Determination of the in-flight spectral calibration of AVIRIS using atmospheric absorption features," Summaries of the Fifth Annual JPL Airborne Earth Science Workshop, JPL Publication 95-1, Vol. 1, Jet Propulsion Laboratory, Pasadena, California, pp. 71-74, 1995b.

Green, R. O., J. E. Conel, M. Helmlinger, J. van den Bosch, C. Chovit, and T. Chrien, "Inflight calibration of AVIRIS in 1992 and 1993," Summaries of the Fourth Annual JPL Airborne Geoscience Workshop, JPL Publication 93-26, Vol. 1, Jet Propulsion Laboratory, Pasadena, California, pp. 69-72, 1993.

Green, Robert O., "Use of Data from the AVIRIS Onboard Calibrator," Summaries of the Fourth Annual JPL Airborne Geoscience Workshop, JPL 93-26, Jet Propulsion Laboratory, Pasadena, California, 1993.

Green, Robert O., Steven A. Larson and H. Ian Novack, "Calibration of AVIRIS digitized data", Proceedings of the Third Airborne Visible/Infrared Imaging Spectrometer (AVIRIS) Workshop, JPL Publication 91-28, Jet Propulsion Laboratory, Pasadena, California, 1991.

Vane, G., R. O. Green, T. G. Chrien, H. T. Enmark, E. G. Hansen, and W. M. Porter, "The Airborne Visible/ Infrared Imaging Spectrometer (AVIRIS)," Remote Sens. Environ., 44:127-143 (1993).

Vane, G., T. G. Chrien, E. A. Miller, J. H. Reimer, "Spectral and radiometric calibration of the Airborne Visible/Infrared Imaging Spectrometer," SPIE Vol. 834, Imaging Spectroscopy II, pp. 91-105, 1987.

8.0 Additional Reading

Sarture, C. M., T. G. Chrien, R. O. Green, M. L. Eastwood, J.J. Raney, and M. A. Hernandez, "Airborne Visible/Infrared Imaging Spectrometer (AVIRIS): sensor improvements for 1994 and 1995," Summaries of the Fifth Annual JPL Airborne Earth Science Workshop, JPL Publication 95-1, Vol. 1, Jet Propulsion Laboratory, Pasadena, California, pp. 145-148, 1995.

Evolution in Imaging Spectroscopy Analysis and Sensor Signal-to-Noise: An Examination of How Far We Have Come

Roger N. Clark and Gregg A. Swayze
U.S. Geological Survey
Mail Stop 964
Box 25046 Federal Center
Denver, Colorado 80228

Imaging spectroscopy is a relatively new field whose instrumentation and analysis methods have grown in sophistication over the last decade. We have studied the signal-to-noise of the NASA/JPL AVIRIS instrument from 1990 to 1995 along with the improvements in our own analysis methods using the Cuprite, Nevada data available each year. The advantage of becoming familiar with a single test site, by studying both the data obtained, as well as conducting field trips to verify results, helps to understand the complexity of the surficial mineralogy at the site. The desert environment of Cuprite provides a relatively stable environment from year to year, which is important for assessing progress in algorithms and sensors.

Because the surficial geology of Cuprite is well understood (Swayze, 1996, Ph.D. thesis, near completion), as are several other AVIRIS sites we have studied, including areas near Barstow, CA (Clark *et al.*, 1996a), the Summitville mining region in Colorado (King *et al.*, 1995a, b, c), and sites on the Colorado plateau (e.g. Clark *et al.*, 1992), we have used our knowledge of the surficial minerals and their mixtures to derive a strategy for analysis. A spectral library of minerals (Clark *et al.*, 1993a), amorphous materials, vegetation, and mixtures of each has been compiled in the last few years, and their spectral features studied to design spectral identification algorithms capable of distinguishing more complex situations.

There are two conditions that have improved the level of detail in what we have been able to map: sensor signal-to-noise, and algorithm sophistication. We examined the effects of these two conditions separately and combined for the Cuprite test site.

We produced maps of materials at Cuprite using 1990, 1993, and 1995 AVIRIS data. For each data set, we produced two materials maps. The first map contains materials whose spectra show electronic absorptions. These absorptions generally occur in the ultraviolet to near infrared (~1 μm), and include iron-bearing minerals. The second map contains materials whose spectra show vibrational absorptions. Such absorptions generally occur in the near-infrared, where many diagnostic features occur in the 2 to 2.5-μm region. These maps include clays (and other phyllosilicates), carbonates and sulfates.

1990 AVIRIS Data

In 1990, the AVIRIS system achieved a signal-to-noise at 50% reflectance over Cuprite of about 150 in the visible, and about 80 at 2.2 μm. In 1993, AVIRIS isignal-to-noise improved to about 600 in the visible and about 140 at 2.2 μm. In 1995, with new detectors, the AVIRIS signal-to-noise improved to about 800 in the visible and about 360 at 2.2 μm. Swayze and Clark (1995), and Swayze *et al.*, (1996) have shown that mineral discrimination ability is directly proportional to the signal to noise with shape-matching algorithms like those we use. Thus, improvements in signal-to-noise of the AVIRIS system directly leads to improved materials maps and the ability to discriminate more complex possibilities.

As AVIRIS signal-to-noise improved, we refined our algorithm, which we call Tricorder. Clark *et al.* (1990, 1991, 1993) analyzed AVIRIS 1990 data for Cuprite using Tricorder version 1.0 which had the ability to map up to about 30 materials at one time. However, separate spectral regions required different runs of the program. The algorithm analyzed multiple spectral features, without continuum constraints. Continuum constraints are additional information, such as level and slope. Calibration for these early studies included only ground targets, resulting in residual atmospheric absorptions as a function of elevation, thus complicating any analysis. Mapping methodology and results were verified with field mapping and X-ray diffraction analysis of hand samples (Swayze *et al.*, 1992).

The mapping results (Clark *et al.*, 1993b) shows 10 phyllosilicates, sulfates, and carbonates and three Fe-bearing oxides and sulfates (goethite, hematite, and jarosite). The vibrational-absorption maps show eastern and western bull's-eye patterns of hydrothermal alteration with their characteristic concentric zoning. The western center consisted of an alunite interior zone, surrounded by a kaolinite zone, in turn surrounded by a muscovite (or sericite) zone. The eastern center shows only the interior alunite zone surrounded by a kaolinite zone. The electronic-absorption map shows the eastern center bleached of Fe-bearing minerals with a hematite-rich halo encircling the bleached areas. The western center has appreciable jarosite and goethite indicating that erosion has exposed a deeper pyrite-rich level of the underlying hydrothermal system.

1993 AVIRIS Data

In 1993, Tricorder was improved to version 2.3, which had the ability to map up to about 120 materials, but separate spectral regions still required multiple runs of the program. Analysis used multiple spectral features, simple continuum constraints and some mineral mixtures. A good spectral library (Clark *et al.*, 1993a) was complete. Calibration improved to include a combination of radiative-transfer-atmospheric modeling and ground-calibration targets (Clark *et al,* 1993c, 1996b) to achieve near laboratory quality surface reflectance spectra from AVIRIS. Verification continued with field mapping, X-ray diffraction analysis of hand samples from the field, and data from portable field spectrometers.

The Tricorder 2.3 results showed multiple iron-bearing minerals, including discrimination of the grain sizes of hematite, and several different Fe^{2+}-bearing minerals, mainly chlorites and muscovites. Our vibrational-absorption materials map shows 16 minerals, including a subdivision

of the solid solutions series of alunites and muscovites. Mapping also showed that most mineral-mixtures occurred on the alluvial fan surfaces as expected.

1995 AVIRIS Data

In 1995, the AVIRIS signal-to-noise was improved to the level of producing spectra equalling the quality of many laboratory-obtained spectra. Extraction of spectra from the calibrated data set showed spectral complexities that were hidden by noise in previous years. Fortunately, improvements in software allowed for a more sophisticated analysis (Clark *et al.*, 1995a). Tricorder 3.3 now has the ability to map for thousands of materials, including simultaneous analysis of spectra of solids, liquids, and gases. Analysis of multiple spectral features in all spectral regions are done simultaneously. Sophisticated shape matching constraints, preprocessing, and specific algorithm selections are done for each analysis. Tricorder does an artificial-intelligent-expert-system analysis and makes decisions on a case by case basis. Algorithms include thresholding of parameters, "not" spectral features (see Clark *et al.*, 1995a), and additional, selectable analyses based on answers to previous analyses. The spectral libraries are improved with spectra of amorphous materials, environmental materials, vegetation, snow, water, and some man-made materials. The analysis uses many mineral mixtures. Calibration is the same as with the 1993 data, but better field-portable spectrometers were used to characterize the ground calibration targets. Previously, samples were returned to the laboratory for analysis, and included only a few square centimeters of sample.

Results of mapping using the 1995 data show amazing complexity. Out of about 160 categories mapped, about 70 were found! The electronic-absorption map shows 16 categories of iron oxides, Fe^{2+}-bearing minerals, and weathered-Fe^{2+}-bearing minerals. The vibrational-absorption map shows 25 categories, including finer discrimination than before of the solid-solution series of alunites, muscovites, and mixtures of these with kaolinites and smectites. These two maps together show 36 categories. More maps would be needed to show the other materials found, which are generally in small spots, or scattered at a low level, or are trace vegetation types, and could not be readily distinguished amid the complexity of the first two maps.

Conclusions

JPL engineers have improved the AVIRIS signal-to-noise remarkably over the last few years and our analysis capabilities have similarly evolved to the point that sophisticated materials maps can be derived with high confidence in the results. Beyond the phenomenal increase in capability is our astonishment at the complexity of the surficial mineralogy expressed at Cuprite. Mineral maps derived from imaging spectroscopy data now convey mineralogic detail which exceeds that of conventional published geologic maps. The superb signal-to-noise of the 1995 AVIRIS system is a two-edged sword: the data have enough precision to show very subtle spectral detail; but that detail is showing us how complex the world really is. Spectra extracted from the Cuprite 1995 data set show more complexity than we have so far mapped, and we must continue to refine our analyses to handle that complexity.

Further Information

The USGS Spectral library, the images referenced in this paper, and additional information on spectroscopy can be found at the web site: "http://speclab.cr.usgs.gov" using a standard web browser.

References

Clark, R.N., A.J. Gallagher, and G.A. Swayze, 1990, Material Absorption Band Depth Mapping of Imaging Spectrometer Data Using a Complete Band Shape Least-Squares Fit with Library Reference Spectra, *Proceedings of the Second Airborne Visible/Infrared Imaging Spectrometer (AVIRIS) Workshop.* JPL Publication 90-54, 176-186.

Clark, R.N., G.A. Swayze, A. Gallagher, N. Gorelick, and F. Kruse, 1991, Mapping with Imaging Spectrometer Data Using the Complete Band Shape Least-Squares Algorithm Simultaneously Fit to Multiple Spectral Features from Multiple Materials, *Proceedings of the Third Airborne Visible/Infrared Imaging Spectrometer (AVIRIS) Workshop,* JPL Publication 91-28, 2-3.

Clark, R.N., G.A. Swayze, C. Koch, A. Gallagher, and C. Ager, 1992a, Mapping Vegetation Types with the Multiple Spectral Feature Mapping Algorithm in both Emission and Absorption, *Summaries of the Third Annual JPL Airborne Geosciences Workshop, Volume 1: AVIRIS Workshop.* JPL Publication 92-14, 60-62.

Clark, R.N., G.A. Swayze, and A. Gallagher, 1992b, Mapping the Mineralogy and Lithology of Canyonlands, Utah with Imaging Spectrometer Data and the Multiple Spectral Feature Mapping Algorithm *Summaries of the Third Annual JPL Airborne Geosciences Workshop, Volume 1: AVIRIS Workshop.* JPL Publication 92-14, 11-13.

Clark, R.N., G.A. Swayze, A. Gallagher, T.V.V. King, and W.M. Calvin, 1993a, The U. S. Geological Survey, Digital Spectral Library: Version 1: 0.2 to 3.0 μm, *U.S. Geological Survey, Open File Report 93-592,* 1340 pages.

Clark, R.N., G.A. Swayze, and A. Gallagher, 1993b, Mapping Minerals with Imaging Spectroscopy, *U.S. Geological Survey, Office of Mineral Resources Bulletin 2039,* pp. 141-150.

Clark, R.N., G.A. Swayze, K. Heidebrecht, A.F.H. Goetz, and R.O. Green, 1993c, Comparison of Methods for Calibrating AVIRIS Data to Ground Reflectance, *Summaries of the Fourth Annual JPL Airborne Geosciences Workshop, Volume 1: AVIRIS Workshop.* JPL Publication 93-26, 31-34.

Clark, R.N. and Swayze, G.A., 1995, Mapping Minerals, Amorphous Materials, Environmental Materials, Vegetation, Water, Ice and Snow, and Other Materials: The USGS Tricorder Algorithm. *Summaries of the Fifth Annual JPL Airborne Earth Science Workshop,* January 23- 26, R.O. Green,Ed., JPL Publication 95-1, p. 39-40.

Clark, R.N., K.E. Livo, and G.A. Swayze, 1996a, Preliminary Mineral Mapping with Imaging Spectroscopy in the Barstow Region, California, *U.S. Geological Survey*, Open File Report 96-__, in review.

Clark, R.N., G.A. Swayze, K. Heidebrecht, R.O. G.A.F.H. Goetz, 1996b, Calibration to Surface Reflectance of Terrestrial Imaging Spectrometry Data: Comparison of Methods, *Applied Optics* in preparation.

King, T.V.V., C.Ager, W.W. Atkinson, L.S. Balistrieri, R.J. Bisdorf, D. Bove, R.N. Clark, M.F. Coolbaugh, J.S. Erdman, L.P. Gough, P.v. Guerard, F.E. Lichte, W.F. Ortz, G.S. Plumlee, W.I. Ridley, K.S. Smith, G.A. Swayze, R.R. Tidball, K. Walton-Day, T.M. Yamosky, 1995a, Environmental considerations of active and adandoned mine lands - Lessons from Summitville, Colorado. T.V.V. King, Editor, U.S. *Geological Survey, Bulletin 2220, 38 p.*

King, T.V.V., R.N. Clark, C. Ager, and G.A. Swayze, 1995b, Remote mineral mapping using AVIRIS data at Summitville, Colorado and the adjacent San Juan Mountains. *Proceedings: Summitville Forum '95,* H.H. Posey, J.A. Pendelton, and D. Van Zyl Eds., Colorado Geological Survey Special Publication 38, p. 59-63.

King, T.V.V., R.N. Clark, C. Ager, and G.A. Swayze, 1995c, Remote mineral mapping using AVIRIS data at Summitville, Colorado and the adjacent San Juan Mountains. *Summaries of the Fifth Annual JPL Airborne Earth Science Workshop,* January 23- 26, R.O. Green, Ed., JPL Publication 95-1, p. 113-116.

Swayze, G.A. R.N. Clark, S. Sutley, and A Gallagher, 1992, Ground-Truthing AVIRIS Mineral Mapping at Cuprite, Nevada, *Summaries of the Third Annual JPL Airborne Geosciences Workshop, Volume 1: AVIRIS Workshop.* JPL Publication 92-14, 47-49.

Swayze, G.A., and Clark, R.N., 1995, Spectral identification of minerals using imaging spectrometry data: evaluating the effects of signal to noise and spectral resolution using the Tricorder Algorithm: *Summaries of the Fifth Annual JPL Airborne Earth Science Workshop,* January 23- 26, R.O. Green, Ed., JPL Publication 95-1, p. 157-158.

Swayze, G.A., R.N. Clark, A. Goetz, and N. Gorelick, 1996, Spectral Identification of Surface Materials using Imaging Spectrometer Data: Evaluating the Effects of Detector Sampling, Bandpass, and Signal to Noise Ratio using the Tricorder Algorithm, in preparation.

Page intentionally left blank

Mapping Surficial Geology, Vegetation Communities, and Environmental Materials in Our National Parks: The USGS Imaging Spectroscopy, Integrated Geology, Ecosystems, and Environmental Mapping Project

Roger N. Clark[1], Gregg A. Swayze[1],

Larry Rowan[2], Eric Livo[1] and Ken Watson[1]

1) US Geological Survey, MS 964
Box 25046 Federal Center
Denver, Colorado 80225
(303) 236-1332 (voice), 236-1425 (FAX)

2) US Geological Survey, MS 927
National Center
Reston, VA 22092

Our National Parks have continuing resource management issues which become more acute as park visitation increases. Many parks have only incomplete geologic maps, and only crude, if any, vegetation species/communities or habitat maps. Past mining activity has resulted in many abandoned mines in what are now National Parks and surrounding lands. Increased visitation may be putting stress on the ecosystems in some regions. Surficial mineralogy has a large influence on an ecosystem, and can control the extent of plant communities and animal habitat. Geologic maps, even if complete, do not distinguish surficial mineralogy in sufficient detail to study habitats, so new methods must be employed to derive the appropriate information.

We have begun a program of using imaging spectroscopy and multispectral thermal data to map surficial mineralogy and exposed lithologies, vegetation species/communities, and potential environmentally-hazardous materials that might be associated with abandoned mines in our National Parks. Specific topics being addressed include habitat mapping and cryptobiotic soils mapping.

The integrated study uses AVIRIS imaging spectroscopy data, and TIMS multispectral thermal data for combined visible, near-infrared, and thermal infrared wavelength coverage. A standard mapping run with the AVIRIS data for each park includes mineral maps for many tens of minerals, amorphous materials such as amorphous iron oxides and hydroxides, percent vegetation cover, vegetation species/communities maps, vegetation green-leaf water content, and possible senescence/stress indicator maps. The detail in the vegetation species/communities maps depends on the state of vegetation at the time of data acquisition (data obtained too late in the growing season reduces the ability to discriminate between species/communities). The mineral

maps include clays (specific clays such as Na-montmorillonite, Kaolinite, etc), sulfates (alunite, gypsum, jarosite etc), carbonates (calcite, dolomite and others), iron oxides (hematite, goethite, and others) and other iron-bearing minerals (pyroxenes, chlorites, and others), solid solution series (e.g. Na-K alunite, muscovite Al content), and even detailed mapping of kaolinite group crystallinity. The maps of individual minerals and vegetation parameters form a 150+ layer GIS database.

AVIRIS and TIMS data were acquired by NASA for this program in May and June of 1995 for Arches and Canyonlands National Parks, Petrified Forest National Park, and Joshua Tree National Park. In addition, we are using AVIRIS data for Arches and Canyonlands National Parks, and Organ Pipe National Monument that were obtained in 1991-1994. Current results will be presented at the conference.

A COMPARISON OF IMAGE PROCESSING METHODS FOR ALTERATION MAPPING AT BODIE, CALIFORNIA, USING 1992 AVIRIS DATA

Alvaro P. Crósta [1]
Charles Sabine [2]
James V. Taranik [2]

[1] Geosciences Institute, State University of Campinas, P.O. Box 6152, 13081-970 Campinas, SP, Brazil
[2] Desert Research Institute, P.O. Box 60220, Reno, NV 89506, U.S.A.

1. INTRODUCTION

Hyperspectral remote sensing, or imaging spectrometry, has been under development for more than a decade since the first experimental sensor of this type, the Airborne Imaging Spectrometer, became operational in 1983. With the appearance of the Advanced Visible/Infrared Imaging Spectrometer (AVIRIS) in 1987 and its continued development by JPL since then, together with development of commercially operated imaging spectrometers such as those built and operated by Geophysical & Environmental Research Corp. (GER), a number of applications have been shown to benefit from this technology. Among these applications is the discrimination of superficial materials for mineral exploration, in particular, mapping hydrothermal alteration minerals. However, the unavailability of hyperspectral sensors and lack of data covering a diverse geological environments in different regions restricted the use of this type of data operationally. Also, hyperspectral data required the development of new image processing algorithms specifically designed to take advantage of the high spectral resolution and to cope with the much larger amount of data than those used with conventional multispectral data (e.g. Landsat TM).

With the continued deployment of AVIRIS in different regions of North America, Europe (1991) and South America (1995), and the continued operation of GER scanners, progressively more data has become available. The development of new algorithms for processing hyperspectral data came next, including those for identifying surface materials. Some of these algorithms have recently been incorporated into commercial image processing software.

Development of new hyperspectral imaging sensors marks a third stage toward operational applications for mineral exploration. In 1994 the Multispectral Infrared and Visible Imaging Spectrometer (MIVIS) was developed by Daedalus and in 1995 two new imaging spectrometers started collecting data: the Hyperspectral Digital Imagery Collection Experiment (HYDICE) and the SWIR Full Spectrum Imager (SFSI). Two other airborne imaging sensors are currently under development: GER's Digital Airborne Imaging Spectrometer-7915 and the Wedge Imaging Spectrometer (WIS) by Santa Barbara Research Center of Hughes Aircraft. TRW was selected by NASA to build the Hyperspectral Imager (HSI), a spaceborne imaging spectrometer to be launched by the end of this decade and which will provide 384 spectral bands with a 30 meter IFOV. All these developments, summarized by Taranik and Crósta (1996), indicate a clear trend toward operational use of hyperspectral data in geological remote sensing in the near future.

This paper examines and compares two different algorithms recently developed for identifying superficial materials in imaging spectrometry data. The objective was to assess the performance of these algorithms and their ability to map alteration minerals for precious metals exploration. Unlike previous mineral mapping studies such as those done at well known localities like Cuprite, Nevada, this exercise tried to simulate a situation often encountered in mineral exploration, in which remote sensing is used as the first tool for defining targets before the geologist sets foot on the ground. Therefore, techniques that do not require the *a*

priori input of ground data were favored for converting the image data to ground reflectance and for identifying superficial materials.

The area selected for this study is the Bodie mining district and part of the neighboring Paramount district, both located in Mono County, California. AVIRIS data for this area was acquired in October 1992 by NASA's ER-2 aircraft.

2. GEOLOGY AND MINERALIZATION OF THE BODIE AND PARAMOUNT DISTRICTS

Bodie was an important gold-silver mining district in the second half of the nineteenth century, whereas only a mercury mine was exploited in the Paramount district. Tertiary (7.8 to 9.4 Ma) intermediate to basic volcanic rocks (dacitic, andesitic and sometimes rhyolitic lavas, plugs, tuffs and breccias) underlie both districts. Hydrothermal alteration associated with precious metal concentration at Bodie is probably the result of intense thermal spring activity, some of which can still be found in this region along fault zones (Silberman et al., 1995).

Bodie has characteristics of a bonanza-type lode quartz vein deposit and a large-scale stockwork system, with gold occurring in quartz veins and quartz-adularia-chalcedony stockworks in the center of the district. Petrographic work by Herrera et al. (1993) showed vertical and lateral zoning in the alteration with silicification in the center surrounded by zones of potassic, argillic and sericitic alteration and an outer zone of propylitic alteration. Not much information is available for the Paramount district due to the lack of important mineralization, but the district has recently been prospected for bulk tonnage precious metal mineralization (Herrera et al., op. cit). Geological characteristics observed at Paramount are very similar to those in Bodie and the origin of the alteration is believed to be similar (Silberman et al., 1995).

The AVIRIS scene used in this study covers the Bodie district almost entirely and the eastern portion of the Paramount district, between Atastra and Rough creeks.

3. DATA CALIBRATION TO SURFACE REFLECTANCE

Identification of surface materials using hyperspectral data is based on quantitative comparisons between pixel and library spectra. In order to make such comparisons, imaging spectrometer data need to be pre-processed for retrieving ground reflectance values from radiance measurements. A number of methods have been proposed for such conversion, some of which require the input of ground data preferentially collected simultaneously with the sensor's overflight. Radiative transfer methods rely on the use of atmospheric models and allow the retrieval of apparent ground reflectance from the radiance values provided by AVIRIS. A comparison of several methods by Clark et al. (1995) showed that a hybrid method which combines simultaneous ground-based data and the radiative transfer method developed by Green et al. (1993a), provides the best results for reflectance retrieval in hyperspectral data, followed by the sole use of the Green's radiative transfer method.

Green's radiative transfer method was selected because it suits the objectives of this study. This method uses the AVIRIS laboratory-calibrated radiance (Chrien et al, 1990) in conjunction with in-flight calibration data obtained over Rogers Dry Lake at the beginning of the 1992 AVIRIS data acquisition season (Green et al., 1993b) and the MODTRAN radiative transfer code. The method requires no *in situ* measurements and compensates for AVIRIS derived estimates of water vapor, aerosol and surface on a pixel by pixel basis. Compared to other radiative transfer methods, it provides a better correction for H_2O and other atmospheric gases, as a function of elevation throughout a scene (Clark et al., 1995). Disadvantages of this method include: (i) errors in the ground measurements during the in-flight calibration at the beginning of the season will propagate into the derived surface reflectance; (ii) computation time is considerable and (iii) the method is still under development at JPL and not yet available for general use.

4. IMAGE PROCESSING METHODS FOR MINERAL MAPPING

Two different methods have been compared for mineral mapping at Bodie and Paramount: the Spectral Angle Mapper (Kruse et al., 1993) and Tricorder (Clark et al, 1990; Clark and Swayze, 1995). Both methods rely on a spectral comparison between pixels from the scene and reference spectra from a spectral library, using different algorithms to compare and measure the similarity between spectra extracted from pixels and reference library spectra. The two methods are insensitive to illumination differences due to topographical shadowing and therefore can be used in all sorts of terrain. The library used for this assessment was the public domain USGS Spectral Library which contains nearly 500 reference spectra of minerals, vegetation and other surface materials (Clark et al., 1993).

4.1 Spectral Angle Mapper Classifier

The Spectral Angle Mapper (SAM) is a supervised classification technique that measures the spectral similarity of image spectra to reference spectra which can be obtained either from a spectral library or from field and laboratory spectra. SAM defines spectral similarity by calculating the angle between the two spectra, treating them as vectors in n-dimensional space, with n being the number of bands used. The angle is the arc-cosine of the dot product of the two spectra. Small values for the angle represent higher spectral similarity between pixel and reference spectra.

This method is not affected by gain (solar illumination) factors, since the angle between two vectors is invariant with respect to the lengths of the vectors. SAM produces an image with the pixels it manages to classify assigned to the respective reference minerals, constrained by a user-specified threshold, together with a set of "rule images", one for each reference mineral used. DN values in these "rule images" are the expression of the angle itself (smaller DNs indicate greater similarity to the respective reference mineral), and these images can be used to assess individual results for each reference mineral. The advantages of SAM are that it has already been implemented in commercial imaging processing packages, it is easy to use and it is computationally fast.

4.2 USGS Tricorder Algorithm

Tricorder is still under development by the U.S. Geological Survey Spectroscopy Laboratory and is expected to be released in early 1996 for general use. It was designed to compare spectra of materials from the USGS Digital Spectral Library to image spectra from hyperspectral sensors, analyzing simultaneously for multiple minerals using multiple diagnostic spectral features for each mineral.

Tricorder works by first removing a continuum from spectral features in the reference library spectra and also from each spectrum in the image data set. Both continuum-removed spectra are then compared using a modified least square procedure. The algorithm uses a linear correlation coefficient to determine the fit by individually fitting all diagnostic absorption features of all reference spectra in the library to each pixel spectrum. The algorithm then calculates an overall fit by weighting each individual fit based on the area under its continuum-removed spectra. The overall fits are then compared and the mineral from the library with the highest fit is assigned to the image pixel.

One of the strengths of Tricorder is that it considers several attributes in the analysis: the depth for particular absorption features, the goodness of fit and the reflectance level of the continuum at the center of the future. By doing this, it can analyze feature shapes using all data points and therefore resolve even complex feature shapes such as doublets in minerals like kaolinite, dickite and halloysite. The method, like SAM, is also not affected by illumination differences.

5. ALTERATION MAPPING AT BODIE AND PARAMOUNT

Both methods, SAM and Tricorder, were applied to the Bodie/Paramount reflectance-calibrated AVIRIS scene (512 x 614 pixels) in order to identify and map alteration minerals in both districts and to compare results.

Two spectral regions were processed separately in SAM: the visible/near-infrared (VNIR) region (0.4 to 1.3 μm) and the shortwave infrared (SWIR) region (2.0 to 2.4 μm). The VNIR bands were analyzed for minerals with diagnostic electronic transition features (hematite, goethite, jarosite, etc.) using 9 reference spectra, and the SWIR bands were analyzed for hydroxyl-bearing minerals and carbonates using 15 reference spectra. These spectra were from the USGS Digital Spectral Library and were convolved to AVIRIS bandwidths prior to running the SAM classification. The threshold value used for the maximum angle between spectra vectors was established empirically at 0.065 radians. Values above this produced too many classified pixels in only one or two classes and values below it produced images with almost entirely "non-classified" pixels.

In the SWIR, SAM classified most of the alteration at Bodie as Na-montmorillonite with some pixels classified as a mixture of kaolinite+smectite at Silver Hill, near the center of the district, and at Bodie Bluff in the northern portion. At the Paramount district, most of the western part was classified as a mixture of kaolinite+smectite with some pixels as Na-montmorillonite, whereas the eastern part of the alteration was classified as Na-montmorillonite plus a very few pixels classified as either poorly crystalline kaolinite or well-crystalline kaolinite. Two of the reference spectra, illite and Ca-montmorillonite, were mapped in a great number of pixels scattered throughout the scene. They were treated as misclassifications and removed from the final result. Computation time for the SWIR 15-mineral classification using 40 AVIRIS bands on a low-end Unix workstation (Sun IPX) was 8 minutes.

In the VNIR, 99 AVIRIS bands were used with nine reference spectra of common Fe^{2+}- and Fe^{3+}-bearing minerals. The results presented by SAM were not satisfactory because it classified most of pixels of the image as a mixture of hematite and quartz. Even after experimenting with different values for the minimum angle and removing the hematite+quartz spectrum from the reference spectra, SAM would classify most of the pixels as a single reference spectrum. It was then decided to use only three reference spectra: hematite, goethite and jarosite. Some empirical work had to be done to find the threshold value for the maximum angle which was 0.31 radians. The results showed goethite in altered areas at Bodie Bluff and Silver Hill together with jarosite in mine dumps and in a tailing pond. A few pixels were mapped as hematite at Silver Hill and in an area to the north of the major alteration. Goethite was also mapped in the Paramount district as well as jarosite which also appeared scattered throughout the western part of the scene and along dirt roads. It took 15 minutes to run SAM using 99 AVIRIS bands and 3 reference spectra on a low-end Unix workstation (Sun IPX).

Tricorder is run through command files which are pre-set to analyze specific groups of minerals. The command file used in this study included 126 materials including minerals, vegetation and ice. All the minerals analyzed using SAM were included in Tricorder's command file. Tricorder also analyzes separately for multiple minerals in the VNIR and SWIR spectral regions. Therefore, the analysis of the whole spectrum for a single pixel may find two different minerals, one for each spectral region, showing that the pixel contains diagnostic features for two minerals in different spectral regions.

Tricorder produced more detailed results than SAM, mapping a greater number and variety of minerals. In the SWIR region, Tricorder distinguished Na- and Ca-montmorillonite in most of the Bodie district and in the eastern part Paramount, two types of kaolinite (well- and poorly-crystalline) in the western part of Paramount, a mixture of kaolinite+smectite in the central part of the Bodie district, halloysite in the western part of Paramount, plus a few pixels as Al-muscovite, mostly at Silver Hill and the center of the Bodie district, and illite in a mine tailing at Silver Hill. Dolomite was given a good fit by Tricorder, and a fair number of pixels were mapped as such, but these pixels were scattered all over the image without any meaningful geological pattern. They were treated as misclassifications and removed from the final result, together with a few other minerals with low fits and small number of pixels: dolomite, phlogopite, hectorite, diaspore, clintonite, palygorskite, elbaite and nontronite.

In the VNIR, Tricorder mapped two different types of hematite. One is a fine-grained variety which was mapped scattered around hydrothermally altered areas in the Bodie and Paramount areas, and the other is a

mixture of hematite and quartz distinctively associated with the alteration at Bodie Bluff, plus a few pixels in the western part of Paramount. It also mapped goethite in the center of the Bodie district and in a tailing pond nearby. A few pixels scattered across the district were mapped as K-jarosite, while some others were classified as Fe^{2+}-bearing minerals in the center of Bodie district and at Silver Hill.

The algorithm took around four hours to complete the analysis for 126 minerals in the VNIR and SWIR running on a medium-performance Unix workstation (HP 9000).

A spatial comparison between the areas of major alteration identified by both methods reveals that in the SWIR, Na-montmorillonite was identified by both methods at approximately the same locations in Bodie and eastern part of Paramount. The mixture of kaolinite+smectite only shows good correlation between both methods at the center of the Bodie district, whereas another major area of occurrence for this mineral mapped by SAM at the western part of Paramount was mapped by Tricorder as well- and poorly-crystalline kaolinite and halloysite. The separation achieved by Tricorder between Na- and Ca-montmorillonite at Bodie, as well as between Na-montmorillonite, halloysite and poorly-crystalline kaolinite in the eastern part of Paramount, did not appear in the SAM results. SAM also mapped the western part of Paramount as a mixture of kaolinite+smectite and Na-montmorillonite, whereas Tricorder identified poorly-crystalline kaolinite, with subsidiary well-crystalline kaolinite and halloysite for the same pixels.

Comparing results obtained by the two methods only for those minerals that could be mapped by SAM (hematite, goethite and jarosite) in the VNIR reveals major differences. SAM did not find much hematite in the whole scene, whereas Tricorder mapped clusters of pixels as hematite in both districts. However, some of the pixels mapped as hematite by Tricorder were assigned to goethite by SAM. On the other hand, pixels that Tricorder mapped as goethite were assigned to jarosite by SAM.

6. CONCLUSIONS

We managed to recognize and map a variety of minerals associated with hydrothermal alteration processes using AVIRIS data at the Bodie and Paramount mining districts, California. The method selected for calibrating the data and for retrieving reflectance from radiance was found to be precise enough to allow mineral mapping without the use of ground data. This represents a major advantage for mineral exploration activities in which ground data acquisition is rarely possible.

Two algorithms were used and compared for mineral mapping: Spectral Angle Mapper (SAM) and Tricorder. In general, Tricorder was able to produce more detailed mineral maps than SAM. Results obtained for the SWIR region showed a relatively good coincidence between the two methods for alteration minerals of major occurrence (montmorillonite and kaolinite). Both methods were able to show a east-west zonation in the alteration at Paramount regarding these minerals, and also some zoning at Bodie. In addition, Tricorder was able to map two types of montmorillonite, two types of kaolinite, plus halloysite, muscovite and illite.

In the VNIR however, results from both methods were quite different. Some of the pixels mapped by SAM as goethite were assigned by Tricorder to hematite. Tricorder managed to map a greater number of pixels as some mineral with diagnostic spectral features than SAM.

Spectral analysis of samples to validate these results is still ongoing, but preliminary results appear to confirm the Tricorder results in the SWIR region. Some of the characteristics of SAM, such as the fact that it is available in commercial image processing packages, easy to use and relatively fast to compute make it a feasible alternative for mineral mapping in exploration activities. Tricorder on the other hand produced more detailed results than SAM, and will be available for general use in the near future, but its complexity will demand some training, basic knowledge of spectroscopy and considerably more computing time than SAM.

7. ACKNOWLEDGMENTS

The authors would like to thank R.O. Green and his collaborators from the AVIRIS project at NASA's Jet Propulsion Laboratory for the support with the atmospheric calibration of the data and Dr. R.N. Clark, at USGS's Spectroscopy Laboratory, for the use of Tricorder and fruitful discussions on mineral mapping. A.P. Crósta acknowledges the support of Fundação de Amparo à Pesquisa no Estado de São Paulo (FAPESP) through research grant # 94/3474-0 and the State University of Campinas (UNICAMP).

8 REFERENCES

Chrien, T.G., Green, R.O., Eastwood, M., 1990, "Accuracy of the spectral and radiometric laboratory calibration of the Airborne Visible/Infrared Imaging Spectrometer (AVIRIS)". *Proc. Second Airborne Visible/Infrared Imaging Spectrometer (AVIRIS) Workshop*, Pasadena, CA, June 4-5, 1990. JPL Publ. 90-54, pp. 1-14.

Clark, R.N., Swayze, G.A., Gallagher, A., King, T.V.V., Calvin, W.M., 1993, The U.S. Geological Survey Digital Spectral Library: Version 1: 0.2 to 3.0 μm. *U.S. Geological Survey, Open File Report 93-592*, 1340 p.

Clark, R.N., Swayze, G.A., Heidebrecht, K., Green, R.O., Goetz, A.F.H., 1995, "Calibration to surface reflectance of terrestrial imaging spectrometry data: comparison of methods". *Summaries of the Fifth Annual JPL Airborne Earth Science Workshop*, Pasadena, CA, January 23-26, 1995. JPL Publ. 95-1, vol. 1, pp. 41-42.

Clark, R.N., Swayze, G.A., 1995, "Mapping minerals, amorphous materials, environmental materials, vegetation, water, ice and snow, and other materials: the USGS Tricorder algorithm". *Summaries of the Fifth Annual JPL Airborne Earth Science Workshop*, Pasadena, CA, January 23-26, 1995. JPL Publ. 95-1, vol. 1, pp. 39-40.

Clark, R.N., Gallagher, A.J., Swayze, G.A., 1990, "Material absorption band depth mapping of imaging spectrometer data using a complete band shape least-square fit with library reference spectra". *Proc. Second Airborne Visible/Infrared Imaging Spectrometer (AVIRIS) Workshop*, Pasadena, CA, June 4-5, 1990. JPL Publ. 90-54, pp. 176-186.

Green, R.O., Conel, J.E., Roberts, D.A., 1993a, "Estimation of aerosol optical depth, pressure elevation, water vapor and calculation of apparent surface reflectance from radiance measured by the Airborne Visible/Infrared Imaging Spectrometer (AVIRIS) using a radiative transfer code". *SPIE*, vol. 1937, pp. 2-11.

Green, R.O., Conel, J.E., Helmlinger, M., Bosch, J., Chovit, C., Chrien, T., 1993b, "Inflight calibration of AVIRIS in 1992 and 1993". *Summaries of the Fourth Annual JPL Airborne Earth Science Workshop*, Pasadena, CA, October 25-29, 1993. JPL Publ. 93-26, vol. 1, pp. 69-72.

Herrera, P.A., Closs, L.G., Silberman, M.L., 1993, "Alteration and geochemical zoning in Bodie Bluff, Bodie mining district, eastern California". *Journal of Geochemical Exploration*, vol. 48, pp. 259-275.

Kruse, F.A., Lefkoff, A.B., Boardman, J.W., Heidebrecht, K.B., Shapiro, A.T., Barloon, P.J., Goetz, A.F.H., 1993, "The Spectral Image Processing System (SIPS) - interactive visualization and analysis of imaging spectrometer data". *Remote Sensing of the Environment*, vol. 44, pp. 145-163.

Silberman M.L., Breit, F., Lawrence, E.F., 1995, *Geology and Ore Deposits of Bodie Hills, Northern Mono Basin Region*. Geological Society of Nevada, Special Publ. 22, 49 p.

Taranik, J.V., Crósta , A.P., 1996, "Remote sensing for geology and mineral resources: an assessment of tools for geoscientists in the near future". *XVIII Congress of the International Society of Photogrammetry and Remote Sensing*, Vienna, Austria, July 9-19, 1996 (in prep.).

MAPPING HYDROTHERMALLY ALTERED ROCK ON MOUNT RAINIER, WASHINGTON: APPLICATION OF AVIRIS DATA TO VOLCANIC HAZARD ASSESSMENTS

James K. Crowley
USGS, MS 927, Reston, Virginia 22092

David R. Zimbelman
University of Colorado, Boulder, Colorado 80309

Hydrothermally-altered rocks on stratovolcanoes are closely linked to edifice failures and the generation of destructive volcanic debris flows (Scott and others, 1992; Lopez and Williams, 1993). Altered rocks (1) form zones of weakness along fractures, dikes, and volcanic bedding surfaces, and (2) contain hydrous clay minerals that modify debris flow physical properties, increasing flow cohesion and extending flow reach. As illustrated by the 1980 edifice failure and eruption at Mount Saint Helens (Lipman and Mullineaux, 1981), and the disasterous 1985 debris flows from Nevado del Ruiz, Columbia (Lopez and Williams, 1993), mass-waste events of catastrophic proportions are not uncommon. Edifice collapses and destructive debris flows can be triggered by eruptions or earthquakes, but can also occur without any precursory activity.

The Cascade volcanoes of the Pacific Northwest are prime settings for volcanic debris flow generation, and because of the potential hazards, Mount Rainier, Washington, was designated as a Decade Volcano study area in 1993. Mount Rainier lies on the outskirts of the Seattle-Tahoma metropolitan area and has been the source of many large Holocene debris flows. Included among these was the massive Osceola Mudflow (ca. 5600 years BP), which traveled 113 km into areas near Puget Sound that are now densely populated (Scott and others, 1992; Crandell, 1971).

This paper describes the use of NASA Airborne Visible/Infrared Imaging Spectrometer (AVIRIS) data for mapping altered rocks on Mount Rainier. AVIRIS data were acquired on July 19, 1994, under favorable conditions of relatively low mid-summer snow cover. The data were calibrated by using a band ratio-based atmospheric correction, followed by calibration to reflectance using laboratory spectral measurements of unaltered rock samples from Mount Rainier. The calibrated data were analyzed using least-squares spectral band fitting and linear spectral unmixing techniques.

Despite the extensive snow and ice cover on Mount Rainier, and the relatively limited rock exposures, AVIRIS data were very useful for mapping known areas of hydrothermally-altered rock. Argillically altered Quaternary volcanic rocks (secondary silica +/- kaolinite-smectite +/- sulfates) were discernable on the AVIRIS image in many areas where they have been mapped in outcrop, including a broad zone that trends E-W and bisects the volcano

through its summit (Zimbelman et al., 1994). Preliminary results distinguish two subtypes of argillic alteration--a relatively clay-rich subtype that is prevalent in younger rocks located on the upper flanks and summit of the mountain, and a relatively silica-rich (esp. cristobalite) subtype that is present in somewhat older rocks on the lower flanks. The clay-rich alteration displays broad spectral features near 2.2 μm produced by mixtures of alunite, kaolinite, smectite, jarosite, and silica (Figure 1, "A"). Spectra of the silica-rich alteration subtype are relatively subdued because of abundant cristobalite, which is spectrally featureless (Figure 1, "B"). The two subtypes of argillic alteration were not recognized prior to these AVIRIS mapping results and their distribution and significance is still being investigated. Fe-oxide rich rocks were mapped on the basis of characteristic spectral bands near 0.85 μm (Figure 1, "C"). Such rocks are widely-distributed on the edifice and probably were produced by ordinary degassing of lavas during flowage and cooling. Chlorite and sericite alteration in Tertiary rocks at the base of the edifice was mapped by using diagnostic spectral features near 2.32 and 2.20 μm, respectively (Figure 1, "D" and "E"). In addition to the altered rocks, several linear E-W spectral anomalies corresponding to local differences in snow particle size were observed on the upper flanks of Mount Rainier. Causes of the anomalies remain to be determined and could include structural controls on crevasse development, or perhaps, alignments of intermittent fumeroles.

Unstable slope conditions and glacial cover at many Cascade volcanoes present severe challenges for ground-based geologic mapping. Effective remote sensing methods for identifying altered rocks will significantly enhance the ability to evaluate volcanic debris flow risks. Ongoing work at Mount Rainier will focus on combining the AVIRIS results with geophysical and geochemical data to aid in the assessment and mitigation of debris flow hazards.

References

Crandell, D. R., 1971, Postglacial lahars from Mount Rainier volcano, Washington: U. S. Geological Survey Professional Paper 677, 75p.

Lipman, P. W., and Mullineaux, D. R., editors, 1981, The 1980 eruptions of Mount Saint Helens, Washington: U. S. Geological Survey Professional Paper 1250, 844p.

Lopez, D. L., and Williams, S. N., 1993, Catastrophic volcanic collapse: Relation to hydrothermal processes: Science, 260, p. 1794-1796.

Scott, K. M., Pringle, P. T., and Vallance, J. W., 1992, Sedimentology, behavior, and hazards of debris flows at Mount Rainier, Washington: U. S. Geological Survey Open File Report 90-385, Vancouver, Washington.

Zimbelman, D.R., Sisson, T.W., Whitney, Gene, and Esposito, K.J., 1994, Relationship of hydrothermal alteration to volcanic hazards at Mount Rainier, Washington-Preliminary results: Geological Society of America Abstracts with Program, v. 26, p. A-114.

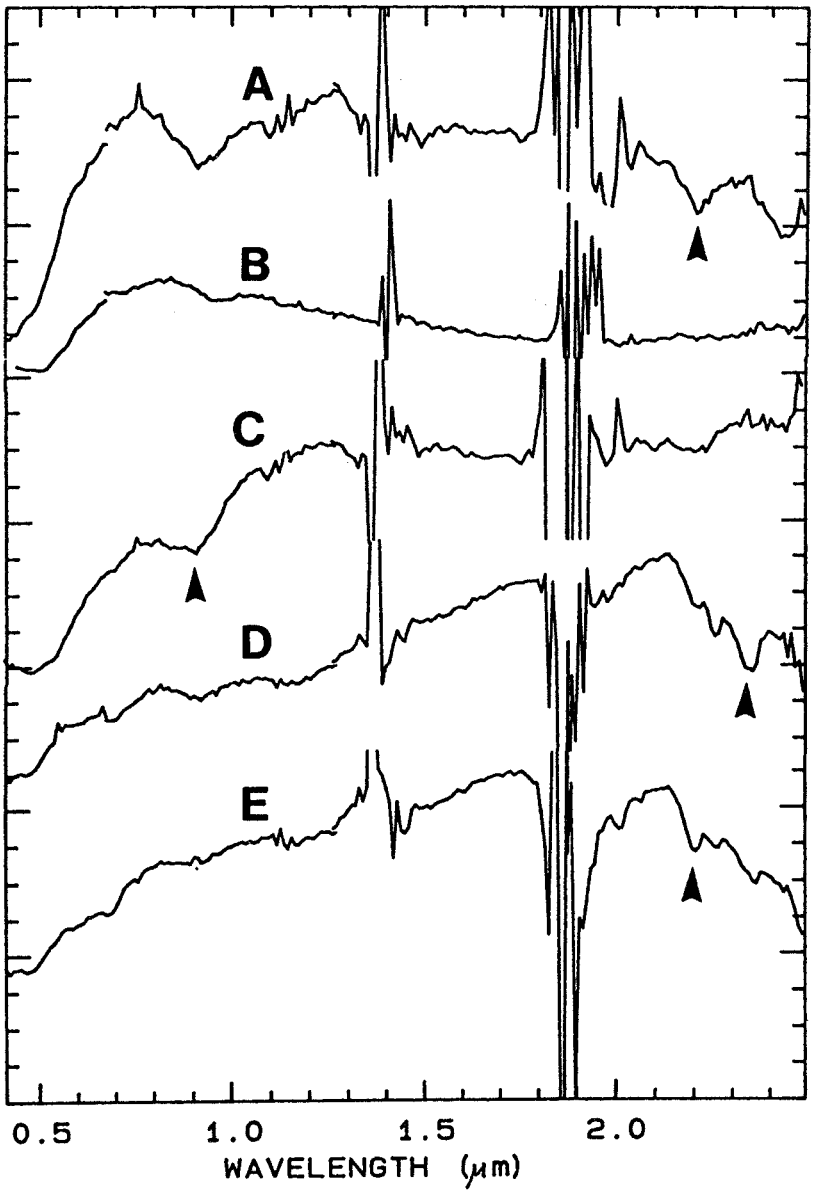

Figure 1. Representative AVIRIS spectra of alteration subtypes. "A", clay-rich argillic alteration; "B", silica-rich argillic alteration; "C", Fe-oxide-rich alteration; "D", Chlorite alteration; "E", sericite alteration. Arrowed spectral features are discussed in the text.

Page intentionally left blank

SURVEYING DEAD TREES AND CO_2-INDUCED STRESSED TREES USING AVIRIS IN THE LONG VALLEY CALDERA

Steven M. de Jong[1]
Jet Propulsion Laboratory
California Institute of Technology, Pasadena, CA 91109

1. INTRODUCTION

Since 1980 the Long Valley Caldera in the eastern Sierra Nevada (California) has shown signs of renewed volcanic activity (Langbein et al., 1993; Hill et al., 1985). Frequent earthquakes, a re-inflation of the caldera, hydrothermal activity and gas emissions are the outer symptoms of this renewed activity. In 1990 and 1991 several areas of dying trees were found around Mammoth Mountain. The cause of the die off of the trees was first sought in the persistent drought in the preceding years. However, the trees died regardless of age and species. Farrar et al. (1995) started a soil-gas survey in 1994 in the dead-tree areas and found carbon dioxide concentrations ranging from 30 to 96% at soil depths between 30 and 60 cm. CO_2-concentrations in the atmosphere are usually around 0.03% and in the soil profile CO_2-levels do commonly not exceed 4 to 5% (Voigt, 1962). Although not much is known about the effect of high levels of carbon dioxide in the soil profile on roots, it is most likely that the trees are dying due to oxygen deprivation: the CO_2 drives the oxygen out of the soil (Drew, 1991; Luxmoore et al., 1986; Voigt, 1962). So far, four sites of dead trees have been mapped around Mammoth Mountain.

The two largest dying trees sites are located near Horseshoe Lake and near Mammoth Mountain Main Lodge covering approximately an area of 10 and 8 ha respectively. Analysis of the gas composition regarding the $^3He/^4He$-ratio and the percentage biogenic carbon reveals the source of the gas: the magma body beneath the Long Valley Caldera (Farrar et al, 1995). Until recently it was not known that volcanoes release abundant carbon dioxide from their flanks as diffuse soil emanations (Baubron et al., 1990). As a result of the magma gas emission around Mammoth Mountain there is an excellent sequence of dead trees, stressed trees, healthy trees and bare soil surfaces. This research site provides excellent opportunities to:

1. Study the capabilities of imaging spectrometry to map stressed (and dead) pine and fir species;
2. Study methods to separate the vivid vegetation, stressed vegetation and dead vegetation from the soil background of glacial deposits and crystalline rocks.

The dead tree areas are located on the flanks of Mammoth Mountain (N:37°37'45" and W:119°02'05") at an elevation between 2600 and 3000 meters. The area is covered by an open type of Montane Forest. The dominant tree species are Lodgepole Pine (Pinus contorta), the Red Fir (Abies magnifica) and the Jeffrey Pine (Pinus jeffreyi). The soil surface near Horseshoe Lake is generally fairly bright. The surface is covered by glacial deposits (till) consisting mainly of weathered granitic rocks.

2. FIELD SPECTRAL MEASUREMENTS

In October 1995 spectral field measurements were carried out in two of the four dead tree sites using the JPL FieldSpec instrument (ASD, 1994). This instrument covers the 350 - 2500 nm spectral region using three individual spectrometers. It samples every 2 nm and the resolution varies between 10 and 11 nm. Together with each set of target measurements a white reference plate and the instrument's dark current were determined.

---

[1] Visiting Scientist from: Department of Physical Geography, Utrecht University, 3508 TC The Netherlands (s.dejong@frw.ruu.nl).

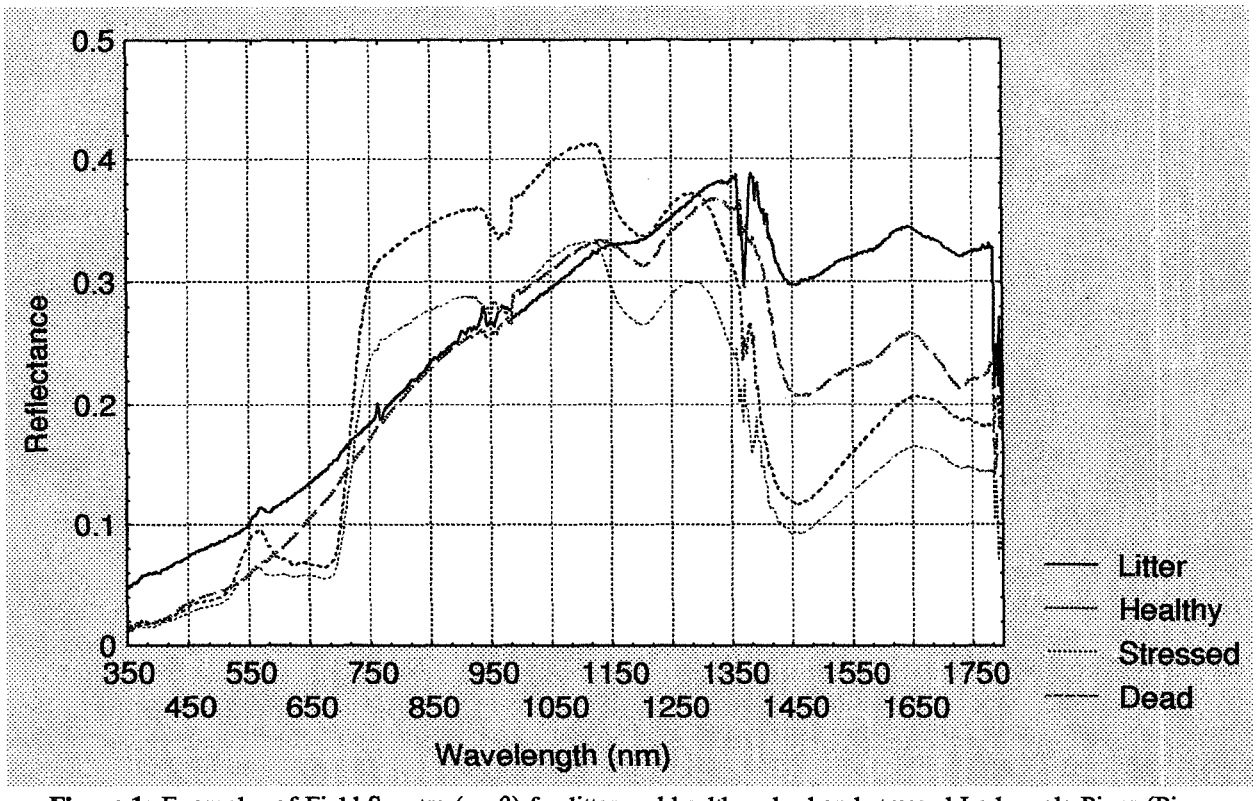

Figure 1: Examples of Field Spectra (n=8) for litter and healthy, dead and stressed Lodgepole Pines (Pinus contorta var. murrayana).

Multiple target measurements were averaged to increase the signal-to-noise ratio. The dark current was subtracted from the raw spectral measurements and the white reference measurements were used to convert the raw data to reflectance. Spectral behaviour of several surfaces was measured: healthy trees (several species), stressed and dead trees, the litter layer, dead trunks, bare soil surfaces and rock outcrops and some reference sites for radiometric image corrections. Trees were considered 'stressed' if several branches were dead or if at least some of the needles had lost color.

The field spectra were then analyzed on their information content regarding healthy, stressed and dead trees and the soil background reflectance. The results yield a physical basis for the interpretation of AVIRIS imagery. Figure 1 shows some examples of the collected field spectra of Lodgepole Pines. The spectra show clearly the presence and the absence of respectively the chlorophyll absorption near 680 nm in the healthy and dead Lodgepole Pine spectra. Analysis methods applied to the field spectra are 1) standard normalization procedures, 2) first derivative transform, and 3) convex hull transform and automatic absorption feature finding.

First derivative analysis (Curran, et al. 1992; Wessman et al., 1989) is a common method to enhance abrupt changes in the spectral curve of objects e.g. to enhance the red edge for vegetation. The convex hull transformation is a method to normalize spectra (De Jong, 1994a; Sedgewick, 1983). The convex-hull technique is analogous to fitting a rubber band over a spectrum to form a continuum. The difference between the hull and original spectrum is subtracted from a constant to obtain a hull-difference. Such a normalization of the spectra allows the application of quantitative absorption feature characterization.

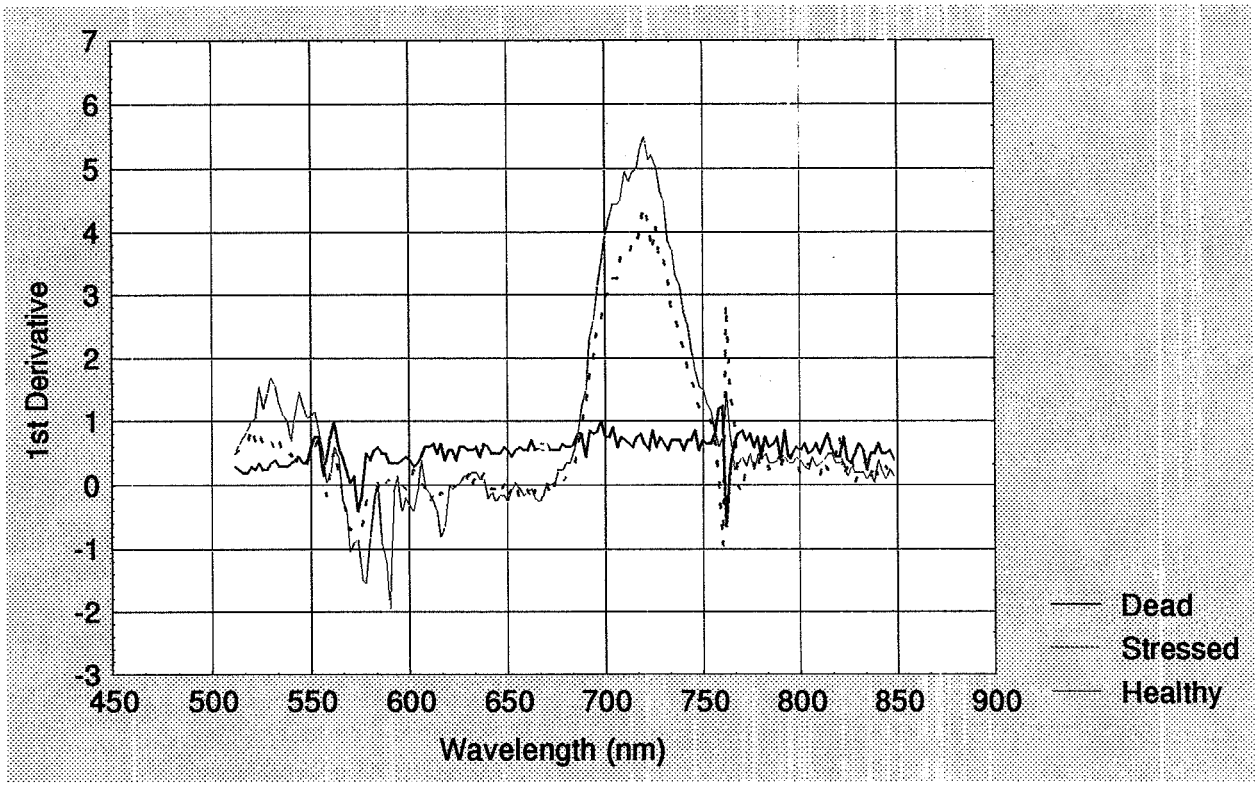

Figure 2: First Derivative Spectra (500 - 850 nm) of Field Measurements of Dead, Stressed and Healthy Lodgepole Pines.

The figures 2 and 3 and table 1 show some preliminary results. Figures 1 and 2 show the reduced chlorophyll absorption for the stressed Lodgepole Pines and the absent chlorophyll absorption for the dead Pines. The red edge or blue shift (Curran et al., 1992) is visible but not very pronounced in the derivative spectra shown in figure 2. The spectral range from 1400 to 1700 nm displays an increasing brightness with decreasing water content (from healthy to dead pines to litter). The spectra for dead pines and litter show the absorption features for lignin around 1720 nm, described by Ustin et al. (1991), Peterson et al. (1988), Wessman et al. (1989) and Weyer (1985). Furthermore, the range from 1500 to 1750 nm shows a positive first derivative for the vegetative features while non-vegetative objects are usually flat or even show the decrease of solar energy in this region. Figure 3 presents spectra derived from an AVIRIS image of August 23rd, 1994. These normalized image spectra also display the lignin absorption features and the positive slope for vegetation between 1500 and 1650 nm. Some first results for the convex hull transformation of the field spectra (0.4 - 2.5 μm) are shown in table 1. Water is the most dominant absorption feature identified by the automatic absorption feature algorithm. The stressed Lodgepole Pine shows a decrease in chlorophyll absorption of approximately 15% compared to the healthy tree. The lignin absorption features for the litter spectrum and for the dead Lodgepole Pine spectrum are only identified if the 'depth tolerance' of the algorithm is reduced. Absorption features are then found at 1724 nm with a relative depth of respectively 1.60 and 3.53.

3. AVIRIS IMAGE ANALYSIS

Three AVIRIS (Airborne Visible/Infrared Imaging Spectrometer) images of the Mammoth Mountain region were retrieved from the JPL archive acquired at the following dates: 21 May 1994, 23 August 1994 and 22 June 1995. The AVIRIS radiance data were converted to reflectance using the empirical line method. A linear regression function was computed between the field reflectance and the AVIRIS data of a dark and a bright surface (a large asphalt parking lot near Mammoth Mountain Lodge and a gravel field south of Mammoth Village).

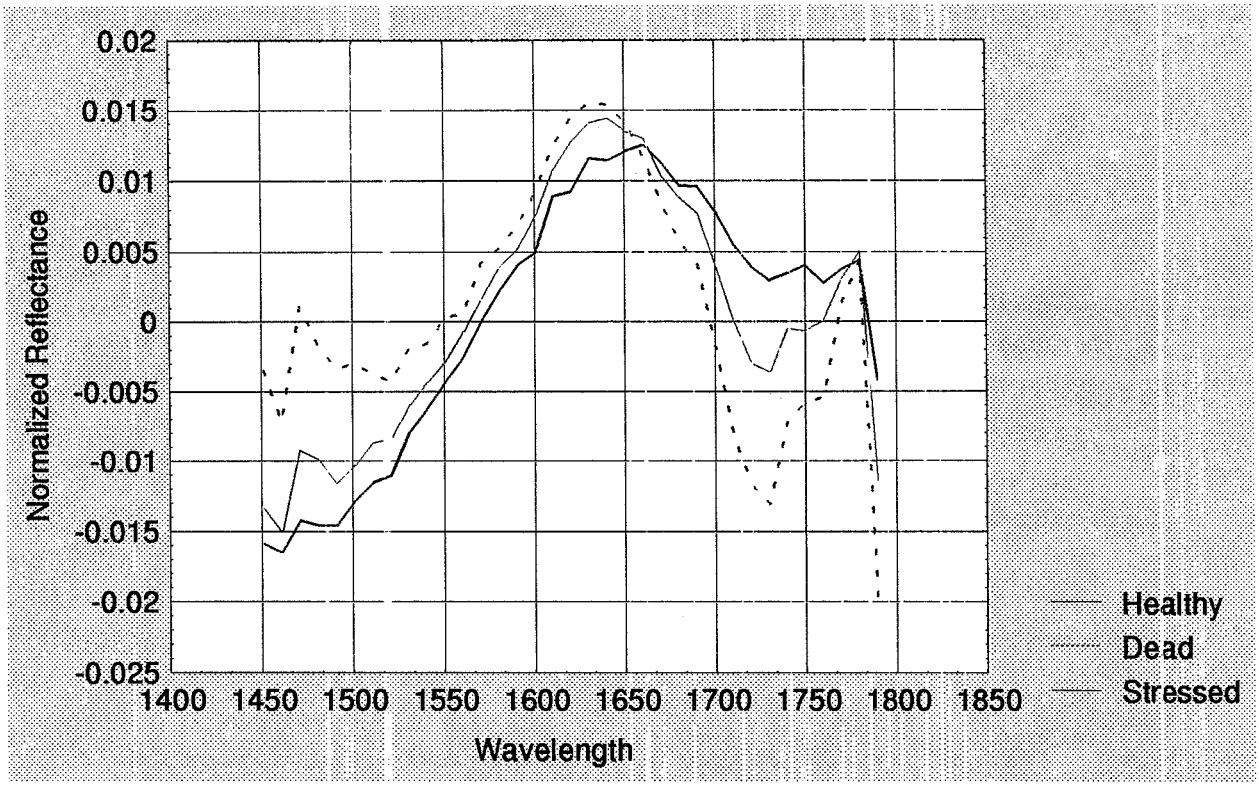

Figure 3: Normalized AVIRIS Spectra (1450 - 1800 nm) of Healthy, Stressed and Dead Pine Species near Horseshoe Lake.

Reflectances of a number of sites throughout the three multi-temporal images were compared to verify the results of the empirical line conversion. The next steps in this research are 1) to study further the AVIRIS spectral properties of the dead trees area at Horseshoe Lake, 2) to examine the temporal changes of the dead trees areas using the AVIRIS images available for different dates, 3) to study stress indicators for the Pine trees and 4) to use spectral unmixing to produce a map of stressed, dead and healthy trees.

3.1 Dead Tree Image Transect

In the August 1994 image a transect was put over the dead tree area near Horseshoe Lake. The transect covers from north-east to south-west: the Borrow pit, stressed trees, dead trees and bare soil areas, dead and stressed trees and healthy trees. Along this transect the spectral information is analyzed regarding chlorophyll absorption, lignin absorption and stress indicators. Figure 4 shows a 3D plot of the transect. The Y-axis shows the AVIRIS spectral bands from 460 to 1250 nm, the X-axis assigns the distance along the transect (total distance is approximately 1200 m) and the Z-axis reflectance. Pixels 74 to 77 (X-axis) show the high reflectance throughout the spectrum of the bright surface of the Borrow pit. Pixels 62 to 74 cover an area of stressed pine trees, the typical vegetation shape of the spectrum is still visible but chlorophyll absorption is reduced. Pixels 46 to 60 cover an area of exclusively dead trees and of bright soil surfaces of weathered granite and glacial till (many trees have been cut and removed from this former campground). Pixels 20 to 45 show a transition zone of stressed and healthy pine trees. The beginning of the transect is an area of vivid deciduous trees and pine species with a strong chlorophyll absorption and a significant infrared reflectance.

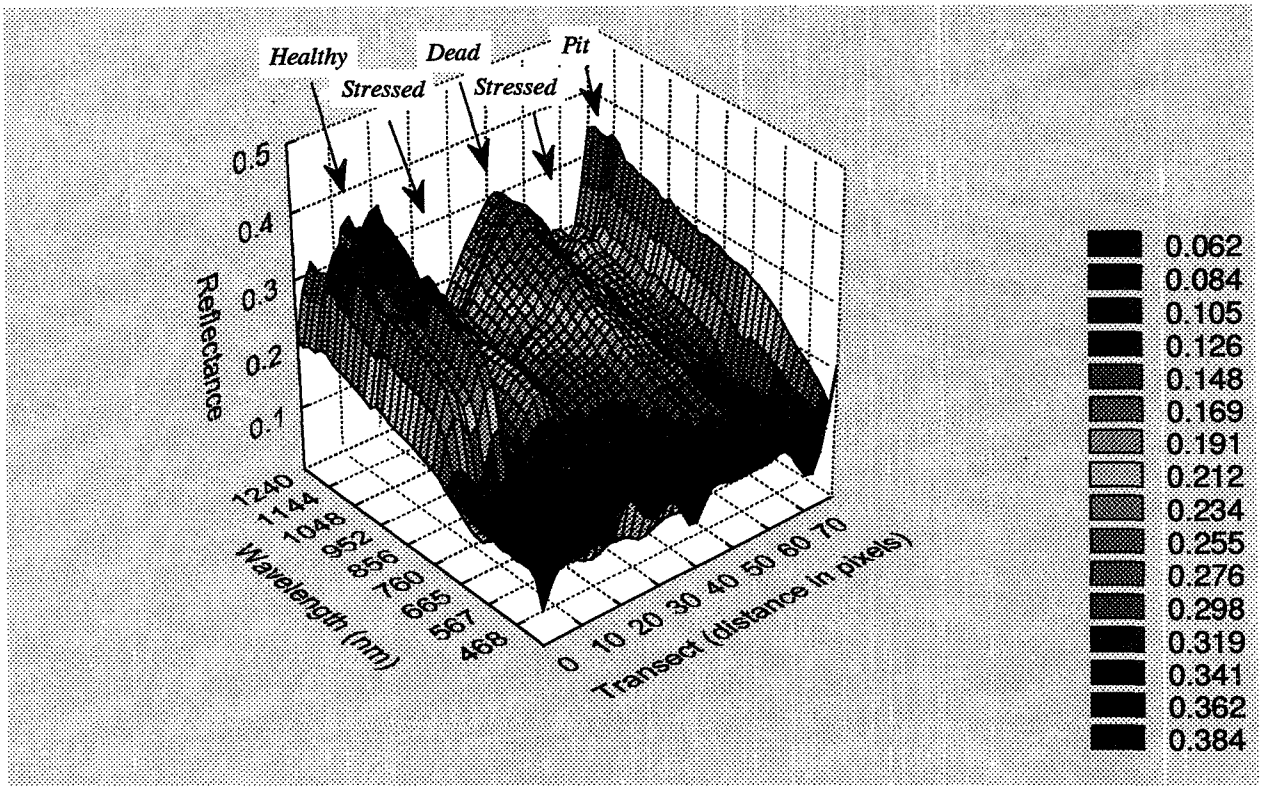

Figure 4: 3-Dimensional Plot of the AVIRIS Image Transect near Horseshoe Lake. The Transect Crosses a Gravel Pit and Healthy, Stressed and Dead Pine Trees. The X,Y,Z Axes Represent Respectively the Distance along the Transect, the AVIRIS Spectral Range from 460 to 1250 nm and the Reflectance.

3.2 Multi-temporal Analysis

A multi-temporal analysis of the three available airborne images was carried out to assess the temporal changes of forest cover between the first available AVIRIS scene (21 May 1994) and the last acquired image (22 June 1995). The three images were geometrically matched to one another using ground control points and a first degree polynomial warping algorithm. Next a Normalized Difference Vegetation Index (NDVI) was computed for each image. Large NDVI values indicate pixels with high proportions of green biomass, low values indicate pixels of bare soil, water bodies or built up areas and intermediate values give an indication of differences in coverage with green vegetation (De Jong, 1994b; Tucker, 1979). The three multi-temporal NDVI images were displayed as a red, green and blue combination and visually interpreted. Different combinations of red, green and blue mark a change of NDVI values, which is an indication for an increase or decrease of vegetative cover. Results show that the Horseshoe Lake dead trees area is fairly constant over the 13 months studied. Only the western edge of this region shows some minor enlargement. The second dead tree area further uphill of Horseshoe Lake shows a significant decrease of NDVI values over time and hence, an important enlargement of the dead tree area since May 1994. At the western flank of Mammoth Mountain uphill of Sotcher Lake another area of diminishing NDVI values was found. It was first identified as a fifth, so far unknown dead tree area. However, image and topographic interpretation revealed that it is most probably an avalanche area where some trees vanished. Fieldwork must reveal the definite cause of the NDVI drop as differences in snow cover hamper multi-temporal image interpretation. The dead tree areas near Red Lake and the Mammoth main lodge are unfortunately outside the coverage of this multi-temporal data set.

3.3 Stress Indicators

The first sign that vegetation is exposed to stress (senescence, water deficiency, or herbicide) is usually a decrease of the absorption of radiation by chlorophyll (Carter, 1994; Carter & Miller, 1994; Hoque & Hutzler, 1992; Ruth et al., 1991). These subtle changes of light absorption are at first detectable at the edges of the chlorophyll absorption feature i.e. around 605 nm and 695 nm. The plant stress indicators proposed by Carter (1994) were applied to the field and image spectra to determine their suitability to map the stressed pines near Mammoth. Reflectance ratios as stress indicators, suggested by Carter (1994), use the following bands: 606 and 760 nm, 695 and 420 nm or 695 and 760 nm. If the Mammoth field data (e.g. figure 2) are compared to Carter's dataset, a small shift of the chlorophyll absorption band towards longer wavelengths seems to occur. This shift might be due to different vegetation species or to a shift in sensor sensitivity.

Carter's first stress indicator (R606/R760) applied to the spectra of figure 1 yields values for healthy, stressed and dead pines of 0.22, 0.25 and 0.45 respectively. Carter (1994) reports values determined in the laboratory ranging from 0.13 to 0.47. The image transect of figure 4 yields values ranging from 0.24 to 0.5 for the tree covered areas. The values for the bare surface areas were not considered. A prerequisite for deriving valuable early stress indications for trees using AVIRIS, requires first a separation of vegetated areas from bare areas. The latter is one of the topics for future planned work.

3.4 Spectral Unmixing

In the next phase of this study spectral unmixing (Roberts et al., 1993; Adams et al., 1993) will be used to assess the spatial distribution of the stressed and dead trees. A group of spectral end members is currently prepared. Results will be presented at the 1996 JPL Airborne Earth Science Workshop.

4. DISCUSSION AND RESULTS

Field and image spectra are used in this study to determine the practical use of AVIRIS images to survey CO_2 induced stress and dead pine trees. First results show that field as well as image spectra contain information on the chlorophyll absorption and a decline of chlorophyll absorption in case of stressed trees. In the dead tree areas the chlorophyll absorption is absent but the presence of dead vegetative material can be revealed from absorption features in the 1500 to 1750 nm range. The use of multi-temporal AVIRIS images appeared useful to detect changes of the surface area of dead and/or stressed trees although the time period of 13 months is rather short and some problems were experienced with differences in snow cover and sun angle. Some preliminary results using AVIRIS images to derive stress indicators for pine trees are encouraging but need further study.

Acknowledgments

The research described in this paper was carried out at the Jet Propulsion Laboratory, California Institute of Technology, and was sponsored by the Netherlands Organization for Scientific Research (NWO Talent program). Mr. D.A. Roberts (University of California, Santa Barbara) is acknowledged for providing the Prism software and for the fruitful discussions.

REFERENCES

Adams J.B., M.O. Smith, A.R. Gillespie, 1993, Imaging Spectroscopy: Interpretation Based on Spectral Mixture Analysis. In: Pieters C.M. & P.A.J. Englert (Eds.), Remote Geochemical Analysis: Elemental and Mineralogical Composition. Cambridge University Press, New York. pp.145-166.

ASD, 1994, FieldSpec FR User's Guide. Analytical Spectral Devices Inc., Boulder CO.

Baubron J.C., P. Allard & J.P. Toutain, 1990, Diffuse Volcanic Emissions of Carbon Dioxide from Volcano Island, Italy. *Nature Vol.344, pp.51-53.*

Carter G.A., 1994, Ratios of Leaf Reflectances in Narrow Wavebands as Indicators of Plant Stress. *International Journal of Remote Sensing vol.15, pp.697-703.*

Carter G.A. & R.L. Miller, 1994, Early Detection of Plant Stress by Digital Imaging within Narrow Stress-Sensitive Wavebands. *Remote Sensing of Environment vol.50, pp.295-302.*

Curran P.J., J.L. Dungan, B.A. Macler, S.E. Plummer & D.L. Peterson, 1992, Reflectance Spectroscopy of Fresh Whole Leaves for the Estimation of Chemical Concentration. *Remote Sensing of Environment 39, pp.153-166.*

De Jong S.M., 1994a, Applications of Reflective Remote Sensing for Land Degradation Studies in a Mediterranean Environment. *Netherlands Geographical Studies 177, KNAG Utrecht. 240pp.*

De Jong S.M., 1994b, Derivation of Vegetative Variables from a Landsat TM Image for Erosion Modelling. *Earth Surface Processes and Landforms, Vol.19, pp.165-178.*

Drew M.C., 1991, Oxygen Deficiency in the Root Environment and Plant Mineral Nutrition. In: M.B. Jackson, Plant Life under Oxygen Deprivation. SPB Academic Pub. The Hague. pp.303-326.

Farrar C.D., M.L. Sorey, W.C. Evans, J.F. Howle, B.D. Kerr, B.M. Kennedy, C.Y. King & J.R. Southon, 1995, Forest-Killing Diffuse CO_2 Emission at Mammoth Mountain as a Sign of magmatic Unrest. *Nature Vol.376, pp.675-678.*

Hill D.P., R.A. Bailey & A.S. Ryall, 1985, Active Tectonic and Magmatic Processes Beneath Long Valley Caldera, Eastern California: An Overview. *Journal of Geophysical Research, Vol.90, pp.11111-11120.*

Hoque E. & P.J.S. Hutzler, 1992, Spectral Blue-Shift of Red Edge Monitors Damage Class of Beech Trees. *Remote Sensing of Environment 39, pp.81-84.*

Langbein J., D.P. Hill, T.N. Parker & S.K. Wilkinson, 1993, An Episode of Reinflation of the Long Valley Caldera, Eastern California: 1989-1991. *Journal of Geophysical Research Vol.98, pp.15851-15870.*

Luxmoore R.J., J.J. Landsberg & M.R. Kaufmann, 1986, Coupling of Carbon, Water and Nutrient Interactions in Woody Plant Soil Systems. Heron Pub., Victoria, Canada. 467 pp.

Peterson D.L., J.D. Aber, P.A. Matson, D.H. Card, N. Swanberg, C. Wessman & M. Spanner, 1988, Remote Sensing of Forest Canopy and Leaf Biochemical Contents. *Remote Sensing of Environment 24, pp.85-105.*

Roberts D.A., M.O. Smith & J.B. Adams, 1993, Green Vegetation, Non-Photosynthetic Vegetation, and Soils in AVIRIS Data. Remote Sensing of Environment 44, pp.255-269.

Ruth B., E. Hoque, B. Weisel & P.J.S. Hutzler, 1991, Reflectance and Fluorescence Parameters of Needles of Norway Spruce Affected by Forest Decline. *Remote Sensing of Environment 38, pp.35-44.*

Sedgewick R., 1983, Algorithms. Addison-Wesley, Reading, Massachusetts.

Tucker, C.J. 1979. 'Red and Photographic Infrared Linear Combinations for Monitoring Vegetation'. *Remote Sensing of Environment 8, pp. 127-150.*

Ustin S.L., C.A. Wessman, B. Curtiss, E. Kasischke, J. Way & V.C. Vanderbilt, 1991, Opportunities for Using the EOS Imaging Spectrometers and Synthetic Aperture Radar in Ecological Models. *Ecology Vol.72, pp.1934-1945.*

Voigt G.K., 1962, The Role of Carbon Dioxide in Soil. *In: T.T. Kozlowski (Ed.), Tree Growth. Ronald Press Company, New York. pp.205-220.*

Wessman C.A., J.D. Aber & D.L. Peterson, 1989, An Evaluation of Imaging Spectrometry for estimating Forest Canopy Chemistry. *International Journal of Remote Sensing, Vol.10, pp.1293-1316.*

Weyer L.G., 1985, Near Infrared Spectroscopy of Organic Substances. *Applied Spectroscopy reviews 21, pp.1-43.*

Table 1: Results of Automatic Absorption Feature Search.

Wavelength	Depth	Area	Asymmetry
Healthy Lodgepole Pine (Pinus contorta):			
1.8040	25.2592	3.6183	0.0314
1.4540	22.2009	4.7954	0.4094
0.6860	18.4455	2.2596	2.6633
1.9860	13.6994	0.3587	0.1768
1.9700	13.6013	0.1553	1.9560
Stressed Lodgepole Pine (Pinus contorta):			
1.8040	18.5023	2.6410	0.0441
1.4460	17.5540	3.5220	0.3128
0.6880	14.2796	1.9255	3.1891
1.9640	12.0939	0.2501	0.3853
1.7940	11.8013	0.1222	4.3238
Dead Lodgepole Pine (Pinus contorta):			
1.8040	25.1266	3.5749	0.0278
1.9640	14.9782	0.1669	0.5096
1.9560	14.1485	0.0831	0.5139
1.4540	13.5969	2.3908	0.3469
2.1060	11.1379	0.2055	1.5145
1.7880	10.8838	0.1313	0.5303
Litter:			
1.8040	31.5548	4.6171	0.0400
1.9560	11.5030	0.0454	1.0037
1.9600	11.3799	0.1287	0.2122
1.7880	9.1239	0.0661	0.8646
1.4460	8.0103	1.1761	0.3211
Healthy Red Fir (Abies magnifica):			
1.4460	25.3815	4.6679	0.0950
1.4280	25.2224	1.0844	20.5118
1.8040	24.0184	3.4357	0.0349
0.6880	23.6689	2.9338	2.9247
1.9640	16.5759	0.2219	1.3108

MAPPING VOLCANIC GAS EMISSIONS IN THE MAMMOTH MOUNTAIN AREA USING AVIRIS

Steven M. de Jong[1] & Thomas G. Chrien
Jet Propulsion Laboratory
California Institute of Technology, Pasadena, CA 91109

1. INTRODUCTION

The Long Valley Caldera located in the eastern Sierra Nevada (California) shows new signs of volcanic activity (Langbein et al., 1993; Farrar et al., 1995). This renewed activity is expressed by gas emissions, hydrothermal activity and frequent earthquakes. Analysis of the gas composition regarding the percentage biogenic carbon and the $^3He/^4He$-ratio (Farrar et al., 1995) revealed that the gas source is the magma body approximately 7 km beneath the Long Valley Caldera. The gas from the magma body surfaces not only via the fumaroles but also emerges along geological faults. Some of the spots where gas surfaces, are marked by dead or stressed trees. Other spots may not yet be identified. It is only recently known, from research at `Vulcano Island' in southern Italy, that volcanoes release abundant carbon dioxide from their flanks as diffuse soil emanations (Baubron et al., 1990). Mammoth Mountain seems to behave in a similar manner. The research described in this paper is designed to determine whether AVIRIS (Airborne Visible/Infrared Imaging Spectrometer) can be used to identify areas of volcanic gas emissions.

2. BACKGROUND

The composition of volcanic gases can vary largely. The ten most common volcanic gas species are: H_2O, CO_2, SO_2, HCl, H_2S, S_2, H_2, CH_4, HF, CO, SiF_4 (Andres & Rose, 1995; Sorey et al., 1993; Gerlach & Graeber, 1985). A number of these gases do not have absorption features in the spectrum covered by AVIRIS (0.4 - 2.5 μm) and are consequently not suitable to map volcanic gas fluxes. In any case, the volcanic gas emissions must be monitored through the earth's atmosphere. The atmosphere contains approximately 30 gases from which several are also found in volcanic gas emissions.

Two approaches can be followed to map the volcanic fluxes near Mammoth:
1. To detect volcanic gas species not normally present in the atmosphere;
2. To image the abundance of normally present gases to detect spatial anomalies.

The most promising approach to trace the volcanic emissions is using the following two gases: carbon dioxide (CO_2) and/or methane (CH_4) as both gases have absorption features in the AVIRIS spectral range. Absorption features for CO_2 are found near 1270, 1575, 1610, 1960, 2005 and 2055 nm (Pieters & Englert, 1993; Wolfe & Zissis, 1989). Fairly strong gaseous absorption occurs in the latter two bands. CH_4 has only absorption features near 2350 nm in the AVIRIS spectral range.

The most promising gas is CO_2 because 1) fumarole gas analysis has shown that 90% of the gas is CO_2 near Mammoth (Farrar, pers. comm.[2]; Sorey et al., 1993), 2) CO_2 is distributed fairly homogeneously throughout the atmosphere and 3) field measurements have shown that the CO_2 flux is large (approximately 1200 tonnes per day for the 20 ha. dead tree area) from the flanks of Mammoth Mountain (Farrar et al., 1995). Unfortunately, it is not

---

[1] Visiting Scientist from: Department of Physical Geography, Utrecht University, 3508 TC Utrecht, The Netherlands (s.dejong@frw.ruu.nl).

[2] C.D. Farrar, personal communication, US Geological Survey, Carnelian Bay, CA, 1996.

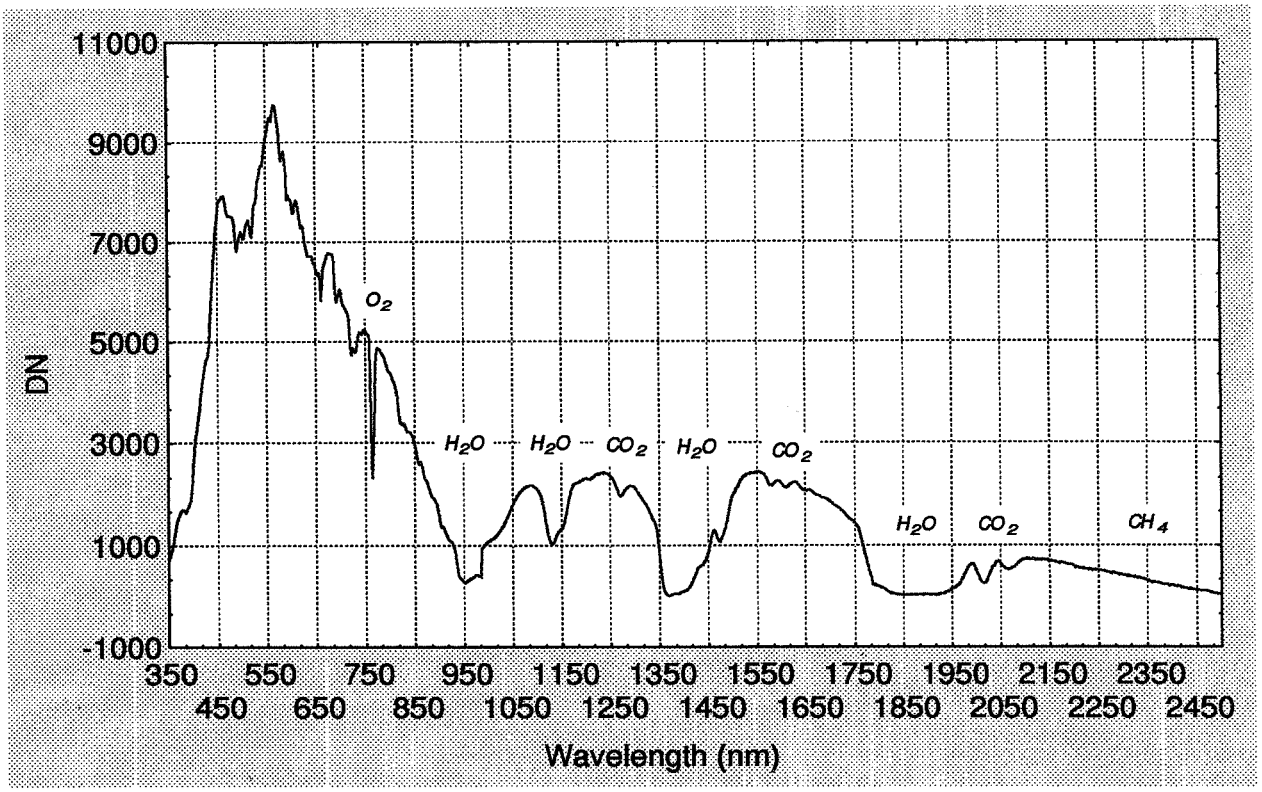

Figure 1: Raw Field Spectrum (Average of Eight Samples) of a Gas Discharge of a Fumarole at Hot Creek Measured over a White Reference Plate. Several CO_2 Absorption Features (1270, 1575, 1610, 2005, 2055nm) are Visible, no Feature at the CH_4 position is visible.

known whether this CO_2 flux at Mammoth is constant in time. The flux depends among other things on magma activity, barometric pressure and changes in soil moisture content.

Some of the problems that play a role in the mapping of volcanic CO_2 emission are the temporal, spatial and vertical distribution of gases in the atmosphere and the temporal (and spatial) distribution of the volcanic CO_2 flux, which is unknown. Research at `Vulcano Island' (Italy) has shown that Fumarole gas composition varies largely over time (Tedesco, 1995) and that the concentration of CH_4 in the gas flux might be too small to detect using AVIRIS (Sorey et al., 1993). Other problems are the low-energy solar irradiance in the 2.0 - 2.5 μm spectral region resulting in a low signal-to-noise ratio at the CO_2 absorption bands. Furthermore, no sufficient field data are available to verify any mapping results.

3. FIELD SPECTRA

In October 1995 a field campaign was organized in the Mammoth Mountain region to survey dead tree areas and to collect field spectral measurements. Field spectra were taken using JPL's FieldSpec spectrometer (ASD, 1994). This instrument covers the spectral region from 350 to 2500 nm using three individual spectrometers. It samples every 2 nm and the resolution varies between 10 and 11 nm. Together with each set of target measurements a white reference plate and the instrument's dark current were determined. Multiple target measurements were averaged to increase the signal-to-noise ratio. The dark current was subtracted from the raw DN spectral measurements and the white reference measurements were used to convert the raw data to reflectance. Figure 1 shows a raw spectrum (average of 8 samples) covering the entire AVIRIS spectral range of a fumarole near Hot Creek in Long Valley Caldera. The raw spectrum shows clear absorption features for water, oxygen and carbon dioxide. An artifact occurs near 980 nm due to a switch of the spectrometers.

Figure 2 shows reflectance spectra (1950 - 2250 nm) of the gas from the Hot Creek fumaroles. Fum1 and Fum2 are measured over the white target, Fum3 is a gas spectrum taken towards the sun. Each spectrum is an average of

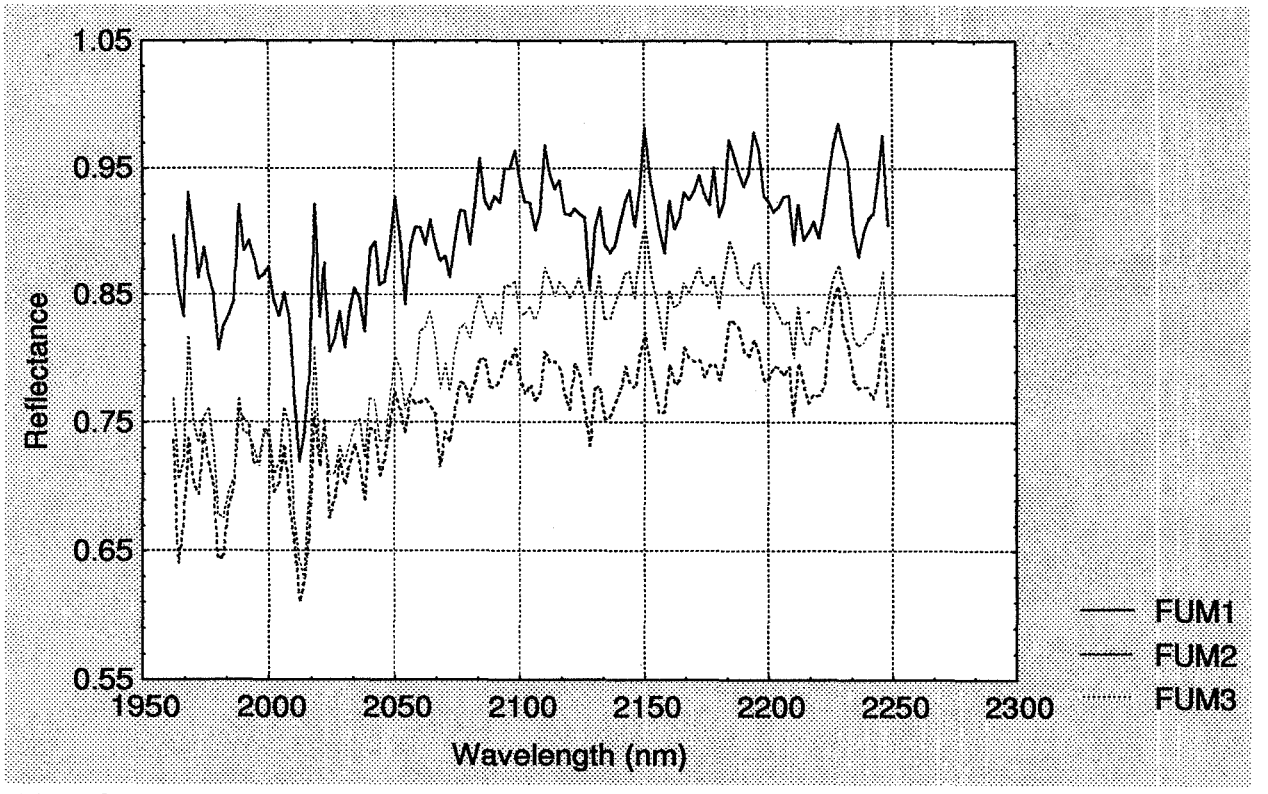

Figure 2: Reflectance Field Spectra (1950 - 2250 nm) of Gas Discharges of Three Fumaroles at Hot Creek. Each Spectrum, Although Noisy, Shows the CO_2 Absorption Features near 2000nm.

8 measurements. The 2005 CO_2 absorption features are visible in all three spectra although the contribution of noise in the spectra is considerable and a small shift to longer wavelengths seems to occur. Methane absorption is not found in any of the field spectra.

4. IMAGE ANALYSIS

Three AVIRIS images of the Mammoth region were extracted from the JPL archive for the following dates: 21 May 1994, 23 August 1994 and 22 June 1995. Radiance images and empirical line corrected images were both used for analysis in this study. Radiance spectra of areas inside and outside the suspected volcanic gas emissions regions were gathered from the August 1994 image. Next a darkest pixel correction was applied to these spectra. Spectra inside the gas emission region were expected to have stronger absorption features in the CO_2 bands than spectra sampled outside this region. The selected areas comprise two areas of rock outcrops at Mammoth Crest and near Heart Lake, the Fumarole area at the flank of Mammoth Mountain, the dead tree area near Horseshoe Lake and the beach of Horseshoe Lake. The spectra of the selected areas were visually interpreted and analyzed using a convex hull transformation.

4.1 Convex Hull Transformation

In order to compare the spectra, they were first normalized using a convex hull method (De Jong, 1994; Green and Graig, 1985; Sedgewick, 1983). The convex-hull technique is analogous to fitting a rubber band over a spectrum to form a continuum (or hull). The difference between the hull and original spectrum is subtracted from a constant e.g. 1000 to obtain a hull-difference. The advantage of analyzing the transformed data is that the depth of absorption features remains constant with respect to the hull whereas depth and position of absorption features in the original spectrum are influenced by the overall shape and brightness of the spectrum. After transformation a feature finding algorithm was applied (Grove et al., 1992) to quantify the absorption features of the spectra in terms of spectral position, depth, area and asymmetry.

Table 1 and figure 3 show the results of the convex hull transform for the 1900 - 2500 nm spectral region. Table 1 and figure 3 show that both the CO_2 absorption features (2004 and 2054) are identified by the feature finding algorithm. For all test areas these two absorption features are dominant regarding depth and area in this spectral region. However, the suspected emission areas (areas 3 and 4) do not produce significant stronger CO_2 absorption in spite of the fact that the convex hull algorithm corrects for differences in brightness.

4.2 CIBR - Algorithm

Several (ratio) algorithms were applied to the spectral domain of the AVIRIS images to detect or enhance the CO_2 absorption. So far, the continuum interpolated band ratio (CIBR) algorithm (Carrère & Conel, 1993) provides the best results. The CIBR algorithm uses the `shoulders' at either side of the absorption feature to interpolate a radiance continuum over the absorption feature of interest. Next, a ratio is computed between the absorption band and the interpolated continuum:

$$CIBR = B_2 / (c_1B_1 + c_2B_3)$$

where B_2 is the radiance at the absorption feature position, B_1 and B_3 are the radiance values at the shoulders and c_1 and c_2 are coefficients. The values of c_1 and c_2 depend on the symmetry of the continuum at either side of the absorption feature. Complete symmetry results in c_1 and c_2 values of 0.5.

The CIBR algorithm shows better results i.e. spatial patterns for the 2003 absorption feature than for the 2053 feature. The CIBR spatial pattern for the 23 August 1994 AVIRIS images shows several areas of large CIBR-values near Mammoth Lakes, near Crater Meadows, near Minaret Summit and north of the Mammoth Mountain Lodge. Furthermore, all the lakes show large CIBR values in a salt and pepper pattern. The lakes might show up not because they contain vast amounts of carbon dioxide but because the reflected radiance near the 2003 absorption feature is small. The CIBR algorithm enhances the noise when the radiance values are small. In order to verify the latter theory, the CIBR algorithm was also applied to the 760 nm oxygen and the 940 and 1140 nm (minor) water absorption bands, which also resulted in a bright salt and pepper pattern for the lakes. The interpretation of the spatial pattern remains very difficult as it displays clearly the dead tree areas nor does it present the geologic pattern of faults, fumaroles or other geologic features shown on the geologic map (Huber & Rinehart, 1986).

5. RESULTS

Preliminary results show that spatial patterns of carbon dioxide absorption can be derived from AVIRIS images. However, it is difficult to separate atmospheric carbon dioxide from the diffuse carbon dioxide emanations from the soil. The soil flux of CO_2 is not visible in the three selected AVIRIS images although the volume of the soil gas flux is considerable. Estimates of the CO_2 gas flux by Farrar et al. (1995) approximate 1200 tons/day for the 20 ha dead tree areas. The reflected radiance around the 2003 absorption feature might be too small (and the resulting AVIRIS spectrum too noisy) to reveal the subtle carbon dioxide concentration differences. Another explanation might be that the temporal variability of the CO_2 does not coincide with the three AVIRIS data acquisition times. The use of methane (CH_4) to trace diffuse volcanic gas release using AVIRIS was not possible. Methane absorption features (near 2350 nm) could not be identified in the field spectra nor in the image spectra. The volume of methane in the gas flux is most probably too small. Future work will investigate spatial patterns in AVIRIS images collected at other dates and times and will refine algorithms to enhance the CO_2 absorption feature.

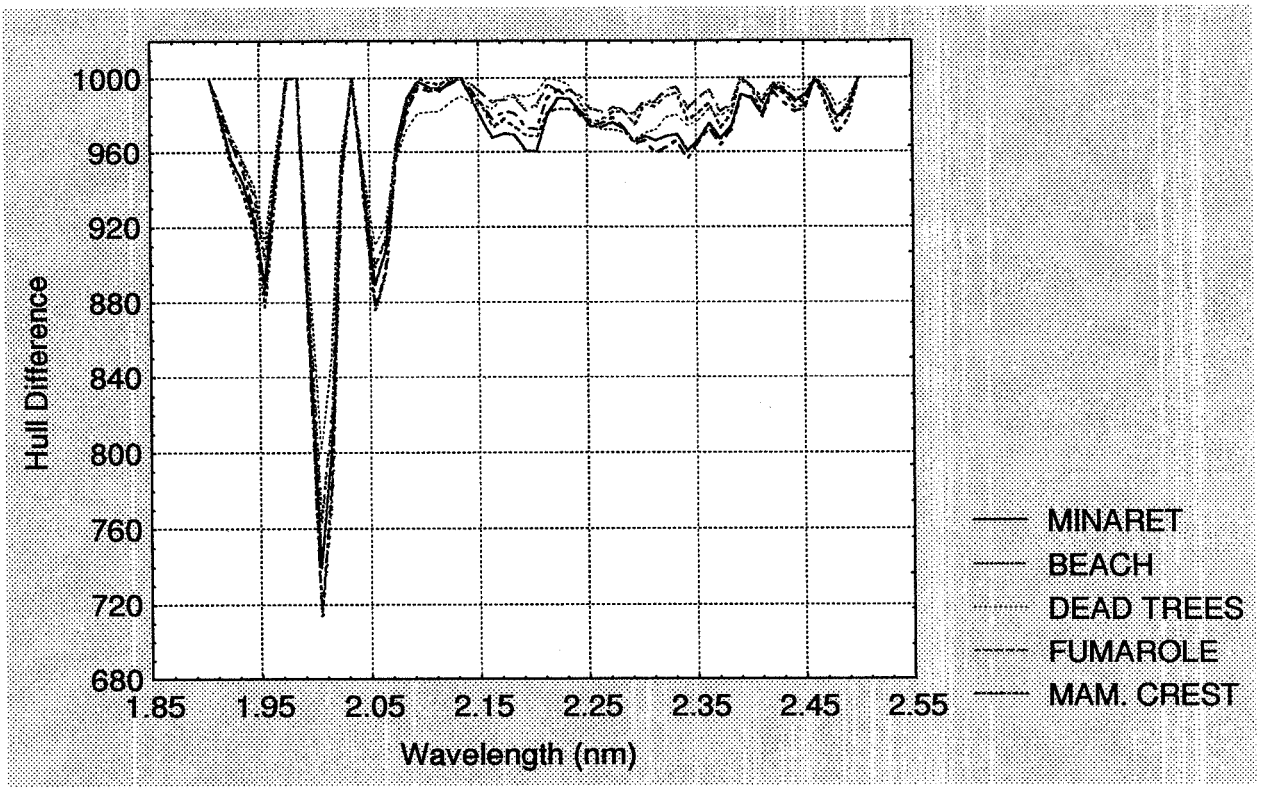

Figure 3: Results of the Conex Hull Transform of Selected Areas in the 23 August 1994 AVIRIS Scene. Absorption Features for CO_2 are Identified near 2005 and 2055 nm.

Acknowledgments

The research described in this paper was carried out at the Jet Propulsion Laboratory, California Institute of Technology, and was sponsored by Netherlands Organization for Scientific Research (NWO-Talent program). Mr. D.A. Roberts (University of California, Santa Barbara) is acknowledged for providing the Prism software.

REFERENCES:

Andres R.J. & W.I. Rose, 1995, Remote Sensing Spectroscopy of Volcanic Plumes and Clouds. In: B. McGuire, C. Kilburn & J. Murray, Monitoring Active Volcanoes. UCL Press, London. pp.301-314.

ASD, 1994, FieldSpec FR User's Guide. Analytical Spectral Devices Inc., Boulder, CO.

Baubron J.C., P. Allard & J.P. Toutain, 1990, Diffuse Volcanic Emissions of Carbon Dioxide from Vulcano Island, Italy. *Nature Vol.344, pp.51-53.*

Carrere V. & J.E. Conel, 1993, Recovery of Atmospheric Water Vapor Total Column Abundance from Imaging Spectrometer Data Around 940 nm - Sensitivity Analysis and Application to Airborne Visible/Infrared Imaging Spectrometer (AVIRIS) Data. Remote Sensing of Environment 44: 179-204.

De Jong S.M., 1994, Applications of Reflective Remote Sensing for Land Degradation Studies in a Mediterranean Environment. *Netherlands Geographical Studies 177, KNAG Utrecht. 240pp.*

Farrar C.D., M.L. Sorey, W.C. Evans, J.F. Howle, B.D. Kerr, B.M. Kennedy, C.Y. King & J.R. Southon, 1995, Forest-Killing Diffuse CO_2 Emission at Mammoth Mountain as a Sign of magmatic Unrest. Nature Vol.376, pp.675-678.

Gerlach T.M. & E.J. Graeber, 1985, Volatile Budget of Kilauea Volcano. Nature 313, pp.273-277.

Green A.A. & M.D. Craig, 1985, Analysis of Aircraft Spectrometer Data with Logarithmic Residuals. *Proc. Airborne Imaging Spectrometer Data Analysis Workshop, 8-10 April, JPL-Publication 85-41, Jet Propulsion Laboratory, Pasadena, CA, pp. 111-119.*

Grove C.I., S.J. Hook & E.D. Paylor II (1992), Laboratory Reflectance Spectra of 160 Minerals, 0.4 to 2.5 Micrometers. JPL-Public. 92-2, Jet Propulsion Laboratory, Pasadena, California, 410 pp.

Huber N.K. & C.D. Rinehart, 1986, Geologic Map of the Devil's Postpile Quadrangle, Sierra Nevada, California. Scale 1:62.500. USGS, Denver.

Langbein J., D.P. Hill, T.N. Parker & S.K. Wilkinson, 1993, An Episode of Reinflation of the Long Valley Caldera, Eastern California: 1989-1991. Journal of Geophysical Research Vol. 98, pp.15851-15870.

Pieters C.M. & P.A.J. Englert, 1993, Remote Geochemical Analysis: Elemental and Mineralogical Composition. Cambridge University Press, New York. 594 pp.

Sedgewick R., 1983, Algorithms. Addison-Wesley, Reading, Massachusetts.

Sorey M.L., B.M. Kennedy, W.C. Evans, C.D. Farrar & G.A. Suemnicht, 1993, Helium Isotope and Gas Discharge Variations Associated with Crustal Unrest in Long Valley Caldera, California, 1989-1992. Journal of Geophysical Research, vol. 98, pp. 15871-15899.

Tedesco D., 1995, Monitoring Fluids and Gases at Active Volcanoes. In: B. McGuire, C. Kilburn & J. Murray, Monitoring Active Volcanoes. UCL Press, London. pp.315-345.

Wolfe W.L. & G.J. Zissis, 1989, The Infrared Handbook. ERIM: Environmental Research Institute of Michigan, Ann Arbor, MI.

Table 1. Results of the Feature Search on AVIRIS (23 August 1994 image) Spectra 2.0-2.5 μm.

Wavelength	Depth	Area	Asymmetry
1. Results, Rock Outcrop near Heart Lake:			
2.0040	194.6203	6.3370	0.7637
2.0540	83.5510	2.8988	0.6137
1.9440	77.1451	3.1312	0.8106
2.1930	33.4868	2.1069	1.5353
2.3420	31.4441	2.1767	0.3884
2.3020	30.2106	2.1063	2.5787
2. Results, Beach of Horseshoe Lake:			
2.0040	216.8107	7.1612	0.7576
2.0540	96.3700	3.4231	0.6072
1.9440	87.1081	3.6082	0.8017
2.1930	28.2608	1.9079	1.2454
2.2630	20.2279	0.7563	2.9223
2.2830	19.2256	0.7830	0.3156
2.3720	18.5714	1.1094	2.3487
3. Results, Dead Trees Area near Horseshoe Lake:			
2.0040	148.8698	4.9070	0.7591
2.0540	70.6569	3.4368	0.3795
1.9440	61.2487	2.4824	0.7761
2.2930	29.0505	2.2499	1.3394
2.3420	21.1022	1.0482	0.2474
2.1530	12.8426	0.7047	0.4311
4. Results, Horse Shoe Lake Fumarole, McCloud Lake:			
2.0040	178.2256	5.8844	0.7572
2.0540	78.5885	2.9428	0.5580
1.9540	67.9872	2.7497	2.1012
2.2830	16.2666	1.2004	1.4645
2.4800	13.6296	0.3108	1.5631
2.1930	12.7289	0.7406	1.8204
2.3720	11.7063	0.7021	2.1843
5. Results, Rock Outcrop Near Mammoth Crest:			
2.0040	211.6600	6.8818	0.7687
2.0540	92.6647	3.3673	0.5694
1.9540	77.1027	2.9865	1.9977
2.3320	34.9856	4.4646	1.3758
2.1930	21.2710	1.1864	1.7262

Page intentionally left blank

PREDICTIVE MODELLING OF AVIRIS PERFORMANCE OVER INLAND WATERS

Dekker, A.G. and Hoogenboom, H.J.
Institute for Environmental Studies, De Boelelaan 1115, 1081 HV Amsterdam, The Netherlands.
Tel 31-20-4449506; Fax 31-20-4449553; email: arnold.dekker@ivm.vu.nl.

1. INTRODUCTION

The availability of imaging spectrometers such as AVIRIS, CASI, ROSIS, HYDICE etc. has created a necessity for spectral methods and models which can predict the performance of these instruments for detecting and estimating a certain parameter, e.g. chlorophyll α as a water quality indicator. The method presented here predicts which wavelength bands are best suited for estimating a parameter quantitatively and uniquely. Based on a model relating the specific inherent optical properties (IOP) to the subsurface reflectance, R(0-) over eutrophic lake waters, simulations of the effects of concentration ranges of chlorophyll α to the reflectance were performed. The other optically active constituents such as aquatic humus, seston dry weight, or the non-phytoplankton part of the seston could be varied also. Using the noise-equivalent-radiance values for AVIRIS the performance of AVIRIS for detecting chlorophyll α could be calculated. By using such a predictive method costly measurement campaigns, involving field and laboratory work, with possible disappointing results may be avoided.

Before describing the model it is useful to point out three different approaches by which measurements of spectral (ir)radiance can be used to estimate concentrations of water constituents in remote sensing. Based on Morel and Gordon (1980) two approaches establish statistical relationships: i.e. the empirical and the semi-empirical approach; whereby the semi-empirical method includes spectral knowledge in the analysis. The third, analytical approach is based on physical modelling and is therefore preferred. Gordon & Morel (1983) give a comprehensive discussion of the analytical models available for clear ocean waters through to turbid coastal waters. Kirk (1983, 1994) and Dekker et al (1994) extended the discussion to inland waters. In the analytical models inherent and apparent optical properties of the water constituents are used to model the reflectance and vice versa. The water constituents are expressed in their specific (per unit measure) absorption and backscatter coefficients. Subsequently, a suite of analysis methods can be used to optimally retrieve the water constituents or water quality parameters from the remotely sensed upwelling radiance or radiance reflectance signal.

Dekker (1993) developed remote sensing algorithms following the analytical approach for estimation of both *in situ* chlorophyll α and cyanophycocyanin concentrations from airborne remotely sensed radiance measurements, calibrated to subsurface irradiance reflectance R(0-). This approach required the estimation of specific absorption and backscattering coefficients for both algal and non-algal particulate matter. The chlorophyll α algorithms were determined from spectrophotometric measurements of apparent absorption and scattering. Chlorophyll α could be derived from the actual airborne remote sensing radiance with an accuracy of 9.5 mg m^{-3} and cyanophycocyanin with an accuracy of approximately 20 mg m^{-3}. These algorithms were developed using only two bands with centres at 676 and 706 nm respectively and a bandwidth of 10 nm wide. This was required because the two airborne scanners used had a limited amount of spectral bands available: The Netherlands CAESAR has nine spectral bands in the Inland Water Mode (using filters) and the CASI had (in 1990 and 1993) 15 programmable spectral bands available in the spatial mode. In order to compare the CASI data with the CAESAR data the bands were kept similar. CASI does allow a selection of 15 bands over the range of 430 to 870 nm.

However, AVIRIS has different wavelength centres, bandwidths and signal-to-noise ratios. Furthermore, AVIRIS measures the optical and nearby and middle infrared spectrum continuously, so a selection of bands is not *a priori* necessary. Thus in order to gain insight into the performance of AVIRIS a spectral model was constructed

that enabled the determination of the effect of increasing chlorophyll α on the spectral R(0-). A subsequent translation of R(0-) to the noise equivalent radiance difference as measured by AVIRIS (without atmospheric influence!), gives a indication of the accuracy for AVIRIS in estimating chlorophyll α.

2. METHOD

The method used in this study contains five steps:

- parameterisation of the bio-optical model
- run bio-optical model for a range of values for the water constituents, especially CHL
- obtain resolvability of R(0-) by calculating the derivative of R(0-) with respect to CHL
- convert R(0-) to upwelling radiance above the air-water interface
- compare the radiance with noise equivalent radiance of AVIRIS (1995)

Before discussing the method and the model a series of subsurface reflectance spectra (R(0-) measured in a variety of inland waters of widely differing trophic status in the Netherlands is presented and discussed. From these measurements two representative water types were selected: i.e. shallow eutrophic lakes and deep lakes. The R(0-) measurements enable validation of the results of the model. The spectra are presented in Fig.1. The chlorophyll α values ranged from 25 mg m^{-3} to 120 mg m^{-3} CHL. Reflectance in these water bodies is low in the blue end of the spectrum (400-500 nm) as a result of relatively high concentrations of aquatic humus(=disolved yellow substance) in nearly all Dutch waters. With increasing wavelength reflectance is markedly affected by particulate matter. Lakes with relatively low phytoplankton and suspended matter concentrations have low reflectance, water bodies with low phytoplankton but high suspended matter concentrations have high reflectance up to 720 nm, and lakes with high phytoplankton and suspended matter concentrations have a similarly high reflectance but punctuated by absorption features due to photosynthetic pigments in phytoplankton. The additional effects of particulate backscattering and humic absorption in inland waters introduce complex interacting relations between the water constituents and subsurface reflectance. From these observations qualitative conclusions can be drawn on the effect of constituent concentration on R(0-) at different wavelengths. By using a bio-optical model a more quantitative analysis becomes feasible.

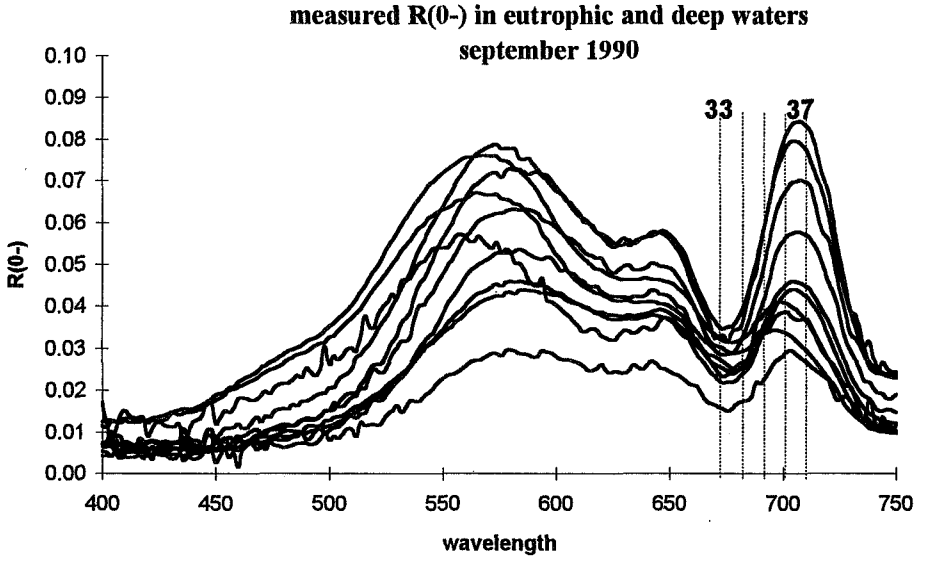

Figure 1. Measured R(0-) representative for shallow eutrophic and deep inland waters with CHL values ranging from 25 to 120 mg m^{-3}. The dotted lines are the centre wavelengths of AVIRIS channels 33 to 37.

3. A BIO-OPTICAL MODEL FOR INLAND WATERS

3.1 The relation between R(0-) and water constituent concentrations in inland waters

The underwater light field is determined by the inherent optical properties (IOP) which are independent of the ambient light field (i.e. independent of changes in the angular distribution of radiant flux). Within the scope of this study these properties are specified by the absorption coefficient a (m^{-1}) and the backscattering coefficient b_b (m^{-1}). In inland waters the spectral reflectance is predominantly a function of: (i) absorption by algal pigments, aquatic humus and tripton (the non-phytoplankton part of the suspended matter) at short wavelengths and by pure water at longer wavelengths, (ii) (back)scattering by phytoplankton and tripton which can be up to 1000 times the backscattering of oceanic waters.

The relation between R(0-) and the inherent optical properties (IOP) for ocean and inland waters systems was investigated by (Gordon *et al.*, 1975, Morel and Prieur, 1977; Whitlock *et al.*, 1981 ; Kirk, 1991; Dekker, 1993; Dekker *et al.*, 1994). Dekker *et al.*, 1994, found that the following linear backscattering albedo model was the most appropriate model for inland waters:

$$R(0-) = r_1 \frac{b_b(\lambda)}{a(\lambda)+b_b(\lambda)}, \qquad \text{eq. 1}$$

Values of r_1 ranged from 0.12 to 0.56 and appeared to be lake-specific. The IOP of all four optically active components are included in the model and are denoted by their first character: phytoplankton (p), tripton (t), aquatic humus (h) and water (w).

3.2 The inherent optical properties: parametrization of the bio-optical model

The model is used to simulate the effect of changes in chlorophyll α (CHL) concentration on R(0-). It is necessary to select appropriate values for each of the specific inherent optical properties, i.e. the inherent optical properties per unit water quality parameter: e.g. the specific inherent absorption by chlorophyll α , a^*_p, is the amount of absorption caused by 1 μg l^{-1} chlorophyll α.

$$\begin{aligned} a &= a_p^* CHL + a_t^* C_t + a_h^* a_h(440) + a_w \\ b_b &= b_{b_p}^* CHL + b_{b_t}^* C_t + b_{b_w} = b_{b_s}^* \{CHL + C_t\} + b_{b_w} \end{aligned} \qquad \text{eq. 2}$$

Specific IOP are denoted by an asterix as superscript. Values for the IOP in this model are:

a_w: The temperature dependent absorption by pure water from Buiteveld et al.(1994)

b_{bw}: The backscattering of pure water from Buiteveld et al.(1994)

a^*_p: specific inherent absorption by chlorophyll α derived from Dekker(1993)

a^*_t: specific inherent absorption by tripton from Dekker (1993). The concentration of tripton C_t in mg l^{-1} cannot be determined directly but was calculated by substracting the algal fraction of seston dry weight from the total seston dry weight (DW). The algal fraction of seston dry weight was estimated using an empirical relation DW(p)= 0.07 CHL (Buiteveld, 1995). The tripton absorption was divided by the tripton dry weight yielding the specific inherent tripton absorption.

b^*_{bs}: specific inherent backscattering of seston (i.e. the sum of tripton and phytoplankton): although it would be preferable to have a separate specific inherent backscattering for tripton and phytoplankton this is not available currently.

a^*_h: the specific absorption coefficient of aquatic humus is calculated by assuming an exponential slope for aquatic humus absorption and taking the absorption by aquatic humus at 440 nm $a_h(440)$ (g440 as defined by Kirk (1994) as a measure of the aquatic humus concentration (c.f. eq. 2):

$$a_h^*(\lambda) = e^{S(\lambda-440)} \qquad \text{eq. 3}$$

This equation is based on the assumption of a fixed slope, where S is stated to be independent of the choice of reference wavelength. An analysis of the a^*_h values obtained between 400 - 800 nm for water bodies in this study showed a correspondence to an exponential function with an average value of S = 0.0146 nm^{-1} (Dekker, 1993).

In natural inland waters there is often a significant correlation between chlorophyll α and both aquatic humus and tripton concentrations. Therefore, increases in chlorophyll α in the model (first series) are associated with, in nature, occurring increases in aquatic humus and tripton. Using linear regression for nine samples in the shallow eutrophic lakes , the following equations were derived:

$$\begin{aligned} a_h(440) &= 1.78 + 0.009 * CHL \qquad r^2 = 0.69 \\ C_t &= 11.54 + 0.042 * CHL \qquad r^2 = 0.74 \end{aligned} \qquad \text{eq. 4}$$

3.3 Resolvability with respect to CHL

The derivative of R(0-) with respect to CHL can be considered as a measure of the resolvability of R(0-) due to changes in CHL. The change in R(0-), $\Delta R(0-)$, due to a user defined accuracy in CHL, ΔCHL, is approximately

$$\Delta R(0-) = \frac{\partial R(0-)}{\partial CHL} \Delta CHL \qquad \text{eq. 5}$$

This means that the sensitivity of the instrument should be sufficient to detect these changes in R(0-). The (partial) derivative of R(0-) with respect to CHL can be found from eq. 2, yielding

$$\frac{\partial R(0-)}{\partial CHL} = r_1 \frac{b^*_{b_p} a_r - a^*_p b_{b_r}}{\left[a_r + b_{b_r} + \left(a^*_p + b^*_{b_p}\right) CHL\right]^2} \qquad \text{eq. 6}$$

From inspection of eq. 6 we can draw some qualitative conclusions:
- in terms of the effect on R(0-) there is a balancing effect between the backscattering and the absorption of phytoplankton;
- the sensitivity of R(0-) due to changes in CHL decreases for increasing values of CHL.

The derivative of R(0-) can not directly be compared with the sensitivity of AVIRIS, but has to be converted to a radiance above the air-water interface as measured by AVIRIS. Using a simplified air-water interface correction (Dekker, 1993) the following expression for the derivative of the above surface upwelling radiance with respect to CHL can be derived:

$$\frac{\partial L_{au}}{\partial CHL} \approx \frac{L_0}{2.89} \frac{\partial R(0-)}{\partial CHL}, \qquad \text{eq. 7}$$

where L_0 is a panel-based downwelling radiance measurement. Eq. 7 expresses the change in upwelling radiance due to a change of 1 mg m^{-3} of CHL (note that this change depends on the CHL already present (c.f. eq. 6)). The absolute values of the changes in radiance can be compared with the noise equivalent radiance of AVIRIS, indicating the performance of AVIRIS for detecting changes in CHL.

4. RESULTS

4.1 Simulations for shallow eutrophic lakes

In the first series of simulations, correlations between the organic compounds were introduced as given above (eq.4) in order to represent natural conditions in shallow eutrophic lakes. Figure 2a and b show the results for R(0-) and the derivative of R(0-) to chlorophyll α . In this simulation the effect of increasing chlorophyll α concentrations is given in increments of 20 mg m^{-3} ranging from 20 to 200 mg m^{-3}. The aquatic humus and tripton concentrations increase linearly according to eq. 4.

The results indicate that at 400 nm there is a hinge point where the R(0-) does not change : the increase in absorption by phytoplankton, tripton and aquatic humus is balanced by the increase in scattering of the phytoplankton and tripton. From 410 to 660 nm there is a decrease in reflectance within the same order of magnitude over this wavelength range, but it becomes exponentially less as the concentration of chlorophyll α increases. In the spectral area between 660 and 720 nm R(0-) changes more. Fig 2a and b both show that the decrease in R(0-) at 676 and 750 nm is constant for all CHL. The maximum of R(0-) initially at 696 nm for CHL=20 mg m^{-3} shifts to a maximum at 710 nm for CHL=200 mg m^{-3}. Thus for AVIRIS the channel 34 centered at 674 nm in combination with channels 36 to 38 are required in order to detect such a range in these type of waters, provided a ratio algorithm is to be used. In fact, channel 36 is most suited for ranges up to 20 mg m^{-3} channel 37 for ranges in CHL of 40 to 120 mg m^{-3} and channel 38 for concentrations from 120 to 200 mg m^{-3}. The derivative of R(0-) in Fig. 2b shows even clearer which wavelengths are suited to discriminate reflectance differences caused by the changes in chlorophyll α. Most interesting however is the stable point at 696 nm which might be a potentially important spectral location for developing new algorithms.

4.2 Simulations for deep lakes (with algae bloom)

In the second series of simulations the concentrations of the phytoplankton, tripton and aquatic humus were assumed to be uncorrelated. In order to model a bloom occurring in a deep lake the $a_h(440)$ and C_t were fixed at specific values of 0.5 m^{-1} and 1 mg l^{-1} respectively. This may be seen as a model of a bloom occurring under maximal growth conditions for the algae with no extra detritus being created during the increase in chlorophyll α. Figure 3a and b show the results for R(0-) and the derivative of R(0-) to chlorophyll α.

The resulting R(0-) spectra (Fig. 3a) are significantly different from series 1 (Fig. 2a). There is a range from 400 to 530 with some change in R(0-). In the derivative (Fig. 3b) there are two hinge points: at 420 and at 530 nm. This may be a similar phenomenon that causes the blue-to-green ratio often used for ocean waters to work. In this case it seems that a blue to green ratio with a band below 420 and a band around 480 nm would discriminate up to 60 mg m^{-3} CHL. From 530 to 650 nm R(0-) increases in the same order of magnitude with increasing CHL (note that in series 1 there was a decrease of R(0-) in this spectral region). At 676 nm the R(0-) is stable with increasing CHL: this points to a counter balance between the increase in absorption and the increase in backscattering by the phytoplankton. The increase in R(0-) at the 700 nm area is the most discriminative of the entire spectrum; especially for concentrations over 60 mg m^{-3} CHL (as compared to anywhere from 530 to 650 nm). Once again it appears that a ratio algorithm involving the 674 nm spectral band and the 696 to 710 nm range is most suited for estimating CHL in a range from 20 to 200 mg m^{-3} CHL. The increase in R(0-) beyond 710 nm through to 750 nm is also remarkable and a clear indication that this nearby infrared region is worth investigating further: e.g. the increase in R(0-) at 750 nm is solely due to the increase in backscattering caused by the phytoplankton. As for the first series the derivative spectrum shows a stable increase of R(0-) at 750 nm with increasing CHL. A spectral band in the area of 710 to 750 nm may thus serve as a reliable indicator of changing backscattering in a lake.

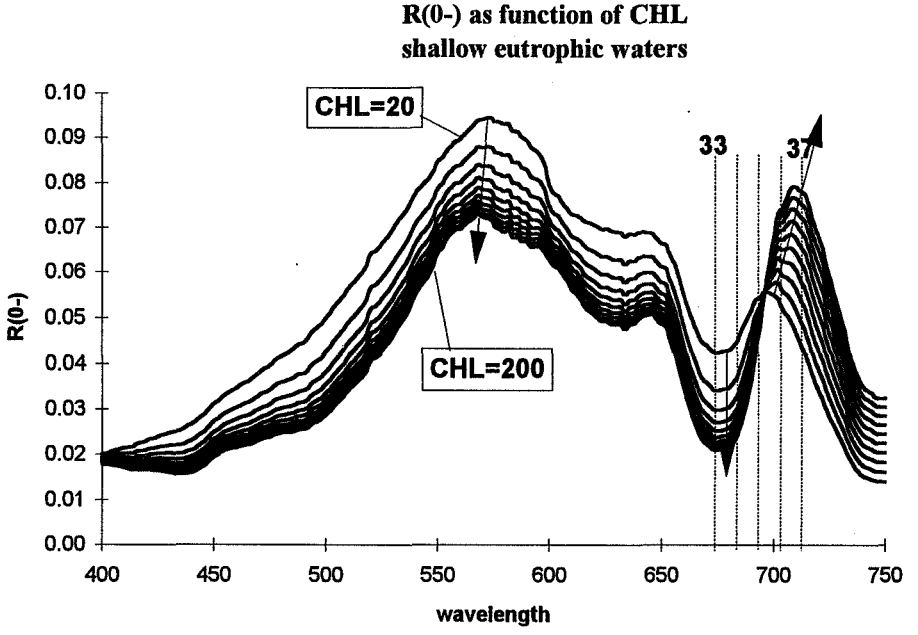

Figure 2a. Modelled R(0-) as a function of increasing CHL with associated increases in tripton and aquatic humus. The CHL ranges from 20 to 200 mg m^{-3} with increments of 20 mg m^{-3}. The dotted lines are the centre wavelengths of the AVIRIS channels 33- 37.

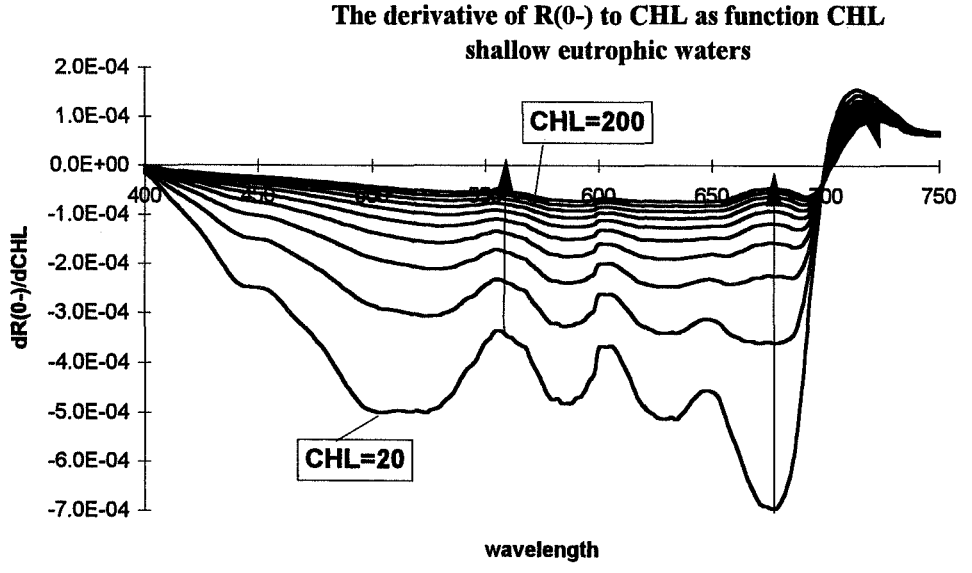

Figure 2b. The derivative of R(0-) to CHL as a function of CHL. The same data as in Fig. 2a are used.

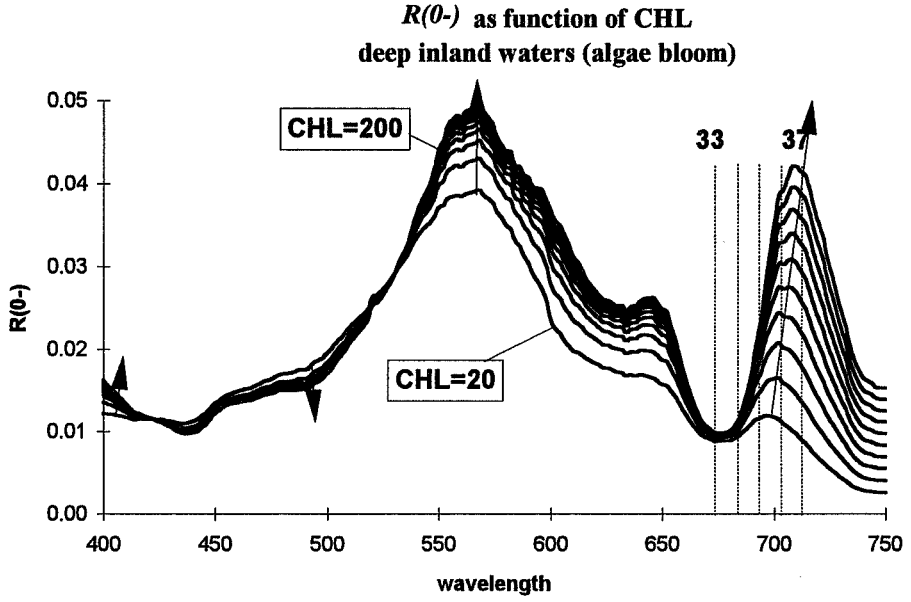

Figure 3a. Modelled R(0-) as a function of increasing CHL levels with fixed values for tripton and aquatic humus. The CHL ranges from 20 to 200 mg m^{-3} with increments of 20 mg m^{-3}. The dotted lines are the centre wavelengths of the AVIRIS channels 33- 37.

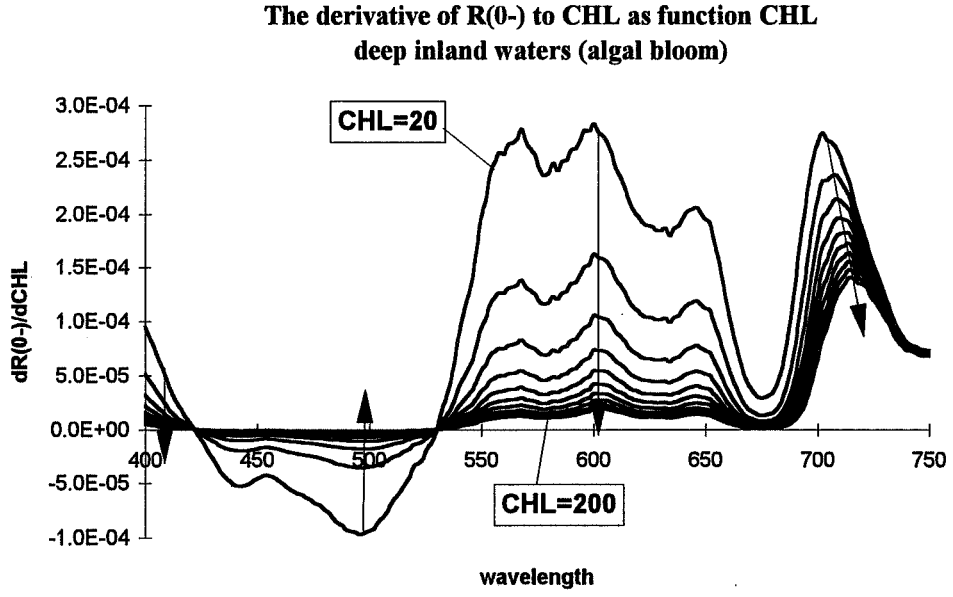

Figure 3b. The derivative of R(0-) to CHL as a function of CHL. The same data as in Fig. 3a are used.

4.3 An estimation of the accuracy with which AVIRIS may estimate chlorophyll α in eutrophic lakes.

Based on the first series of simulations an estimate was made for the accuracy with which AVIRIS may detect CHL levels in inland waters. A downwelling radiance as was calculated for a solar zenith angle of 30°, a horizontal visibility of 10 km was entered into eq. 7 and absolute values of the derivative of L_{au} were calculated, see Fig 4. The noise equivalent radiance (NEDL) of AVIRIS(1995) is also given in Fig. 4 (the dashes) and from the comparison it shows that at low concentrations of CHL = 20 mg m^{-3} AVIRIS can discriminate differences of 2.8 mg m^{-3} at 674 nm (CH 34). However, with increasing CHL this resolving power reduces to 42 mg m^{-3} at 200 mg m^{-3} at 676 nm. If, however, a ratio of the 674 to e.g. a 713 band (CH 38) is used for estimating CHL these figures will improve. Especially for the higher concentrations of CHL, because the derivative of Lau to CHL is in the order of 22 mg m^{-3} over the 20 - 200 mg m^{-3} range at 700 to 720 nm. This accuracy is, in general, sufficient for inland water management purposes. Of course, during an actual flight of AVIRIS, the atmospheric and air-water interface effects may add considerable noise and reduce the accuracy of the signal, thereby reducing AVIRIS's effective resolving power.

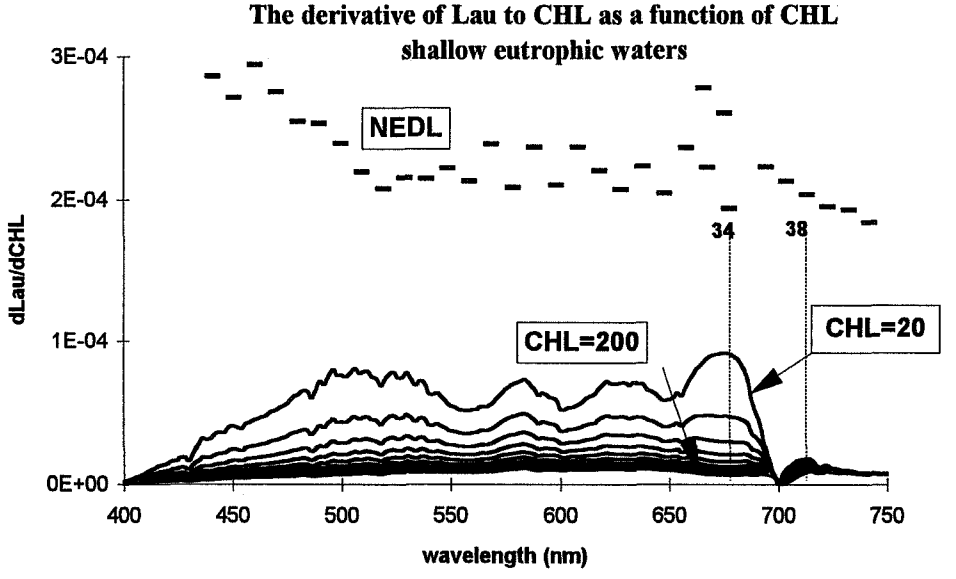

Figure 4. The derivative of the upwelling radiance L_{au} with respect to CHL for a range of CHL levels from 20 to 200 mg m^{-3} with increments of 20 mg m^{-3}. The NEDL of AVIRIS is denoted by the dashes. The graph should be read as follows: At a concentration of CHL= 20 mg m^{-3} the line dLau/dCHL represents the NEDL required to discriminate a CHL concentration difference of 1 mg m^{-3}.

5. CONCLUSIONS AND DISCUSSION

A predictive model for estimating the effect of varying concentrations of a water quality parameter on the relectance signal from a waterbody is a powerful tool in assessing the potential of remote sensing instruments such as AVIRIS. These models may also play an important role in defining preset spectral bands for instruments such as the CASI or the (planned) ESA satellite imaging spectrometer MERIS or for MODIS. Another important role for such models is for developing robust algorithms for detecting chlorophyll α or any other optical water quality parameter. Especially the capability to simulate co-varying , or independently varying optical water quality parameters is a valuable asset and pushes the development of algorithms beyond the scope offered by the empirical or semi-empirical approach.

Two simulations series, assuming increases of CHL in steps of 20 mg m^{-3} from 20 to 200 mg m^{-3}, one with covarying concentrations of aquatic humus and tripton and one with stable concentrations of aquatic humus and tripton, showed significant influence on the size and shape of the R(0-) spectra and the derivative spectra of R(0-) to CHL. In fact several hinge points in the R(0-) were identified, that indicate spectral areas where increases in absorption are compensated by increases in backscattering. It was also possible to identify areas in the derivative spectra where the rate of change of R(0-) with increasing CHL levels was either exponential or linear. A preliminary comparison with actual *in situ* measured spectra showed a good comparison with the modelled spectra. If a ratio algorithm for chlorophyll were to be used of the form $R(0-)_{676}/R(0-)_{700}$, it has become obvious from this modeling exercise that several adjacent bands of AVIRIS are required in order to monitor the shift in the nearby infrared reflectance: the peak shifts from 696 at 20 mg m^{-3} to 710 nm at 200 mg m^{-3} CHL, requiring the use of AVIRIS channels 36, 37 and 38. Another important conclusion drawn from the modelling results is that AVIRIS has a sufficient NEDL for detecting concentration differences of CHL: based on the 1995 performance values AVIRIS can detect 2.8 mg m^{-3} CHL at concentration levels of 20 mg m^{-3} and 22 mg m^{-3} CHL at 200 mg m^{-3} CHL. Using smart algorithms these accuracies may even improve. Ofcourse in a real remote sensing mission these values will deteriotate due to the influence of the atmosphere and a rough water surface.

The parameters as they have been defined here are representative only for these lakes. E.g. the phytoplankton fraction of seston dry weight was calculated using the data from Buiteveld (1995). Other phytoplankton occuring in these lakes such as Prochlorothrix hollandica have a different ratio: DW= 0.048 CHL (Rijkeboer et al. 1990). For samples of 12 lakes taken in May 1994 the value for phytoplankton equivalent dry weight fraction was DW=0.059 CHL(calculated from data in Gilijamse, 1994) . This value is perhaps more realistic as it is representative for natural populations of algae.

The model presented here is part of a pilot study on the use of forward models (from the inherent optical water properties to remotely sensed radiance). The model needs to be tested more thoroughly with field and laboratory data. The input parameters may be improved and made more generally applicable. Foreseen developments are the inclusion of a realistic air/water interface including waveglint and whitecapping; as well the inclusion of an atmosphere model. It is also intended to use the forward model for developing inverse analytical methods for estimating water quality parameters from remotely sensed radiance data.

6. REFERENCES

Buiteveld, H., 1995, A model for calculation of diffuse light attenuation (PAR) and secchi depth *Netherlands journal of aquatic ecology*, vol. 29, pp. 55-65, 1995.

Buiteveld, H., J. H. M. Hakvoort, and M. Donze, 1995, Optical properties of pure water ed. J. S. Jaffe. XII, pp. 174-183, 1994. Ocean Optics XII. SPIE. Bellingham, Washington, USA.

Dekker, A.G., 1993, Detection of optical water quality parameters for eutrophic waters by high resolution remote sensing, pp. 1-240

Dekker, A.G. and M. Donze, 1994, Imaging spectrometry as a research tool for inland water resources analysis. In: ed. J.Hill. Dordrecht, The Netherlands: Kluwer AP.

Dekker, A.G., H. J. Hoogenboom, L. M. Goddijn, and T. J. M. Malthus, 1994, The relationship between spectral reflectance, absorption and backscattering for four inland water types pp. 245-252, 1994. 6th Intern. Symp. on Physical Measurements and Signatures in Remote Sensing. CNES, France. Val d'Isere.

Gilijamse, L.I., 1994, Absorptioncoefficients of phytoplankton and tripton in some Netherlands lakes; Student Report nr. 1994, Netherlands Institute for Ecological Research, Centre for Limnology, Royal Dutch Academy of Sciences, Nieuwersluis, The Netherlands. pp 1-53.

Gordon, H. R., O. B. Brown, and M. M. Jacobs, 1975, Computed relationships between the inherent and apparent optical properties of a flat homogeneous ocean *Applied Optics*, vol. 14, pp. 417-427.

Gordon, H. R. and A. Morel. *Remote assessment of ocean color for interpretation of satellite visible imagery: a review*, New York: Springer-Verlag, 1983. pp. 1-114.

Jerlov, N.G., 1976, *Marine Optics*, Amsterdam, the Netherlands.

Kirk, J. T. O., 1991, Volume scattering function, average cosines, and the underwater light field *Limnol. Oceanogr.* vol. 36, pp. 455-467.

Kirk, J. T. O., 1994, *Light & photsynthesis in aquatic ecosystems*,. pp. 1-509.

Morel, A. and H. R. Gordon, 1980, Report of the working group on water color *Boundary-Layer Meteorology.* vol. 18, pp. 343-355.

Morel, A. and L. Prieur, 1977, Analysis of variations in ocean colour *Limnol. Oceanogr.* vol. 22, pp. 709-722.

Whitlock, C. H., L. R. Poole, J. Usry, W. M. Houghton, W. G. Witte, W. D. Morris, and E. A. Gurganus, 1981, Comparison of reflectance with backscatter and absorption parameters for turbid waters *Applied Optics*, vol. 20, pp. 517-522.

A GROUND TRUTHING METHOD FOR AVIRIS OVERFLIGHTS USING CANOPY ABSORPTION SPECTRA

John A. Gamon[1], Lydia Serrano[1], Dar A. Roberts[2], and Susan L. Ustin[3]

[1]Department of Biology & Microbiology
California State University, Los Angeles
5151 State University Drive
Los Angeles, CA 90032

[2]Department of Geography
University of California
Santa Barbara, CA 93106

[3]Department of Land, Air and Water Resources
University of California
Davis, CA 95616

1. INTRODUCTION

Remote sensing for ecological field studies requires ground truthing for accurate interpretation of remote imagery. However, traditional vegetation sampling methods are time consuming and hard to relate to the scale of an AVIRIS scene. The large errors associated with manual field sampling, the contrasting formats of remote and ground data, and problems with coregistration of field sites with AVIRIS pixels can lead to difficulties in interpreting AVIRIS data. As part of a larger study of fire risk in the Santa Monica Mountains of southern California (see Roberts et al. and Ustin et al., this volume), we explored ground-based optical method of sampling vegetation using spectrometers mounted both above and below vegetation canopies. The goal was to use optical methods to provide a rapid, consistent, and objective means of "ground truthing" that could be related both to AVIRIS imagery and to conventional ground sampling (e.g., plot harvests and pigment assays).

2. METHODS

Ground measurements were conducted at several sites in the Santa Monica Mountains of southern California in June and October, 1995 (coincident with AVIRIS overflights of this region). Vegetation was characteristic of either chaparral or coastal sage scrub (Munz and Keck, 1959), representing various stages of post-fire succession. The June sampling occurred at the end of a season of particularly heavy rain (an "el Niño" year), and the October sampling occurred at the end of a summer dry period characteristic of this region's Mediterranean climate. At each site, above and below-canopy measurements were made with a narrow-band spectrometer (model SE590, Spectron Engineering, Denver CO, USA) outfitted with hemispherical, cosine corrected fore-optics. In some cases (e.g., during below-canopy measurements), a fiber-optic extension was used between the spectrometer and the cosine head to minimize contamination by radiation scattered by the user's clothing or body. In tall canopies, above-canopy measurements were made using either a tall tripod or a bucket truck. Canopy absorption was calculated several ways, and expressed here as "spectral absorbance," estimated as follows:

$$\text{absorbance} = \log (I_o/I) \qquad (1)$$

where I_o is the above-canopy spectral irradiance, and I is the below-canopy spectral irradiance.

3. RESULTS

Canopy absorbance spectra showed striking differences between sites and dates. For example, large differences were noted between stands of different species composition and time since last fire (Figure 1). In this between-site comparison, absorbance, particularly visible absorbance (400-700 nm) was much greater in the taller and older stands that had greater biomass.

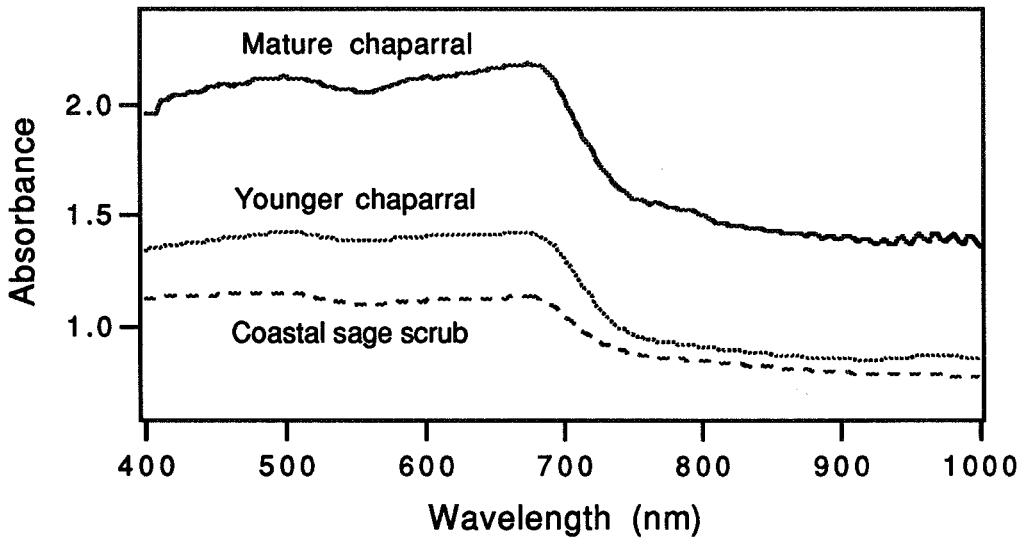

Figure 1. Canopy absorbance spectra measured in June, 1995, for three sites composed of mature chaparral (tall vegetation, at least 50 years since fire), younger chaparral (medium stature, burned 17 years ago) and coastal sage scrub (short stature, burned 17 years ago).

There were also striking seasonal differences in absorbance spectra, both for coastal sage scrub (which included both evergreen and partially drought-deciduous, perennial species) and for mature chaparral (composed primarily of "evergreen" species) (Figure 2). The seasonal decline in absorption in the blue and red spectral regions in both vegetation types is consistent with a loss of chlorophyll pigments associated with the progression of the summer drought. The decline in absorbance in the near-infrared region (e.g., above 700 nm in the mature chaparral spectra) is consistent with either seasonal foliage loss or leaf reorientation. This particular stand was largely composed of *Ceanothus* sp., a common chaparral genus known to adopt a more vertical leaf orientation with the onset of summer drought (Comstock and Mahall 1985).

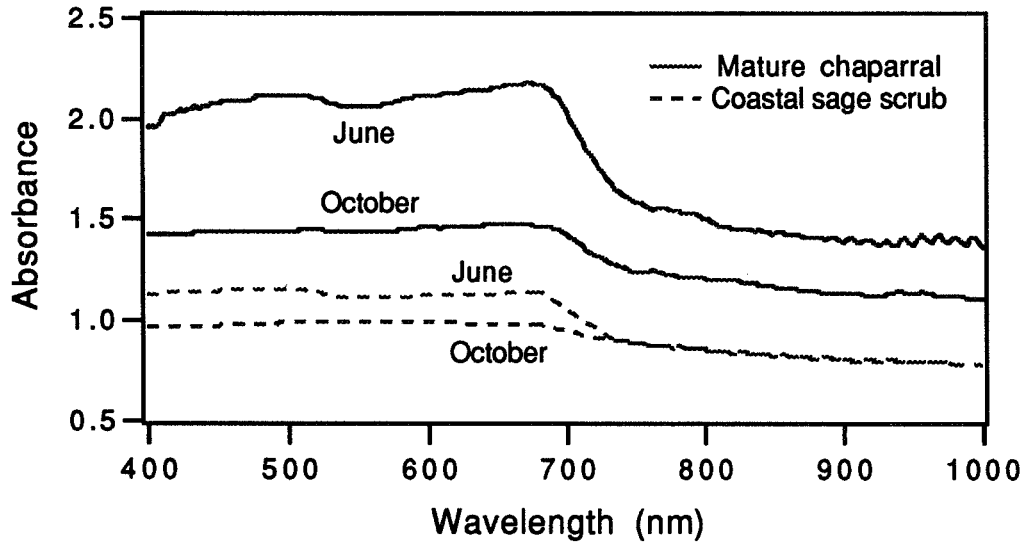

Figure 2. Seasonal change in canopy absorbance spectra for two vegetation types (mature chaparral and coastal sage scrub). The loss of blue and red absorption features between June and October suggests a loss of chlorophyll pigments in these canopies. The large decline in canopy absorbance in the mature chaparral (composed largely of *Ceanothus* sp.) can partly be explained by seasonal leaf reorientation in this evergreen canopy.

4. DISCUSSION

Patterns in whole canopy absorption spectra clearly varied with changes in stand structure and composition associated with different vegetation types, seasonal state, and stand age. Because these factors reflect fire history and are often good correlates with fire hazard, canopy absorption spectra may be useful in assessing fire risk in the Mediterranean climate vegetation characteristic of the Santa Monica Mountains.

In a medium that obeys Beer's law, and at low (≤ 1) absorbance values, absorbance is directly related to the concentration of absorbing compounds (Hipkins and Baker, 1986). Clearly both conditions were violated in this case. However, the clearly discernible patterns in these canopy absorbance spectra suggest that spectral absorbance (or some similar expression of radiation absorption) might provide a useful measure of canopy structure, and function. Furthermore, because radiation absorption influences both canopy energy balance and photosynthetic fluxes, measurements of canopy spectral absorption might provide a more direct way to link remotely sensed spectra to stand-level processes than is possible with traditional field methods (e.g., plot harvests). Unlike destructive field sampling, this optical method is non-destructive and relatively rapid. If spectra obtained with this optical sampling technique can be reliably linked to features present in AVIRIS spectra, then this method might be a useful ground-truthing tool for AVIRIS overflights. Further goals are to relate these spectra to canopy pigment content, harvest data, and AVIRIS imagery as it becomes available.

5. ACKNOWLEDGEMENTS

Project equipment was funded by grants from NASA and NSF, and student assistance supported by a grant from the US EPA. Thanks to several Cal State LA Students, including Vache Marcarian, John Scott Surfus, and Kokeb Tefera, for their enthusiastic technical support.

6. REFERENCES

Comstock J.P. and B.E. Mahall (1985) Drought and changes in leaf orientation for two California chaparral shrubs: *Ceanothus megacarpus* and *Ceanothus crassifolius*. *Oecologia* (Berlin) vol. 65, pp. 531-535.

Hipkins M.F. and N.R. Baker (1986) *Photosynthesis Energy Transduction: A Practical Approach.* IRL Press Limited, Oxford, pp. 58-59.

Munz, P.A.and D.D. Keck (1959) *A California Flora.* University of California Press, Berkeley, CA, pp. 11-18.

Page intentionally left blank

UNDERSTANDING UNMIXED AVIRIS IMAGES IN CUPRITE, NV USING COINCIDENT HYDICE DATA

Alexander F. H. Goetz[1,2] and Bruce Kindel[1]

[1]Center for the Study of Earth from Space/CIRES,
[2]Department of Geological Sciences
University of Colorado, Boulder CO 80309

1. INTRODUCTION

For more than a decade, techniques for determining the relative abundance of materials within a pixel have been applied to multispectral and hyperspectral images from sensors such as Landsat and AVIRIS (Adams et al., 1993; Boardman, 1993). It has been difficult if not impossible to verify the correctness of the results objectively because no supporting data, such as field spectral reflectance measurements, could be acquired in sufficient quantity and at appropriate scales. In this paper we analyze data sets that, for the first time, give insight into the accuracy of unmixing analysis of AVIRIS images and also place bounds on the minimum detectable size of unique components within a pixel.

2. DATA ACQUISITION

As a part of a campaign to analyze the quality and utility of the data from the recently-completed airborne imaging spectrometer HYDICE (Hyperspectral Data and Information Collection Experiment) (Basedow et al., 1995), images were collected over Cuprite, NV on June 22, 1995. The next day, AVIRIS made an overpass of the same region. Both overpasses were made within one hour of local noon providing the highest radiance values possible at this latitude. Field spectral measurements, using an ASD Inc. FieldSpec®-FR instrument, were made of Stonewall Playa and several artificial targets laid out on the playa surface. A second set of spectral measurements of natural surfaces as well as additional targets were made on December 20, 1995. The targets were sheets of 10 mil Mylar and crushed dolomite having an average particle size of approximately 1 cm. The Mylar was laid out on the playa as was one 3x3 m target of dolomite. In the area south of Kaolinite Hill, dolomite targets ranging in size from 3.5 m to 30 cm on a side were laid out in an arc and surveyed in using differential GPS.

Figure 1 shows the area chosen for analysis as imaged by AVIRIS and HYDICE. AVIRIS is flown at an altitude of 20 km yielding a pixel size of approximately 18 m while HYDICE was flown at an altitude of 7.6 km, or 6.0 km above the surface, resulting in a 3 m pixel. Therefore, there are 36 HYDICE pixels for every AVIRIS pixel.

3. DATA REDUCTION AND ANALYSIS

Both the AVIRIS and HYDICE data sets were reduced to apparent reflectance using the empirical-line method in which field spectra of light and dark targets are used to determine gain and offset values for each of the wavelength channels. Figure 2 shows the field spectra taken on December 20 of Stonewall Playa and the area of desert pavement southwest of Kaolinite Hill used in the empirical-line calibration. An average spectrum of sagebrush clumps is also shown. These clumps cover 5-10 % of the surface of the desert pavement.

Figure 3 shows average spectra from both sensors taken from small patches in low and high reflectance areas. The coincidence of the spectra is greatest in the dark areas and poorest in the light areas. The source of these differences may be in the reduction to apparent reflectance but is not yet understood. This result points to areas of uncertainty when comparing spectra from the two different sensors.

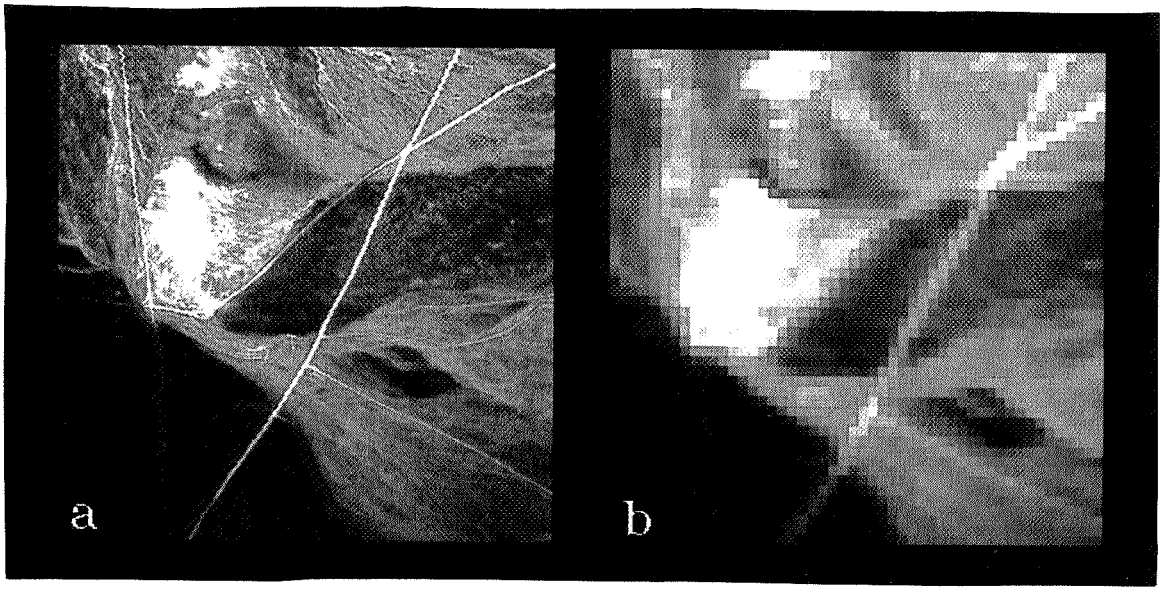

Figure 1. (a) HYDICE image at 0.8 μm of an approximately 1x1 km area south and east of Kaolinite Hill at Cuprite, NV. (b) Subset of a 20x20 km AVIRIS image of the same region as (a).

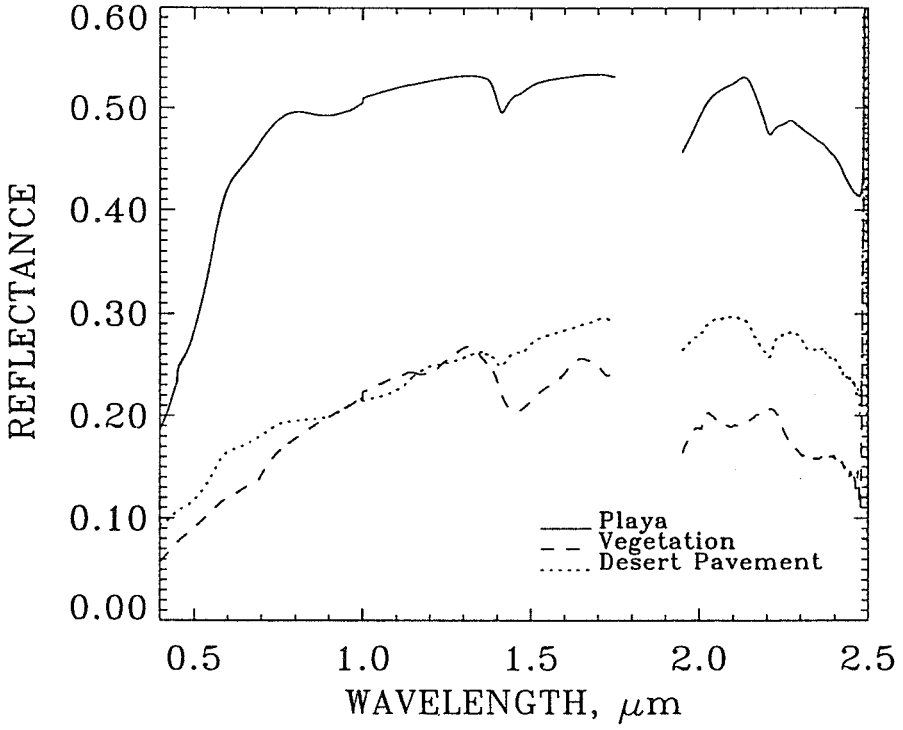

Figure 2. Field spectral measurements of Stonewall Playa and an area of desert pavement south of Kaolinite Hill used in the empirical line calibration to reduce both HYDICE and AVIRIS data to apparent reflectance.

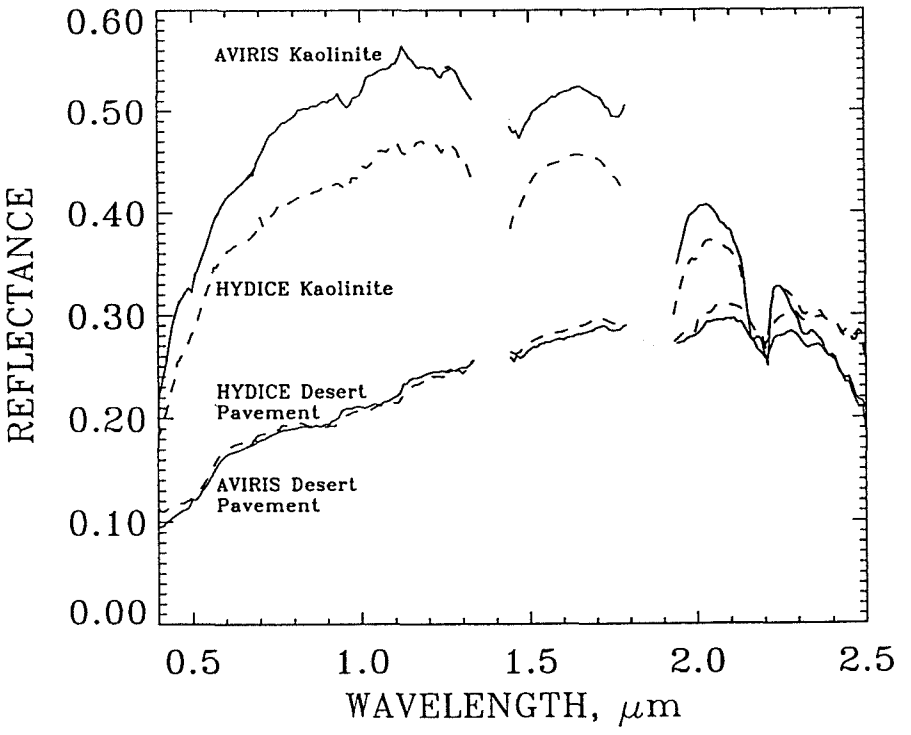

Figure 3. Comparison of AVIRIS and HYDICE pixel spectra of two regions. An average of 3 AVIRIS and 136 HYDICE pixels were used in the spectra displayed.

4. UNMIXING

The goal of unmixing analysis is to identify and quantify the component surface materials that make up individual pixels in hyperspectral images. The technique used here was unconstrained unmixing using end members derived from the HYDICE images. This algorithm is contained in the ENVI software package (Research Systems, Inc., 1995). The accurate selection of end members is one of the major uncertainties in unmixing analysis. By calibrating both datasets to the same areas in the scene, variations in atmospheric transmission and scattering as well as sensor calibration were removed. Using image-derived end members reduced an additional uncertainty associated with the relationship of the average spectrum of a heterogeneous pixel and library spectra of pure materials.

Figure 4 shows the HYDICE pixel spectra of the 5 end members chosen. The small pixel size of HYDICE made it possible to choose "pure" end members. This selection would not be possible with the coarser AVIRIS pixels. In spite of the 3 m pixels available from HYDICE, all the end member spectra are the result of mixtures of surface materials that were observed in the field to be heterogenous on a scale of one centimeter or less. Potential errors associated with this natural scale of heterogenity must be taken into account when unmixing analysis is undertaken using field or laboratory spectra as end members.

5. RESULTS

Figures 5-8 are HYDICE / AVIRIS pairs of unmixed images of the region shown in figure 1. The most striking feature is the factor of six ratio in the linear pixel dimension. The other most obvious feature common to all the figures is the overall good match between the abundances of each of the end member materials depicted as gray levels, with the lighter tones indicating higher abundances. In general the darkest tones represent negative abundances that are inevitable in an unconstrained unmixing analysis.

The kaolinite end member abundance is shown in figure 5. The major difference between the HYDICE and AVIRIS images is in the differentiation between the hilltop of relatively pure kaolinite and the colluvium draining down the eastern slope. This differentiation is obvious on the HYDICE image but not on the AVIRIS image.

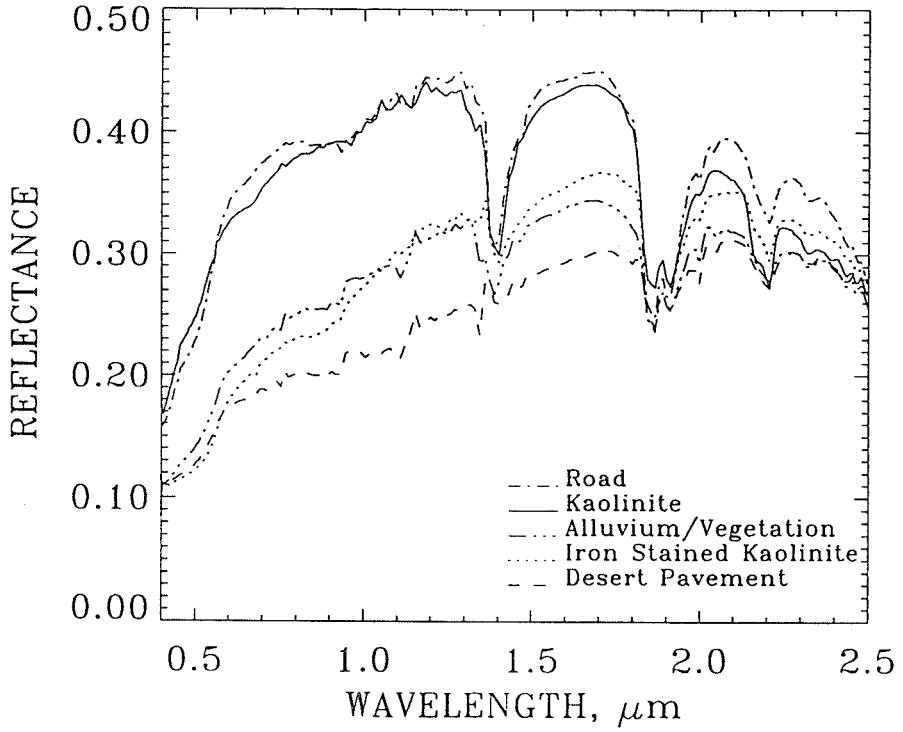

Figure 4. Reflectance spectra of end members taken from HYDICE pixels, picked visually as representative of the purest regions in each class.

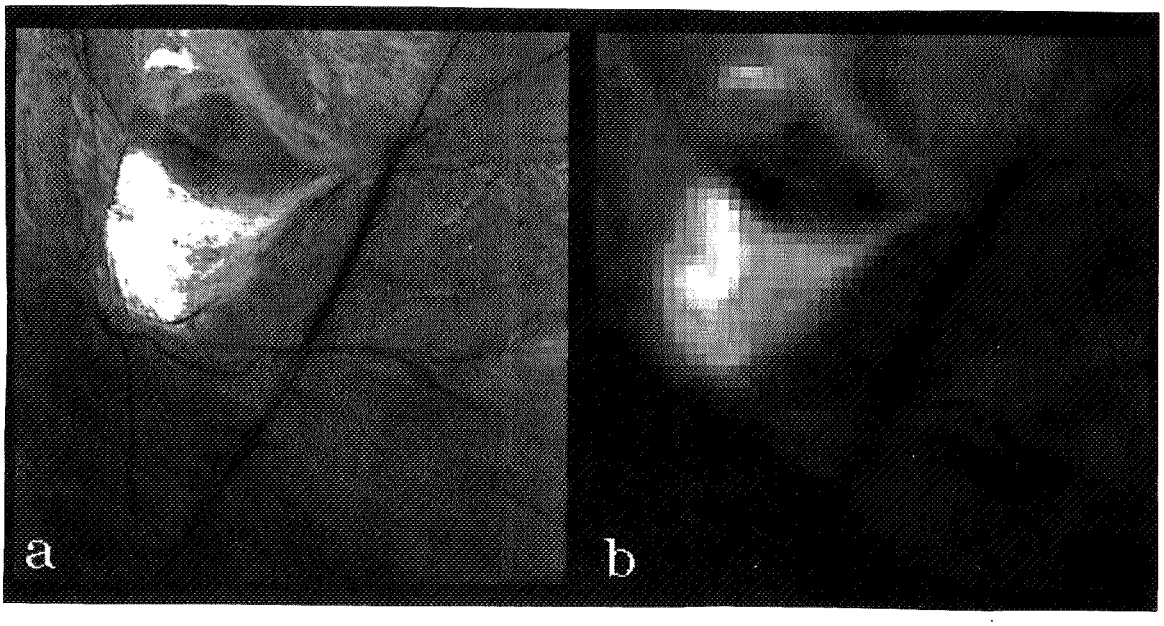

Figure 5. (a) HYDICE and (b) AVIRIS pair of abundance images of the kaolinite end member.

The central part of Kaolinite Hill is hematite-stained, altered tuff containing kaolinite. The 0.9 μm Fe^{3+} absorption is visible in the spectrum shown in figure 4. The abundance images of iron-stained kaolinite are shown in figure 6. The bright stripes at the edges of the HYDICE image are artifacts of the sensor dark current characteristics that are more pronounced beyond 2 μm. In general there is good correlation between the two abundance images.

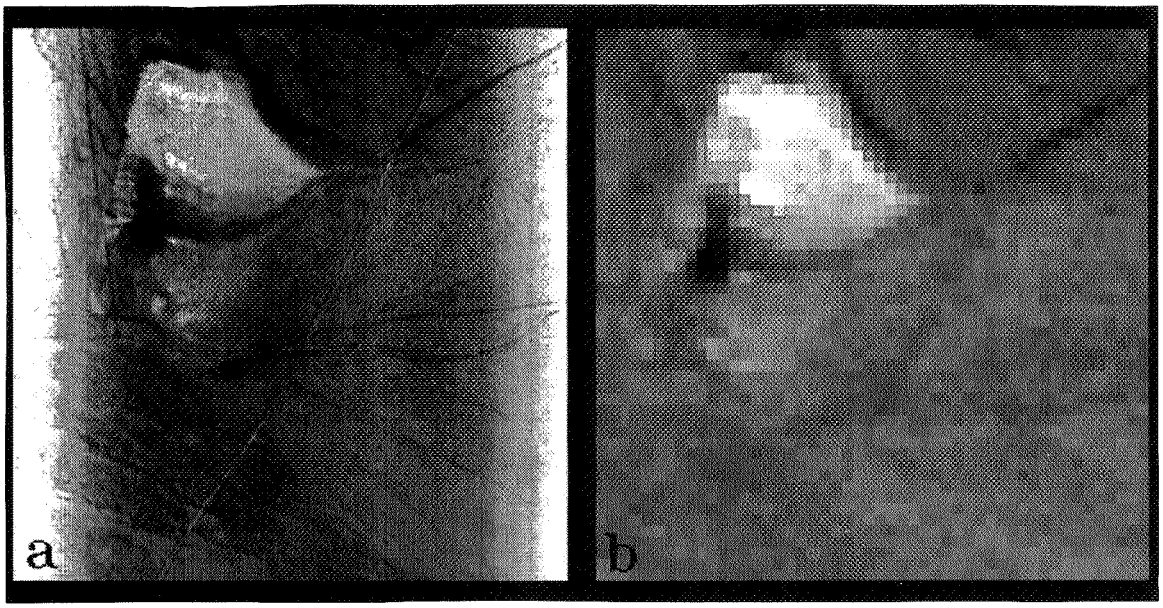

Figure 6. (a) HYDICE and (b) AVIRIS abundance images of the iron stained kaolinite end member.

Figure 7 shows the abundance of road material. The spectrum of the road end member is nearly identical to that of Kaolinite Hill short of 2.0 μm. In the HYDICE image these two end members are clearly differentiated while in the AVIRIS image Kaolinite Hill appears very dark, indicating a negative kaolinite component. The relatively evenly-spaced dark spots in the HYDICE image are clumps of sage brush.

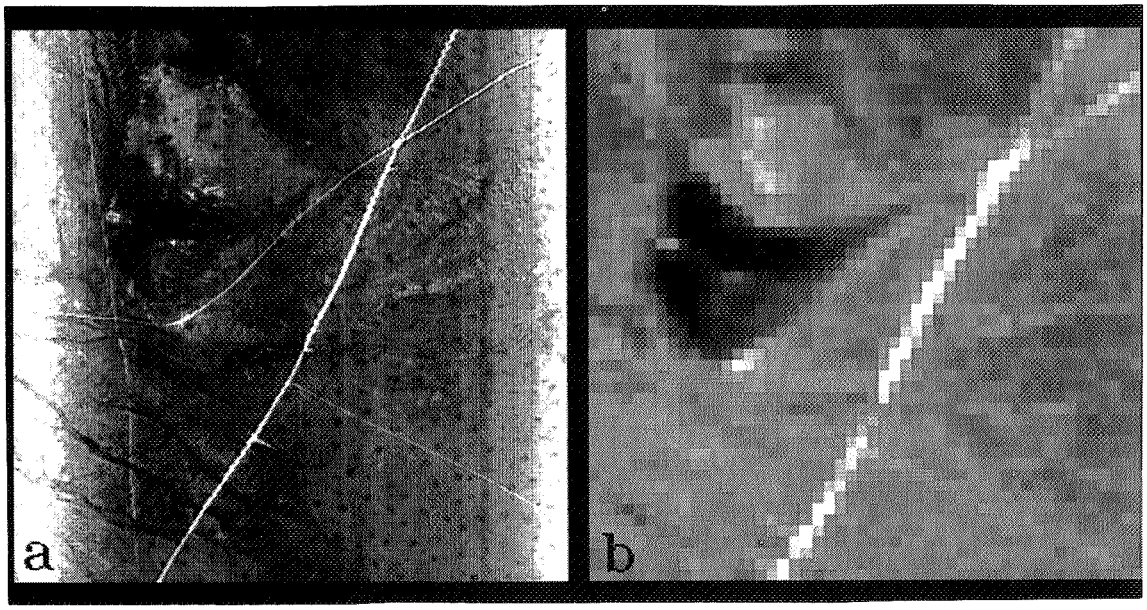

Figure 7. Abundance images for the road end member.

The power of unmixing analysis is shown in the AVIRIS image in which a jeep track running northwest from the lower right-hand corner of the image is seen. This track is approximately 2 m wide and less than 75% of road material is exposed. This represents approximately 1% of an AVIRIS pixel, a very small number. Of course, the road is only detectable because of its linear character.

The abundance images for the desert pavement end member are shown in figure 8. This figure demonstrates perhaps the best correlation between the two sensors. A clue to this agreement can be found in figure 3 that shows the nearly identical reflectance for desert pavement areas derived from HYDICE and AVIRIS short of 2.2 μm. The dark spots are sage brush clumps that are also faintly visible on the AVIRIS image. These clumps comprise less than 3% of an AVIRIS pixel.

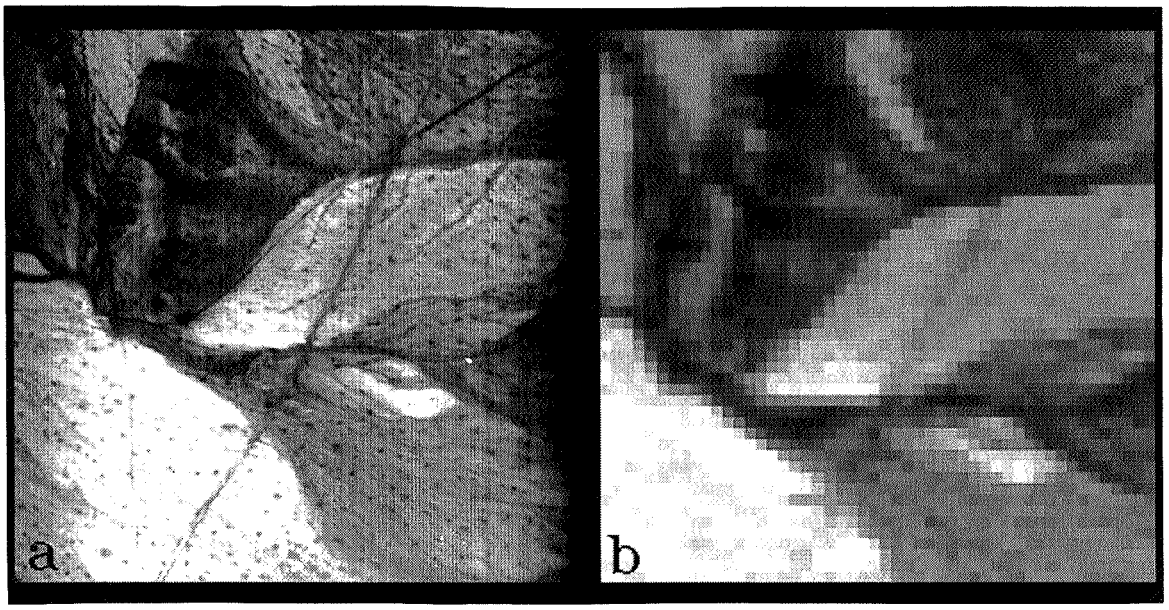

Figure 8. Abundance images of the desert pavement end member.

6. CONCLUSIONS

For the first time it has been possible to compare hyperspectral images from two sensors having a significantly different GIFOV. This factor of 36 difference in pixel area between HYDICE and AVIRIS has made it possible to choose appropriate and accurate end member spectra from the higher resolution sensor and use them in an unmixing analysis of both sensors.

The results show a high correlation between the abundance images of both sensors and indicate the accuracy and lack of major artifacts in the unmixing results derived from the lower resolution AVIRIS data.

7. ACKNOWLEDGMENTS

The authors wish to thank Kathy Heidebrecht of CSES for discussions and suggestions. This research was supported by contract number 66BP0192221 with the Desert Research Institute.

8. REFERENCES

Adams, J. B., Smith, M. O. and Gillespie, A. R., 1993, "Imaging spectroscopy: Interpretation based on spectral mixture analysis," in *Remote Geochemical Analysis: Elemental and Mineralogical Composition,* Pieters, C. M. and Englert, P. A., eds., Cambridge University Press.

Boardman, J. W., 1993, "Automating spectral unmixing of AVIRIS data using convex geometry concepts," *Proceedings Fourth Annual JPL Airborne Geoscience Workshops*, vol. 1, pp. 11-14.

Basedow, R. W., Armer, D. C. and Anderson, M. E., 1995, "HYDICE system: Implementation and performance, " *Proceedings SPIE*, vol. 2480, pp. 258-267.

Research Systems Inc., 1995 ENVI users manual.

Page intentionally left blank

Estimation of Biomass Fire Temperature and Areal Extent from Calibrated AVIRIS Spectra

Robert O. Green

Jet Propulsion Laboratory, California Institute of Technology, Pasadena, CA 91109
and
University of California, Santa Barbara, CA 93106

ABSTRACT

Biomass burning is an important process on the Earth at the local, regional and global scales. To investigate issues related to biomass burning, a range of remotely acquired data were measured as part of the NASA Smoke Cloud Aerosol and Radiation experiment in Brazil, 1995. As part of this experiment, images of calibrated spectral radiance from 400 to 2500 nm at 10 nm intervals were acquired by AVIRIS.

To investigate the expression of biomass fires in AVIRIS spectra, a model of the upwelling radiance from a burning fire was developed. This spectral model accounts for four components in the 20 by 20 m AVIRIS spatial resolution element. These are: (1) the atmospheric path radiance, (2) the solar reflected radiance from unburnt vegetation and soil, (3) the apparent temperature and area of a primary fire, and (4) the apparent temperature and area of a secondary fire. A nonlinear least squares spectral fitting algorithm was developed to invert this model for the AVIRIS spectra. The derived biomass burning parameters from this algorithm are presented for AVIRIS spectral images acquired over Cuiaba, Brazil on 25 August 1995.

INTRODUCTION

Biomass burning is an important process on the Earth at the local, regional and global scales. At the local scale, destruction of human infrastructure is the dominant concern. At the regional scale, destruction of habitat and modification of regional climate are at issue (Kirchhoff 1989). At the global scale, production of carbon dioxide (a greenhouse gas), modification of the terrestrial carbon balance, and introduction of aerosols into the atmosphere (direct and indirect impacts on the global energy balance) are at issue (Levine, 1995). Biomass burning occurs unpredictably in detail around the globe where there is dry vegetation as a function of numerous natural and human factors. Because of this global and intermittent nature, a satellite or airborne method to detect, measure and monitor biomass burning and fire parameters is desirable.

This paper describes an approach to derive a range of biomass fire parameters from spectra measured by NASA's Airborne Visible/Infrared Imaging Spectrometer (AVIRIS). AVIRIS measures images of the upwelling spectral radiance from 400 to 2500 nm at 10 nm intervals. Images are measured of 11 by up to 100 km with 20 by 20 m spatial resolution.

Biomass fires emit radiance as a function of temperature. Spectra across the AVIRIS range for Planck function emitted radiance over a range of fire temperatures are shown in Figure 1. The shape and intensity of spectrally emitted radiance vary strongly over this spectral range for these temperatures. This spectral sensitivity to temperature was investigated with AVIRIS for volcano hot spots (Oppenheimer 1993). Related satellite multi-spectral approaches to estimate fire temperature and fraction were pursued previously (Dozier 1981; Prins, 1992). However, there is additional leverage on these fire parameters in the combined shape and intensity measured in the AVIRIS spectrum.

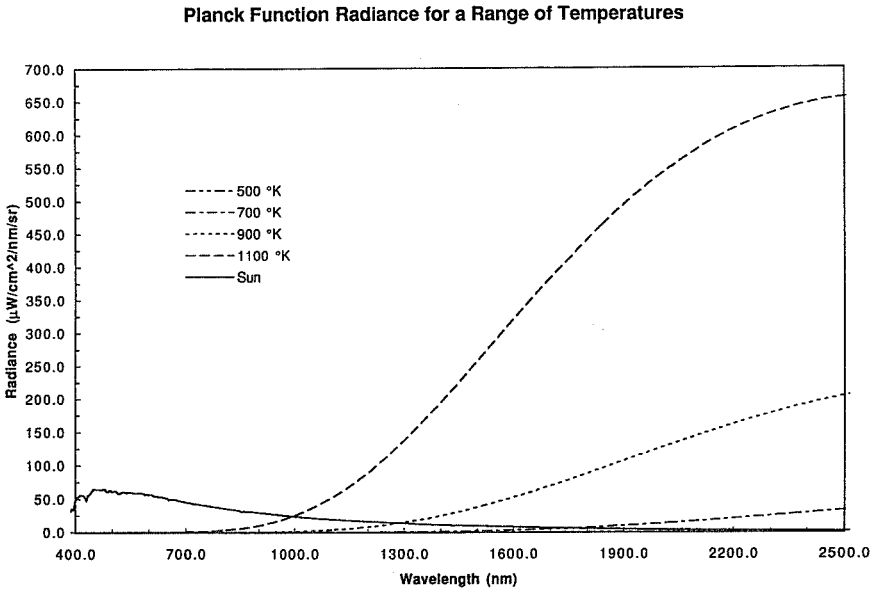

Figure 1. Planck function emitted radiance spectra for a range of fire temperatures from 400 to 2500 nm.

A model of the radiance incident at AVIRIS for 20 by 20 m spatial resolution has been developed. The model relies on the MODTRAN3 (Kneizys, 1988, Berk, 1989) radiative transfer code for calculation of atmospheric parameters. MODTRAN3 was used to model the atmospheric path radiance. A mixture of measured spectra of vegetation and soil was used to represent unburnt components of the surface. The Planck function was used to model the radiance emitted by two fires having different temperatures and areal extents. This model was linked to the simplex nonlinear least squares fitting algorithm (Press 1986) to invert the AVIRIS measured radiance for biomass fire parameters. The algorithm has been applied to an AVIRIS data set acquired near the city of Cuiaba, Brazil on the 25th of August 1995. Results of the application of this algorithm to the Cuiaba data set are presented in this paper.

MEASUREMENTS

An image from the 500.5 nm wavelength region from the AVIRIS August 25 Cuiaba data set is shown in Figure 2. Several fires are burning with the most prominent in the central left portion of the image. The smoke plume from the biomass fire is dominant at this wavelength and trends towards the city of Cuiaba in the lower right corner of the image. Figures 3 and 4 show the spectral images at 1000.2 nm and 2000.5 nm wavelength respectively. In the 1000.2 nm AVIRIS wavelength image, the smaller particle and less dense portions of the smoke plume are no longer evident and the higher temperature edges of the fires are showing emitted radiance. In the 2000.5 nm AVIRIS wavelength image, the smoke plume is largely transparent and the entire burning area is evident through the fire emitted radiance. These effects are shown spectrally in Figure 5. The first AVIRIS spectrum of the non-burning vegetation at some distance from the smoke plume shows the solar reflected radiance due to absorption and scattering in the atmosphere and reflection at the surface. The surface vegetation absorption due to chlorophyll is expressed between 680 and 720 nm in this spectrum. The second spectrum of

non-burning vegetation in the smoke plume shows little to no influence of surface reflectance below 1000 nm due to the scattering of smoke. Beyond 1000 nm the influence of smoke scattering is decreased and this spectrum resembles the first vegetation radiance. The third radiance spectrum from burning vegetation shows the smoke scattering effects below 1000 nm. Between 2000 and 2500 nm this spectrum is higher in radiance than the non-burning spectra. This increased radiance results from the emission of the fire. A full AVIRIS spectrum from 400 to 2500 nm for every 20 by 20 m spatial element is present in the Cuiaba data set. These spectra provide the basis for derivation of the fire temperature, areal extent and associated parameters.

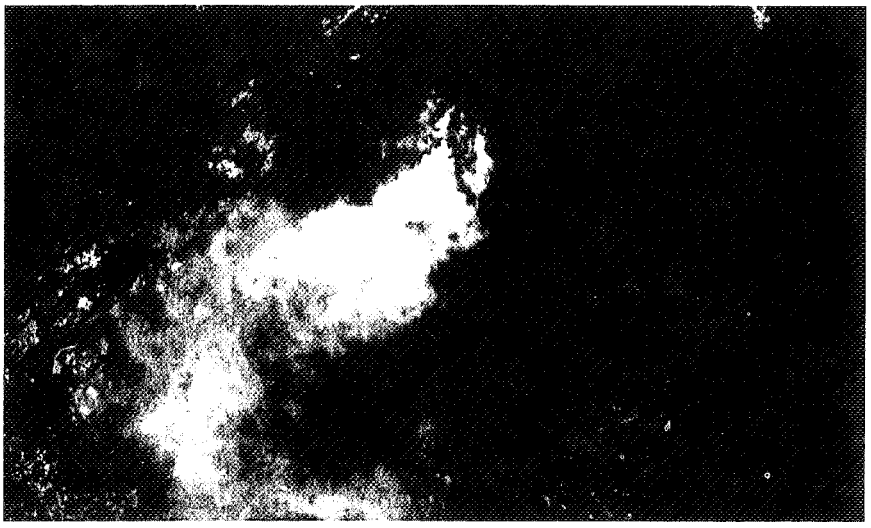

Figure 2. AVIRIS image at 500.5 nm of the biomass fires at Cuiaba, Brazil. Smoke particles are scattering the solar radiance at this wavelength.

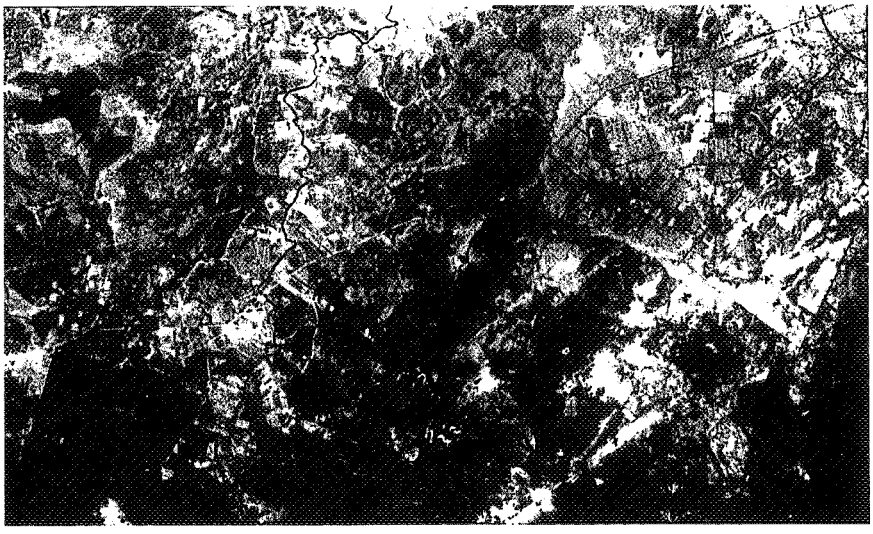

Figure 3. Image at 1000.2 nm. At this wavelength the smoke is penetrated. The blackened burned area is evident. At the fringe of the burned area active burning is apparent as radiance emitted by the fire.

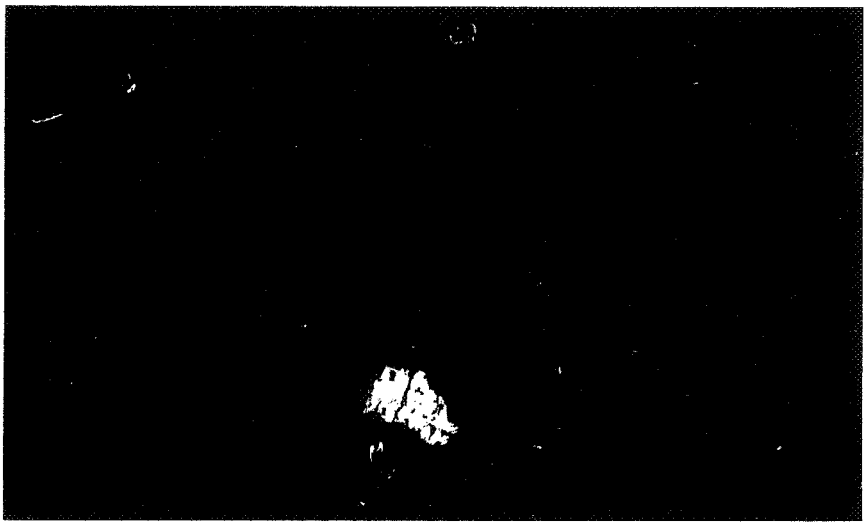

Figure 4. Image at 2000.5 nm showing emission of active fire dominating the calibrated radiance measured by AVIRIS. Scattering due to smoke is not apparent.

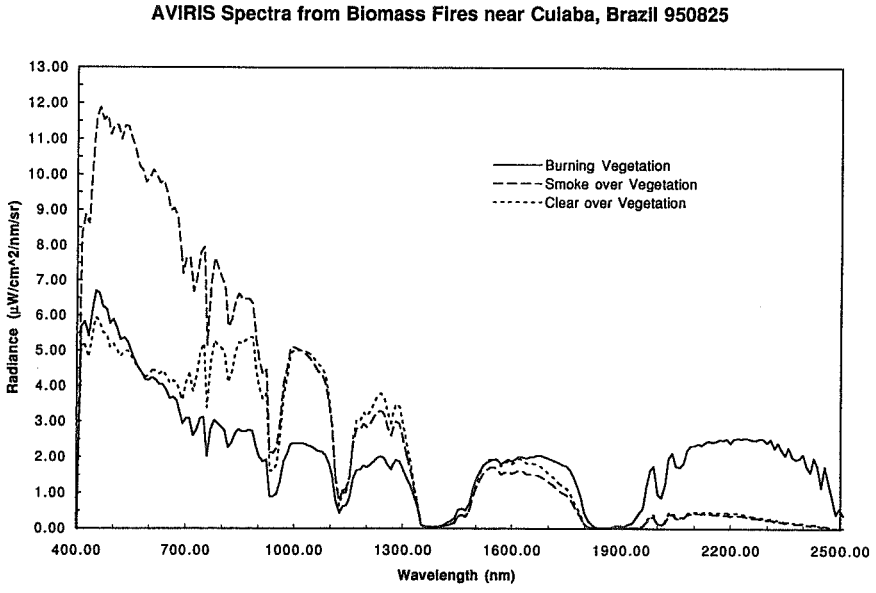

Figure 5. Three spectra from the 25th of August 1995 Cuiaba AVIRIS data set. Non-burning vegetation spectra both in and out of the central smoke plume as well as a spectrum from the burning area are shown. Towards 2500 nm the fire emitted radiance dominates the spectrum from the burning vegetation.

MODEL

To derive biomass burning parameters from the calibrated spectra, a model of the upwelling radiance incident at AVIRIS that included fire emitted energy was developed. The spectral radiance incident at AVIRIS from a 20 by 20 spatial element is modeled as the sum of the path radiance from the atmosphere; the reflected radiance from unburnt vegetation and soil; and the emitted radiance from two fire sources. A simplified expression of the model is given in equation 1.

$$Lt = Lp + Lr + Lb1 + Lb2 \qquad (1)$$

Lt is the total upwelling spectral radiance measured by AVIRIS for a 20 by 20 m spatial resolution element. Lp is the atmospheric path radiance incident at AVIRIS that has not been reflected by the surface. Lr is the reflected radiance. Lr is modeled as the two way transmitted radiance from the sun for a mixture of vegetation and soil. Lb1 is the one way transmitted radiance from a Planck function source for a given temperature and areal extent. Lb2 is the radiance from a second Planck function source and areal extent. The areal extent of the solar reflected radiance and the two Planck function radiance sources are constrained to a value of 1.0. The reflectance of the vegetation and soil were selected from a library of pre-existing field measurements. The MODTRAN3 radiative transfer code was used to provide the atmospheric path radiance for a range of highly scattering atmospheric conditions. MODTRAN3 was also used to calculate the one way and two way transmittances of the atmosphere. A recent compilation of the exoatmospheric solar irradiance was used (Gao and Green, 1995). Radiance emitted by the fires was modeled by the Planck function. The spectral region fit by the model was limited to wavelengths greater than 1000 nm, where the smoke scattering is reduced and the fire emitted radiance effect is strong. The illumination and observation geometry for the model are based on the time and place of AVIRIS data acquisition.

The model was linked to a downhill simplex nonlinear least squares algorithm (Press, 1986) and applied to the Cuiaba AVIRIS data set. Portions of spectra where AVIRIS saturation occurred were excluded from the fit. However, no spectra were fully excluded due to saturation.

ANALYSIS AND RESULTS

Figure 6 shows an example of the spectral fit for a single spectrum in the central Cuiaba fire. To achieve a good fit for this AVIRIS measured spectrum, emitted radiance from two Planck functions with two temperatures and areal extents was required: one at 1183 K and 0.04 fractional extent and a second at 691 K and 0.42 fractional extent. Also shown is the radiance expected for a surface of 1.0 reflectance.

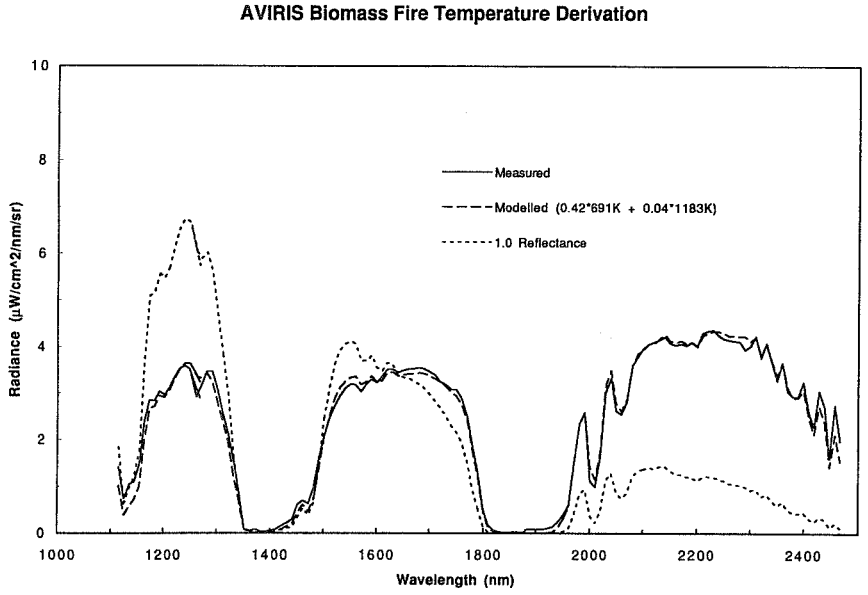

Figure 6. Spectral fit from inversion of the forward model. The measured spectrum, model fit spectrum and residual spectrum are shown. Two fire temperatures and areal extents were required to model these measured spectrums.

This spectral fire parameter algorithm was applied to the entire Cuiaba AVIRIS data set covering 11 by 20 km at 20 by 20 m spatial resolution. Images of the primary fire temperature and areal extent produced by the algorithm are shown in Figures 7 and 8. Fires are mapped throughout the image with temperatures ranging from 500 K to 1700 K. Smaller fires are detected and mapped that were not well expressed in the 2000.5 nm radiance image. Temperatures of the smaller fires and the edges of the larger fires are typically higher than the internal regions of the larger fires. Fire fractional areas range from 0.01 to 0.30. The hotter, smaller and edge fires show lower fractional extent. This temperature distribution and this areal extent distribution are consistent with the availability of unburnt fuel near the small fires and edges of larger fires. These temperature and areal extent results are constant with the biomass burning process. Furthermore, the agreement between the AVIRIS measured radiance and physically based model radiance of the fires supports the validity of this approach and algorithm for deriving fire parameters from calibrated AVIRIS spectra.

The algorithm generated additional image parameters of the secondary fire and areal extent for each spectrum. Unburnt soil and vegetation fractions as well as estimates of atmospheric scattering attenuation by smoke were produced.

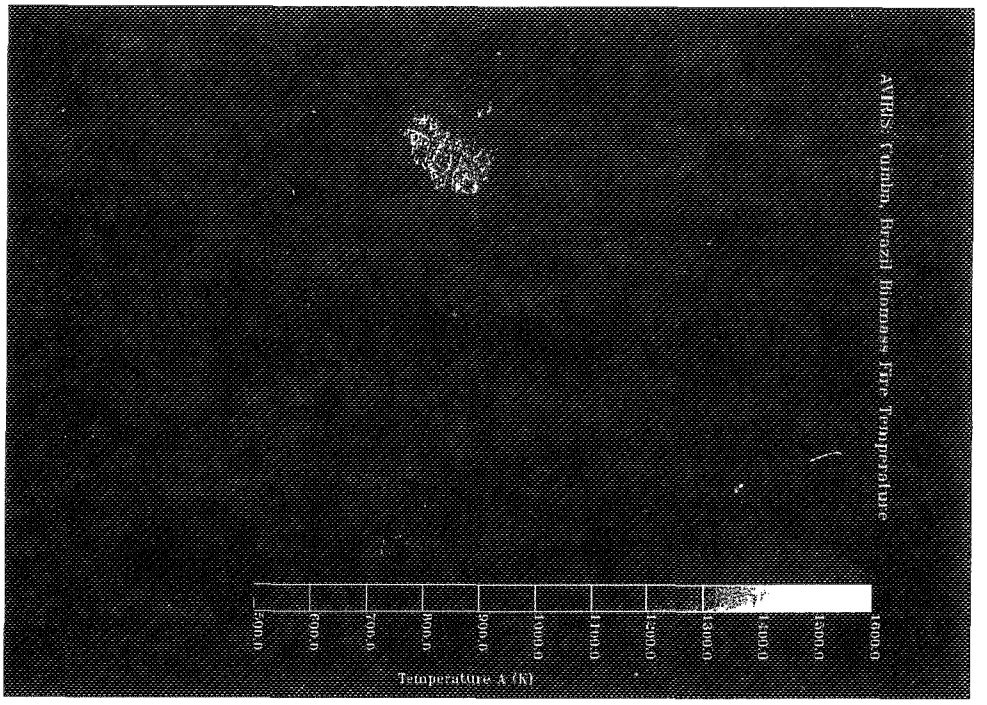

Figure 7. Image of the derived dominant fire temperature for AVIRIS Cuiaba spectra.

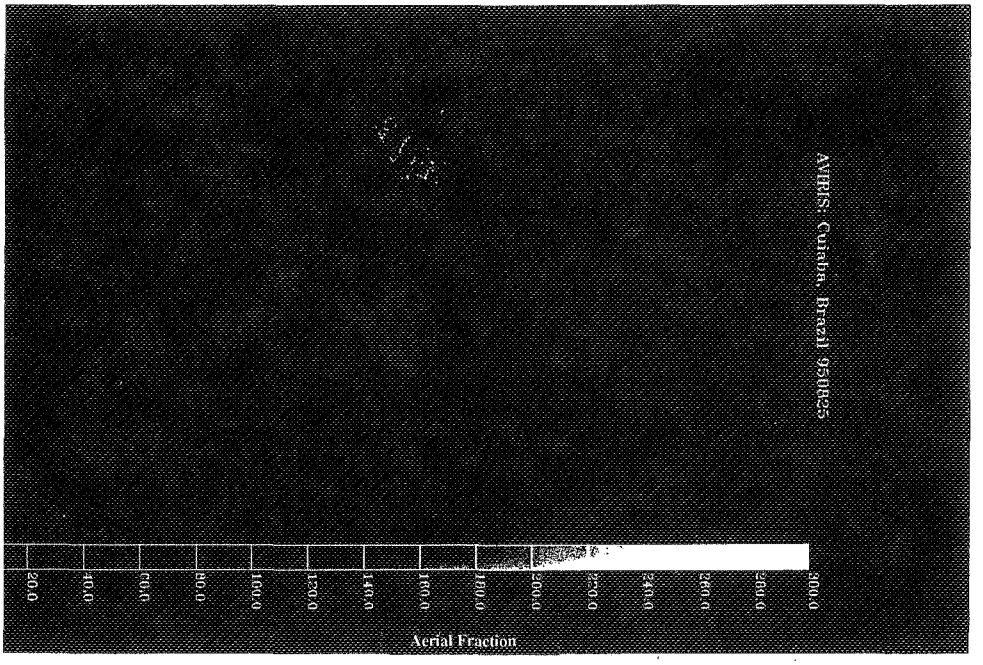

Figure 8. Image of areal fraction of dominant fire for AVIRIS Cuiaba spectra. The units of this image as numbered on the "Aerial Fraction" scale are parts per thousand.

CONCLUSION

A spectral fire parameter algorithm was developed to derive fire temperature and areal extent information from calibrated spectra measured by AVIRIS as images with 20 by 20 meter spatial resolution. The algorithm is based on the spectral shape and intensity of the fire emitted radiance expressed in the AVIRIS spectra. Fires are spectrally modeled as both primary and secondary fire sources in each AVIRIS spatial element. Effects of atmospheric path radiance, atmosphere transmittance, and solar reflected radiance from unburnt vegetation and soil are accounted for. Good agreement is achieved between the measured AVIRIS spectra and modeled spectra of the algorithm. The spectral fire temperature algorithm was applied to an 11 by 20 km AVIRIS image near Cuiaba, Brazil. The spatial distribution of the fire temperatures and areal extents was consistent with the biomass burning process. This algorithm coupled with AVIRIS data provides an improved strategy for derivation of biomass fire parameters. Remotely derived biomass fire parameters are needed to detect, measure and monitor fires at the local, regional and global scales.

FUTURE WORK

Future work will focus on validation of the derived biomass fire parameters. In addition, the algorithm model will be extended to allow for variation in water vapor and carbon dioxide. A sensitivity analysis will be performed to understand the influence of the constraining parameters on the modeled spectrum.

ACKNOWLEDGMENTS

The majority of this research was carried out at the Jet Propulsion Laboratory, California Institute of Technology, under contract with the National Aeronautics and Space Administration. A portion of the work was performed at the Institute for Computational Earth System Science, University of California, Santa Barbara, CA.

REFERENCES

Berk, A. (1989), "MODTRAN: A moderate resolution model for LOWTRAN 7", Final report, GL-TR-0122, Air Force Geophys. Laboratory, Hanscom AFB, MA, 42pp.

Dozier, J. (1981), "A method for satellite identification of surface temperature fields of subpixel resolution." *Remote Sensing of Environment*, 11, 221-229.

Gao, B.C., Green, R.O. (1995), "Presence of terrestrial atmospheric gas absorption bands in standard extraterrestrial solar irradiance curves in the near-infrared spectral region," *Applied Optics, Vol. 34, No. 27,* 6263-6268.

Kirchhoff, V.W.J.H. (1989), "Biomass burning in Amazonia: Seasonal effects on atmospheric O_3 and CO," *Geophysical Research Letters, Vol. 16, No. 5*, 469-472.

Kneizys, F.X. (1988), "*User's Guide* to LOWTRAN7," Rep. AFGL-TR-88-0177, Hanscom AFB, Air Force Geophys. Lab., Bedford, MA.

Levine, J.S. (1995), "Biomass burning, a driver for global change", *Environmental Sci. & Technology, Vol. 29, No. 3,* 120-125.

Oppenheimer-C; Rothery-DA; Pieri-DC; Abrams-MJ; Carrere-V. (1993), "Analysis Of Airborne Visible/Infrared Imaging Spectrometer (AVIRIS) Data Of Volcanic Hot-Spots", Open Univ., Dept. Earth Sci./Milton Keynes/MK7 6AA/Bucks./ENGLAND/*International Journal Of Remote Sensing*, 14, (16), 2919-2934.

Press, W.H., ***Numerical Recipes: The Art of Scientific Computing***, Cambridge University Press, Cambridge, England, 1986.

Prins, E.M. (1992), "Geostationary satellite detection of biomass burning in South America", *Int. J. Remote Sensing, Vol. 13, No. 15*, 2783-2799.

ADDITIONAL READING

Anderson, G.P. (1995), "MODTRAN3: An update and recent validations against airborne high resolution interferometer measurements", *Summaries of the Fifth Annual JPL Airborne Earth Science Workshop, JPL 95-1, Vol. 1*, 5-8.

Page intentionally left blank

In-Flight Calibration and Validation of the Airborne Visible/Infrared Imaging Spectrometer (AVIRIS)

Robert O. Green[1,2], James E. Conel[1], Jack Margolis[1], Chris Chovit[1], and Jessica Faust[1]

[1]Jet Propulsion Laboratory, California Institute of Technology, Pasadena, CA 91109
[2]University of California, Santa Barbara, CA 93106

ABSTRACT

Calibrated spectra acquired remotely as images allow determination of surface and atmospheric properties based on absorption and scattering expressed in the spectra. AVIRIS measures spectra as images in the solar reflected portion of the electromagnetic spectrum. To use these spectra for scientific research and applications, the calibration of the spectra must be known at the time of measurement in flight. To validate the calibration of AVIRIS in flight, an in-flight calibration experiment was performed for an over-flight on May 9, 1995 at Ivanpah Playa, California. In-situ measurements of the atmosphere and surface at a calibration target were measured. These measurements were used to constrain a radiative transfer code and predict the total upwelling spectral radiance incident at AVIRIS. This prediction was compared to the radiance measured by AVIRIS for the calibration target. An agreement of 96.5% was determined. The in-flight signal-to-noise was determined and shown to have more than doubled over the previous year.

INTRODUCTION

Calibrated spectra acquired remotely as images, allow determination of surface and atmospheric properties, based on molecular absorption and constituent scattering characteristics. AVIRIS measures images of 11 by up to 100 km at 20-m by 20-m spatial resolution that consist of spectra from 400 to 2500 nm at 10 nm intervals. The spectral, radiometric and spatial characteristics of AVIRIS are calibrated in the laboratory (Chrien et al., 1990, 1996) prior to each flight season.

In order for AVIRIS to be used for scientific research and applications, the calibration of AVIRIS must be valid at the time spectra are measured from the ER-2 airborne platform. The operational environment inside the Q-bay of the ER-2 at 20 km altitude is different from that in the AVIRIS laboratory.

In-flight calibration experiment methodologies were developed for AVIRIS to confirm the accuracy of AVIRIS calibration in flight (Conel et al., 1988; Green and Gao, 1993; Green et al., 1988, 1990, 1992a). In these experiments the surface and atmosphere at a homogeneous ground calibration site are determined with in-situ measurements. These measurements are used to constrain MODTRAN3 (Berk et al., 1989; Anderson et al., 1995) radiative transfer code and predict the spectral radiance incident at AVIRIS. Comparison and analysis of the predicted and AVIRIS measured radiance are used to calibrate and validate the performance of AVIRIS in flight.

This paper describes the calibration target, measurements, analysis and results from the in-flight calibration experiment at Ivanpah Playa in 1995.

MEASUREMENTS

On May 9, 1995, an in-flight calibration experiment was held at Ivanpah Playa, California, located 100 km south of Las Vegas, Nevada at 35.5150 degrees north latitude and

115.3990 degrees west longitude. Ivanpah Playa is a dry lake bed approximately 3 km by 15 km in size at 740 m elevation.

A calibration target was designated on a portion of the playa surface based on visually apparent homogeneity. The target was 40-m by 200-m (2 by 10 AVIRIS spatial resolution elements). The long axis of the target was oriented in the AVIRIS flight-line direction and demarked by blue tarps at each end of the target.

At the calibration target an automated sun photometer was used to collect data from sunrise through the time of the AVIRIS data acquisition. The sun photometer measures data at 370, 400, 440, 520, 620, 670, 780, 870, 940, and 1030 nm wavelengths. These calibrated measurements were used to derive instantaneous optical depths through the day as shown in Figure 1. Figure 2 shows the water vapor determined from 940 nm sun photometer measurements (Reagan et al., 1987, Bruegge et al., 1990). Some cirrus clouds affected the measurements around 10:00 a.m. local time.

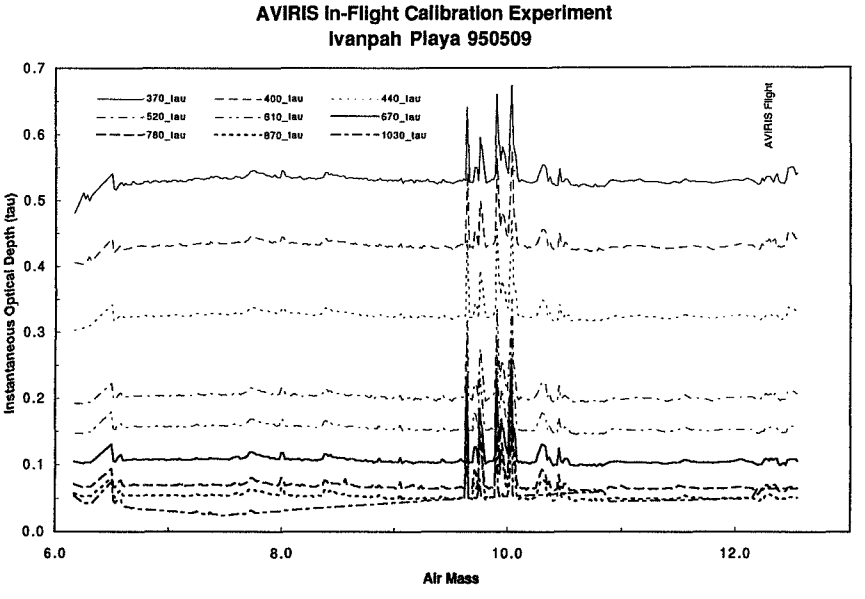

Figure 1. Derived optical depths of the non-water-vapor measurements of the sun photometer.

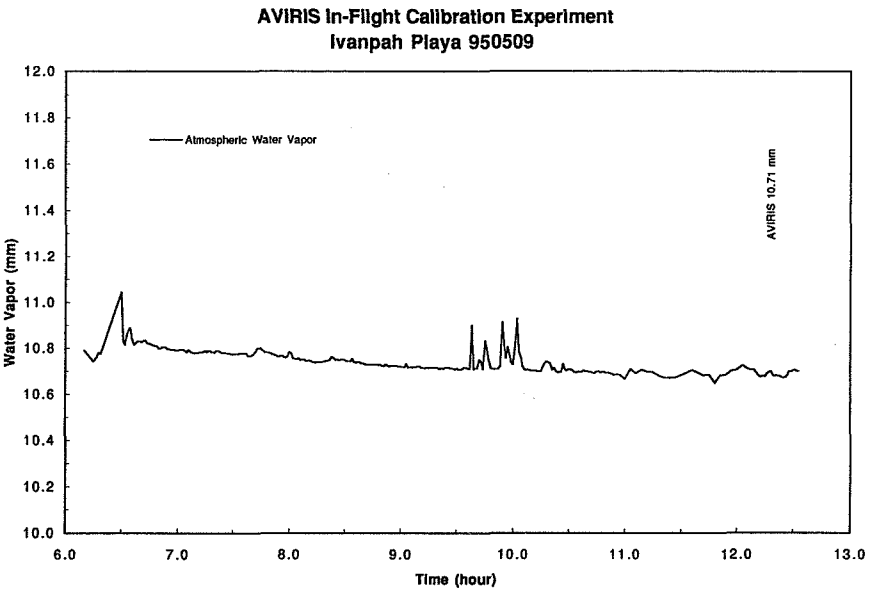

Figure 2. The water vapor abundance determined from the 940 nm sun photometer measurements.

During the time of the AVIRIS data acquisition, the surface spectral reflectance was measured using a field spectrometer that covers the AVIRIS spectral range. A total of 160 measurements were acquired. These measurements were evenly spaced over the target and averaged to determine the calibration target spectral reflectance as shown in Figure 3.

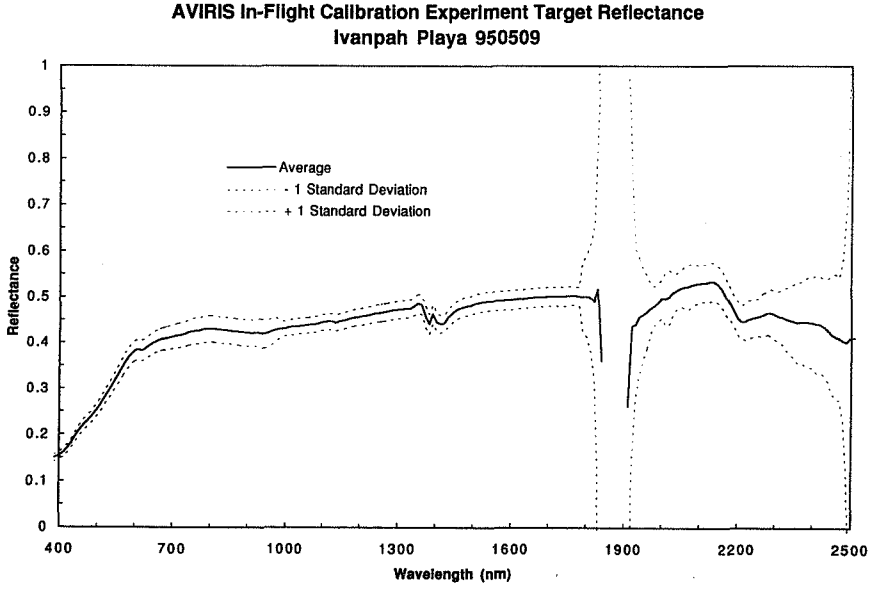

Figure 3. Calibration target spectral reflectance. The average and two standard deviations are shown.

At 19:19 hours UTC, AVIRIS acquired data over the Ivanpah Playa calibration target. Figure 4 shows an image of Ivanpah Playa from 647.7 nm wavelength. The enhanced image in Figure 5 shows the two dark blue demarcations on the left edge of the playa one third of the way from the top of the image. The uncalibrated AVIRIS spectra extracted from the calibration target are shown in Figure 6.

Figure 4. AVIRIS image of Ivanpah Playa from 647.7 nm.

Figure 5. Enhanced Ivanpah Playa image showing the two calibration target tarps on the left edge of the playa, one-third of the way from the top of the image.

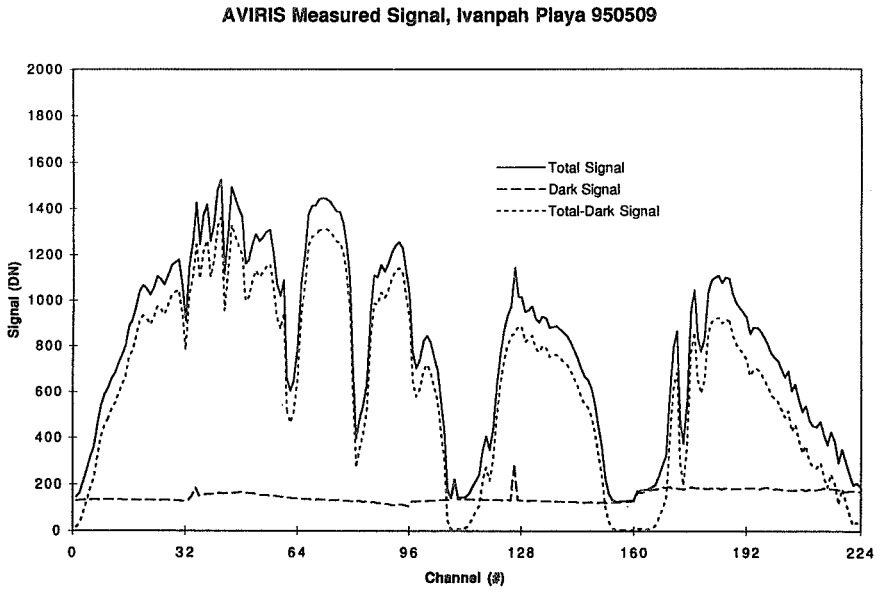

Figure 6. AVIRIS signal from the calibration target. The total signal, dark signal and dark subtracted signal are shown.

ANALYSIS

Optical depths calculated at the time of the AVIRIS overpass were used to constrain the aerosol model used in MODTRAN3 for the calibration experiment. The measured and modeled optical depths are shown in Figure 7. These optical depths in conjunction with the surface spectral reflectance and atmospheric water vapor were used to constrain MODTRAN3 for the time of AVIRIS data acquisition. An updated exo-atmospheric solar irradiance spectrum (Green, 1993) was used in MODTRAN3. The MODTRAN3 predicted upwelling radiance for the calibration target is shown in Figure 8.

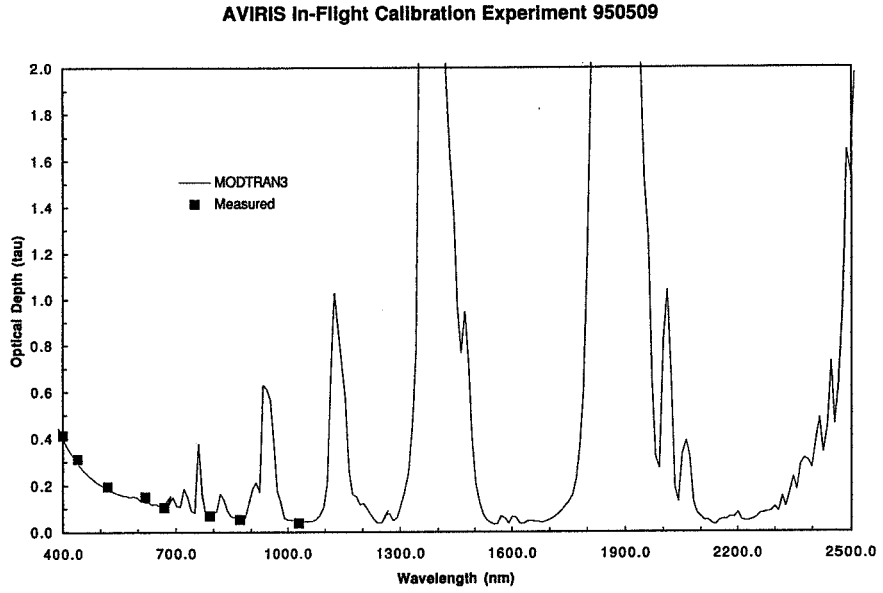

Figure 7. Measured and MODTRAN3 modeled optical depths of the Ivanpah Playa calibration experiment.

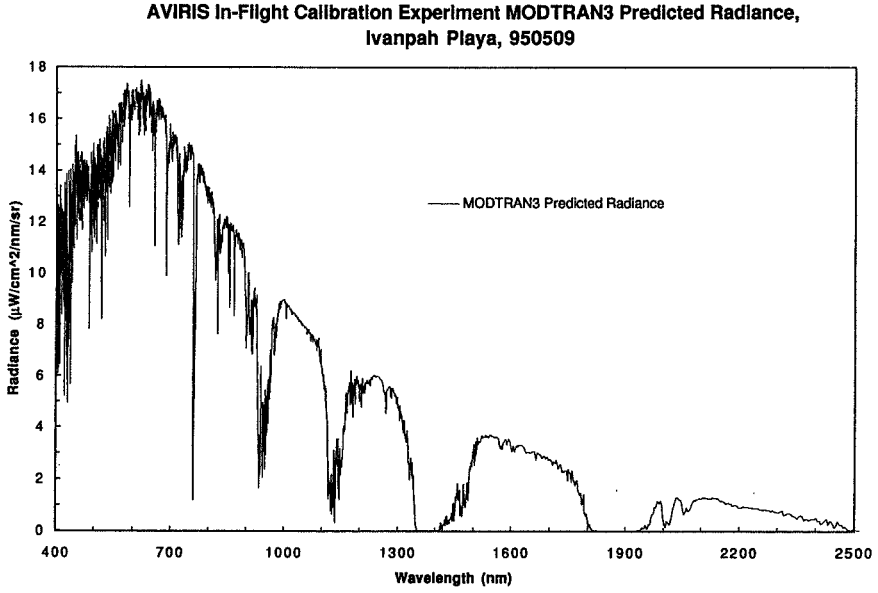

Figure 8. MODTRAN3 prediction of the upwelling spectral radiance incident at AVIRIS.

AVIRIS signal spectra were calibrated (Green et al., 1991) with the laboratory determined radiometric calibration coefficients and spectral calibration (Chrien et al., 1990; Chrien et al., 1996). AVIRIS on-board calibrator coefficients were derived as the ratio of the in-flight on-board calibrator signal to the signal at the time of laboratory calibration (Green 1993). These on-Board calibrator coefficients are shown in Figure 9 and were applied to the AVIRIS calibration target data.

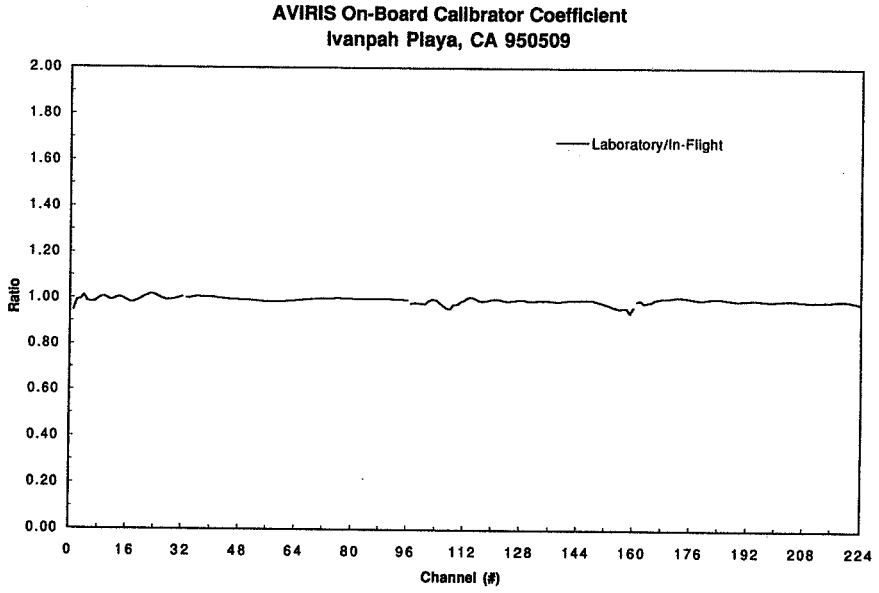

Figure 9. AVIRIS on-board calibrator coefficients. These coefficients compensate for small changes in AVIRIS performance from the laboratory to the in-flight condition.

RESULTS

The MODTRAN3 predicted spectrum convolved to AVIRIS spectral response functions and the AVIRIS laboratory calibrated spectrums are shown in Figure 10. The average absolute agreement across the spectral range was 96.5 % for this experiment. The spectral regions of near-zero radiance at 1400 and 1900 nm were excluded. This result is improved over the 1994 in-flight calibration experiment result of 95.3 %. The disagreement was attributed to the in-situ measurements, the MODTRAN3 model, the AVIRIS instrument and to the calibration standards. Figure 11 shows the AVIRIS to MODTRAN3 ratio for the calibration target. In this ratio, disagreement occurs in the 400 nm region and near the atmospheric absorptions of water vapor, oxygen and carbon dioxide. These discrepancies are attributed to uncertainties in the MODTRAN3 model used in AVIRIS spectral calibration. Nevertheless, the agreement between the MODTRAN3 prediction and the AVIRIS measurement is within 4 % and this experiment initially validates the performance of AVIRIS in flight in 1995.

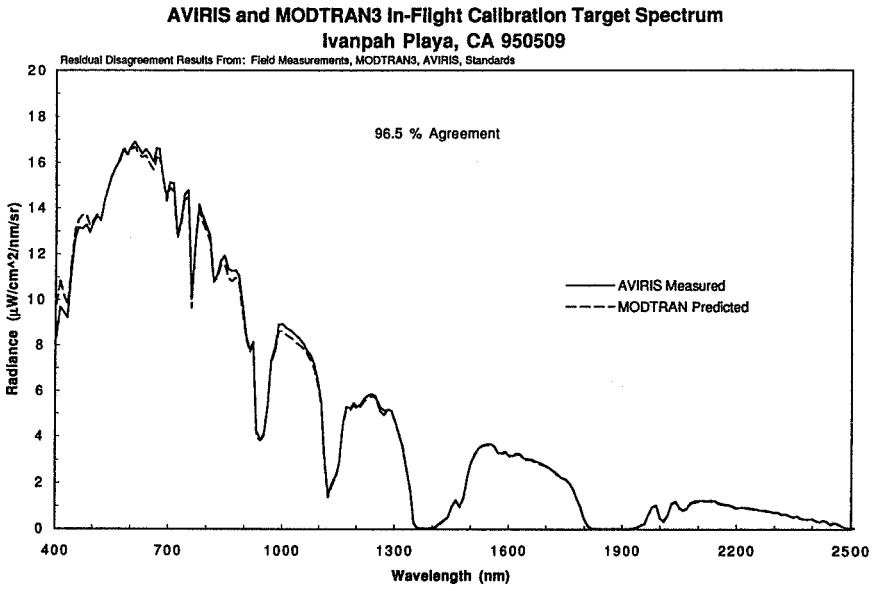

Figure 10. Comparison of the MODTRAN3 predicted and AVIRIS measured upwelling spectral radiance for the calibration target.

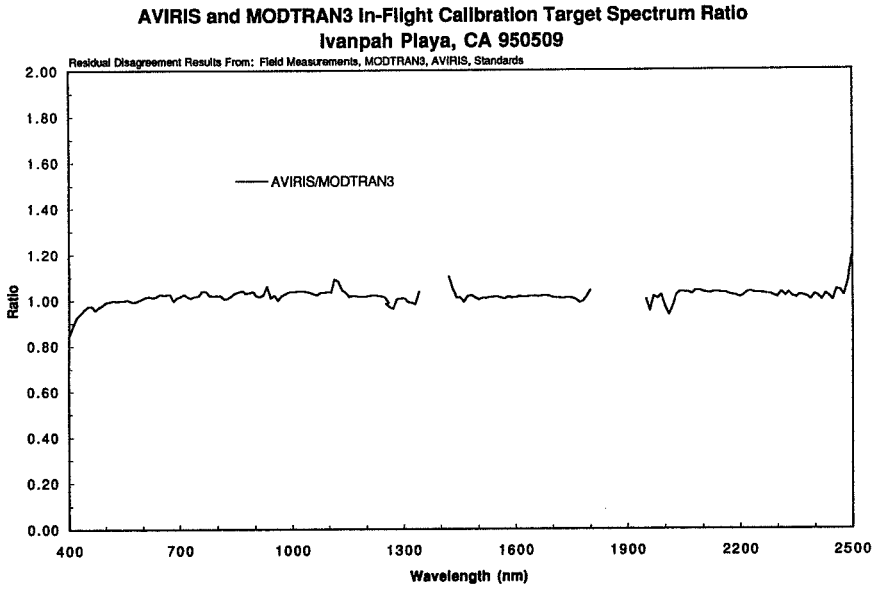

Figure 11. Calibration target ratio of AVIRIS to MODTRAN3.

In-flight radiometric precision (signal-to-noise ratio) was determined with data from this calibration experiment. Noise was estimated as the standard deviation of the dark signal measured at the end of each image line. The AVIRIS signal spectrum was extracted from the calibration target. The conversion factor of photons to signal was used to estimate the additional

photon-noise for the calibration target. The photon-noise and dark-signal noise were root-sum-squared. The extracted signal was scaled to the AVIRIS reference radiance (Green et al., 1988) and divided by the noise to give the AVIRIS in-flight signal-to-noise ratio for 1995. This signal-to-noise is improved by more than a factor of two compared to that of 1994 as shown in Figure 12. AVIRIS signal-to-noise is greater than 500:1 over much of the spectral range. A calculation of noise-equivalent-delta-radiance was also performed for a dark target and is shown in Figure 13. The noise-equivalent-delta-radiance represents the precision uncertainty in radiance for each AVIRIS spectrum.

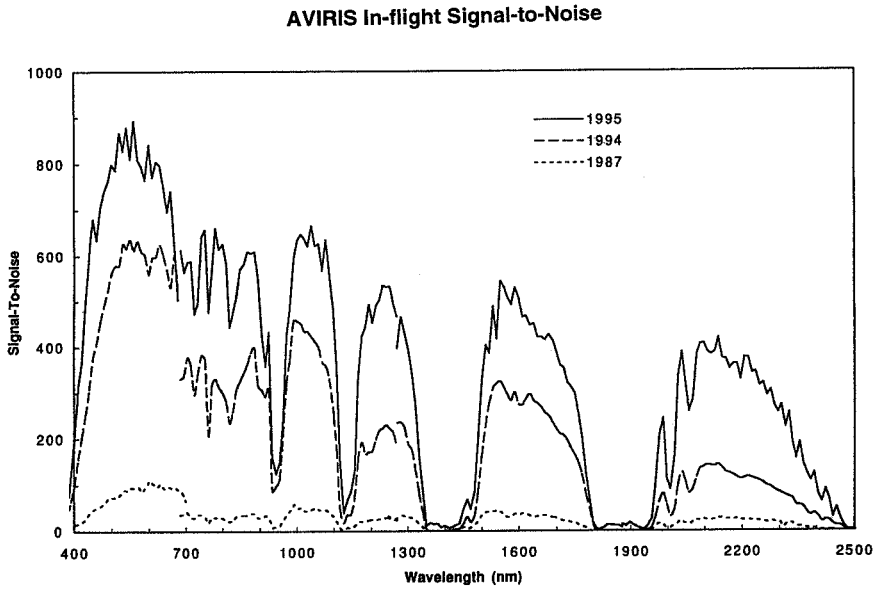

Figure 12. AVIRIS signal-to-noise for the 1995 in-flight calibration experiment.

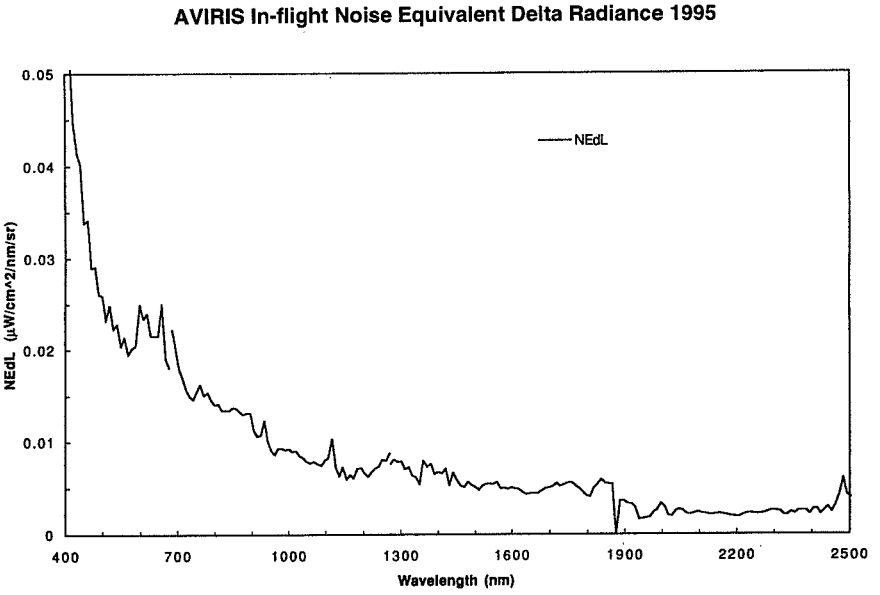

Figure 13. AVIRIS noise-equivalent-delta-radiance for 1995.

Additional analysis was performed to investigate the homogeneity of Ivanpah Playa at the AVIRIS spatial resolution. An image was produced of the ratio of the average to the standard deviation for all 10 by 10 spatial elements in the AVIRIS image. This image was produced from the sum of 20 AVIRIS channels in the visible band to suppress the influence of AVIRIS noise. The resulting image is shown in Figure 14. For 10 by 10 area at AVIRIS 20 by 20 m spatial resolution the homogeneity ranges from near zero to 500:1. At the calibration target, values of 100:1 are found. This analysis shows that relatively few in-situ measurements are required to characterize the surface of Ivanpah Playa. However, the surface is not homogeneous enough to estimate the signal-to-noise of AVIRIS which is greater than 1000:1 in portions of the spectrum.

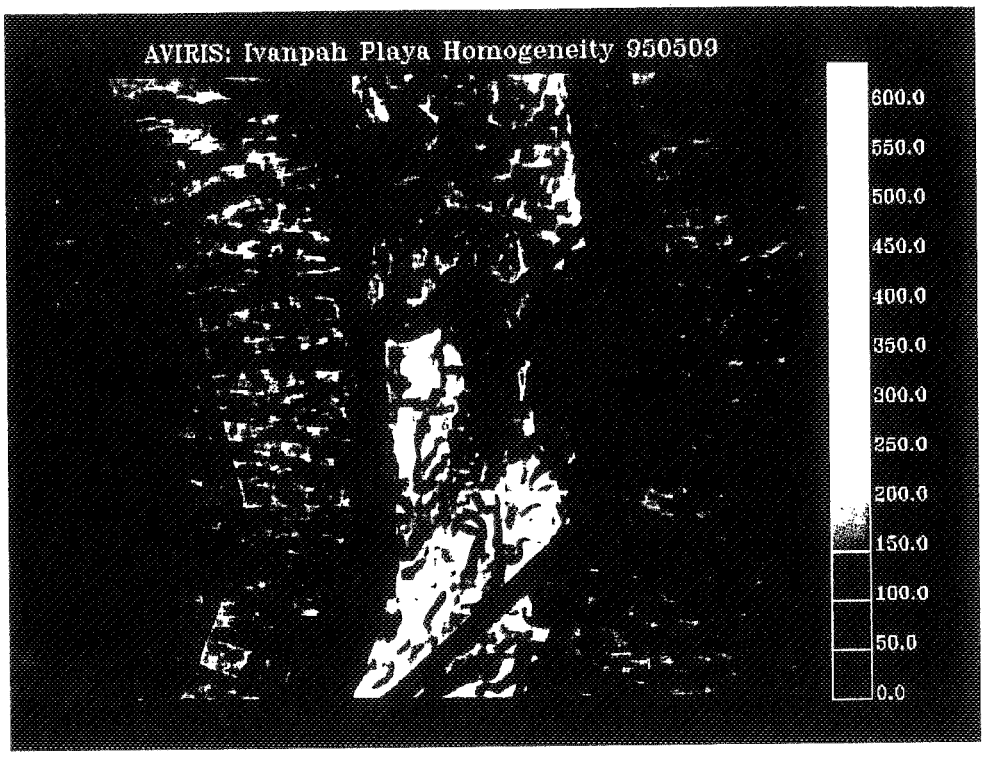

Figure 14. Ivanpah Playa homogeneity map May 9, 1995.

CONCLUSION

An in-flight calibration experiment was held at Ivanpah Playa on May 9, 1995. Concurrent in-situ and AVIRIS measurements were acquired for a calibration target on the homogeneous playa surface. The MODTRAN3 radiative transfer code was constrained by the in-situ measurements to predict the total upwelling spectral radiance incident at AVIRIS. This prediction was compared with the AVIRIS measured (calibrated based on the laboratory and on-board calibrator coefficients) spectrum from the calibration target. A comparison showed 96.5 % agreement with the remaining 3.5 % attributed to the in-situ measurements, MODTRAN3, AVIRIS and the calibration standards. The in-flight precision of AVIRIS was assessed. Across the spectral range the AVIRIS precision was more than double that of any previous year. This experiment validates the calibration of AVIRIS in flight in 1995. The level of calibration and precision achieved supports use of AVIRIS for scientific research and applications that are based

on the absorption and scattering characteristics of the atmosphere and surface expressed in the spectra.

REFERENCES

Anderson, G. P., J. Wang, and J. H. Chetwynd (1995), "MODTRAN3: An update and recent validations against airborne high resolution interferometer measurements", *Summaries of the Fifth Annual JPL Airborne Earth Science Workshop, JPL Publication 95-1, Vol. 1, pp. 5-8, Jet Propulsion Laboratory, Pasadena, California, 1995.*

Berk, A., L. S. Bernstein, and D. C. Robertson, "MODTRAN: A moderate resolution model for LOWTRAN 7," Final report, GL-TR-0122, Air Force Geophys. Lab., Hanscom AFB, MA, 42 pp., 1989.

Bruegge, C. J., J. E. Conel, J. S. Margolis, R. O. Green, G. Toon, V. Carrere, R.G. Holm, and G. Hoover, In-situ atmospheric water-vapor retrieval in support of AVIRIS validation, *SPIE Vol. 1298, Imaging spectroscopy of the terrestrial environment, 1990.*

Chrien, T. G., R.O. Green, and M. Eastwood, Laboratory spectral and radiometric calibration of the Airborne Visible/Infrared Imaging Spectrometer (AVIRIS), *SPIE Vol. 1298, Imaging spectroscopy of the terrestrial environment,* 1990.

Chrien, T. G., R. O. Green, C. J. Chovit, M. L. Eastwood, and C. M. Sarture, Calibration of the Airborne Visible/Infrared Imaging Spectrometer in the Laboratory, *Summaries of the Sixth Annual JPL Airborne Earth Science Workshop, JPL Publication 96-4, Jet Propulsion Laboratory, Pasadena, California, 1996.*

Conel, J. E., R. O. Green, R. E. Alley, C. J. Bruegge, V. Carrere, J. S. Margolis, G. Vane, T. G. Chrien, P. N. Slater, S. F. Biggar, P. M. Teillet, R. D. Jackson and M. S. Moran, In-flight radiometric calibration of the Airborne Visible/Infrared Imaging Spectrometer (AVIRIS), *SPIE Vol. 924, Recent Advances In Sensors, Radiometry And Data Processing For Remote Sensing,* 1988.

Green, R. O., G. Vane, and J. E. Conel, "Determination of in-flight AVIRIS spectral, radiometric, spatial and signal-to-noise characteristics using atmospheric and surface measurements from the vicinity of the rare-earth-bearing carbonatite at Mountain Pass, California", Proceedings of the Airborne Visible/Infrared Imaging Spectrometer (AVIRIS) Performance Evaluation Workshop, *JPL Publication 88-38, pp. 162-184, Jet Propulsion Laboratory, Pasadena, California, 1988.*

Green, R. O., J. E. Conel, V. Carrere, C. J. Bruegge, J. S. Margolis, M. Rast, and G. Hoover, "In-flight Validation and Calibration of the Spectral and Radiometric Characteristics of the Airborne Visible/Infrared Imaging Spectrometer (AVIRIS)," *Proc. SPIE Conference on Aerospace Sensing, Imaging Spectroscopy of the Terrestrial Environment, Orlando, Florida, 16-20* , April 1990.

Green, R. O., J. E. Conel, C. J. Bruegge, J. S. Margolis, V. Carrere, G. Vane and G. Hoover, "In-flight Calibration of the Spectral and Radiometric Characteristics of AVIRIS in 1991," *Summaries of the Third Annual JPL Airborne Geoscience Workshop, JPL Publication 92-14, Vol. 1., pp. 1-4, Jet Propulsion Laboratory, Pasadena, CA, 1992a.*

Green, R. O. and B. C. Gao, "A Proposed Update to the Solar Irradiance Spectrum Used in LOWTRAN and MODTRAN," *Summaries of the Fourth Annual JPL Airborne Geoscience Workshop, JPL 93-26, Vol. 1, pp. 81-84, Jet Propulsion Laboratory, Pasadena, California, 1993.*

Green, R. O., Larson, S. and Novack, H. I., "Calibration of AVIRIS Digitized Data", *Proc. Third Airborne Visible/Infrared Imaging Spectrometer (AVIRIS) Workshop, JPL Publication 91-28, pp. 109-118, Jet Propulsion Laboratory, Pasadena, California, 1991.*

Green, R. O., "Use of Data from the AVIRIS Onboard Calibrator", *Summaries of the Fourth Annual JPL Airborne Geoscience Workshop, JPL Publication 93-26, Vol. 1, pp. 65-68, Jet Propulsion Laboratory, Pasadena, California, 1993.*

Reagan, J. A., K. Thome, B. Herman, and R. Gall, Water vapor measurements in the 0.94 micron absorption band: calibration, measurements and data applications, *Proc. IGARSS, Ann Arbor, pp. 18-21, May 1987.*

ACKNOWLEDGMENTS

The majority of this research was carried out at the Jet Propulsion Laboratory, California Institute of Technology, under contract with the National Aeronautics and Space Administration. A portion of the work was performed at the Institute for Computational Earth System Science, University of California, Santa Barbara, California. We would like to express our appreciation for the efforts of the AVIRIS Team at the Jet Propulsion Laboratory, Pasadena, California.

Retrieval of Surface Snow Grain Size and Melt Water from AVIRIS Spectra

Robert O. Green[1,2] and Jeff Dozier[2]

[1]Jet Propulsion Laboratory, California Institute of Technology, Pasadena, CA 91109

[2]University of California, Santa Barbara, CA 93106

ABSTRACT

The Earth's energy balance and hydrology are affected by the distribution and characteristics of snow cover on the surface. Snow grain size and snow melt influence surface albedo and hydrology. A model of snow reflectance that depends on both grain size and surface melt water was developed to derive these parameters from remote spectral measurements. This reflectance model is based on a discrete ordinate radiative transfer approach that uses Mie calculations of snow optical properties, which are based on the complex refractive index of ice and water. This snow model was linked to an atmospheric radiative transfer code and a nonlinear least squares fitting algorithm. The resulting combined algorithm was applied to an AVIRIS snow data set acquired over Mammoth Mountain, California. Maps of grain size and surface snow melt were generated that are consistent with the expected ranges and distributions for conditions at the site.

INTRODUCTION

Snow is an important component of the Earth system with influences on the Earth's energy balance and hydrology. The high albedo of snow affects the amount of solar radiation reflected from the surface to space. The storage and release of water by snow are essential components of the hydrologic cycle in many regions. Snow occurrence and snow properties are variable over space and through time, in the mid and high latitudes of the Earth. The spatial and temporal variability of snow, coupled with the importance to the Earth's energy balance and hydrology, justifies pursuit of new measurements and algorithms for the remote derivation of snow parameters.

Two important properties of snow are grain size and snow melt. The albedo of snow is a function of grain size and the release of liquid water from snow, which occurs through melting. The reflectance of snow in the solar reflected spectrum was shown to be sensitive to grain size (Wiscombe and Warren, 1980; Dozier, 1987). This sensitivity was used with spectra acquired by the Airborne Visible/Infrared Imaging Spectrometer (AVIRIS) to estimate grain size remotely (Nolin and Dozier, 1993). AVIRIS spectra are measured from 400 to 2500 nm at 10-nm intervals and are acquired as images of 11 km up to 100 km with 20-m by 20-m spatial resolution. More recently, the presence of liquid water in melting snow was shown to be expressed in the reflectance spectrum (Green and Dozier, 1995). This paper presents a new algorithm and results showing the simultaneous derivation of grain size and snow melt water from calibrated AVIRIS spectra.

MEASUREMENTS

AVIRIS data were acquired over Mammoth Mountain, in east central California on May 21, 1994, at 18:35 UTC (Figure 1). The air temperature at the site at 2926 m was measured at 15-minute intervals during the day preceding the AVIRIS data acquisition. At this location the air temperature remained above freezing; on the night of May 20, it rose to 6°C by the time of

the overflight on May 21. These temperature conditions are consistent with snow melt water at the surface over portions of Mammoth Mountain when the AVIRIS data were acquired.

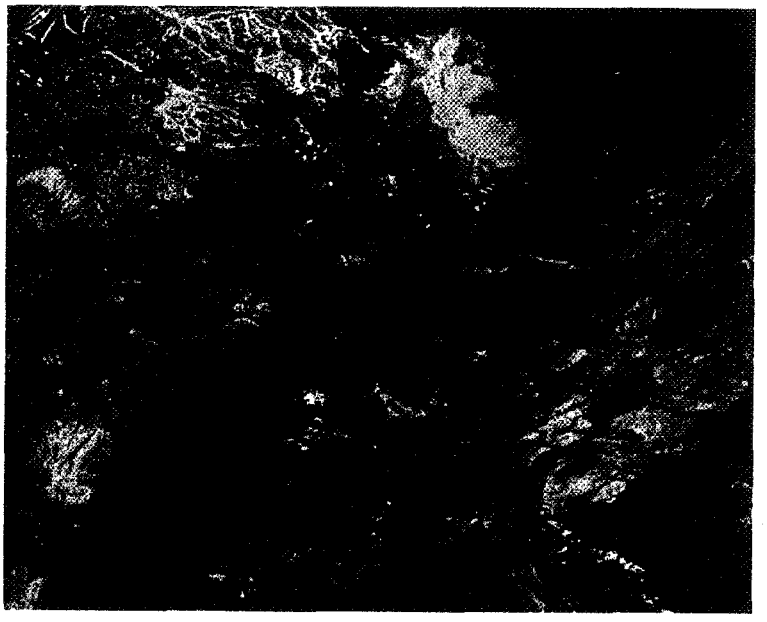

Figure 1. AVIRIS image of Mammoth Mountain, CA, acquired on May 21, 1994.

MODELS

Snow reflectance is modeled as a function of grain size and liquid water based on the inherent optical properties of ice and liquid water. The real and imaginary components of the complex refractive index for ice and water (Warren 1982) are shown in Figures 2 and 3.

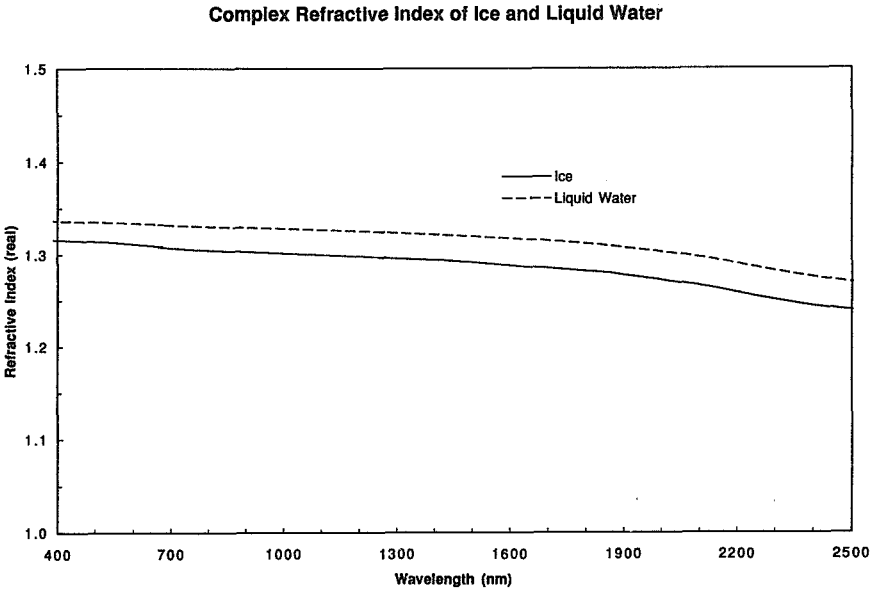

Figure 2. Real components of the complex refractive index of ice and liquid water.

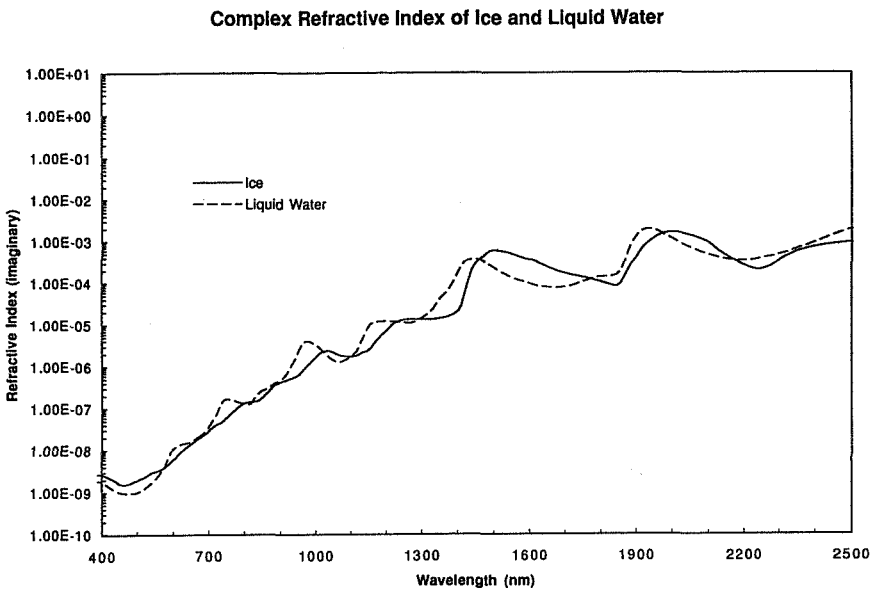

Figure 3. Imaginary components of the complex refractive index of ice and liquid water.

The refractive indices were used to model snow reflectance as a mixture of ice and liquid water spheres. This approach allows the use of Mie (Wiscombe, 1980) calculations for the single-scattering-albedo and scattering phase functions for different grain sizes and liquid water amounts. Figure 4 shows these parameters for 500-μm grain-size snow with 0.0 and 25.0 % liquid water of total water by volume. The presence of the liquid water decreases and shifts the regions of spectral absorption towards shorter wavelengths.

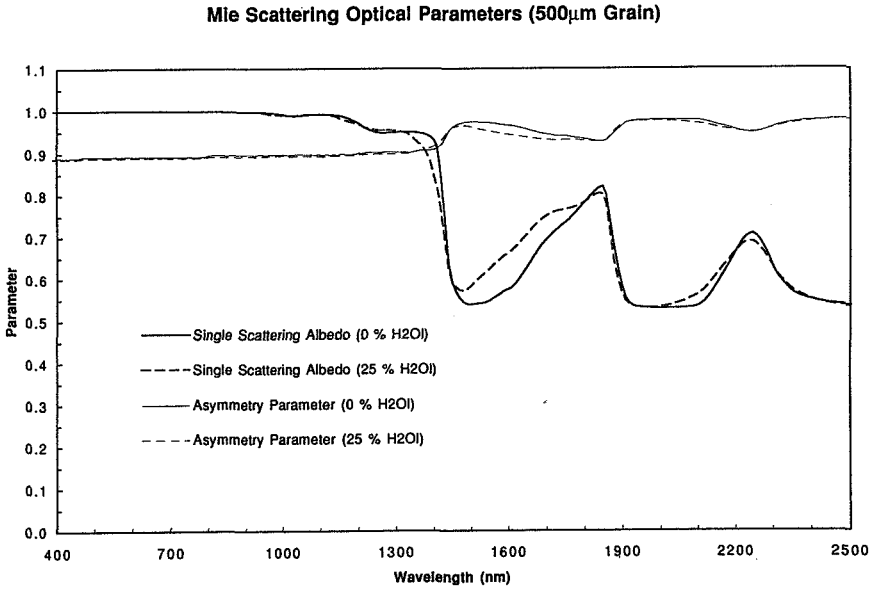

Figure 4. The single-scattering-albedo and asymmetry parameter from Mie calculations for 500-μm grain-size snow with 0.0 and 25.0 % liquid water.

These Mie parameters were used to constrain a discrete ordinate radiative transfer code, DISORT (Stamnes et al., 1988), and model the directional-hemispherical reflectance of snow. A semi-infinite snow thickness was adopted. The solar illumination angle was 19.3°, the same as that at the time of AVIRIS data acquisition. Modeled reflectance for 500-μm grain size with 0.0 and 25.0 % liquid water is shown in Figure 5. The presence of liquid water modifies the regions of absorption in the modeled reflectance. This effect is strongly apparent near the 1030-nm ice absorption where the reflectance of the snow is high.

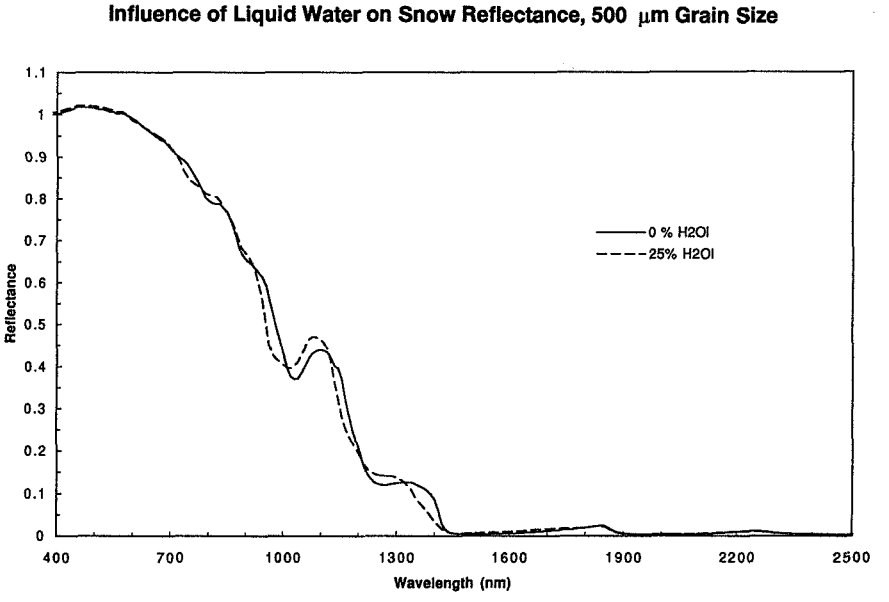

Figure 5. Directional-hemispherical DISORT modeled snow reflectance for 500-μm grain-size snow with 0.0 and 25.0 % liquid water.

To derive the snow grain size and liquid water of snow melt from AVIRIS data, the MODTRAN3 (Kneizys et al., 1988) radiative transfer code was linked to the snow reflectance model to allow compensation for the atmosphere (e.g., water vapor). The combined surface and atmosphere model was integrated with the simplex nonlinear least squares fitting algorithm (Press, 1986).

ANALYSIS AND RESULTS

The resulting combined snow parameter algorithm was applied to every spectrum in the AVIRIS Mammoth Mountain data set. A spectral range from 8500 to 1100 was used in the fit, based on the expressed dependence of the reflectance on grain size and melt water in this region. A spectral fit result at low elevation and high elevation on the Mammoth Mountain are given in Figures 6 and 7, respectively. At low elevation, a grain size of 900 μm and melt water of 15.9 % are required. For the high elevation case, a grain size of 230 μm and melt water of 2.1% are derived. Figures 8 and 9 show the grain size and snow melt maps for the entire image. Over the full data set, the distribution of grain size ranges from 1000 to 100 μm from the lower mountain to the summit. Melt water ranges from 16 to 2 % for homogeneous snow regions from the lower mountain to the summit. Snow melt water values are anomalously high in regions where vegetation occurs on the mountain. The expression of liquid water in the leaves of the vegetation results in overestimates of the melt water in snow.

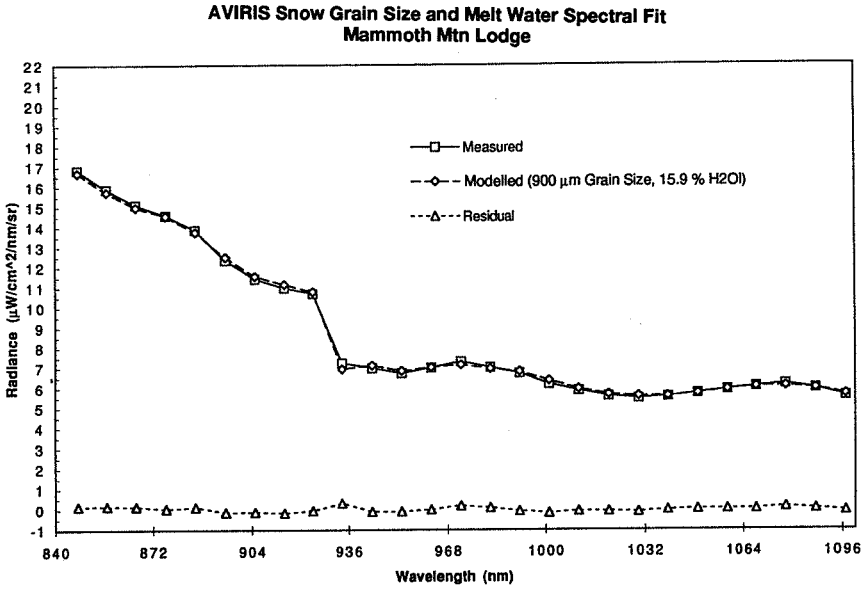

Figure 6. Snow grain size and melt water spectral fit. This result is from a homogeneous snow area low on the mountain. A large grain size and high melt water content are required for the fit.

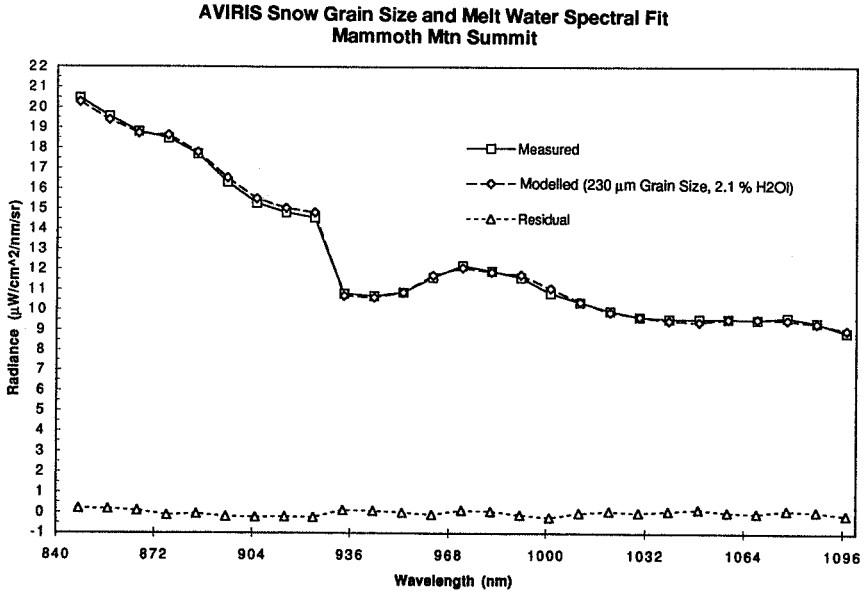

Figure 7. Spectral fit from high on Mammoth Mountain. A small grain size and low melt water content are produced from the algorithm.

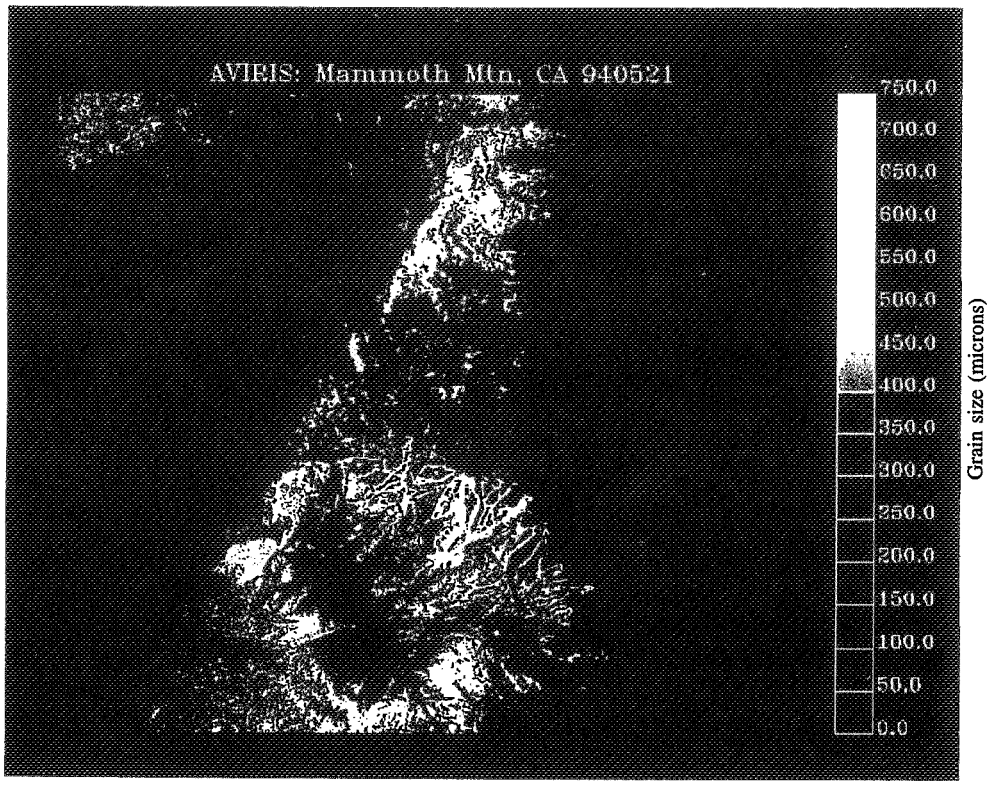

Figure 8. Image result of grain-size distribution for the AVIRIS Mammoth Mountain data set.

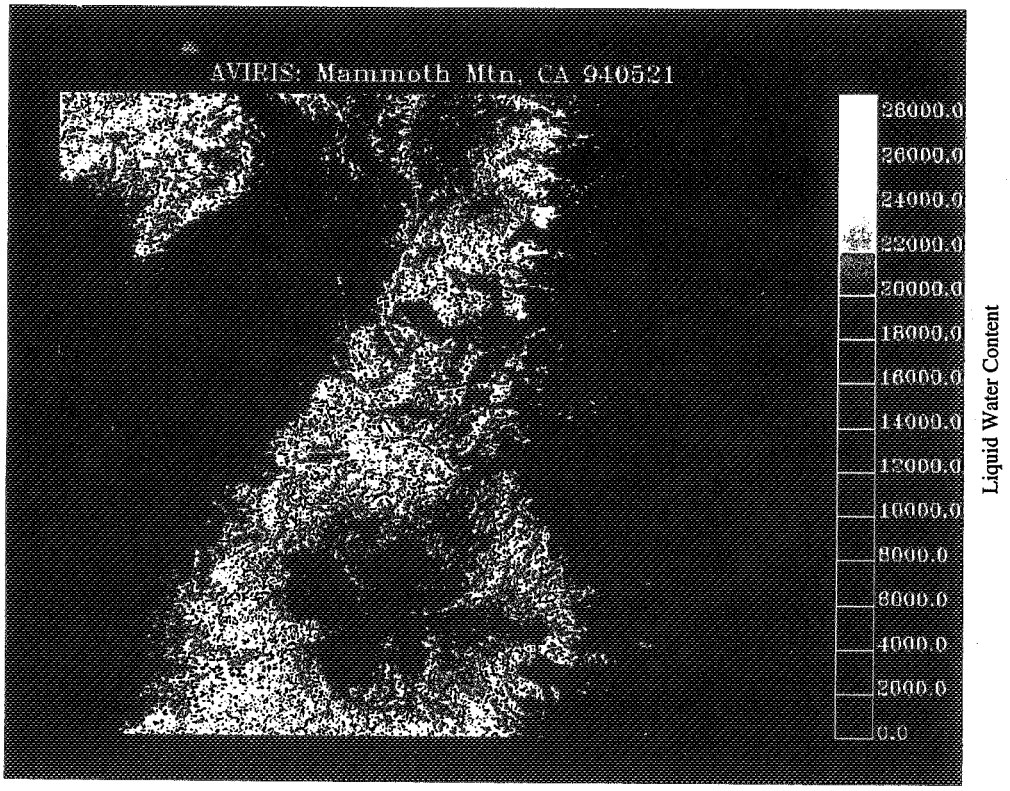

Figure 9. Snow surface melt water distribution from AVIRIS data set. Anomalously high melt water is derived in areas where vegetation and leaf water are present with snow.

CONCLUSION

The optical properties of ice and water were used to develop a model of snow reflectance based on grain size and surface melt water. This model was linked with the MODTRAN3 atmospheric radiative transfer code and a nonlinear, least squares fitting algorithm. The resulting integrated snow grain size and surface melt water algorithm was applied to an AVIRIS data set acquired over Mammoth Mountain, California. Derived grain size and melt water distribution were consistent with the range of elevations and temperatures for the data set. Anomalous estimates of melt water were observed when vegetation leaf water was present with the snow. This methodology and algorithm demonstrate a basis for derivation of the snow parameters of grain size and surface melting from remote measurements. Derivation of snow parameters remotely is essential to detect, measure, and monitor snow in the Earth system through space and time.

FUTURE WORK

Results of snow grain size and surface melt will be validated with available in situ measurements for these and other data sets. The model will be augmented to account for and compensate for the presence of vegetation with the snow. An alternate approach to modeling liquid water in snow as liquid water coated spheres of ice will be developed and evaluated with respect to this model. Sensitivities to the bi-directional distribution function of snow and the dependence on grain size and melt water will be investigated.

ACKNOWLEDGMENTS

The majority of this research was carried out at the Jet Propulsion Laboratory, California Institute of Technology, under contract with the National Aeronautics and Space Administration. A portion of the work was performed at the Institute for Computational Earth System Science, University of California, Santa Barbara, CA.

REFERENCES

Dozier, J. (1987), "Spectral Signature Of Alpine Snow Cover From The Landsat Thematic Mapper," *Remote Sens. Environ.* 28:9-22.

Green, R.O., and Dozier, J. (1995), "Measurement Of The Spectral Absorption Of Liquid Water In Melting Snow With An Imaging Spectrometer," *Summaries of the Fifth Annual JPL Airborne Earth Science Workshop, JPL Publication 95-1, Jet Propulsion Laboratory, Pasadena, CA, Vol. 1*, 91-94.

Kneizys, F.X., Shettle, E. P., Abreu, L. W. (1988), *"User's Guide* to LOWTRAN7," Rep. AFGL-TR-88-0177, Air Force Geophys. Laboratory, Bedford, MA.

Nolin, A.W., and Dozier, J. (1993), "Estimating Snow Grain Size Using AVIRIS Data," *Remote Sens. Environ.* 44:231-238.

Press, W.H., ***Numerical Recipes: The Art of Scientific Computing***, Cambridge University Press, Cambridge, 1986.

Stamnes, K., Tsay, S., Wiscombe, W., and Jayaweera, K. (1988), "Numerically Stable Algorithm For Discrete-Ordinate-Method Radiative Transfer In Multiple Scattering And Emitting Layered Media," *Appl. Opt.* 27:2502-2509.

Warren, S.G. (1982), "Optical Properties Of Snow," *Rev. Geophys. Space Phys.* 20:67-89.

Wiscombe, W. J., and Warren, S.G. (1980), "A Model For The Spectra Albedo Of Snow I. Pure Snow," *J. Atmos. Sci.* 37: 2712-2733.

Wiscombe, W. J. (1980), "Improved Mie Scattering Algorithms," *Applied Optics* 19: 1505-1509.

Characterization and Compensation of the Atmosphere for the Inversion of AVIRIS Calibrated Radiance to Apparent Surface Reflectance

Robert O. Green[1, 2], Dar A. Roberts[2] and James E. Conel[1]

[1]Jet Propulsion Laboratory, California Institute of Technology, Pasadena, CA 91109
[2]University of California, Santa Barbara, CA 93106

ABSTRACT

Calibrated radiance spectra measured remotely record the integrated effects of the solar source, the atmosphere, and the surface. To pursue scientific research and applications, based on the molecular absorptions and constituent scattering properties of the surface, the solar source and atmosphere must be characterized and compensated in the spectra. This paper describes a set of radiative transfer spectral fitting algorithms that characterize the absorbing and scattering constituents of the atmosphere from calibrated AVIRIS spectra. These atmospheric characteristics were used in conjunction with the illumination and observation geometries to invert the AVIRIS calibrated radiance spectra to apparent surface reflectance. A validation of the algorithm was performed with in-situ reflectance spectra acquired at the time of the AVIRIS overflight over Pasadena, California, in 1994.

INTRODUCTION

Remotely measured data from satellites and aircraft are essential to support the measurement and monitoring of Earth surface processes over a range of spatial and temporal scales. In the solar reflected portion of the spectrum, the data acquired at the sensor are a record of the integrated effects of the solar source, the atmosphere, and the surface. A set of algorithms was developed to characterize and compensate for the atmospheric effects in the calibrated spectra acquired by AVIRIS. AVIRIS measures the solar reflected spectrum from 400 nm to 2500 nm at 10-nm intervals from 20 km altitude in the Q-bay of a NASA ER-2 aircraft. These spectra are acquired as images of 11 km by up to 100 km with 20-m by 20-m spatial resolution. AVIRIS is calibrated in the laboratory and the calibration is validated in flight (Conel et al., 1988; Green et al., 1988; Green, 1990; Green et al., 1993; Green and Conel, 1995).

Algorithms were developed to characterize the water vapor, well-mixed gases, molecular scattering, and aerosol scattering from calibrated spectra acquired by AVIRIS. The atmospheric characteristics were used to invert the AVIRIS measured radiance to apparent surface reflectance. These algorithms rely on the atmospheric models of the MODTRAN3 radiative transfer code (Kneizys et al., 1987; Berk et al., 1989; Anderson et al., 1995). MODTRAN3 was used in conjunction with the downhill simplex nonlinear spectral fitting algorithm (Press 1986) to invert for the atmosphere characteristics. The comparison of MODTRAN3 and AVIRIS spectra from the 1994 in-flight calibration experiment was used to link the calibration of AVIRIS to that of MODTRAN3. This paper describes the application and validation of these algorithms to an AVIRIS data set acquired over Pasadena, California.

MEASUREMENTS

AVIRIS acquired a data set of the total spectral upwelling radiance over the Pasadena, California, region at 18.55 UTC on April 11, 1994. The latitude and longitude of the Rose Bowl contained in the data set is 34.16° latitude and -118.33° longitude. Figure 1 shows a single wavelength image from the AVIRIS data set. The Jet Propulsion Laboratory is in the center left of the image and the Rose Bowl is located at the lower left. Mount Wilson is located at the

upper center of the image. An AVIRIS radiance spectrum from the Rose Bowl parking lot and adjacent grass field is shown in Figure 2. At the time of the AVIRIS overflight, surface spectra's reflectance measurements were acquired in the Rose Bowl parking lot and adjacent grass field. These are shown in Figure 3. Comparison of the AVIRIS measured radiance and in-situ reflectance measurement shows the effect of the solar source and atmosphere in the total upwelling spectral radiance measured by AVIRIS.

Figure 1. April 11, 1994, AVIRIS image of Pasadena, California.

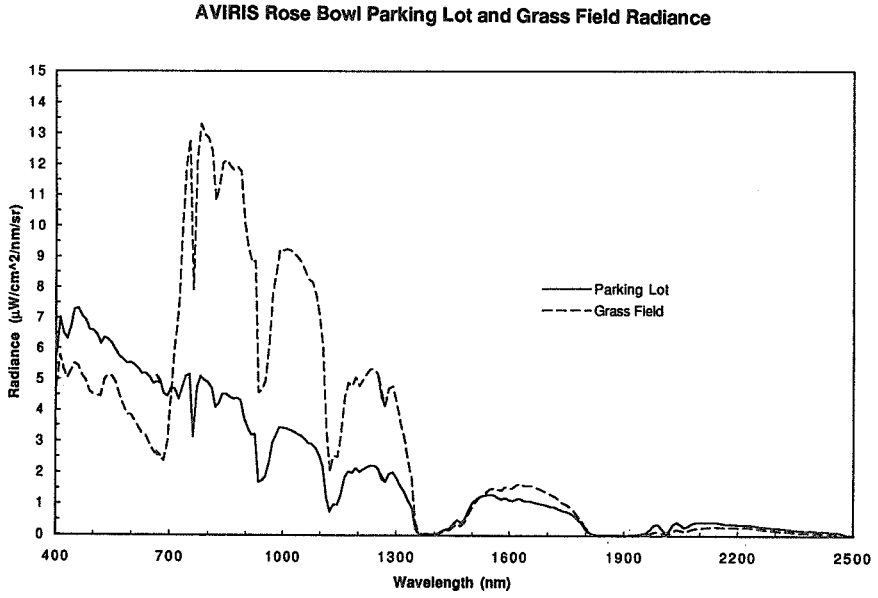

Figure 2. AVIRIS spectra of the total upwelling radiance for the Rose Bowl parking lot and adjacent grass field.

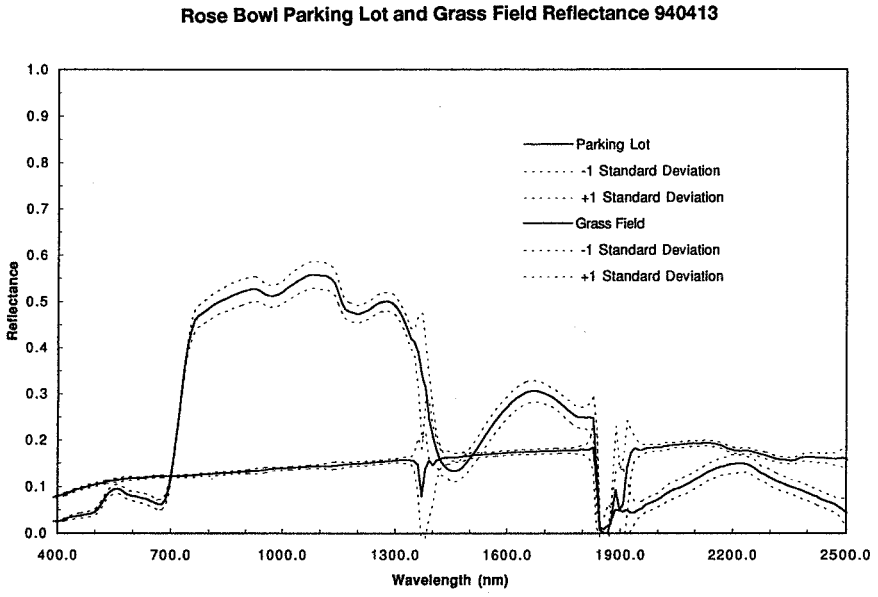

Figure 3. In-situ measured surface reflectance at the Rose Bowl at the time of the AVIRIS overflight.

ANALYSIS

AVIRIS calibration

In 1994 the AVIRIS in-flight calibration experiment (Green and Conel, 1995), a comparison of MODTRAN3 predicted radiance and AVIRIS measured radiance showed AVIRIS calibrated better than 95%. However, in detail, the residual 5% disagreement is spectrally featureful as shown in Figure 4. These spectral differences were attributed to errors in the MODTRAN3 model of the atmosphere. The ratio of AVIRIS to MODTRAN3 was used as an additional calibration factor to compensate for these errors. In addition, the AVIRIS sensor performance changed slightly from the time of the calibration experiment to the time of the Pasadena data acquisition. This variation in performance is shown in Figure 5 and was used to calibrate AVIRIS performance to that of the in-flight calibration experiment.

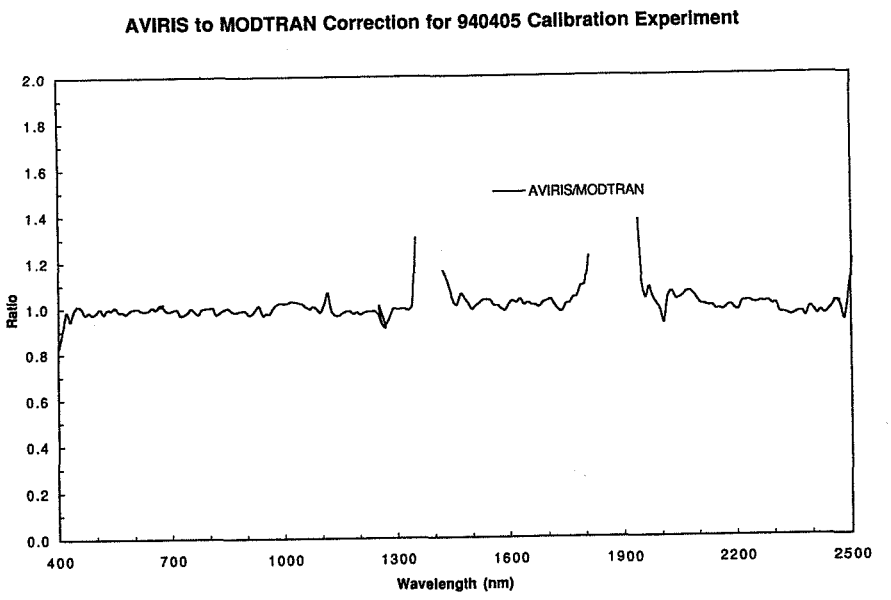

Figure 4. Calibration ratio between AVIRIS and MODTRAN3 derived from the in-flight calibration experiment on April 4, 1994.

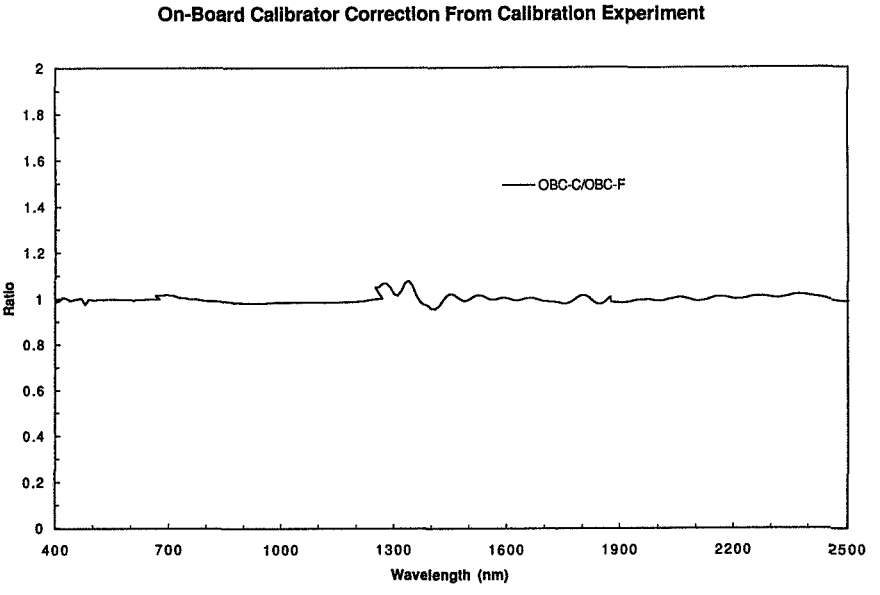

Figure 5. Calibration ratio of the onboard calibrator signal for the Pasadena flight to the signal for the in-flight calibration experiment.

Surface Pressure Height

The radiance measured by AVIRIS is affected by the absorption and scattering due to the well-mixed gases of the atmosphere (e.g., carbon dioxide and oxygen). To characterize the well-mixed atmospheric gases and the effect of atmospheric molecular scattering, an algorithm was developed to estimate the surface pressure elevation from the AVIRIS measured radiance. This algorithm assesses the strength of the 760-nm oxygen absorption band measured in the AVIRIS spectrum (Green et al., 1991; Green et al., 1993). The oxygen-band strength is calibrated to

surface pressure elevation using the oxygen-band model in the MODTRAN3 radiative transfer code. Figure 6 shows the AVIRIS-derived image of surface pressure height for the Pasadena data set. Pressure heights range from 50 to 1900 m and correspond generally to the topographic elevation. The sensitivity of AVIRIS to the oxygen pressure height is moderate. To enhance the AVIRIS precision, a 5-by-5 spatial-sample average was used. The resulting precision is estimated at 200 m.

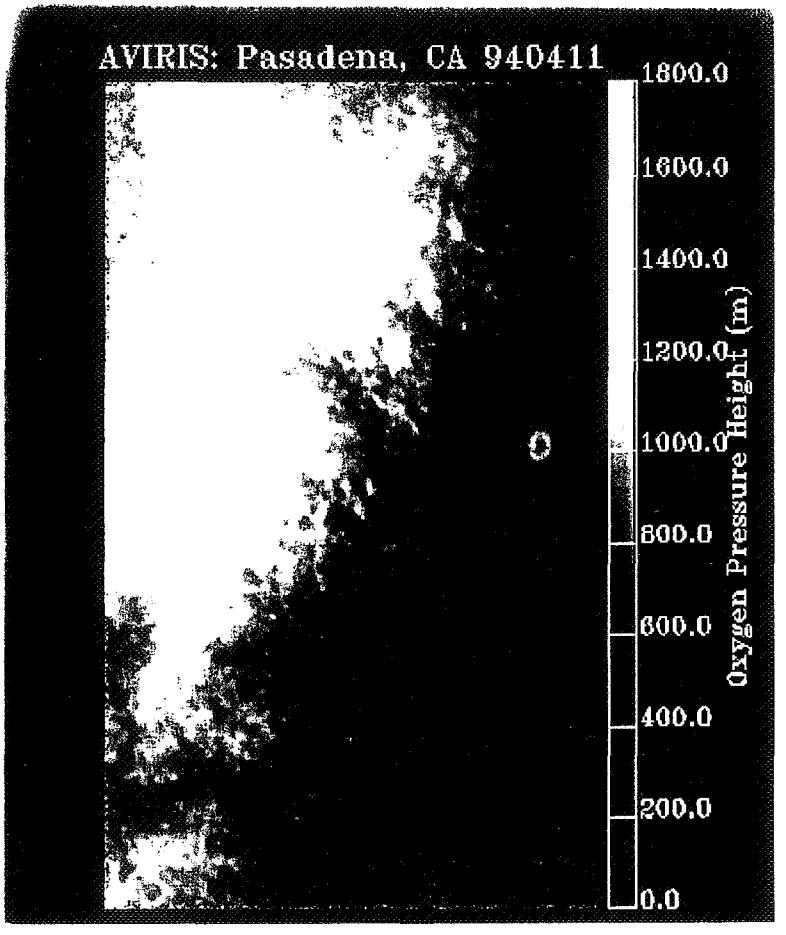

Figure 6. AVIRIS-derived surface pressure height for Pasadena data set.

Aerosol Optical Depth

The spectral radiance incident at AVIRIS is affected by scattering in the atmosphere due to aerosols. The effect of aerosol scattering is strong in the 400-nm to 700-nm region and increases towards shorter wavelengths. A nonlinear least-squares spectral fitting algorithm was developed to estimate the aerosol optical depth directly from the AVIRIS measured radiance. This algorithm optimizes the fit between the AVIRIS radiance and a MODTRAN3 modeled radiance with the aerosol optical depth as the primary fitting parameter. A MODTRAN3 model atmosphere must be initially selected. Parameters describing the reflectance magnitude, reflectance spectral slope, and the leaf chlorophyll absorption were included. Surface pressure height is used as a constraint. The algorithm was applied to the Pasadena AVIRIS data set using the MODTRAN3 urban atmospheric model. Figure 7 shows the spectral fit and derived aerosol scattering presented as visibility in km for the Rose Bowl parking lot. Figure 8 shows the aerosol visibility for the AVIRIS Pasadena data set. To improve the uniformity of the estimated

aerosol effect, the data were averaged over 11-by-11 spatial elements. Derived visibility ranged from 40 km to 140 km. The trend of greater visibility at high elevations and less visibility at lower elevations is consistent with the expected distribution of aerosols in the Pasadena region.

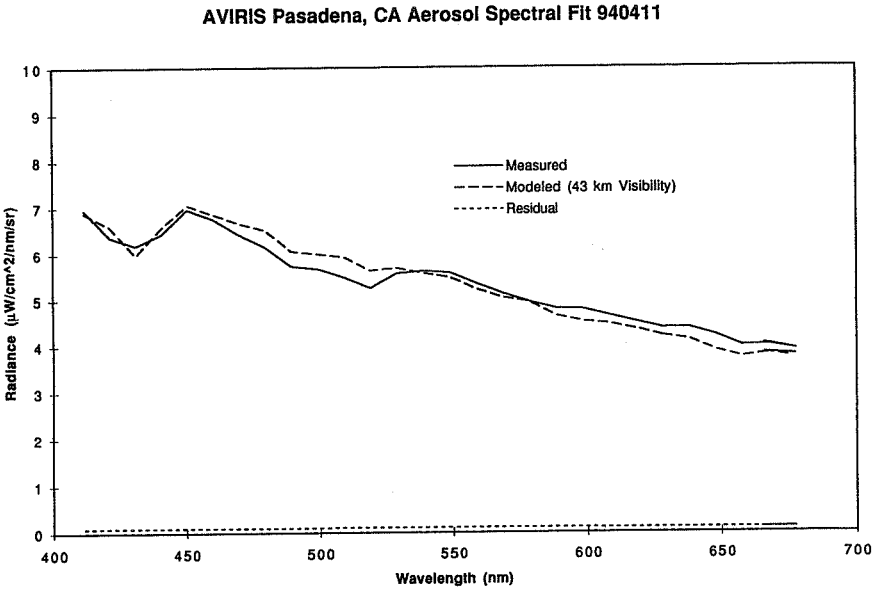

Figure 7. Spectral fit for aerosols at the Rose Bowl parking lot.

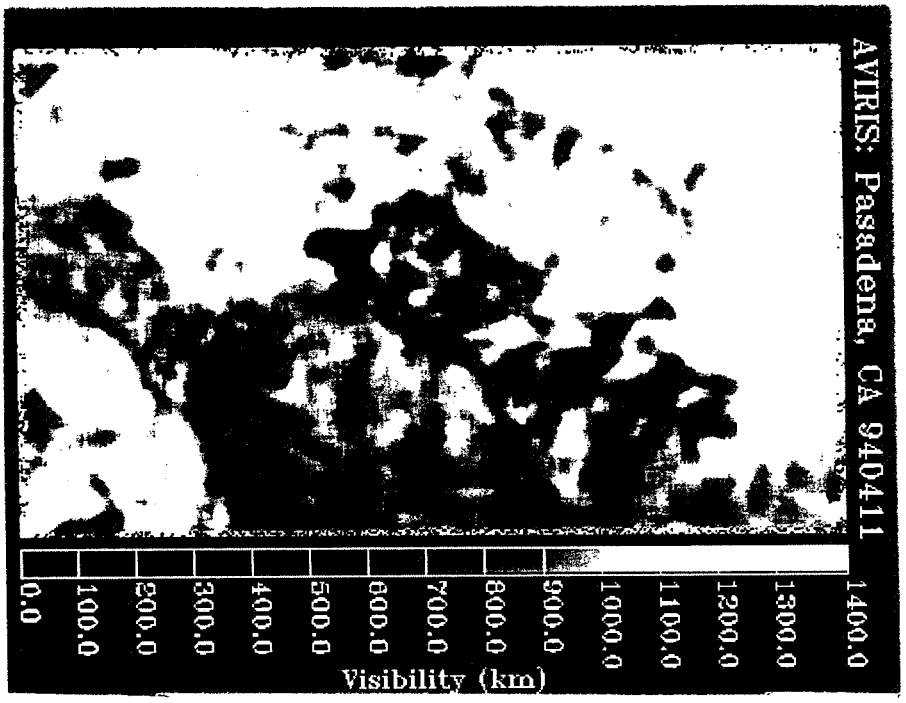

Figure 8. Image of derived aerosol expressed visibility for the MODTRAN3 urban aerosol atmospheric model.

Water Vapor

Across the AVIRIS spectral range, the strongest atmospheric absorber is water vapor. The effect on the upwelling radiance arriving at AVIRIS is shown in Figure 9 as the atmosphere varies from 0 to more than 36.5 precipitable mm of water vapor. In addition to absorbing strongly, water vapor in the terrestrial atmosphere varies both spatially and temporally (Green et al., 1991, Green and Conel, 1995).

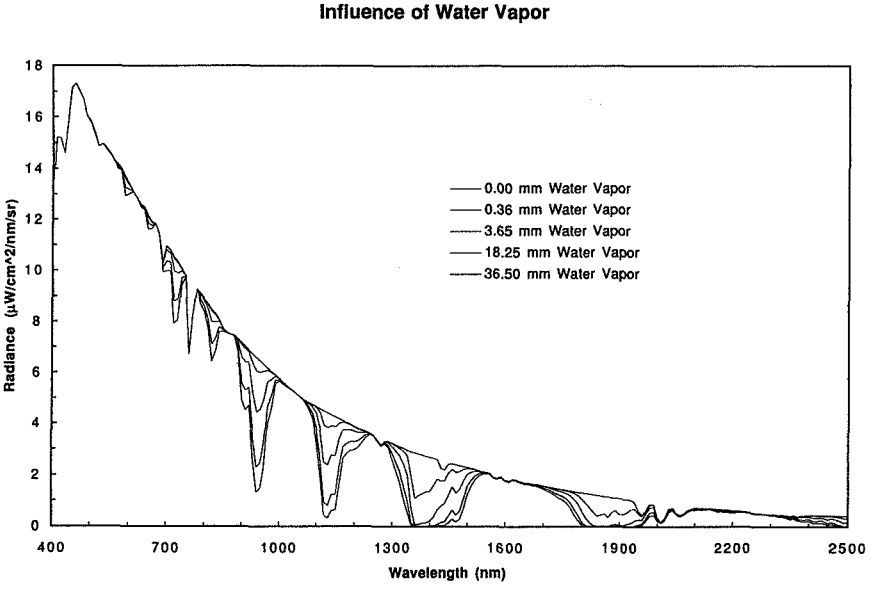

Figure 9. Influence of water vapor on the upwelling spectral radiance measured by AVIRIS.

To compensate for water vapor absorption in AVIRIS spectra, a determination of total path water vapor is required for each spatial element. Water vapor algorithms for AVIRIS have been developed (Conel et al., 1988; Green, 1991; Green and Conel, 1995) based initially on the LOWTRAN (Kneizys et al., 1987) and currently on the MODTRAN3 (Berk et al., 1989, Anderson et al., 1995) radiative transfer code. Alternate approaches for characterization of the atmospheric water vapor have been pursued (Gao and Goetz, 1990).

The water vapor algorithm used here fits the AVIRIS measured radiance for the 940-nm water band to a radiance spectrum MODTRAN3. In addition to a parameter controlling water vapor, the spectral fit includes a three-parameter surface reflectance model with leaf water. Inclusion of leaf-water absorption is essential to achieve good fits over vegetated surfaces. This algorithm was applied to the AVIRIS Pasadena data set. Figures 10 and 11 show the fits for the Rose Bowl and Mount Wilson spectra, respectively. Values of 9.87 and 3.42 mm were derived. The water vapor image for the entire data set is shown in Figure 12. Total column water vapor amounts were derived from 3.19-mm to 10.22-mm across the Pasadena image. The changes in the atmospheric path length due to elevation are strongly expressed in this result.

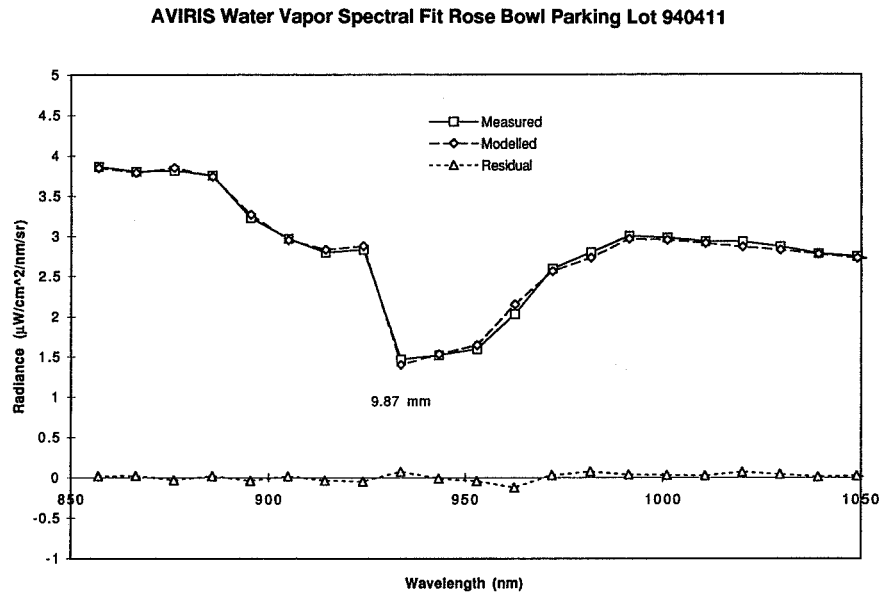

Figure 10. AVIRIS water vapor spectral fit for the Rose Bowl parking lot.

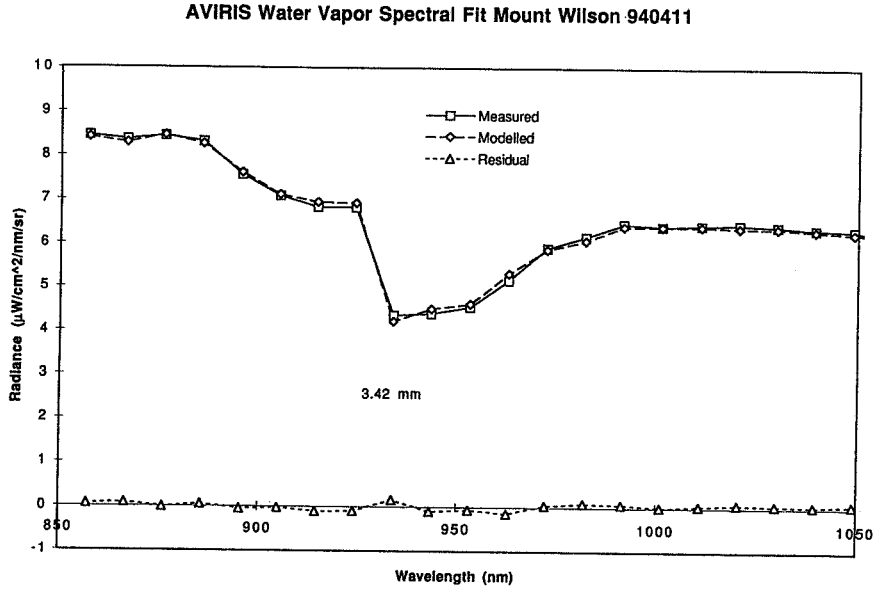

Figure 11. Water vapor spectral fit at Mount Wilson.

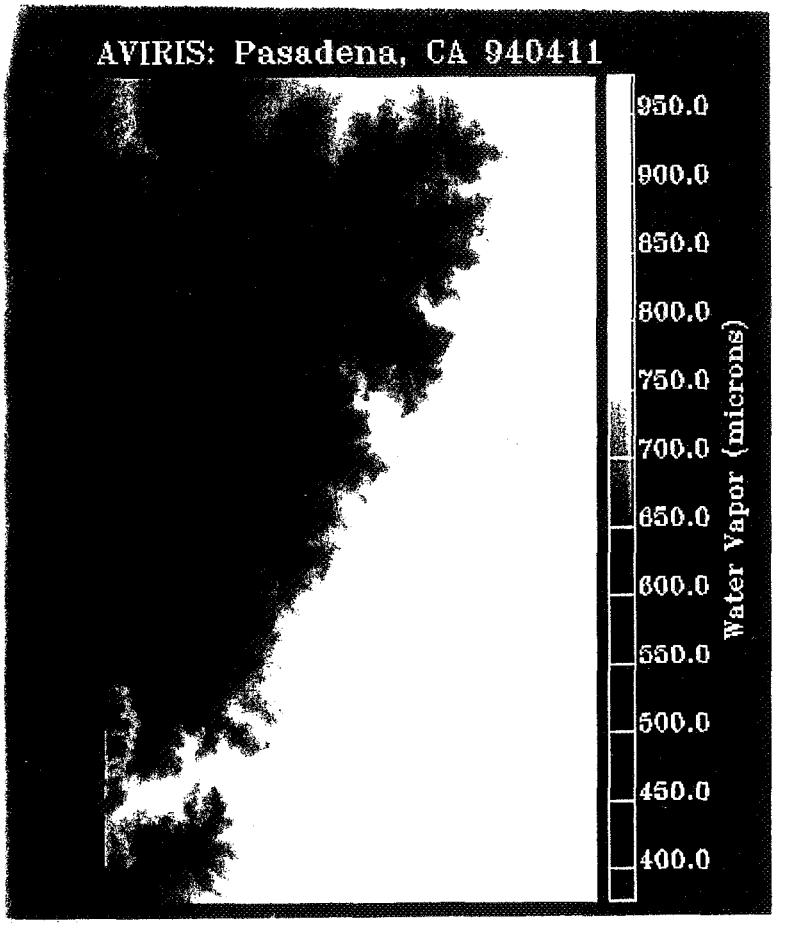

Figure 12. Water vapor image of Pasadena region from AVIRIS.

Radiance to Reflectance Inversion

Calculation of surface spectral reflectance from the total upwelling radiance measured by AVIRIS using a radiative transfer code has been pursued since the flights of AVIRIS in 1989 (Green, 1990, Green et al., 1991; Green et al., 1993). A related method for radiance-to-reflectance inversion (Gao et al. 1993) was pursued with AVIRIS data. In direct comparisons (Clark et al., 1995) the MODTRAN-based algorithm showed superior results.

The total upwelling spectral radiance at the top of the atmosphere in the observation direction may be expressed in terms of the solar illumination of a lambertian reflectance surface (Chandrasekhar, 1960). For a given illumination and observation geometry as well as atmospheric absorption and scattering characteristics, this relationship is given as:

$$L_t = F_0 r_a/p + F_0 T_d\, r_g T_u/p/(1-Sr_g) \qquad (1)$$

where L_t is the total upwelling spectral radiance at AVIRIS, F_0 is the exoatmospheric solar irradiance, r_a is the atmospheric reflectance, T_d is the downward direct and diffuse transmittance of the atmosphere, r_g is the apparent lambertion surface reflectance, T_u is the upward total atmospheric transmittance to the AVIRIS, and S is the albedo of the atmosphere above the surface.

This equation may be solved for r_g:

$$r_g = 1 / [\{(F_0 T_d T_u / p) / (L_t - F_0 r_a / p)\} + S] \qquad (2)$$

Using the water vapor, pressure elevation, and aerosol optical depth estimations derived in the algorithms described, the two-way transmitted radiance and atmospheric reflectance were calculated for each spatial element with MODTRAN3. A recent compilation of the exoatmospheric solar irradiance was used (Green and Gao, 1993). Computer look-up tables were used to accelerate MODTRAN3 calculations. With these determined parameters, the surface reflectance was calculated as shown in Equation 2. Figure 13 shows a comparison of the AVIRIS-derived reflectance for the Rose Bowl parking lot and adjacent grass field. The solar source and atmospheric effects present in the measured upwelling spectral radiance are compensated for with this algorithm. Also shown are in-situ reflectance measurements acquired for these surfaces 3 days after the AVIRIS flight. The effects of the average agreement between the derived and measured reflectance are 5.6 % and 9.4 % for the parking lot and grass field, respectively.

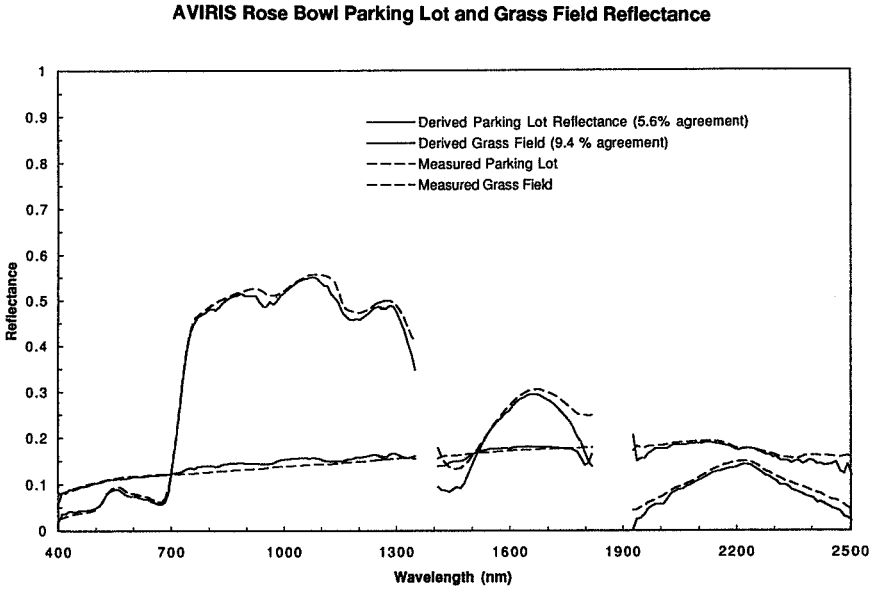

Figure 13. Inversion results for AVIRIS radiance to apparent surface reflectance for the Rose Bowl parking lot and adjacent grass field.

CONCLUSION

Algorithms were developed and used to characterize the surface pressure height, aerosol scattering, and atmospheric water vapor from calibrated AVIRIS spectra. The algorithms used in the MODTRAN3 radiative transfer code model of the atmospheric absorption and scattering are coupled with a nonlinear least-squares fitting algorithm. AVIRIS calibration was augmented to account for the current residual disagreement between AVIRIS and MODTRAN3 measured and modeled radiance based on an in-flight calibration experiment. These algorithms were applied to a data set acquired over Pasadena, California, on April 11, 1994. An equation relating the apparent surface reflectance to the total upwelling spectral radiance for a given atmosphere and illumination geometry was described. This equation was constrained by inputs of the derived

atmospheric absorption and scattering characteristics to MODTRAN3. Apparent surface reflectance was derived for the complete AVIRIS data set. Solar source and atmospheric effects were compensated in the derived apparent reflectance spectra. At the Rose Bowl parking lot and adjacent grass field, the derived apparent reflectance was compared with in-situ measurements. An agreement of 5.6 % and 9.4 % was shown, providing an end-to end validation of the algorithm. Physically based derivation of the apparent surface spectral reflectance from calibrated upwelling radiance using only the spectra themselves is essential for research and application that are based on absorption and scattering characteristics of the surface.

ACKNOWLEDGMENT

The majority of this research was carried out at the Jet Propulsion Laboratory, California Institute of Technology, under contract with the National Aeronautics and Space Administration. A portion of the work was performed at the Institute for Computational Earth System Science, University of California, Santa Barbara, CA.

REFERENCES

Anderson, G. P., J. Wang, and J. H. Chetwynd (1995), "MODTRAN3: An Update And Recent Validations Against Airborne High Resolution Interferometer Measurements," *Summaries of the Fifth Annual JPL Airborne Earth Science Workshop, Jet Propulsion Laboratory, Pasadena, CA, JPL 95-1, Vol. 1*, 5-8.

Berk, A., L. S. Bernstein, and D. C. Robertson, MODTRAN: A Moderate Resolution Model for LOWTRAN 7, *Final Report, GL-TR-0122, AFGL, Hanscom AFB, MA, 42 pp., 1989.*

Chandrasekhar, S., "Radiative Transfer," *Dover Press*, New York, 1960.

Clark, R. N., G. A. Swayze, K. Heidebrecht, R. O. Green, and A. F. H. Goetz, "Calibration to Surface Reflectance of Terrestrial Imaging Spectrometry Data: Comparison of Methods," *Summaries of the Fifth Annual JPL Airborne Earth Science Workshop, Jet Propulsion Laboratory, Pasadena, CA, JPL Pub. 95-1, Vol. 1, 1995.*

Conel, J. E., R. O. Green, R. E. Alley, C. J. Bruegge, V. Carrere, J. S. Margolis, G. Vane, T. G. Chrien, P. N. Slater, S. F. Biggar, P. M. Teillet, R. D. Jackson and M. S. Moran, In-flight Radiometric Calibration of the Airborne Visible/Infrared Imaging Spectrometer (AVIRIS), *SPIE Vol. 924, Recent Advances in Sensors, Radiometry and Data Processing for Remote Sensing, 1988.*

Gao, B. C., and Goetz, A. F. H., "Column Atmospheric Water-Vapor And Vegetation Liquid Water Retrievals From Airborne Imaging Spectrometer Data," *Journal Of Geophysical Research Atmospheres, Vol. 95, No. D4, 1990.*

Gao, B. C., Heidebrecht, K. B., Goetz, A. F. H., "Derivation Of Scaled Surface Reflectances From AVIRIS Data", *Remote Sensing Of Environment, Vol. 44, No. 2-3*, 1993.

Green, R. O., G. Vane, and J. E. Conel, "Determination of AVIRIS Spectral, Radiometric, Spatial and Signal-to-Noise characteristics Using atmospheric and surface measurements from the vicinity of the Rare-Earth-Bearing carbonatite at Mountain Pass, California," in the *Proceedings of the Airborne Visible/Infrared Imaging Spectrometer (AVIRIS) Performance Evaluation Workshop, JPL Pub. 88-38, Jet Propulsion Laboratory, Pasadena, CA, pp. 162-184, 1988.*

Green, R. O., Retrieval of Reflectance from Calibrated Radiance Imagery Measured by the Airborne Visible/Infrared Imaging Spectrometer (AVIRIS) for Lithological Mapping of the Clark Mountains, California, *Proc. Second AVIRIS Workshop, JPL Publication 90-54, Jet Propulsion Laboratory, Pasadena, CA, pp. 167-175, 1990.*

Green, R. O., Retrieval of Reflectance From AVIRIS-Measured Radiance Using a Radiative Transfer Code, *Proc. Third AVIRIS Workshop, JPL Publication 91-28, Jet Propulsion Laboratory, Pasadena, CA, pp. 200-210, 1991.*

Green, R. O., J. E. Conel, J. Margolis, C. Bruegge and G. Hoover, "An Inversion Algorithm for Retrieval of Atmospheric and Leaf Water Absorption from AVIRIS Radiance with Compensation for Atmospheric Scattering," *Proceedings of the Third AVIRIS Workshop, R.O. Green, editor, JPL Publication 91-28, pp. 51-61, Jet Propulsion Laboratory, Pasadena, CA, 1991.*

Green, R. O., J. E. Conel and D. A. Roberts, "Estimation of Aerosol Optical Depth and Calculation of Apparent Surface Reflectance from Radiance Measured by the Airborne Visible/Infrared Imaging Spectrometer (AVIRIS) Using MODTRAN2," *SPIE Conf. No. 1937, Imaging Spectrometry of the Terrestrial Environment, p. 12, 1993.*

Green, R. O., and B. C. Gao, "A Proposed Update to the Solar Irradiance Spectrum Used in LOWTRAN and MODTRAN," *Summaries of the Fourth Annual JPL Airborne Geoscience Workshop, JPL Publication 93-26, Jet Propulsion Laboratory, Pasadena, CA, 1993.*

Green, R. O., and J. E. Conel, "Movement of Water Vapor in the Atmosphere Measured by an Imaging Spectrometer at Rogers Dry Lake, CA," *Summaries of the Fifth Annual JPL Airborne Earth Science Workshop, JPL Publication 95-1, Vol. 1, Jet Propulsion Laboratory, Pasadena, CA, 1995.*

Kneizys, F. X., E. P. Shettle, G. P. Anderson, L. W. Abrew, J. H. Chetwynd, J. E. A. Shelby, and W. O. Gallery, "*Atmospheric Transmittance/Radiance; Computer Code LOWTRAN 7," AFGL, Hanscom AFB, MA, 1987.*

Press, W. H., "***Numerical Recipes: The Art of Scientific Computing***," Cambridge University Press, Cambridge, 1986.

COASTAL BATHYMETRY FROM HYPERSPECTRAL DATA

Ronald J. Holyer and Juanita C. Sandidge
Naval Research Laboratory
Stennis Space Center, MS 39529-5004

ABSTRACT

A study is underway at the Naval Research Laboratory to investigate relationships of water depth, bottom type, and water inherent optical properties to upwelling spectral radiance of coastal waters. A neural network and data from the Airborne Visible/Infrared Imaging Spectrometer (AVIRIS) are used to investigate these relationships. The present paper focuses on the extraction of water depth from AVIRIS data at two Florida test areas: Tampa Bay and Santa Rosa Sound. Sounding data obtained from the National Ocean Survey (NOS) hydrographic database serves as water depth ground truth for this study.

Spectral radiance data over the two test areas is shown to be of relatively low dimensionality, indicating that hyperspectral imaging of these coastal waters represents a high degree of spectral over sampling. Algorithms relating spectral radiance to water depth in these test areas will, therefore, require significantly fewer spectral bands than the total available from AVIRIS. However, the hypothesis explored is that, although high spectral resolution is not required for radiance to depth relationships at a single site, spectral over sampling can be exploited to develop radiance to depth relationships that can be universally applied to diverse sites, where water optical properties, bottom reflectance, and atmospheric conditions vary.

The neural network is the paradigm chosen to map spectral radiance into water depth. Neural networks are trained using the NOS ground truth to estimate water depth from AVIRIS measurements of spectral radiance. This training is done for each site individually and for combined data from both sites. Each test image contains a portion of clear atmosphere and a portion of considerable aerosol contamination. Both clear areas and combined clear and contaminated areas are included in the neural network training tasks. The results presented support the hypothesis that spectral over sampling can be exploited to form universal algorithms.

Page intentionally left blank

DEFINING THE INTERDEPENDENCE OF VOLCANISM, TECTONISM, AND FLUID AVAILABILITY IN THE FORMATION OF EPITHERMAL MINERALIZATION AT AURORA-BODIE CA/NV USING AVIRIS DATA

Trude V.V. King, Byron R. Berger, Ian Ridley, and Roger N. Clark
U.S. Geological Survey, Denver, CO 80225

GEOLOGIC BACKGROUND AND RATIONALE FOR STUDY

Precious metal epithermal deposits have been studied extensively over the last 80 years and there is broad agreement that the circulation of large fluid volumes plays an essential role in their formation. This is also consistent with the premise that high-temperature geothermal systems are modern analogs of ancient epithermal systems. A link between the distribution of epithermal deposits and tectonic structures can also be made (Berger and Henley,1989). However, volcanism, tectonism, and fluid availability, if considered independently, cannot explain the occurrence and distribution of epithermal deposits. There is an essential interdependence between these three elements in the formation of epithermal systems that has not been thoroughly investigated.

We have integrated several lines of evidence from different localities to support the idea of interdependence between volcanism, tectonics, and fluid availability.
Evidence of the role of volcanism can be illustrated by examining the Great Basin. In the Great Basin the large volumes of Eocene-Oligocene volcanic rocks are rarely accompanied by epithermal mineralization. However, such mineralization is commonly associated with Miocene and younger volcanics, suggesting that volcanism must be only one factor in the development of the mineralized deposits. In another example, data from the Taupo Volcanic Zone (TVZ), New Zealand can be used to illustrate that tectonic setting is an important, but not exclusive, factor in the occurrence of geothermal systems. In the TVZ high-enthalpy geothermal activity is widespread, and commenced with the development of pull-apart basins bounded by crustal-scale faults. However, metalliferous geothermal systems are not randomly distributed along these structures, but are colinear along one boundary of the Taupo graben. As a third example, in the western United States the common association of epithermal deposits with lacustrine deposits and/or high altitude water sheds illustrates the importance of fluid availability in the mineralization process. We believe this association is genetic and that these reservoirs were necessary to provide an adequate supply of fluid to the original geothermal systems. However, most lacustrine deposits in the western United States are not associated with epithermal mineralization and most modern lakes are not associated with geothermal activity. We conclude that volcanism, tectonism and large fluid reservoirs cannot act independently to produce epithermal mineral deposits, but must act in concert.

To develop a more complete understanding of these interactions we have selected to examine the Aurora-Bodie volcanic field, California-Nevada, just north of Mono Lake, California. Volcanism commenced in the present-day Bodie Hills and eastward ~ 17 Ma ago with eruption of calc- alkaline andesite, dacite, and rhyodacite onto a peneplained surface. Initial geothermal activity followed at ~ 13 Ma at Masonic in the northern Bodie Hills. Andesitic constructional volcanism was active in the Aurora District between 15.4-13.5 Ma (Kleinhampl et al., 1975) with associated andesite and rhyolite emplaced between 12.5-11 Ma.

During the Miocene a 35 km^3 complex of small alkali-calcic, high-potassium andesite to dacite stratovolcanoes and cumulodome complexes (13.3 +/-0.4 to 7.7+/-0.4 Ma) covered these older volcanics. Mineralization in the Aurora District was probably associated with the Brawley Peaks andesitic stratovolcano that was built between 15.4+/-0.3 Ma and 11.2+/-0.2 Ma. Alteration in the core of this edifice, resulting from geothermal activity, has been dated at 13.7+/-0.5 Ma (M.L. Silberman, pers. comm.). Two other geothermal events occurred at 11.0+/-0.2 Ma and 10.3+/-0.3 Ma, the latter forming the economic quartz-adularia veins in the Aurora district. Two distinct episodes of geothermal activity at 7.8+/-0.2 Ma and 7.2+/-0.1 Ma (Silberman et al., 1972), produced economic mineralization in the Bodie District. These episodes are geochemically and mineralogically distinct (based on data in Brown, 1907) and were focused on the southeast flank of the alkali-calcic Bodie Mt.-Potato Peak stratovolcano and nearby domes. Bimodal Pliocene (<5.7 Ma) to Pleistocene (~250,000 yrs) andesitic and basaltic volcanic rocks were erupted from small, readily recognizable vents associated with rhyolitic domes and flows (Kleinhampl et al., 1975). The youngest epithermal mineralization in the region is associated with the early Pliocene activity at ~ 5 Ma at Borealis on the flank of the Wassuk Range. Recent geothermal activity can be observed in the environs of the town of Bridgeport. There are two prominent tectonic features in this region. First, the Fletcher Valley-Coal Valley basin bounded by northeast-trending faults on the southern margin and northwest-trending faults on the west and east margins. This structural basin developed between ~13 Ma and the present. It was lake-filled between ~ 12.5 Ma and 7 Ma, and was intermittently lacustrine to 5-4 Ma (Gilbert and Reynolds, 1973). The gradual loss of the lacustrine environment records the uplift of the Sierra Nevada and continuation of vertical tectonics in the local area. Second, a northeast-trending arch forms the northern margin of the Mono Basin. The Aurora, Bodie and Borealis Districts are aligned along this structure. Summarily, volcanism has been episodic in the Bodie Hills for the past 17 Ma, and the area has been tectonically active since 13 Ma. Nevertheless, mineralization is restricted to the interval 13-5 Ma, with the most productive geothermal systems active in the period 11-7 Ma. Consequently, the Aurora-Bodie volcanic field is an appropriate initial test area because of 1) the presence of several ages of epithermal mineralization associated with Neogene volcanism; 2) a well defined structural setting; 3) the presence of dated lacustrine sediments associated with mineralization, and; 4) the availability of data on climatic conditions during the Neogene.

AVIRIS data is being used to help answer a number of questions including: 1) What is the timing of geothermal activity, and how many individual geothermal episodes exist in the Aurora-Bodie area? 2) How were the epithermal systems aerially redistributed, how extensive is each hydrothermal event, and to what igneous events can they be related? 3) What was the relation of the geothermal activity to the volcanic landforms, and timing of structural activity, and can the paleohydrology be reconstructed from this information? 4) Do the different precious- and base-metal paragenesis reflect temporally/spatially distinct phases of mineralization or only spatially separated parts of one event?

IMAGING SPECTROMETER DATA

The AVIRIS data used in this study was collected on August 20, 1992 and consists of two flight lines containing 760 km^2 of data. A combined method of radiative transfer modeling and empirical ground calibration site reflectance were used to correct the flight data

to surface reflectance (Clark *et al.*, 1996). This method corrects for variable water vapor in the atmosphere and produces smooth spectra with spectral channel to channel noise approaching the signal to noise of the raw data. Thus, the data can be compared to standard laboratory measurements. The calibration sites consisted of two maars that were vegetation free and appeared mineralogically uniform. Samples from the maars were collected after the overflight and measured on the USGS laboratory spectrometer (Clark *et al*, 1990b). The spectra of the calibration sites are spectrally bland and serve as an ideal calibration standard.

TRICORDER ANALYSIS

Clark *et al.*, (1990a, 1991,1996) developed a new analysis algorithm that uses a digital spectral library of known reference materials and a fast, modified-least-squares method of determining if a diagnostic spectral feature for a given material is present in the image. This algorithm is called "tricorder." The tricorder analysis compares continuum-removed spectra from the remotely sensed data, to a database of continuum-removed spectral features from the reference spectral library (Clark et al., 1993). Multiple features from multiple materials are compared and the material with the closest match is mapped. The algorithm does not force a positive match which makes it different from many other algorithms in use. The tricorder algorithm attempts to map only minerals included in the reference database.

For the present study we mapped minerals based on the presence of absorption features in the ~0.45 μm to ~1.0 μm, 1.5 μm, and 2.2 μm to 2.3 μm wavelength region, which represent the visible and near-infrared portions of the elector-magnetic spectrum. In this Dadaist we looked for 165 different materials. The materials we mapped for included silicates, phyllosilicates, sulphates, carbonates, amorphous iron compounds, cyanide compounds, as well as mineral mixture which contain two or more of these individual mineral groups.

Absorption bands in the visible portion of the spectrum (~0.4-0.8 μm) are caused by electronic processes including crystal field effects, charge transfer, color-centers, and conduction bands. The absorptions resulting in the visible portion of the spectrum involve elements of the first transition series which have an outer unfilled d-shell in their electronic distribution. The energy levels are determined by the valence state of the element, its coordination number and its site symmetry. Differences in these parameters are manifested in individual diagnostic absorption bands. Absorptions in this wavelength region are commonly associated with the presence of iron in the mineral structure.

Near-infrared radiation (1-2.45 μm, in this study) absorbed by a mineral is converted into molecular vibrational energy. The frequency or wavelength of the absorption depends on the relative masses and geometry of the atoms and the force constants of the bonds. There are two main types of molecular vibrations: stretching and bending. A stretching vibration is a movement along the bond axis which either increases or decreases the interatomic distances. Bending vibrations consist of a change in the angle between bonds with a common atom or the movement of a group of atoms with respect to the remainder of the molecule, but without movement of the atoms in the group with respect to one another (Silverstein et al., 1981). Only vibrations that result in a change in the dipole-moment of the molecule will be infrared active.

Absorption features in the 2.2 to 2.3-μm region result from a combination of the OH-stretching fundamental with either the Al-O-H bending mode absorbing at approximately 2.2 μm, or Mg-O-H bending mode absorption at 2.3 μm. At high resolution these bands also

appear as characteristic multiple, complex absorption features. Based on previous work (King and Clark,1989, Clark et al., 1990b, Clark et al., 1993), it is known that the strength, position and shape of these features is a function of the mineral chemistry.

In this study we searched for 54 minerals plus 5 vegetation and water and snow mixtures with absorption features at wavelengths near or less than 1.0 μm. We mapped 12 of the 54 potential minerals in significant areal extent. Comparison of spectra of these minerals extracted from the remotely sensed data with our laboratory standards shows good matches.

To detect the presence of minerals that have absorption features in the 2.2-2.3 μm wavelength region we used 93 material standards including minerals, snow and ice mixtures plus vegetation standards. Of these 93 standard materials we detected 15 different phases of significant areal extent.

In addition, we have mapped 13 different types of vegetation plus vegetation water content and relative stress. These measurements were based on absorption features in both the 1 μm and 2 μm wavelength regions.

DISCUSSION

The AVIRIS data provides new insights into both mineralogical and structural evolution of the of the Aurora-Bodie volcanic field. The AVIRIS data delineates large tectonic features and areas of epithermal alteration. At least five major areas of epithermal alteration not associated with mining districts, in addition to areas of alteration associated with the mining districts of Aurora and Bodie, have been identified in the AVIRIS scenes. Mineral maps based on absorption features primarily in the 1 μm wavelength region, resulting from the presence of Fe-bearing minerals (electronic absorption features), and maps based on the presence of alteration associated with the presence of absorption features in the 2.2-2.3 μm region (vibrational absorptions) define these areas of alteration. Data analysis suggests that geologic information on the composition of parent rock can be gained from comparing the distribution patterns of the 1 μm and 2 μm absorption feature maps. It appears that Fe-bearing minerals without the association of materials having a 2 μm absorption feature occur in regions of basaltic composition and the absorptions result from the superficial Fe-staining on the rocks. The area on the west side of Beauty Peak provides an example. Similarly, areas that show alteration materials having a 2 μm absorption feature, and lack alteration minerals having a 1 μm absorption feature, appear to be Fe-poor rhyolitic or dacitic rocks. However, field verification will be necessary to confirm these correlations.

The area of oldest alteration (observed on the eastern edge of the AVIRIS scenes) is associated with the Aurora mining district (15.4-11.2 Ma) and youngest (observed on the western most edge) is in the region of Travertine Springs near Bridgeport. Between these two locations are the 4-5 other areas of alteration which are intermediate in age. The Bodie mining district is mineralogically distinct on the AVIRIS scene. However, the heavy reworking of the upper most geologic material during the mining process suggests that it will be difficult to extract information on the type and extent of alteration from the AVIRIS data. Other areas of epithermal alteration occur near Brawley Peak, Beauty Peak, Paramount Creek, Aurora Canyon, and Murphy Spring. These areas differ in size, amount of a particular mineral and the spatial relation between the mineral phases, but all are similar in the hematite, Fe-bearing minerals, amorphous iron oxide, sulphates (including alunites and jarosite), phyllosilicates (montmorillonite and kaolinites), and chalcedony. Many of these areas of

alteration are associated with tectonic features.

The most obvious tectonic feature in this data set is a prominent Sierra front range fault that bounds the western most edge of the data set. Zones of alteration (Travertine Hot Springs and Murphy Springs) seem to be bound by this large fault. Other areas of alteration (Paramount Creek and Aurora Canyon) seem to be associated with a fault or series of faults that extends (NE to SW trending) nearly the length of the data set.
Faulting, to a lesser extent, is associated with the other areas of epithermal alteration.

SUMMARY

Although we are at the preliminary stage of relating the results of the AVIRIS mapping with age dating and field verifications, we are confident that imaging spectroscopy data is a valuable tool for providing new first-order insights into the aerial extent and mineralization associated with epithermal systems. These insights, combined with other field studies, mineralogic and age-dating techniques, can be used as a predictive tool in assessment studies and in the development of new exploration strategies.

REFERENCES

Berger, B.R., and Henley, R.W., 1989, Advances in the understanding of epithermal gold-silver deposits, with special reference to the western United States, in Keays, R.R., Ramsay, W.R.H., and Groves, D.I., eds., *The Geology of Gold Deposits: The Perspective in 1988: Economic Geology Monograph* 6, p. 405-423.

Clark, R.N., A.A. Gallagher, and G.A. Swayze, Material absorption band depth mapping of imaging spectrometer data using a complete band shape least-squares fit with library reference spectra: *Proceedings of the Second Airborne Visible/Infrared Imaging Spectrometer (AVIRIS) Workshop*, JPL Publication 90-54, p. 176-186, 1990a.

Clark, R.N., T.V.V. King, M. Klejwa, G. Swayze, and N. Vergo, High Spectral Resolution Reflectance Spectroscopy of Minerals: *J. Geophys Res.* **95,** 12653-12680, 1990b.

Clark, R.N., G.A. Swayze, A. Gallagher, N. Gorelick, and F. Kruse, Mapping with Imaging Spectrometer Data Using the Complete Band Shape Least-Squares Algorithm Simultaneously Fit to Multiple Spectral Features from Multiple Materials, *Proceedings of the Third Airborne Visible/Infrared Imaging Spectrometer (AVIRIS) Workshop,* JPL Publication 91-28, 2-3, 1991.

Clark, R.N., G.A. Swayze, A. Gallagher, T.V.V. King, and W.M. Calvin, The U. S. Geological Survey, Digital Spectral Library: Version 1: 0.2 to 3.0 μm, *U.S. Geological Survey, Open File Report 93-592,* 1340 pages, 1993. (Also being published as a USGS Bulletin, 1300+ pages, 1996 *in* press.)

Clark, R.N., G.A. Swayze, K. Heidebrecht, R.O. G.A.F.H. Goetz: Calibration to Surface Reflectance of Terrestrial Imaging Spectrometry Data: Comparison of Methods, *Applied Optics in* review, 1994.

Clark, R.N., G.A. Swayze, and T.V.V. King, Imaging Spectroscopy:A New Tool for Identifying and Mapping Materials: Minerals, Amorphous Materials, Environmental and Man-made Materials, Vegetation Species, Health and Water Content, Water, Ice, Snow, and Atmospheric Gases: The USGS Tricorder Algorithm, in preparation, 1996.

Gilbert, C.M., and Reynolds, M.W., 1973, Character and chronology of basin development, western margin of the Basin and Range Province: *Geol. Soc. Amer. Bull*, **84**, p. 2489-2510.

Henley, R.W., Truesdell, A.H., and Barton, P.B., Jr., 1984, Fluid-Mineral Equilibria in Hydrothermal Systems: Society of Economic Geologists Reviews in Economic Geology vol. 1, 267 p.

King, T.V.V. and R.N. Clark, Spectral Characteristics of Chlorites and Mg-Serpentines Using High-Resolution Reflectance Spectroscopy. *J. Geophys. Res.*, **94**, 13,997-14,008, 1989.

Kleinhampl, F.J., Davis, W.E., Silberman, M.L., and Chesterman, C.W., and Gray, C.H., Jr., 1975, Aeromagnetic and limited gravity studies and generalized geology of the Bodie Hills: *USGS Bulletin 1384*, 38 p.

Silberman, M.L., Chesterman, C.W., Kleinhampl, F.J., and Gray, C.H., Jr., 1972, K-Ar ages of volcanic rocks and gold-bearing quartz-adularia veins in the Bodie mining district, Mono County, California: *Econ. Geol.*, **67**, p. 597-604.

Silverstein, R.M., G.C. Bassler, and T.C. Morrill, Spectrometric Identification of Organic Compounds. John Wiley, New York, New York, 442p., 1981.

THE 1995 AVIRIS GEOLOGY GROUP SHOOT

Fred A. Kruse
Analytical Imaging and Geophysics LLC
Louisville, Colorado 80027 USA
and
Jonathan F. Huntington
CSIRO, Division of Exploration and Mining
North Ryde, NSW 8112, Australia

1. INTRODUCTION

An Airborne Visible/Infrared Imaging Spectrometer (AVIRIS) geology "Group Shoot" was conducted during summer 1995 by Analytical Imaging and Geophysics (AIG) in cooperation with the CSIRO Division of Exploration and Mining, NASA Ames Research Center, and the Jet Propulsion Laboratory/California Institute of Technology (JPL). The purpose of this effort was to give mining companies and other interested commercial entities a chance to acquire high quality imaging spectrometer data for selected sites of specific interest.

AIG/CSIRO determined company interest, compiled targets and signed an MOU and Space Act Agreement with NASA prior to the mission. Funds were collected from company sponsors and forwarded to NASA Ames Research Center in accordance with these agreements. The sites were flown in late July 1995 under near-optimum conditions. High quality AVIRIS data were collected during this mission for sites in Arizona, Nevada, California, Utah, Wyoming, and Colorado, USA. A typical site consisted of two-to-four approximately 10 x 12 km AVIRIS scenes. While the original mission concept was to have all of the sites flown on one day, the geographic spread of the sponsors' sites and weather conditions at the sites required both NASA and AIG to be flexible in scheduling acquisitions. Table 1 gives a list of sites acquired. Figure 1 shows the approximate locations of the sites, the number of scenes acquired, and the date of data acquisition.

Table 1. Sites Flown During 1995 AIG/CSIRO AVIRIS Group Shoot

SITE	LAT 1/LON 1	LAT 2/LON 2
1) Cheyenne WY (Nunn, CO)	N40d 48m 15s/W104d 27m	N40d 48m 15s/W104d 52m 30s
2) Lander, WY	N42d 35m 16s/W108d 39m 36s	Center Point for 2 scenes, Fly grid az of 90 or 270 degrees
3) Tintic, UT	N39d 48m 27.61s/W112d 06m 35.94s	N39d 59m 16.21s/W112d 06m 45.82s
4) S. Oqhirrh Mtns, UT	N40d 14m 37.77s/W112d 8m 52.35s	N40d 23m 25.85s/W112d 17m 4.29s
5) Mule Ear 1, UT	N37d 2m 30s/W109d 50m	N37d 15m/W109d 40m
Mule Ear 2, UT	N37d 13m/W109d 44m	N37d 3m/W109d 46m
6) Railroad Valley, NV	N38d 37' 2.2/W115d 37' 17.9W	Center Point for 4 scenes, Fly grid AZ of 115d or 295degrees
7) Goldfield, NV	N37d 50m/W117d 13m	N37d 24m/W117d 13m
8) Oatman, AZ	N35d 07m 30s/W114d 25m	N34d 58m 30s/W114d 25m
9) Virginia City, NV #1	N39d 10m/W119d 43m	N39d 26m/W119d 34m
Virginia City, NV #2	N39d 25m/W119d 45m	N39d 15m/W119d 35m

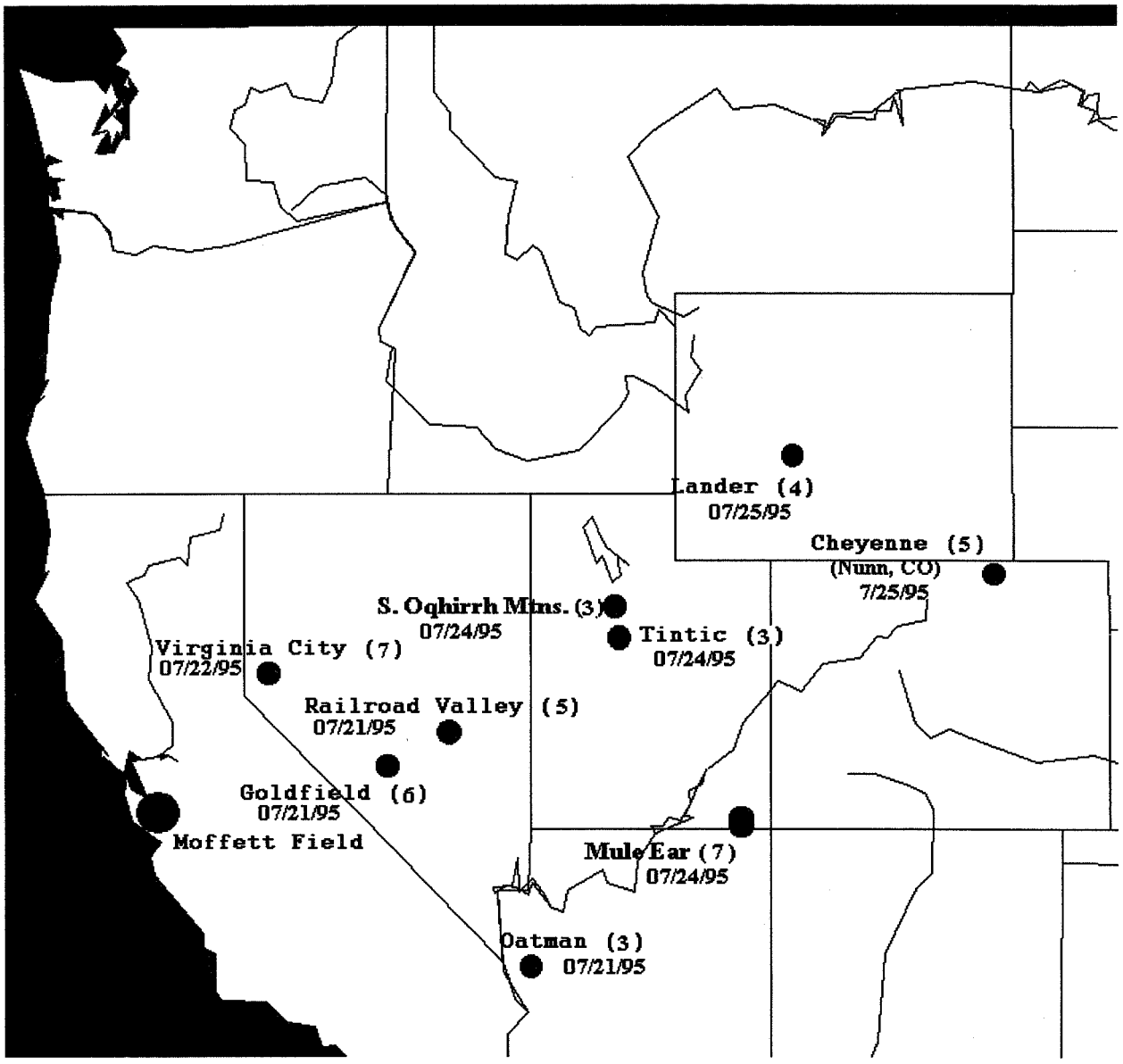

Figure 1. AIG/CSIRO Group Shoot Approximate Target Locations, Number of Scenes Acquired, and Data Acquisition Dates.

2. INSTRUMENT INFORMATION

The Airborne Visible/Infrared Imaging Spectrometer (AVIRIS) is an imaging spectrometer that simultaneously acquires 224 spectral images at 20 meter spatial resolution and 10 nanometer spectral resolution. Each "scene" covers an approximately 10 x 12 kilometer area. Imaging spectrometers collect images, however, in addition, a complete spectrum can also be extracted from each picture element (pixel) of the image, thus allowing detailed mapping based on the spectroscopic characteristics of minerals (Goetz et al., 1985, Boardman et al., 1995).

Despite major revisions to the instrument prior to the 1995 flight season, AVIRIS operated without problems during the Group Shoot flights. Some minor irregularities were

observed with the data, however, the order of magnitude of these is near the noise level in the data (R.O. Green, Personal Communication). Problems encountered with the data included 1) dropped bits in individual pixels resulting in anomalous spectra, 2) multiplexer lag in the instrument resulting in spatial shifting between bands (bands 13 and 35 were discarded because of a 1 pixel or greater shift). According to Rob Green at JPL, "the multiplexer lag artifact is similar to the detector-readout-delay that has been in all AVIRIS data before 1995. The artifact expresses itself very close to the level of the AVIRIS noise." What this means, is that the size of the instantaneous field of view (IFOV) of AVIRIS varies slightly as a function of the intensity of the signal. According to Green, the AVIRIS calibration without any correction is still at the 96% level. Based on preview processing by AIG, the AVIRIS data were judged to be satisfactory for the purposes of flight sponsors. In general, the data appeared to be of high quality in both the spatial and spectral domains.

3. THE GOLDFIELD/CUPRITE GROUP SITE

The Goldfield/Cuprite area, Nevada, was chosen by AIG as the shared group site for the 1995 AVIRIS Group Shoot because considerable previous remote sensing information exists for the area, and AIG principals have analyzed previous AVIRIS acquisitions for these sites and conducted field verification studies. This site acted as the "control" for the 1995 AVIRIS data acquisition and the processing performed was useful as an example for the other sites. Four AVIRIS scenes were analyzed. Table 3 outlines AIG's "standardized" procedure for analyzing AVIRIS data for a typical site.

Table 3. AIG "Standardized" AVIRIS Processing Methodology

1. Download Quicklook Data
2. Review Spatial Coverage
3. Preliminary Assessment of Spatial Data Quality
4. Define Areas for Further Processing
5. Order AVIRIS Radiance Data for Selected Scenes
6. Download Radiance Data from Tape
7. Data Quality Assessment
   - Spatial Browsing
   - Spectral Browsing
   - SNR Calculations
8. Calibration to Apparent Reflectance
   - ATREM
   - Empirical Line Calibration if ground information available
   - "Eff" correction if no ground information available
   - Spectral Browsing
9. Report Data Problems to JPL
10. MNF Transform
11. Pixel Purity Index
12. n-Dimensional Visualization (Endmember Definition)
13. Spectral Angle Mapper (SAM)
14. Spectral Unmixing and/or Match Filtering
15. Annotation, Output, and Report

3.1 Download Quicklook Data

JPL processing to AVIRIS Quicklooks for some sites was completed within two weeks, with all of the quicklook processing completed by mid-August 1995. Quicklook data were obtained via anonymous FTP from JPL on-line at: "ophelia.jpl.nasa.gov" in the directory "/pub/95qlook. AIG downloaded the quicklooks for all of the sites, reviewed the spatial coverage and produced hardcopy output, which was provided to the sponsors. All of the requested sites were covered per the flight specifications. Standard processed, full AVIRIS scenes for each site were ordered from JPL following the preview by AIG. Initial radiance data arrived the last week in September and the first week in October. AIG copied the data tapes and provided datasets to each of the sponsors for evaluation. The Goldfield/Cuprite data were calibrated to reflectance by AIG and processed to mineral maps to assess the data quality. This processing is discussed below.

3.2 Read Data From Tape

The Goldfield/Cuprite AVIRIS data and wavelength file were read from tape on a SUN SPARC system in Band-Interleaved-by-Line (BIL) format.

3.3 Preview Data and Assess Quality

Calibrated radiance data were both spatially and spectrally previewed. The spatial coverage of the two sites was good and the spatial fidelity of the data was excellent. Spatial browsing of different bands indicated that bands 13 and 35 were spatially offset from the rest of the bands (by one pixel horizontally. Another apparent anomaly was that some pixels exhibited what appeared to be dropped bits in one or more spectral bands. This was only for about 10-30 pixels per 614 x 1024 scene, or well less than 1% of the data. These were not used in subsequent processing.

3.4 ATREM Calibration

The Goldfield/Cuprite AVIRIS data were initially calibrated to apparent reflectance using the "ATREM" software available from the Center for the Study of Earth from Space (CSES) at the University of Colorado, Boulder. This software can be obtained via anonymous FTP from "cses.colorado.edu" in the directory "pub/atrem. Get the readme file for download instructions.

ATREM is an atmospheric model-based calibration routine, and requires input of data parameters such as the acquisition date and time, the latitude and longitude of the scene, and the average elevation, along with atmospheric model parameters (CSES, 1992). AIG used the ATREM version 1.31, which had to be updated to work with the 1995 data. An updated version should be available for most UNIX platforms from CSES. The output of the ATREM procedure is apparent reflectance calibrated data and a water vapor image for each scene. Typically, the water vapor image mimics topographic expression. Higher water vapor concentrations occur in the valleys, and lower water vapor concentrations over the higher elevations. In the Goldfield/Cuprite case, however, it appears as if there may have been some modulation by clouds. No clouds were visible in the images, however, and the ATREM apparent reflectance data appear to have adequately removed water vapor contributions from the spectra.

3.5 Evaluate Apparent Reflectance Data

Spectral browsing through both the apparent reflectance calibrated Goldfield and Cuprite data sets was used to get an idea of the success of the calibration as well as to identify specific minerals. This procedure indicated that the spectral quality of the data was excellent and the apparent reflectance calibration adequate. Band bands at 0.5001 μm (band 13) and 0.6824 μm (band 35), the overlap regions between spectrometers in bands 32-34 (~0.67 μm) and in bands 97-98 (~1.26 μm), as well as the spectral regions between approximately 1.3 - 1.4 μm and 1.84 and 1.96 μm corresponding to the major atmospheric water bands were masked out during subsequent processing. Individual spectra could be recognized in the apparent reflectance calibrated data that contained absorption features attributable to kaolinite, alunite, buddingtonite, muscovite, and calcite (Figure 2).

3.6 MNF Transformation

The next step of the processing was to perform a "Minimum Noise Fraction" (MNF) Transform to reduce the number of spectral dimensions to be analyzed. The MNF transformation is used to determine the inherent dimensionality of the data, to segregated noise in the data, and to reduce the computational requirements for subsequent processing (Green et al., 1988; Boardman and Kruse, 1994). The process is essentially two cascaded Principal Components transformations. The first transformation, based on an estimated noise covariance matrix decorrelates and rescales the noise in the data. This results in data in which the noise has unit variance and no band-to band correlations. The second step is a standard PC transformation of the noise-whitened data. The inherent dimensionality of the data is determined by examination of the eigenvalues and associated eigenimages. The data space is divided into two parts: one associated with large eigenvalues and coherent eigenimages, and a second with near-unity eigenvalues and noise-dominated images. By using only the coherent portions in subsequent processing, the noise is separated from the data, thus improving spectral processing results. Similar results are obtained when the MNF transformation is run on either the Goldfield or the Cuprite AVIRIS data. The eigenvalue plots fall sharply for the first 10 eigenvalues and flatten out. Examination of the eigenimages shows that while the first 10 images contain most of the information, images 11 through 20 still contain coherent spatial detail. The higher numbered MNF bands contain progressively lower signal-to-noise. Vertical bands, probably caused by multiple scattering in the AVIRIS optical path were observed in the visible-region MNF bands 7 - 11. This problem was reported to JPL.

3.7 Pixel Purity Index (PPI)

Based on the above MNF results, the lower order MNF bands were discarded and the first 20 MNF bands were selected for further processing. These were used in the "Pixel Purity Index" (PPI), processing designed to locate the most spectrally extreme (unique or different or "pure") pixels (Boardman et al., 1995). The most spectrally pure pixels typically correspond to mixing endmembers. The PPI is computed by repeatedly projecting n-dimensional scatterplots onto a random unit vector. The extreme pixels in each projection are recorded and the total number of times each pixel is marked as extreme is noted. A PPI image is created in which the digital number of each pixel corresponds to the number of times that pixel was recorded as extreme. A histogram of these images shows the distribution of "hits" by the PPI. A threshold was interactively selected using the histogram and used to select only the purest pixels in order to

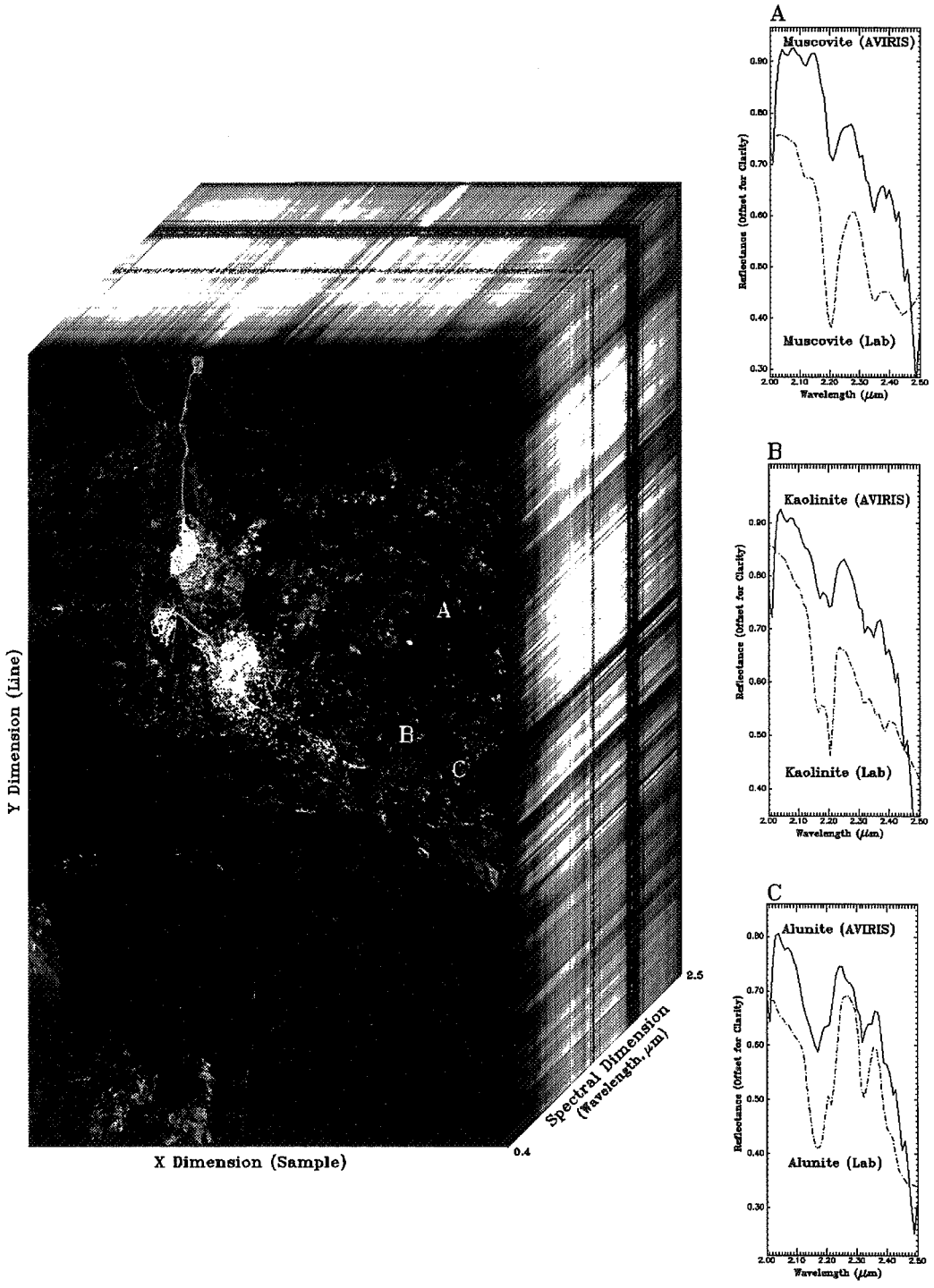

Figure 2. 3-D perspective cube of band 30 (0.67 μm) for the Goldfield 1995 AVIRIS site. Representative AVIRIS spectra are compared to Library Spectra on the right.

keep the number of pixels to be analyzed to a minimum. These pixels were used as input to an interactive visualization procedure for separation of specific endmembers.

3.8 n-Dimensional Visualization

Spectra can be thought of as points in an n-dimensional scatterplot, where n is the number of bands (Boardman, 1993; Boardman et al., 1995). The coordinates of the points in n-space consist of "n" values that are simply the spectral reflectance values in each band for a given pixel. The distribution of these points in n-space can be used to estimate the number of spectral endmembers and their pure spectral signatures. This geometric model provides an intuitive means to understand the spectral characteristics of materials. In two dimensions, if only two endmembers mix, then the mixed pixels will fall in a line in the histogram. The pure endmembers will fall at the two ends of the mixing line. If three endmembers mix, then the mixed pixels will fall inside a triangle, four inside a tetrahedron, and so on. Mixtures of endmembers "fill in" between the endmembers. All mixed spectra are "interior" to the pure endmembers, inside the simplex formed by the endmember vertices, because all the abundances are positive and sum to unity. This "convex set" of mixed pixels can be used to determine how many endmembers are present and to estimate their spectra.

The Goldfield/Cuprite AVIRIS dataset were analyzed using these geometric techniques. The thresholded pixels from the MNF images above were loaded into an n-dimensional scatterplot and rotated in real time on the computer screen until "points" or extremities on the scatterplot were exposed. These projections were "painted" using Region-of-Interest (ROI) definition procedures and then rotated again in 3 or more dimensions (3 or more bands) to determine if their signatures were unique in the AVIRIS MNF data. Once a set of unique pixels were defined, then each separate projection on the scatterplot (corresponding to a pure endmember) was exported to a ROI in the image. Mean spectra were then extracted for each ROI to act as endmembers for spectral unmixing. Using the IR data only from 2.0 to 2.4 μm, 9 endmembers were defined for the Goldfield/Cuprite AVIRIS data. These include the minerals calcite, buddingtonite, kaolinite, muscovite, alunite, and zeolite-group minerals. Another mineral, with an "unknown 2.2 μm absorption feature" was also located. Based on the spatial distribution of spectra matching this endmember and known information about the sites, this endmember was identified as representing opaline silica. Unfortunately, similar spectra also occur on alluvial fans away from the altered areas, probably because of weathering and/or spectral mixing. Finally, both "light" and "dark", relatively aspectral endmembers were defined. These endmembers or a subset of these endmembers were used for subsequent classification and other processing.

3.9 Spectral Angle Mapper (SAM) Classification

The Spectral Angle Mapper (SAM) is an automated method for comparing image spectra to individual spectra (Boardman, Unpublished data; Kruse et al., 1993). The algorithm determines the similarity between two spectra by calculating the "spectral angle" between them, treating them as vectors in a space with dimensionality equal to the number of bands. Because this method uses only the vector "direction" of the spectra and not their vector "length", the method is insensitive to illumination. The result of the SAM classification (not shown) is an image showing the best SAM match at each pixel. Additionally, rule images are calculated that

show the actual angular distance (in radians) between each spectrum in the image and each reference or endmember spectrum. Darker pixels in the rule images represent smaller spectral angles and thus spectra that are more similar to the endmember spectra. For the purposes of display, the dark pixels are inverted, so that the best matches appear bright. These images present a good first cut of the mineralogy at the sites.

3.10 Spectral Unmixing

While the SAM algorithm does provide a means of identifying and spatially mapping minerals, it only picks the best match to a spectrum. Natural surfaces are rarely composed of a single uniform material, thus it is necessary to use mixture modeling to determine what materials cause a particular spectral "signature" in imaging spectrometer data. Spectral mixing is a consequence of the mixing of materials having different spectral properties within a single image pixel. If the scale of the mixing is large (macroscopic), then the mixing occurs in a linear fashion. A simple additive linear model can be used to estimate the abundances of the materials measured by the imaging spectrometer. Each mixed spectrum is a linear combination of the "pure" spectra, each weighted by their fractional abundance within the pixel, a simple averaging (Boardman, 1991).

In order to determine the abundances, we must first determine what materials are mixing together to give us the spectral signature measured by the instrument. Selection of "endmembers" is the most difficult part of linear spectral unmixing. The ideal spectral library used for unmixing consists of endmembers that when linearly combined can form all other observed spectra. This can be presented as a simple mathematical model in which the observed spectrum (a vector) is the result of a multiplication of the mixing library of pure endmember spectra (a matrix) by the endmember abundances (a vector). An inverse of the original spectral library matrix is formed by multiplying together the transposes of the orthogonal matrices and the reciprocal values of the diagonal matrix (Boardman, 1989). A simple vector-matrix multiplication between the inverse library matrix and an observed mixed spectrum gives an estimate of the abundance of the library endmembers for the unknown spectrum.

Linear Spectral Unmixing was used as the final step in producing mineral maps for the Goldfield/Cuprite AVIRIS data. The endmember library defined using the n-dimensional visualization procedure was used in the unmixing process and abundance estimates were made for each mineral. These results can be presented in two ways. First, a set of gray-scale images stretched from 0 to 50% (black to white) provides a means of estimating relative mineral abundances. These results are shown in Figure 3. Secondly, color composite images can be used to highlight specific minerals and mineral assemblages. Pure colors in these images represent areas where the mineralogy is relatively pure. Mixed colors indicate spectral mixing, with the resultant colors indicating how much mixing is taking place and the relative contributions of each endmember. For example, in a color composite for Goldfield (not shown), the minerals Kaolinite, Alunite, and Muscovite when assigned to Red, Green, and Blue in the color output result in distinctive image colors. Areas that are pure red in such an image correspond to areas where kaolinite is the spectrally dominant (~most abundant) mineral. Areas that are green are dominated by Alunite. Areas that are blue contain primarily muscovite. The yellow pixels are an example of mixed pixels, where the contribution of red from kaolinite and of green from alunite results in the mixed yellow color.

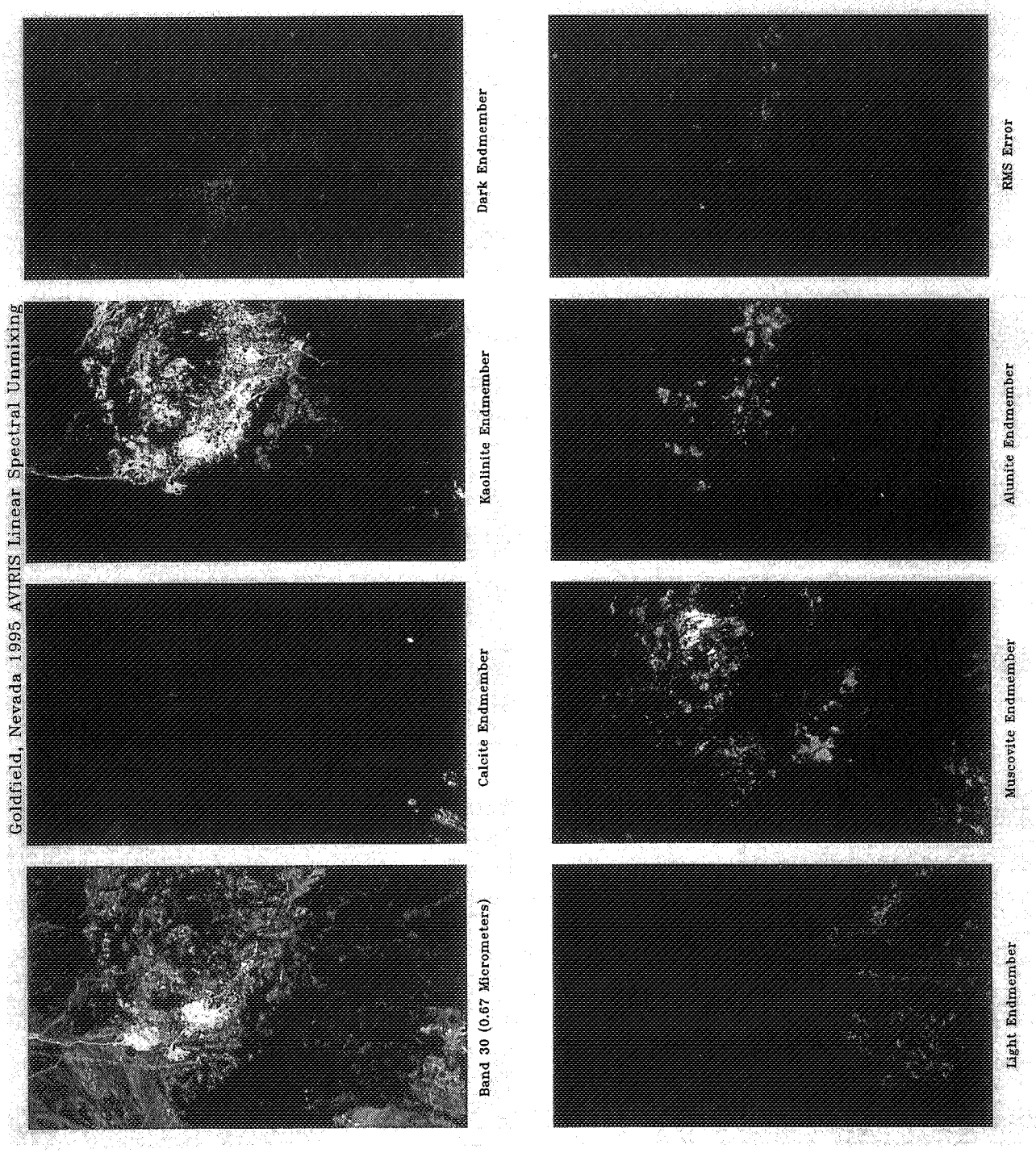

Figure 3. 1995 Goldfield AVIRIS Unmixing Results. Bright pixels represent higher abundances stretched from 0 - 50% (black to white).

4. CONCLUSIONS

This paper summarizes the organization, data collection, and group-site processing of the 1995 AVIRIS Group Shoot organized by Analytical Imaging and Geophysics. Data were successfully acquired for all sponsors' sites, and data delivery and processing have been completed. AIG has processed the shared group site data for Goldfield/Cuprite and used these well-known sites to define a "standardized" analysis strategy. This methodology was successfully used to produce detailed mineral maps of the Group Site and other sponsors' sites.

This Group Shoot effort has demonstrated that a cooperative industry/NASA effort can provide an efficient means for organizations to share some of the costs and apparent risks of using a new technology while getting data specific to their needs. Based on the results of this Group Shoot, AIG plans to organize and conduct a similar mission during the summer of 1996.

5. REFERENCES

Boardman, J. W., 1989, Inversion of imaging spectrometry data using singular value decomposition,: in Proceedings: IGARSS '89, 12th Canadian Symposium on Remote Sensing, V. 4, p. 2069 - 2072.

Boardman, J. W., 1991, Sedimentary facies analysis using imaging spectrometry: A Geophysical Inverse Problem: Unpublished Ph. D. Thesis, University of Colorado, Boulder, 212 p.

Boardman, J. W., 1993, Automated spectral unmixing of AVIRIS data using convex geometry concepts: in Summaries, Fourth JPL Airborne Geoscience Workshop, JPL Publication 93-26, v. 1, p. 11-14

Boardman, J. W., and Kruse, F. A., 1994, Automated spectral analysis: A geologic example using AVIRIS data, north Grapevine Mountains, Nevada: in Proceedings, Tenth Thematic conference on Geologic Remote Sensing, Environmental Research Institute of Michigan, Ann Arbor, MI, p. I-407 - I-418.

Boardman, J. W., Kruse, F. A., and Green, R. O., 1995, Mapping target signatures via partial unmixing of AVIRIS data: in Summaries, Fifth JPL Airborne Earth Science Workshop, JPL Publication 95-1, v. 1., p. 23 - 26.

CSES, 1992, Atmosphere REMoval Program (ATREM) User's Guide, Version 1.1, Center for the Study of Earth from Space, Boulder, Colorado, 24 p.

Goetz, A. F. H., Vane, G., Solomon, J. E., and Rock , B. N., 1985, Imaging spectrometry for earth remote sensing: Science, v. 228, p. 1147 - 1153.

Green, A. A., Berman, M., Switzer, B., and Craig, M. D., 1988, A transformation for ordering multispectral data in terms of image quality with implications for noise removal: IEEE Transactions on Geoscience and Remote Sensing, v. 26, no. 1, p. 65 - 74.

Kruse, F. A., Lefkoff, A. B., Boardman, J. B., Heidebrecht, K. B., Shapiro, A. T., Barloon, P. J., and Goetz, A. F. H., 1993, The Spectral Image Processing System (SIPS) - Interactive Visualization and Analysis of Imaging Spectrometer Data: Remote Sensing of Environment, Special issue on AVIRIS, May-June 1993, v. 44, p. 145 - 163.

PRELIMINARY ANALYSIS OF AVIRIS DATA FOR TECTONOSTRATIGRAPHIC ASSESSMENT OF NORTHERN GUERRERO STATE, SOUTHERN MEXICO

Harold R. Lang[1] and Enrique Cabral-Cano[2]

[1]Jet Propulsion Laboratory, California Institute of Technology, Pasadena, CA 91109 USA
[2]Instituto de Geofisica, Universidad Nacional Autonoma de Mexico, Ciudad Universitaria, Mexico DF 04510, MEXICO

1. PURPOSE

The tectonostratigraphic evolution of the southern margin of the North America Plate in Mexico is still in debate. Recent explanations assert Laramide age (Campanian-Eocene) accretion of far-travelled oceanic terranes (Campa and Coney, 1983; Sedlock et al., 1993). In 1989, we began an effort to bring new data to this debate through field mapping, incorporating Landsat Thematic Mapper and digital elevation data, along a 30 km by 250 km, east-west geologic transect of northern Guerrero State. Covering the region from Huetamo, Michoacan, to Papalutla, Guerrero (between latitude 18-19°N and longitude 101-99°W), our mapping results show that no stratigraphic incompatibilities suggesting terrane accretion exist in the region (Lang et al., 1996).

In November 1994, AVIRIS data were acquired along the geologic transect in order to refine our stratigraphic assessment. One objective of this hyperspectral survey was to improve mapping of limestone, dolostone and gypsum-bearing facies of the Morelos Formation which record rudist carbonate platform environments during mid-Cretaceous time.

2. RESULTS AND CONCLUSIONS

Preliminary analysis of these AVIRIS data show that signal-to-noise is sufficiently high to allow us to map the 2.34 μm calcite band, the 2.30 μm dolomite band, and 1.20 μm and 1.74 μm gypsum bands using simple ratio-based algorithms. When incorporated into our tectonostratigraphic model, AVIRIS-based mapping results: 1) support the existence of a coherent mid-Cretaceous depositional system in southern Mexico, and 2) are inconsistent with proposed terrane accretion models.

3. ACKNOWLEDGMENTS

This paper presents the results of one phase of research conducted as part of the Multispectral Analysis of Southwest Mexico Project. The research described in this paper was carried out by the Jet Propulsion Laboratory, California Institute of Technology, under contract with the National Aeronautics and Space Administration.

4. REFERENCES

Campa, M.F. and P.J. Coney, 1983, "Tectonostratigraphic Terranes and Mineral Resources Distribution in Mexico", *Canadian Journal of Earth Science*, vol. 20, pp. 299-313.

Lang, H.R., J.A. Barros, E. Cabral-Cano, G. Draper, C.G.A. Harrison, P.A. Jansma, and C.A. Johnson, 1996, "Terrane Deletion in Southern Mexico", *Geofisica Internacional*, submitted.

Sedlock, R.L., F. Ortega-Gutierrez and R.C. Speed, 1993, "Tectonostratigraphic Terranes and Tectonic Evolution of Mexico", *Geological Society of America Special Paper 278*, 153 pp.

534-43
046094

DETERMINING FOREST SPECIES COMPOSITION USING HIGH SPECTRAL RESOLUTION REMOTE SENSING DATA

M.E. Martin[1], S.D. Newman[1], J.D. Aber[1] and R.G. Congalton[2]

[1]Complex Systems Research Center, University of New Hampshire, Durham, NH USA 03824
[2]Department of Natural Resources, University of New Hampshire, Durham, NH USA 03824

The primary goal of this research project was to investigate the use of high spectral resolution remote sensing imagery for the identification of forest species composition. In previous work we have successfully used data from AVIRIS to identify the nitrogen and lignin concentration in forest canopy foliage (Martin 1994; Aber and Martin 1995). We have extended this research by using these AVIRIS canopy chemistry data products to identify forest species composition.

The study site for this project is the Prospect Hill tract at the Harvard Forest, in central Massachusetts (Latitude 42°32'N Longitude 72°11'W). This 400 hectare research site contains a combination of natural hardwood, mixed hardwood/conifer, hemlock, and white pine stands as well as red pine and Norway spruce plantations. Image data for this site were acquired using NASA's Airborne Visible Infrared Imaging Spectrometer (AVIRIS) on 15 June 1992. Atmospheric corrections of the AVIRIS data were done by the Atmosphere Removal Program (ATREM) (Gao *et al.* 1991, 1992).

In a 1986 stand survey, 252 stands within the study site were identified from aerial photos. Basal area by species was measured at variable radius plots within each stand. The relative basal area of each species was used to place each stand into one of 11 categories which we then classified using AVIRIS spectral data (Table 1). These categories include stands of pure conifer species (red pine, Norway spruce, white pine and hemlock). Within the study area there were few stands containing single hardwood species. For this reason, the classification for this site concentrates on conifer stands.

An investigation of leaf samples analyzed for nitrogen and lignin concentrations demonstrates that individually these constituents cannot be used to differentiate between species. However, species identification can be made on the basis of both foliar nitrogen *and* lignin information (Figure 1). For example, red pine and hemlock have similar nitrogen concentrations but very different lignin concentrations, whereas red maple and black cherry have similar lignin concentrations and different nitrogen concentrations.

Multiple linear regression analysis previously used to select AVIRIS bands correlated with field measured canopy chemistry provided a subset of AVIRIS bands for this study. Bands in both the visible and near infrared (NIR) regions of the spectra were used in this analysis. The species map generated from the AVIRIS classification (Figure 2), uses 4 bands centered at the following wavelengths: 627, 755, 822 and 1641nm. The 3 shorter wavelength bands are used in equations predicting foliar lignin concentration, and the band centered at 1641nm is used to predict foliar nitrogen concentration (Martin 1994; Aber and Martin 1995). A supervised classification (ERDAS 1992) was done in which 2-8 polygons from each of the 11 species categories were used to extract spectral signatures for each class. These polygons were identified using the stand map generated from field data. A maximum likelihood algorithm

was used, with a first pass parallelepiped classification, to assign all pixels in the image into one of the 11 signature classes.

Samples were selected from the classified image to assess the accuracy of the classification algorithm. Samples were selected from the center of classified polygons and compared to the field survey data (3x3 pixels per sample). Approximately 13% of the classified map was used in this accuracy assessment, with the number of samples per class relative to the total area of the class. The overall accuracy of the classification is 73.4%, with 127 out of 174 samples correctly classified. The only 'pure' species stands that we attempted to separate were conifer stands of hemlock, Norway spruce, white pine, red pine and black spruce bog. In the random samples chosen for our accuracy assessment, these species were correctly classified by AVIRIS data in 100, 90, 50, 89 and 87% of the samples, respectively.

We also validated these predictions against a number of plots in which canopy biomass had been measured by litterfall collections. Litterfall collections were made on 33 plots within this study site duing 1992 and 1993. These plots matched only 4 of the 11 classes described in Table 1. The number of these plots correctly classified with AVIRIS data is as follows: hemlock: 1/1, Norway spruce: 3/3, hardwood: 19/24, and red pine: 4/5.

The overall appearance of the AVIRIS classified map shows more spatial heterogeneity than the field classified map. It is possible that small scale spatial variation which might be missed in this type of field survey could be measured by remote sensing data, where spectral data is available for every pixel. The field sampling involved three or more measurements within each stand polygon (with some stands containing several hundred 20x20m pixels). Subsequent field observations have shown that a number of stands classified as mixed hardwood/conifer actually contained clusters of conifer species within the primarily hardwood stand.

This work demonstrates that the same bands used to derive foliar chemistry from high spectral resolution data can be used to classify forest species. Remote sensing of canopy chemistry has been possible only in the recent past with the availability of data from such instruments as AVIRIS. Additional work must be done to fully explore the potential of high spectral resolution data in determining forest species composition. Selection of signature training sites based on field measured canopy composition, rather than basal area, may result in a more accurate classification, particularly in mixed hardwood/conifer stands. Improvements may also be made in the classification of hardwood/conifer mixed stands by first using leaf-on and leaf-off data to determine the foliar biomass proportion of this mix before attempting species classification.

REFERENCES

Aber, J. and Martin, M. (1995). High spectral resolution remote sensing of canopy chemistry. In R. O. Green, editor, *Summaries of the Fifth Annual JPL Airborne Earth Science Workshop*, pages 1–4, Pasadena, California, USA. Jet Propulsion Laboratory.

ERDAS (1992). *ERDAS Field Guide.* ERDAS, Inc, Atlanta, GA.

Gao, B., Goetz, A. F. H., and Zamudio, J. A. (1991). Removing atmospheric effects from AVIRIS data for surface reflectance retrievals. In R. O. Green, editor, *Proceedings of the Third Airborne Visible/Infrared Imaging Spectrometer (AVIRIS) Workshop*, pages 80–86, Pasadena, California, USA. Jet Propulsion Lab.

Gao, B., Heidebrecht, K. B., and Goetz, A. F. H. (1992). *Atmosphere removal program (ATREM) user's guide.* Center for the Study of Earth from Space/CIRES, University of Colorado.

Martin, M. E. (1994). *Measurements of Foliar Chemistry Using Laboratory and Airborne High Spectral Resolution Visible and Infrared Data.* Ph.D. thesis, University of New Hampshire, Durham, NH.

	Stand Type	Classification Criteria
1	open	no trees
2	hemlock/hardwood	$\geq$ 70% hemlock
3	softwood	$\geq$ 80% mixed softwood
4	Norway spruce	$\geq$ 80% norway spruce
5	white pine	$\geq$ 80% white pine
6	red pine	$\geq$ 80% red pine
7	spruce bog	black spruce wetland
8	hardwood bog	wetland with mixed hardwood
9	hardwood	$\geq$ 80% mixed hardwood
10	hardwood/conifer 1	26-79% hardwood
11	hardwood/conifer 2	$\leq$ 25% hardwood

Table 1: Stand classification criteria

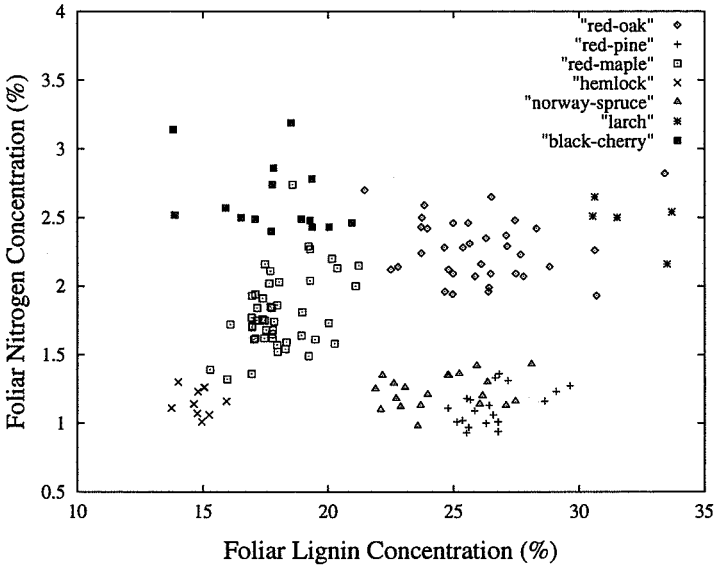

Figure 1: Harvard Forest leaf samples: foliar nitrogen vs foliar lignin

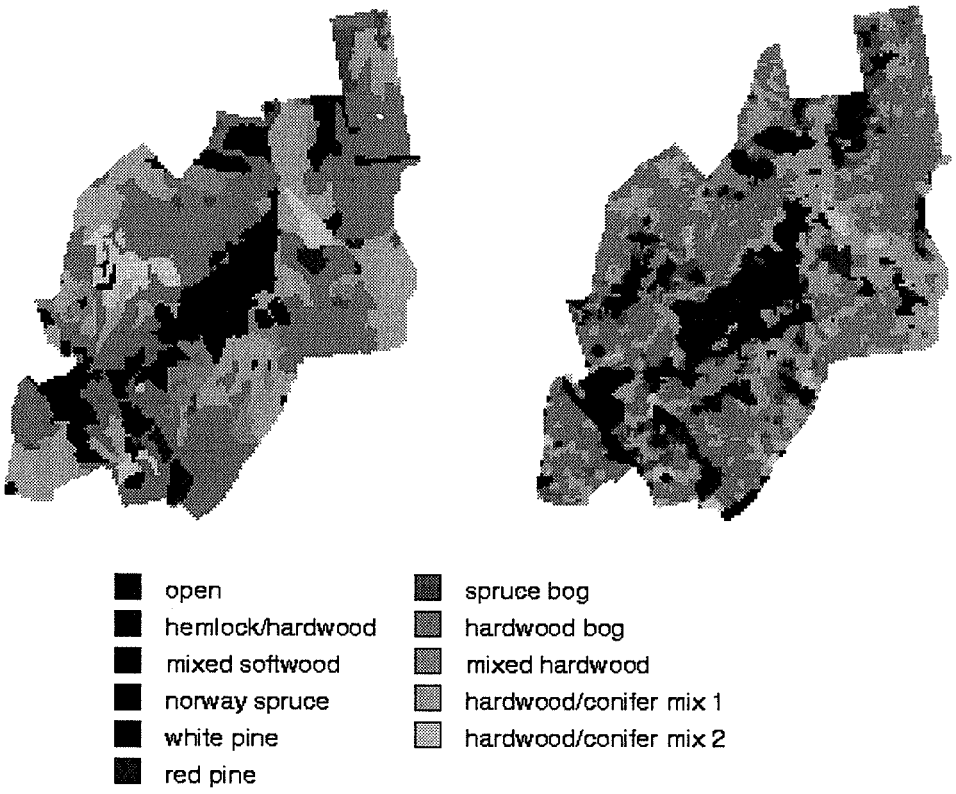

Figure 2: Harvard Forest: a. Species stand classification determined from field measurements of basal area. b. Species stand classification from AVIRIS data using bands centered at 627, 755, 822 and 1641nm.

525-63
046095
317381

QUANTITATIVE COMPARISON OF NEURAL NETWORK AND CONVENTIONAL CLASSIFIERS FOR HYPERSPECTRAL IMAGERY

4 p.

Erzsébet Merényi[1], James V. Taranik[2], Tim Minor[2], and William H. Farrand[3]

[1]Planetary Image Research Laboratory,
University of Arizona, LPL, Tucson, AZ 85721

[2]Desert Research Institute,
7010 Dandini Blvd, Reno, Nevada 89512

[3]Analytical Imaging & Geophysics, LLC
540 W. Arrowhead St., Louisville, CO 80027

The Problem

High spatial and spectral resolution measurements made by advanced remote sensors such as *e.g.,* NASA's AVIRIS or the Naval Research Laboratory HYDICE instruments can provide high quality data for analyzing the complex variability of landscape surface cover in different global environments. However, the application of traditional multispectral data analysis tools to hyperspectral data has not yielded satisfactory results because of mathematical and practical limitations. For example, the Maximum Likelihood classifier commonly used for multispectral data consisting of less than 10 bands, requires as many training samples per class as the number of sensor bands plus one. Hyperspectral sensors have hundreds of bands for measurement of landscape cover and therefore hundreds of discrete spectral classes are possible, thus complicating the collection of field samples. The extremely large amount of data that a spectral image represents today also poses problems with regard to processing time.

Combined analysis of hyperspectral data with digital topographic or other geophysical data is usually a complex process, not suitable for traditional methods. Covariance-based methods often fail to detect subtle, but compositionally important, spectral differences. Using feature extraction, to limit the analysis of hyperspectral data to only those bands having "significant" spectral variability, often results in the loss of subtle, but important, landscape information.

Motivation for Systematic ANN Studies

The use of Artificial Neural Networks (ANNs) is motivated by their power in pattern recognition/classification due to the ultimately fine distribution and non-linearity of the process. The textbook of *e.g.,* Pao (1989) gives a good background on the numerous ANN architectures developed for various types of tasks. As a successful implementation of the

parallel computational technique they also hold the promise to provide adequate speed for hundreds of megabytes of data, especially when supported by specialized hardware, which may open the possibility for on-board data reduction in the future.

However, one must have confidence in the quality of the classification before taking real advantage of the speed that Artificial Neural Networks can offer. Artificial Neural Networks have been shown to be well suited for pattern recognition and classification for complicated, noisy patterns. During the past ten years several works demonstrated their power for remote sensing spectral data of Earth and other planetary surfaces (*e.g.,* Benediktsson *et al.* 1990a; Hepner *et al.* 1990; Howell *et al.* 1994; Merényi *et al.* 1993, 1994, 1995a, 1995b, 1995c, 1996; Wang and Civco, 1995). For example, with an ANN researchers have detected compositionally meaningful spectral classes of asteroids that were missed by Principal Component Analysis from the same 60-channel data (Howell *et al.* 1994). Various workers have reported good classification results using ANNs on lower spectral resolution terrestrial images or laboratory data (*e.g.,* Ninomiya and Sato, 1990; Hepner *et al.* 1990, Merényi *et al.* 1994).

A limited number of valuable previous studies tested ANN performace against conventional methods classifying modest amounts of low-resolution data (Huang and Lippman, 1987), or medium resolution synthetic data into 3–4 classes (Benediktsson *et al.* 1990b). The latter favored the Maximum Likelihood classifier by virtue of Gaussian data construction. Benediktsson *et al.* (1990b), Yuan *et al.* (1995) and Merényi *et al.* (1996) are examples of studies for using ANNs to classify fused disparate data. Few (Howell *et al.* 1994, Merényi *et al.* 1993, 1995a, 1995b) have attempted ANN classification of hyperspectral data into a larger number of classes even though that is where the shortcomings of classical methods become debilitating.

Systematic evaluation of ANN classification performance, however, has not yet been conducted on real, hyperspectral data and on the scale of real applications (many classes, large images). This is critical for the confident use of ANNs in large scale integrated, (semi-) automated, on-board or commercial applications. The target of our study is to conduct such a systematic investigation on real data.

This Study and Preliminary Results

This work will present a comparision among ANN classifiers and several traditionally used sequential classification methods such as Maximum Likelihood, Minimum Distance, Mahalonobis Distance, using real hyperspectral data. In particular, a Kohonen type (Kohonen, 1989) Self-Organizing ANN architecture is tested. This neural network paradigm (implementation by NeuralWare, 1991) was selected over the most frequently used backpropagation network for the relative ease in training, and for its capability to make good predictions based on a small amount of training samples. A subset of a 1994 224-channel AVIRIS image is classified into more than a dozen classes after conversion to reflectances with atmospheric correction. The study area is the Lunar Crater Volcanic Field site in Nevada, with a great variety of cover units.

Classifications are performed for several spectral subsampling levels including full spectral resolution. Based on field knowledge and geologic maps, we conclude that the ANN produces comparable or better results than the classical methods in terms of map accuracy. The difference in quality between the performance of classical techniques and ANN classifiers appears to increase in favor of the ANNs with increasing number of channels. We will present spectra for all cover types to demonstrate the subtle discriminating features that the ANN makes use of to distinguish among certain geologically different species. Besides classification accuracy, an additional criterion of performance is the prediction capability based on a very small amount (less than 1%) of the data for training. This aspect is very important in remote sensing image analysis, as the collection of field samples can be costly or in some cases it may be impossible to collect the necessary number of samples for a traditional classifier.

References

Benediktsson, J. A., P. H. Swain, O. K. Ersoy and D. Hong (1990a), Classification of Very High Dimensional Data Using Neural Networks, in *IGARSS'90 10th Annual International Geoscience and Remote Sensing Symp.* 2, p 1269

Benediktsson, J.A., P.H. Swaini, and O.K. Ersoy (1990b), Neural Network approaches versus statistical methods in classification of multisource remote sensing data, *IEEE Transactions on Geoscience and Remote Sensing*, 28:4 pp 540–551

Hepner, G. F., T. Logan, N. Ritter, N. Bryant (1990), Artificial Neural Network Classification Using a Minimal Training Set: Comparision to Conventional Supervised Classification, *Photogramm. Eng. Remote Sens.* 56:4, pp 469–473

Howell, E. S., E. Merényi, L. A. Lebofsky (1994), Classification of Asteroid Spectra Using a Neural Network, *JGR Planets*, 23:E5, pp 10,847–10,865

Huang, W. and R. Lippman (1987), Comparisions Between Neural Net and Conventional Classifiers, *IEEE First International Conference on Neural Networks* IV, San Diego, pp 485–494

Kohonen, T. (1988), *Self-Organization and Associative Memory*, Springer-Verlag, New York

Merényi, E., Csathó, B., Bodrogi, M., Gulyás, Á., Utilization of Landsat Images For Mapping Natural Resources and For Environmental Protection In Hungary, *Proc. Tenth Thematic Conference on Geologic Remote Sensing*, San Antonio, TX, 9–12 May 1994

Merényi, E., R. B. Singer, W. H. Farrand (1993), Classification of the LCVF AVIRIS Test Site with a Kohonen Artificial Neural Network, *Proc. Fourth Airborne Geoscience Workshop*, Washington, D.C., Oct 25–29 1993, pp 117–120

Merényi, E., Singer, R.B., Miller, J.S., Mapping of Spectral Variations On the Surface of Mars From High Spectral Resolution Telescopic Images, submitted to *ICARUS*, 1994

Merényi, E., K. S. Edgett, R. B. Singer (1995b), Deucalionis Regio, Mars: Evidence for a New Type of Immobile, Weathered Soil Unit, *under review, ICARUS*

Merényi, E., Howell, E.S., Rivkin, A.S., and Lebofsky, L.A., Asteroid Classification Based on Water of Hydration: a Neural Network Study, *Bull. A.A.S.*, **27** No. 3 (1995c), p 2. Abstract.

Merényi, E., Csathó, B., Bodrogi, M., Gulyás, Á., Integration of Landsat Images, Geophysical and Radar Data For Mapping Soil Composition In Temperate Climate Environment, abstract submitted to the *Eleventh Thematic Conference, Geologic Remote Sensing, of ERIM*, Las Vegas, NE, 27-29 February 1996.

NeuralWare, Inc. (1991), *NeuralWorks Professional II Manual*

Ninomiya, Y. and I. Sato (1990), Estimation of SiO2 Content Using Thermal Infrared Reflectance Spectra of Rocks, in *Proceedings IGARSS' 90 Symposium* II, p 979

Pao, Y. H. (1989), *Adaptive Pattern Recognition and Neural Networks*, Addison-Wesley, 1989.

Wang, Y. and Civco, D.L. (1995), Artificial Neural Networks in High Dimensional Spatial Data Classification: A Performance Evaluation, in *ACMS/ASPRS Annual Convention & Exposition Technical Papers* 3, Charlotte North Carolina, February 27 – March 2 1995, pp 662–671

Yuan, D., D. Worthy, and B. Nassersharif (1995), The prototype of a knowledge and neural network based image classification system using both remotely sensed and digital elevation model data.

S36-47
046096

SURFACE AND ATMOSPHERIC PARAMETER RETRIEVAL FROM AVIRIS DATA: THE IMPORTANCE OF NON-LINEAR EFFECTS

317383
10P.

Jose F. Moreno(*) and Robert O. Green
Jet Propulsion Laboratory, MS 300-243
4800 Oak Grove Drive, Pasadena, CA 91109-8099
Tel. 818-3543865, Fax: 818-3936943, Email: moreno@blacks.jpl.nasa.gov

(*) on leave from: Remote Sensing Unit - Faculty of Physics, University of Valencia,
46100 Burjassot, Valencia, Spain

1. INTRODUCTION

AVIRIS data represent a new and important approach for the retrieval of atmospheric and surface parameters from optical remote sensing data. Not only as a test for future space systems, but also as an operational airborne remote sensing system, the development of algorithms to retrieve information from AVIRIS data is an important step to these new approaches and capabilities. Many things have been learned since AVIRIS became operational, and the successive technical improvements in the hardware and the more sophisticated calibration techniques employed have increased the quality of the data to the point of almost meeting optimum user requirements.

However, the potential capabilities of imaging spectrometry over the standard multispectral techniques have still not been fully demonstrated. Reasons for this are the technical difficulties in handling the data, the critical aspect of calibration for advanced retrieval methods, and the lack of proper models with which to invert the measured AVIRIS radiances in all the spectral channels. To achieve the potential of imaging spectrometry, these issues must be addressed.

In this paper, an algorithm to retrieve information about both atmospheric and surface parameters from AVIRIS data, by using model inversion techniques, is described. Emphasis is put on the derivation of the model itself as well as proper inversion techniques, robust to noise in the data and an inadequate ability of the model to describe natural variability in the data. The problem of non-linear effects is addressed, as it has been demonstrated to be a major source of error in the numerical values retrieved by more simple, linear-based approaches. Non-linear effects are especially critical for the retrieval of surface parameters where both scattering and absorption effects are coupled, as well as in the cases of significant multiple-scattering contributions. However, sophisticated modeling approaches can handle such non-linear effects, which are especially important over vegetated surfaces.

All the data used in this study were acquired during the 1991 Multisensor Airborne Campaign (MAC-Europe), as part of the European Field Experiment on a Desertification-threatened Area (EFEDA), carried out in Spain in June–July 1991.

2. DATA PREPROCESSING STEPS

The AVIRIS Data Facility provides users with spectrally, radiometrically, and geometrically calibrated data, but significant additional processing steps are required by the end user based on the final application. Processing steps are critical, because of the necessity of geometrical registration in order to properly account for solar illumination and viewing geometry in the spectral reflectance modeling, and the presence of some spatial noise in the data (which must be removed before any inversion technique is applied).

Geometric processing includes registration (geocoding), with appropriate resampling if the final output is to be in a cartographic reference. Because of the high stability of the ER-2 platform and the roll-angle compensation of the AVIRIS instrument, geometric registration of AVIRIS data is simple compared to that of other airborne systems. Navigation data for the ER-2 were used for a preliminary geometric correction (including panoramic distortion due to aircraft altitude and scan angle). The result was re-corrected to UTM projection by using a first-degree polynomial warping technique. Because the study area is quite flat (height differences of less than 20 m over the full scene), the additional sophistication required in topographically structured areas is not necessary in our case.

A problem encountered in the retrieval of parameters from AVIRIS data is the presence of some kind of spatial coherent noise pattern. This noise does not become apparent in the original images; however, it turns out to be very significant in the retrieval of some parameters, such as atmospheric water vapor. Removal of this spatial noise is required to interpret spatial variability derived in the resulting water vapor map. Filtering methods have to be used to keep the spatial structure present, while eliminating most of the interfering noise. The approach for removing this noise from the image is similar to that used by Rose (1989). The algorithm works over the power spectrum in the Fourier transform of the image (see Fig. 1). The noise is characterized by systematic spikes. Each spike is modeled as a double Gaussian, and the center position and width of the Gaussians are empirically determined from the

display of the power spectrum by assuming an exponential relationship between the distances of the spike centers to the origin of spatial frequencies, and the widths and amplitudes of the spikes.

A critical problem in the pre-processing of AVIRIS data is the instability in spectral channel positions. Although for recent data this problem has been greatly reduced (Figs. 2 and 3), validation of the spectral calibration is necessary before applying inversion techniques. One spectral sensitivity test is based on the derivation of water vapor maps on a channel-by-channel basis for all the channels included in the spectral range between 850 and 1100 nm. A second-degree polynomial is assumed for surface reflectance in this spectral range and the model applies only over bare soil (dry) areas where no coupling absorption due to liquid water content of vegetation (Fig. 4) is expected to give disturbances (Carrere and Conel, 1993). In principle, the value of water vapor derived from each channel should be always the same (within the range allowed by noise). Systematic tendencies in the retrieved water vapor values (especially overestimation in one edge of the absorption band and underestimation in the other edge of the band) are an indication of spectral shift. The water vapor values can be used to estimate spectral shifts and provide a first-order correction for that. An alternative to these image-based approaches is the use of simultaneous ground measurements of reflectance; however, they are sensitive to other uncertainties, so that image-based auto-calibrations are preferable to provide a temporal series of consistent data.

3. PHYSICAL MODELING OF SURFACE REFLECTANCE AND TRANSFER OF RADIATION THROUGH THE ATMOSPHERE

Atmospheric effects are modeled by using a modified version of the Modtran 2 code (Green et al., 1991). Modifications are related only to computational efficiency, and the physics and parameters used in Modtran are unchanged. Limitations in the atmospheric model are then directly related to the accuracy of Modtran to represent atmospheric processes and the availability of some additional data to model the vertical profile. In the absence of the external measurements, the vertical profile is constrained by the altitude of the target for which the reflectance is derived (Green et al., 1993).

As the model is intended for application over vegetated surfaces, emphasis is placed on the modeling of the vegetation and soil components. The surface reflectance model has been developed by combining independent elements: a model for the spectral reflectance and transmittance of leaves, a model for the reflectance of the soil background, and a model for the canopy structure consisting of leaves over the background (Nilson and Kuusk, 1989; Kuusk, 1994). For the reflectance and transmittance of the leaves, an adaptation of the "prospect" model (Jacquemoud and Baret, 1990) is used. The main advantage of this parameterization is that only three parameters (leaf specific biomass, leaf chlorophyll concentration, and leaf liquid water content) determine the spectral reflectance and transmittance of the leaves over the range 0.4–2.5 μm with reasonable accuracy. For the reflectance of bare soil, the model used starts from the same assumptions as the "soilspect" model (Jacquemoud et al., 1992)—that is, separability between macroscopic morphological structure of the soil (giving angular dependences), assumed to be wavelength independent, and the microscopic optical properties (single scattering albedo), assumed to be wavelength dependent. The difficulties in modeling angular behavior, and, especially, spectral behavior, of bare soil reflectances are well known, and a pragmatic modeling with simple assumptions is all that can be expected for realistic approaches. Trying to cover the most general situations possible, the canopy model developed in this case uses eight parameters to characterize the canopy: leaf-area index (LAI), ground vegetation cover, canopy height, two parameters determining leaf distribution, and three more canopy structural parameters. Some structural and hot-spot effects are included only in first-order scattering contributions, while multiple scattering contributions are calculated by using a discrete-ordinate code (applied to a simplified canopy model to save computation time, as architectural effects have less importance for multiple-scattering contributions). To account for the effects of the direct/diffuse irradiance ratio and to model directional irradiance, the surface reflectance model is coupled with an atmospheric model, which is actually a modification of a part of the 6S code. The atmospheric model provides the irradiance field over the scene as a function of wavelength, as the diffuse/total irradiance ratio is highly dependent on wavelength.

Once the surface and atmospheric models are coupled, measured radiances in AVIRIS channels can be inverted to fit the model and give the full set of required surface and atmospheric parameters to explain the measured radiance values. The model runs with a spectral resolution of 2.5 nm, and full bidirectional effects are considered for each single 2.5-nm channel. After final reflectance is calculated for each 2.5-nm channel, AVIRIS bands are simulated by using a Gaussian filter for each band, with the FWHM given by the specifications for the AVIRIS data being used. The final accuracy depends essentially on the accuracy with which the central band positions are known (see Figs. 2 and 3). For old AVIRIS data, the uncertainty in band center positions was such that the spectral band position was adjusted as a parameter. After 1994, the spectral calibration (see Fig. 3) is precise enough to use the spectral model without additional fitting in spectral shifts.

4. RETRIEVAL OF ATMOSPHERIC AND SURFACE PARAMETERS FROM AVIRIS DATA: A MODEL INVERSION TECHNIQUE

After a theoretical model is available, the second step is the development of an appropriate inversion technique in order to retrieve information from the measured data (Jacquemond, 1993). The inversion technique is a critical

issue. Three main aspects have to be considered. The first one is that the model will not be able to fit the data perfectly, and that some degree of freedom must be allowed in the inversion method. In this case, we use a multi-resolution constrained method to isolate pixels to which the model does not apply and to obtain more robust estimates from those pixels where the model does apply. The second aspect is the problem of noise in the data. In the case of AVIRIS, two types of noise have to be taken into account: the spatial noise (Rose, 1989; see also Fig. 1) and the problem of knowing the exact spectral position of each channel (see Figs. 2 and 3). The spectral stability being a critical issue, the inversion technique must allow some kind of fine tuning in the center positions of channels (or equivalent recalibration in the measured radiances), so that the model can properly fit the measured data. The third aspect is computational efficiency. Because of the large number of channels and parameters in the model, any optimization becomes critical. The use of first guesses as accurate as possible to start the iterative inversion is critical to decrease the number of iterations needed. In this case, we use semiempirical relationships derived by running the model over typical situations and fitting the results to polynomials, so that first guesses can be easily estimated for initialization of model parameters before inversion. The method used for numerical inversion of the reflectance model is the downhill simplex method, with two limiting conditions: maximum error and maximum number of iterations allowed. This method has been preferred over potentially more powerful algorithms (Smith, 1993) because of computational simplicity and robustness to disturbances.

5. RESULTS: THE IMPORTANCE OF NON-LINEAR EFFECTS

a. atmospheric parameters retrieval

The results obtained for atmospheric water vapor retrieval (Fig. 5) agree with the simultaneous radiosoundings that are available as part of the intensive field campaign in the EFEDA'91 experiment. Radiosoundings were made exactly from the same spatial position as the image shown in Figs. 5, 6, and 7 and were calibrated and quality checked as part of the atmospheric experiment. The problem in the intercomparison with AVIRIS data is the altitude of the radiosoundings. Extrapolation to the highest atmospheric levels requires some modeling by using a standard atmosphere, as the altitude of AVIRIS (20 km) is over the available radiosounding measurements. The correspondence of values is in the order of the experimental errors. Although only atmospheric water vapor has been taken into account in this study, the technique used here can be used to retrieve other atmospheric constituents (Barduci and Pippi, 1995). Retrieval of other atmospheric constituents has not been attempted in this area because, as the area is so flat, no spatial variability is expected. Aerosol concentration is also retrieved by the algorithm, but no rigorous attempt has been made to validate such retrievals because of the insufficient quality of in-situ atmospheric transmittance data available for the area. Intercomparisons between AVIRIS data and simultaneous Differential Absorption Lidar (DIAL) data have been made, but no clear conclusions can be derived from such comparisons because of the different type of data as well as differences in spatial resolution.

b. surface parameters retrieval

The main parameter in which we are interested in this study is the leaf (canopy) water content, as part of a more general project to provide inputs to surface energy balance models by using remote sensing data. Estimated values of canopy water content agree reasonably with ground measurements in the case of low LAI (or low vegetation cover), even when a linear model is used for the retrieval of the amount of water in the leaves. As the LAI increases, the non-linear effects due to multiple scattering contributions (Figs. 8 through 13) and canopy geometry (Fig. 14) start to be significant, and we have found errors as large as case (b) in Table 1. In order to explain such anomalous behavior, we have developed the alternative, more sophisticated method previously described, in which a full non-linear model is used to retrieve simultaneously both LAI and leaf water content as separate contributions to the measured reflectance. The new results require the use of a large spectral window in order to isolate the contribution of water from that of LAI and fractional cover separately. As the spectral window used is enlarged, the problem becomes linked to the variability, and uncertainty, in soil background reflectances for non-dense canopies. In the present algorithm, this effect is compensated by allowing variability in surface reflectance (actually total albedo) as a new free parameter for a given single-scattering albedo contribution for bare soil. In the case of large soil variability, a way to model the single-scattering albedo of the soil as a function of soil composition (still keeping soil roughness as an additional free parameter) must be introduced in the model.

Table 1. Comparison of the retrievals of canopy water content from AVIRIS data and simultaneous ground measurements over two reference corn fields, by using a linear fit to a reference absorption depth and compensation of atmospheric water vapor absorption by using the Modtran 2 radiative transfer code. The extreme case (b) is a clear example of the differences that can be introduced due to non-linear effects of multiple scattering.

	LAI value	Estimated canopy water content (g/m^2)	Measured canopy water content (g/m^2)
(a)	0.87	763	710
(b)	3.31	5728	178

A pending work for the future is the validation of the theoretical model developed, as well as the inversion technique, over areas with more ground-truth data for all the required surface and atmospheric parameters. Improvements in the model are also possible, mainly by incorporating new Modtran versions in the atmospheric module. Because of the recent improvements in the AVIRIS instrument, the advantages of using advanced modeling/inversion techniques will be fully realized when working with new data, instead of the 1991 data used in the present study.

ACKNOWLEDGMENTS

This work has been supported by the Commission of the European Union (Project EV5V-CT93-0284, DG12 DTEE) and the Spanish Inter-Departmental Commission for Science and Technology (CICYT Project AMB 94-0019-C05-CE). A portion of the research described in this paper was performed at the Jet Propulsion Laboratory, California Institute of Technology, under a contract with the National Aeronautics and Space Administration. J.F.M.'s work at JPL is supported by a grant from the Spanish Ministry of Education and Science.

REFERENCES

Barduci A., I. Pippi, "Retrieval of atmospheric parameters from the hyperspectral image data," Proceedings IGARSS'96 Symposium, Firenze, Italy, 1995, vol. I, pp. 138-140, 1995.

Carrere V., J.E. Conel, "Recovery of atmospheric water vapor total column abundance from imaging spectrometer data around 940 nm - Sensitivity analysis and application to Airborne Visible/Infrared Imaging Spectrometer (AVIRIS) data," Remote Sensing Environ., vol. 44, pp. 179-204, 1993.

Green R.O., J.E. Conel, J.S. Margolis, C.J. Bruegge, and G.L. Hoover, "An inversion algorithm for retrieval of atmospheric and leaf water absorption from AVIRIS radiance with compensation for atmospheric scattering," Summaries of the Third JPL AVIRIS Workshop, JPL Pub. 91-28, pp. 51-61, Jet Propulsion Laboratory, Pasadena, California, 1991.

Green R.O., J.E. Conel, and D.A. Roberts, "Estimation of aerosol optical depth and additional atmospheric parameters for the calculation of apparent reflectance from radiance measured by the Airborne Visible/Infrared Imaging Spectrometer," Summaries of the Fourth Annual JPL Airborne Geoscience Workshop, JPL Pub. 93-26, vol. 1, pp. 73-76, Jet Propulsion Laboratory, Pasadena, California, 1993.

Jacquemoud S., "Inversion of the Prospect+SAIL canopy reflectance model from AVIRIS equivalent spectra: theoretical study," Remote Sensing Environ., vol. 44, pp. 281-292, 1993.

Jacquemoud S., and F. Baret, "Prospect: a model of leaf optical properties spectra," Remote Sensing Environ., vol. 34, pp. 75-91, 1990.

Jacquemoud S., F. Baret, and J.F. Hanocq, "Modeling spectral and bidirectional soil reflectance," Remote Sensing Environ., vol. 41, pp. 123-132, 1992.

Kuusk A., "A multispectral canopy reflectance model," Remote Sensing Environ., vol. 50, pp. 75-82, 1994.

Nilson T., and A. Kuusk, "A reflectance model for the homogeneous plant canopy and its inversion," Remote Sensing Environ., vol. 27, pp. 157-167, 1989.

Rose J.F., "Spatial interference in the AVIRIS imaging spectrometer," Photogram. Engin. Remote Sensing, vol. 55, pp. 1339-1346, 1989.

Smith J.A., "LAI inversion using a back-propagation neural network trained with a multiple scattering model," IEEE Trans. Geosci. Remote Sensing, vol. 31, pp. 1102-1106, 1993.

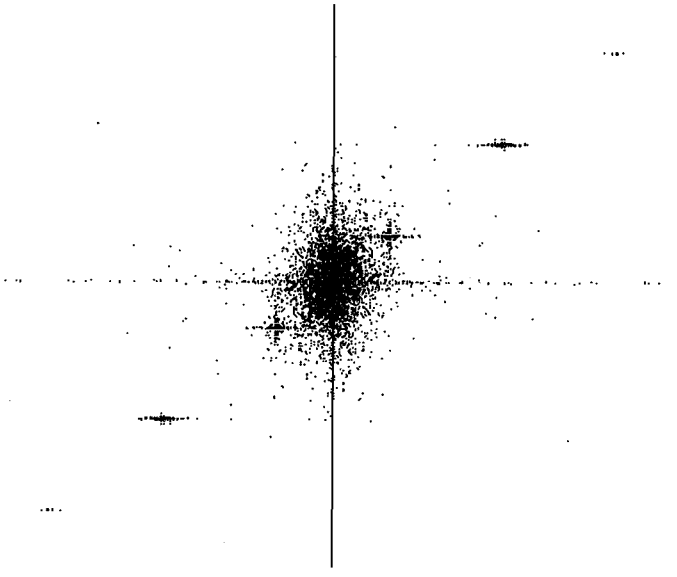

Fig. 1 Fourier power spectrum of the derived spatial water vapor map from AVIRIS data by using a non-linear fit to Modtran-derived radiance and compensation for leaf water absorption. The regular pattern of noise spikes (crosses) along the diagonal causes the spatial interference observed in the original water vapor map, which has been removed in the map shown in Fig. 5.

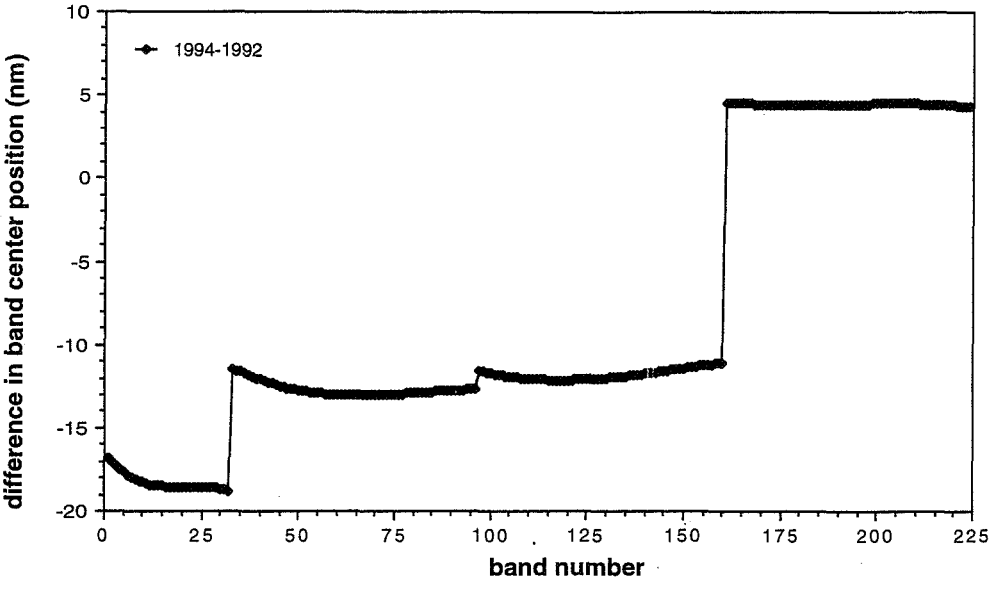

Fig. 2 Difference in AVIRIS band center positions between 1992 and 1994. Changes in the band center positions over time must be accurately known in order to use data inversion techniques based on radiative transfer modeling.

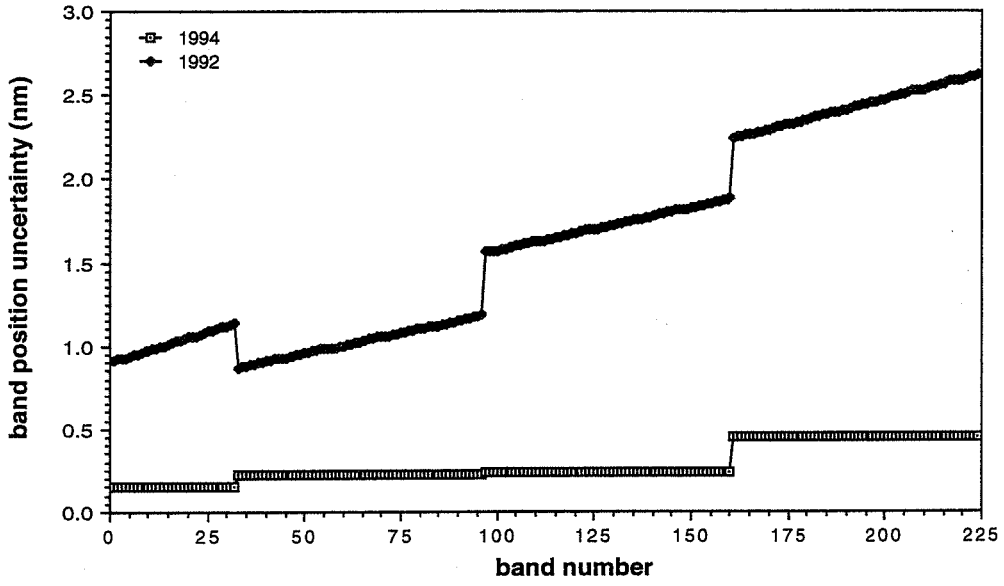

Fig. 3 Uncertainty in band center position, for each AVIRIS channel, for 1992 and 1994 data. Present technical specifications provide data accurate enough to make possible the use of theoretical model-inversion methods which require very precise radiometric and spectral calibrations, with a stability better than 0.5 nm over the full spectral range. Such spectral stability was a major difficulty for old AVIRIS data.

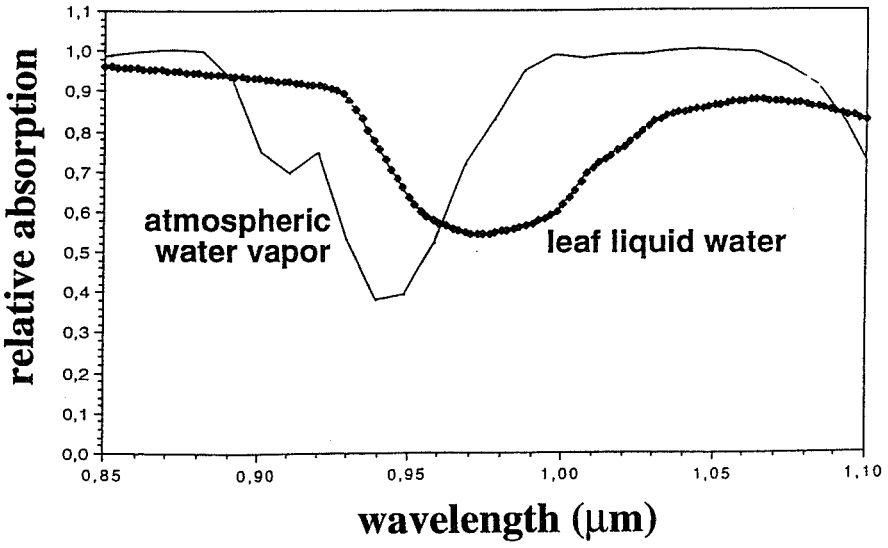

Fig. 4 Coupling of spectral absorption bands for atmospheric water vapor and leaf liquid water in vegetated surfaces. Separation between both absorption components is required to determine accurately atmospheric water vapor, giving also surface liquid water content as residual information.

Fig. 5 Column atmospheric water vapor map derived from AVIRIS for one of the pilot areas of the EFEDA'91 experiment in Central Spain (June 29, 1991), by using a model-inversion technique based on the radiative transfer code Modtran 2.

Fig. 6 Leaf liquid water content derived from AVIRIS data for the same area shown in Fig. 5, obtained as a secondary result in the determination of atmospheric water vapor by non-linear fitting of the shape of the absorption bands (as shown in Fig. 4)

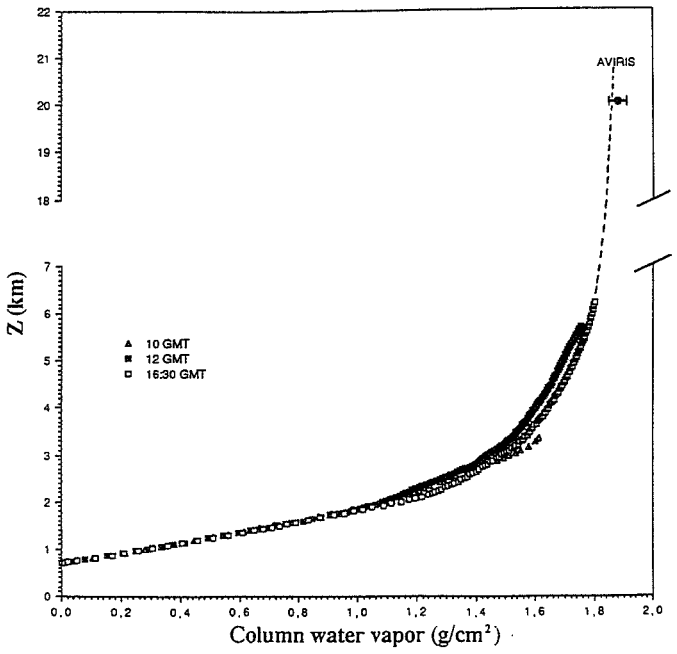

Fig. 7 Comparison between AVIRIS-derived column-integrated atmospheric water vapor content and simultaneous radiosoundings in the area during the EFEDA'91 experiment. The horizontal bar in the AVIRIS-derived value corresponds to the standard deviation within the full scene (about 126 km^2).

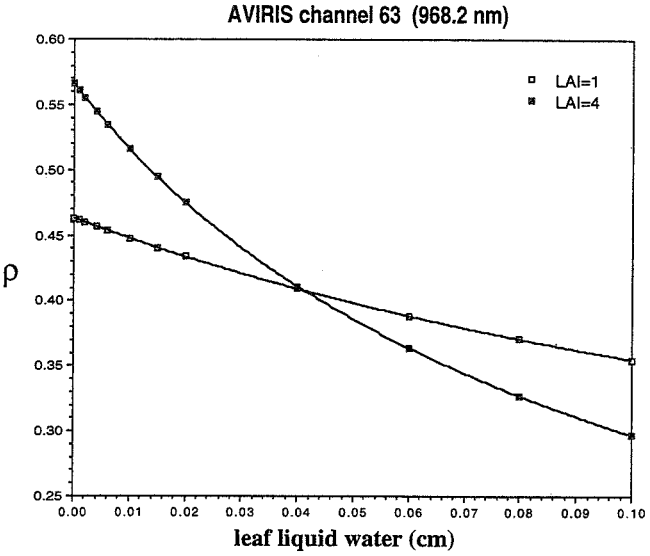

Fig. 8 Relationship between reflectance in AVIRIS channel 63 (the closest to the center of the liquid water absorption band) and leaf liquid water for two values of Leaf Area Index, keeping as constant the rest of the parameters in the model. Differences are essentially due to canopy multiple scattering contributions.

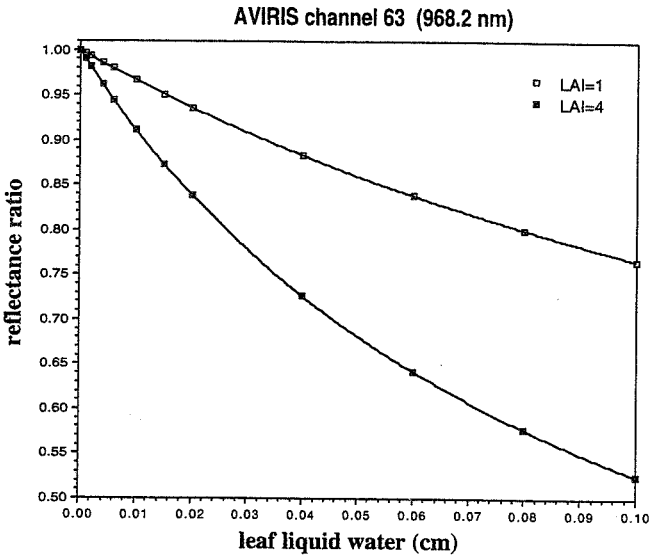

Fig. 9 All the retrievals of liquid water content are somehow based on the ratio between the measured reflectance in the center of the absorption band and the estimated 'maximum' reflectance (in the case of no absorption) for the same other conditions. The changes in this ratio with LAI due to non-linear effects are so important that the retrieved value can vary by more than a factor 3, as in the case illustrated in the figure.

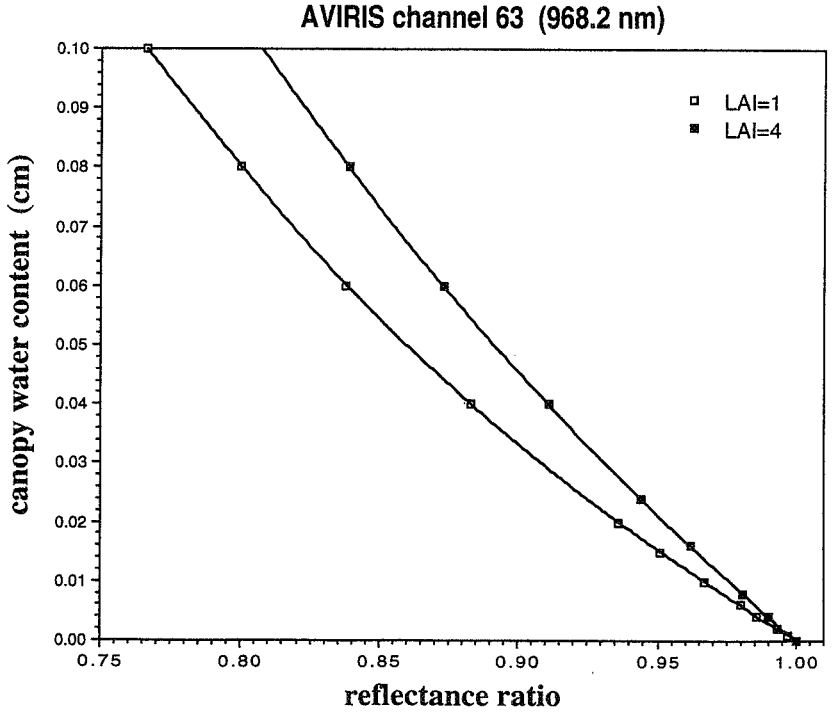

Fig. 10 The same reflectance ratio plotted in Fig. 9, but now as a function of the total canopy water content (LAI*leaf liquid water density). Even when total canopy water is considered, the relationship is still not unique because of non-linear effects.

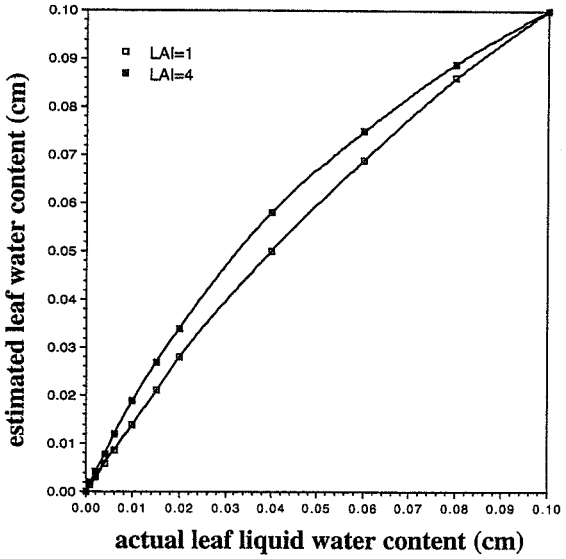

Fig. 11 Comparison between the actual leaf water content and the leaf water content that would be retrieved by using a linear-mixing algorithm (neglecting non-linear effects), but with proper compensation for the 'depth of reference absorption' as a function of LAI. Non-linear effects still produce differences in this case.

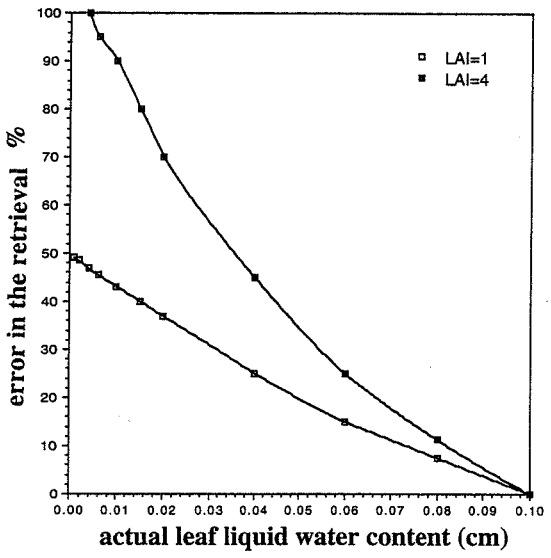

Fig. 12 Relative error in the retrieval of leaf water content by assuming a linear-mixing approach based on 'maximum absorption' features, for two reference LAI values, for the same case shown in Fig. 11.

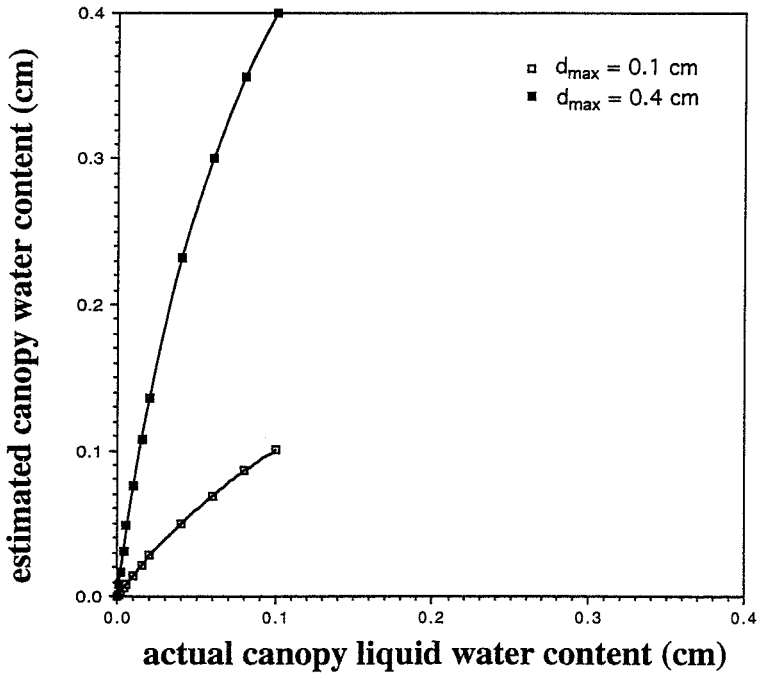

Fig. 13 Comparison between the actual canopy water content and the canopy water content that would be retrieved by using a linear-mixing algorithm (neglecting non-linear effects) and using the 0.4 cm 'depth' absorption as reference, for two values of LAI. The strong overestimation in the case of actually very low water content is the reason for the case (b) shown in Table 1. Errors are actually enhanced because of the coupling to the atmospheric absorption of water vapor and due to the change in the shape of the absorption band with varying LAI.

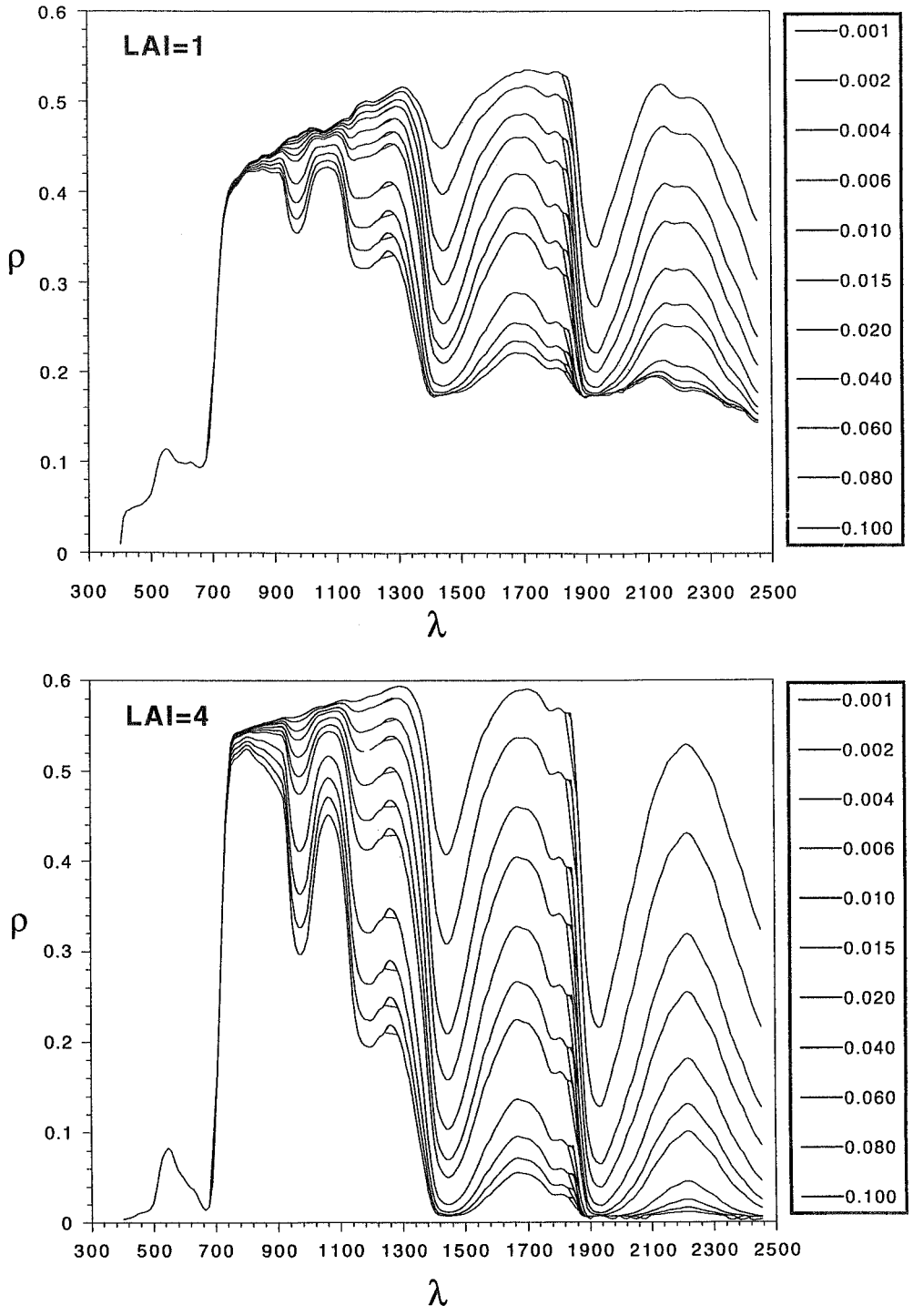

Fig. 14 Simulation of surface reflectance in AVIRIS channels for two different values of Leaf Area Index and several values of leaf water content (numbers on the right column correspond to leaf water content in cm and the order, top-to-bottom, is the same as the curves in both figures). Reflectance values are simulated by a full spectral-bidirectional model, including soil-vegetation multiple scattering, as described in the text. The artifacts appearing around 707 nm, 1286 nm, and 1866 nm are due to the overlaps of channels between adjacent spectrometers, as the simulation is done independently for each AVIRIS channel.

SUBPIXEL SNOW-COVERED-AREA AND SNOW GRAIN SIZE FROM MIXTURE ANALYSIS WITH AVIRIS DATA

Thomas H. Painter[1,2], Dar A. Roberts[1,2], Robert O. Green[1,2,3] and Jeff Dozier[1,2,4]

[1]Department of Geography, University of California, Santa Barbara 93106
[2]Institute for Computational Earth System Science, University of California, Santa Barbara 93106
[3]Jet Propulsion Laboratory, California Institute of Technology, Pasadena, California 91109
[4]School of Environmental Science and Management, University of California, Santa Barbara 93106

INTRODUCTION

Snow-covered-area (SCA) and snow grain size are crucial inputs to hydrologic and climatologic modeling of alpine and other seasonally snow-covered regions. SCA is necessary to parameterize energy budget calculations in climate models, to determine in which regions point snowmelt models are to be run for distributed snowmelt modeling efforts [Harrington et al., 1995] and to provide a basis from which estimates of snow water equivalent (SWE) may be made [Martinec and Rango, 1981]. Snow grain size, SWE and snow impurities determine the spectral albedo of snow, which controls the net solar flux at the snowpack surface. Snow albedo is of the utmost importance in snowmelt modeling, yet the difficulty with which grain size, SWE, and impurities are mapped has left the spatial distribution of snow albedo in alpine catchments poorly understood [Kirnbauer et al., 1994]. The Airborne Visible/Infrared Imaging Spectrometer (AVIRIS) has been used to estimate sub-pixel snow-covered-area and snow grain size independently [Nolin, 1993]. In this paper we present a technique which improves estimates of both snow parameters by treating their mapping simultaneously.

BACKGROUND

The spectral signature of snow is characterized by near-100% reflectance in visible wavelengths and moderate reflectance in NIR wavelengths. While visible reflectance is strongly affected by absorbing impurities and shallow snow, and nearly independent of grain size, NIR reflectance is primarily dependent on grain size with reflectance decreasing as grain size increases. Snow reflectance is most sensitive to grain size in the wavelength range 1.0 - 1.3μm, which spans the diagnostic ice absorption features at 1.03μm and 1.26μm. The large spectral contrast of snow reflectance is due to a variation of seven orders of magnitude in the absorption coefficient of ice at wavelengths from 0.4 - 2.5μm [Dozier, 1989]. The above relationships are those exploited in grain size mapping [Dozier and Marks, 1987; Nolin, 1993].

Alpine snow-covered regions frequently exhibit large grain size gradients, correlated strongly with altitude and aspect. When snow is deposited on the surface, grains immediately begin the modifying process called 'metamorphism'. Initially, grain size decreases when thermodynamically-unstable dendritic crystal branches are destroyed through collisions and water vapor transfer. Larger grains then grow at the expense of smaller grains via vapor transport and melt-refreeze. Because metamorphism is faster at higher temperatures and under larger temperature gradients [Langham, 1981], the absorption of short-wave radiation at the snowpack surface and the transfer of longwave radiation at and below the snowpack surface play dominant roles in grain modification. Alpine regions then exhibit grain size gradients driven by aspect and elevation with largest grains at low elevations on southerly aspects and smallest grains at high elevations on northerly aspects. The sensitivity of snow spectral reflectance to grain size translates these grain size gradients into spectral gradients.

In *Painter et al. 1995*, we demonstrated that due to these grain size and spectral gradients, multiple snow endmembers spanning the imaged domain's grain size gradient are required to accurately estimate sub-pixel SCA with spectral mixture analysis. Succinctly put, mapping sub-pixel SCA requires knowledge of the spatial grain size distribution. Estimates of grain size have been made previously from optical data, yet these have relied on the assumption of pure-snow pixels [Dozier and Marks, 1987; Nolin, 1993]. The propensity of mixed pixels in alpine- and forested-regions makes such an assumption suspect. Hence, mapping grain size distribution requires knowledge of sub-pixel SCA distribution. It then follows that the problems of estimating sub-pixel snow fraction and snow grain size are intimately tied.

METHODS AND DATA

We present here a technique which simultaneously estimates sub-pixel SCA and snow grain size by optimization of mixture analysis with multiple snow endmembers. From AVIRIS data collected over Mammoth Mountain, CA on April 5,1994, a suite of snow image endmembers corresponding to the region's grain size range were extracted. Mixture models with fixed vegetation, rock, and shade image endmembers were applied with each snow endmember. For each pixel, the snow-fraction estimated by the model with least mixing error (RMS) was selected to produce an optimal map of sub-pixel SCA [Figure 1]. Grain size for the snow within each pixel was then estimated by the grain size of the selected snow endmember [Figure 2]. This step bypasses the pure-snow pixel assumption by producing a snow grain size estimate for any permutation of snow, vegetation, rock, and shade, provided that the snow-fraction is non-zero.

Numerical simulations demonstrate that in the simple linear mixing case, the technique is very accurate at estimating sub-pixel SCA and snow grain size for any permutation of surface constituents, provided that the non-snow endmembers are well-known and the snow fraction is non-zero. To validate image results, optimal sub-pixel SCA from AVIRIS data were compared with coregistered aerial photos and individual model SCA maps. Grain size results were compared with size distributions estimated by stereology of field snowpack samples [Davis et al., 1987] and contrasted with AVIRIS results using techniques incorporating the pure-snow assumption.

DISCUSSION

Results demonstrated that the technique is accurate at estimating sub-pixel SCA and appears to be more accurate at estimating snow grain size than pure-snow assumption techniques, particularly in forested and patchy-snow areas. Some limitations do exist though when applying the technique to AVIRIS data. We mentioned above that numerical simulations demonstrated that the technique is very accurate in the linear mixing case; however, in forested and thin-snow areas, mixing may be non-linear. Errors are then introduced into the estimates of SCA and grain size. Additionally, in using image endmembers, the number of snow endmembers is limited (e.g. six snow endmembers in this work) whereby the resolution of grain size will be coarse. Further work needs to *i)* evaluate non-linear mixing in alpine regions, *ii)* incorporate techniques from the literature to compensate for non-linearity in vegetated areas, *iii)* continue with the development of a technique to map thin/impure snow, and *iv)* incorporate snow reference endmembers at far greater grain size resolution for grain size estimates. The incorporation of reference endmembers will require the elimination of discrepancies between modeled spectral signatures and those derived from AVIRIS.

ACKNOWLEDGEMENTS

This work was sponsored under NASA EOS MTPE grant NAGW-2602 and performed at the University of California, Santa Barbara and the Jet Propulsion Laboratory, Pasadena, CA. We wish to thank Anne K. Nolin for the use of AVIRIS grain size mapping code.

REFERENCES

Davis, R.E., J. Dozier, and R. Perla, 1987, Measurement of snow grain properties, in *Seasonal Snowcovers: Physics, Chemistry, Hydrology*, H.G. Jones and W.J. Orville-Thomas, eds., pp63-74, NATO ASI Series, D. Reidel Publishing Company.

Dozier, J., 1989, Spectral signature of alpine snow cover from the Landsat Thematic Mapper, *Remote Sensing of Environment,* v28, pp9-22.

Dozier, J. and D. Marks, 1987, Snow mapping and classification from Landsat Thematic Mapper data, *Annals of Glaciology*, v9, pp97-103.

Harrington, R.F., K. Elder, and R.C. Bales, 1995, Distributed snowmelt modeling using a clustering algorithm, *Biogeochemistry of Seasonally Snow-Covered Catchments,* IAHS Publication 228, pp167-174.

Kirnbauer, R., G. Bloschl, and D. Gutknecht, 1994, Entering the era of distributed snow models, *Nordic Hydrology,* v25, pp1-24.

Langham, E.J., 1981, Physics and properties of snowcover, *Handbook of Snow*, D.M. Gray and D.H. Male, eds., pp275-337, Pergamon Press.

Martinec, J. and A. Rango, 1981, Areal distribution of snow water equivalent evaluated by snow cover monitoring, *Water Resources Research*, v17, n5, pp1480-1488.

Nolin, A.W., 1993, *Radiative Heating in an Alpine Snowpack*, Ph.D. Thesis, University of California, Santa Barbara.

Painter, T.H., D.A. Roberts, R.O. Green, and J. Dozier, 1995, Improving alpine-region spectral unmixing with optimal-fit snow endmembers, in *Summaries of the Fifth Annual JPL Airborne Earth Science Workshop*, R.O. Green, ed., JPL Publication 95-1, v1, Jet Propulsion Laboratory, Pasadena, CA, pp125-128.

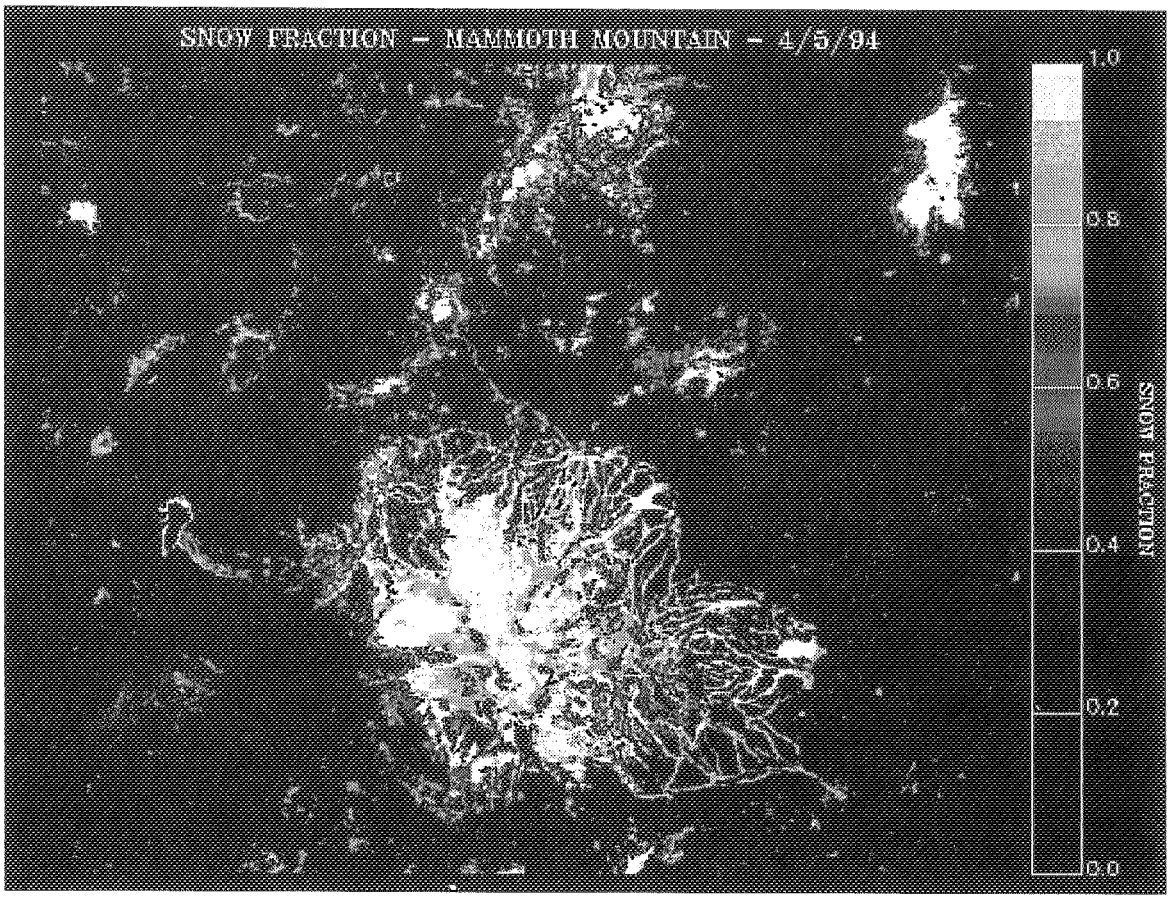

Figure 1. AVIRIS-derived subpixel snow fraction at Mammoth Mountain, CA, optimized with multiple snow endmembers.

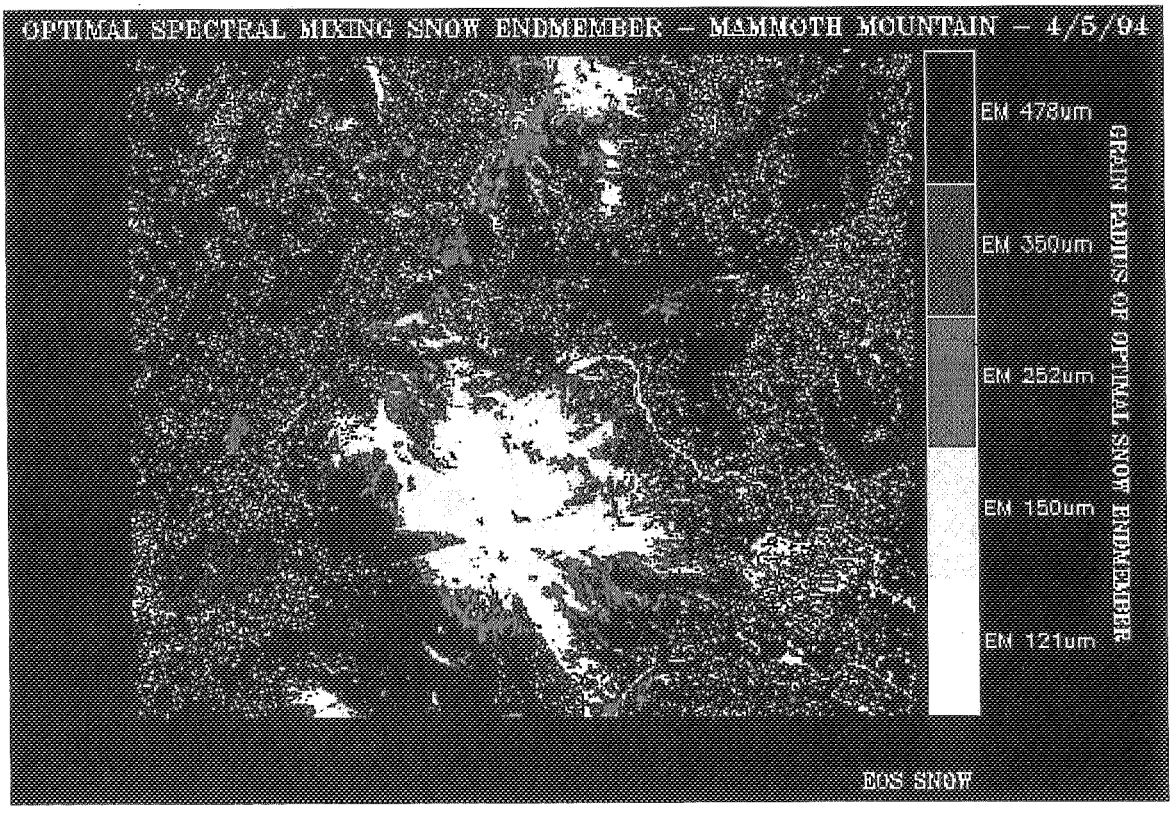

Figure 2. Map of snow endmember used and grain size estimate at Mammoth Mountain, CA from AVIRIS.

ALGAL ACCESSORY PIGMENT DETECTION USING AVIRIS IMAGE-DERIVED SPECTRAL RADIANCE DATA

Laurie L. Richardson, Florida International University, Miami, Florida,
and Vincent G. Ambrosia, JCWS, Inc., NASA Ames Research Center, Moffett Field, California.

1. INTRODUCTION

Visual and derivative analyses of AVIRIS spectral data can be used to detect algal accessory pigments in aquatic communities (Richardson et al. 1994). This capability extends the use of remote sensing for the study of aquatic ecosystems by allowing detection of taxonomically significant pigment signatures which yield information about the type of algae present. Such information allows remote sensing-based assessment of aquatic ecosystem health, as in the detection of nuisance blooms of cyanobacteria (Dekker et al., 1992) or toxic blooms of dinoflagellates (Carder and Steward, 1985).

Remote sensing of aquatic systems has traditionally focused on quantification of chlorophyll *a*, a photoreactive (and light-harvesting) pigment which is common to all algae as well as cyanobacteria (bluegreen algae). Due to the ubiquitousness of this pigment within algae, chl *a* is routinely measured to estimate algal biomass both during ground-truthing and using various airborne or satellite based sensors (Clark, 1981; Smith and Baker, 1982; Galat and Verdin, 1989; Mittenzwey et al., 1992), including AVIRIS (Hamilton et al., 1993).

Within the remote sensing and aquatic sciences communities, ongoing research has been performed to detect algal accessory pigments for assessment of algal population composition (Gieskes, 1991; Millie et al., 1993; Richardson, 1996). This research is based on the fact that many algal accessory pigments are taxonomically significant, and all are spectrally unique (Foppen, 1971; Morton, 1975; Bjørnland and Liaaen-Jensen, 1989; Rowan, 1989). Aquatic scientists have been refining pigment analysis techniques, primarily high performance liquid chromatography, or HPLC, (e.g. Mantoura and Llewellyn, 1983 and Wright and Shearer, 1984) to detect specific pigments as a time-saving alternative to individual algal cell identifications and counts (Gieskes and Kraay, 1983; Leavitt et al., 1989; Lizotte and Priscu, 1993; Soma et al., 1993; Wilhelm et al., 1991). Remote sensing scientists (Dekker et al., 1992; Richardson et al., 1991, 1994) are investigating the use of pigment signatures to construct pigment libraries analogous to mineral spectral libraries used in geological remote sensing applications (Farrand and Harsanyi, 1995).

The accessory pigment approach has been used successfully in remote sensing using data from the Thematic Mapper (Richardson et al., 1991), low-altitude, multiple channel scanners (Dekker et al., 1992), field spectroradiometers (Dekker et al, 1992; Richardson, 1991, 1995) and the AVIRIS hyperspectral scanner (Richardson et al., 1994). Due to spectral and spatial resolution capabilities, AVIRIS is the sensor of choice for such studies. We present here our results on detection of algal accessory pigments using AVIRIS data.

2. METHODS

AVIRIS data were collected 13 April 1989 over leveed salt ponds in the vicinity of Moffett Field, California. The AVIRIS sensor was flown at an altitude of 19.8 km on NASA Ames Research Center's ER-2 high-altitude aircraft. Spectral profiles in the visible/near IR wavelengths (channels 1-94) for the various ponds were derived from the data using the ERDAS IMAGINE (version 8.2) image processing software system,

residing on a SUN SPARC-Station 2 at the Ecosystems Science and Technology Branch (Code SGE) at NASA Ames Research Center. No atmospheric corrections were made to the AVIRIS data. Profiles for specific ponds were derived by averaging the radiance values over the full extent of the pond, excluding any surface vegetation or levee surfaces. Spectral signatures were derived for all ponds containing various concentrations of algae and photosynthetic bacteria.

The AVIRIS derived spectra were further processed at Florida International University on a 386 Zenith personal computer using MATLAB (The MathWorks, Inc.), a high-performance computation oriented interactive software package. Processing included location and identification of accessory pigment absorbance features. Fourth order derivative spectra were generated by computing the cubic polynomial differentiations according to the simplified least squares procedure described in Savitzky and Golay, 1964, and previously used in processing both AVIRIS and spectroradiometer data (Richardson et al., 1994). Prior to the convolution procedure it was necessary to convert the spectral data to a fixed, uniform wavelength interval. Thus the AVIRIS derived spectra (band widths ranged from 8.30 to 11.22 nm) were fixed at 2 nm intervals. After the derivative spectra were computed, they were plotted and absorbance features identified by comparison with known pigment characteristics (Morton, 1975; Rowan, 1989) as well as our in-house algal spectral signature data base. Because the fourth derivative was used, absorption in the AVIRIS derived spectra could be directly compared with absorption in the derivative spectra.

3. RESULTS AND DISCUSSION

As discussed above, remote sensing of aquatic ecosystems has focused on mapping the distribution of chlorophyll *a*. Figure 1 is a one-band (band 30) AVIRIS image of the ponds that shows radiance data from 675.7-684.9 nm, which covers the chlorophyll red absorbance feature. Many of the ponds in the image appear the same. All ponds had dense, mixed populations of algae and cyanobacteria, and exhibit fairly uniform chlorophyll associated radiance.

Figure 2 is AVIRIS radiance data for band 23 (extracted from the same AVIRIS data set). Band 23 covers 606.8-616.0 nm, a spectral region specifically absorbed by the algal accessory pigment phycocyanin. In contrast to Figure 1, spectral variability is readily apparent among the individual ponds. In particular, ponds A and B are annotated for comparison. Ponds A and B appear virtually identical in Figure 1, but are distinctly different in Figure 2. This is due to varying amounts of cyanobacteria, which possess phycocyanin as a major light-harvesting accessory pigment, within the mixed populations of the two ponds. Thus pond B, which has a higher concentration of phycocyanin containing cyanobacteria, exhibits greater absorbance in band 23.

These differences are even more visible when analysing the AVIRIS derived spectra. Figure 3 shows spectra from both ponds. Each spectrum exhibits a typical cyanobacterial-dominated spectral radiance signature (Richardson et al., 1991, 1994) in which a green reflectance peak (due to red and blue absorbance by chlorophyll *a* as well as carotenoid absorbance in the blue) is accompanied by two absorbance features near 590 and 620 nm (due to the cyanobacterial accessory pigments phycoerythrin and phycocyanin respectively). The stronger absorbance due to the higher concentration of cyanobacteria in pond B is apparent when comparing the two spectra.

Accessory pigment estimates within spectral data can be enhanced using derivative analysis of spectra (Demetriades-Shah et al, 1990). Figure 4 shows the fourth derivatives of (smoothed) spectra from ponds A and B. In the derivative analysis, changes in the slope of a curve which are caused by absorbance features are represented as negative peaks, and reflectance features are seen as positive peaks. It can be seen that the chlorophyll *a* signal near 686, as well as atmospheric absorption features (e.g. at 760 nm) are virtually the same for each derivative spectrum. However, the phycoerythrin (near 590) and phycocyanin (near 620) peaks are different. As the areas under the peaks are directly proportional to the quantity of substances present which contain absorbance/reflectance qualities (Demetriades-Shah et al., 1990), this approach can be used to quantitate pigments (e.g. Bidigare et al., 1989; Goodin et al., 1993). When absorbance/reflectance features are very close

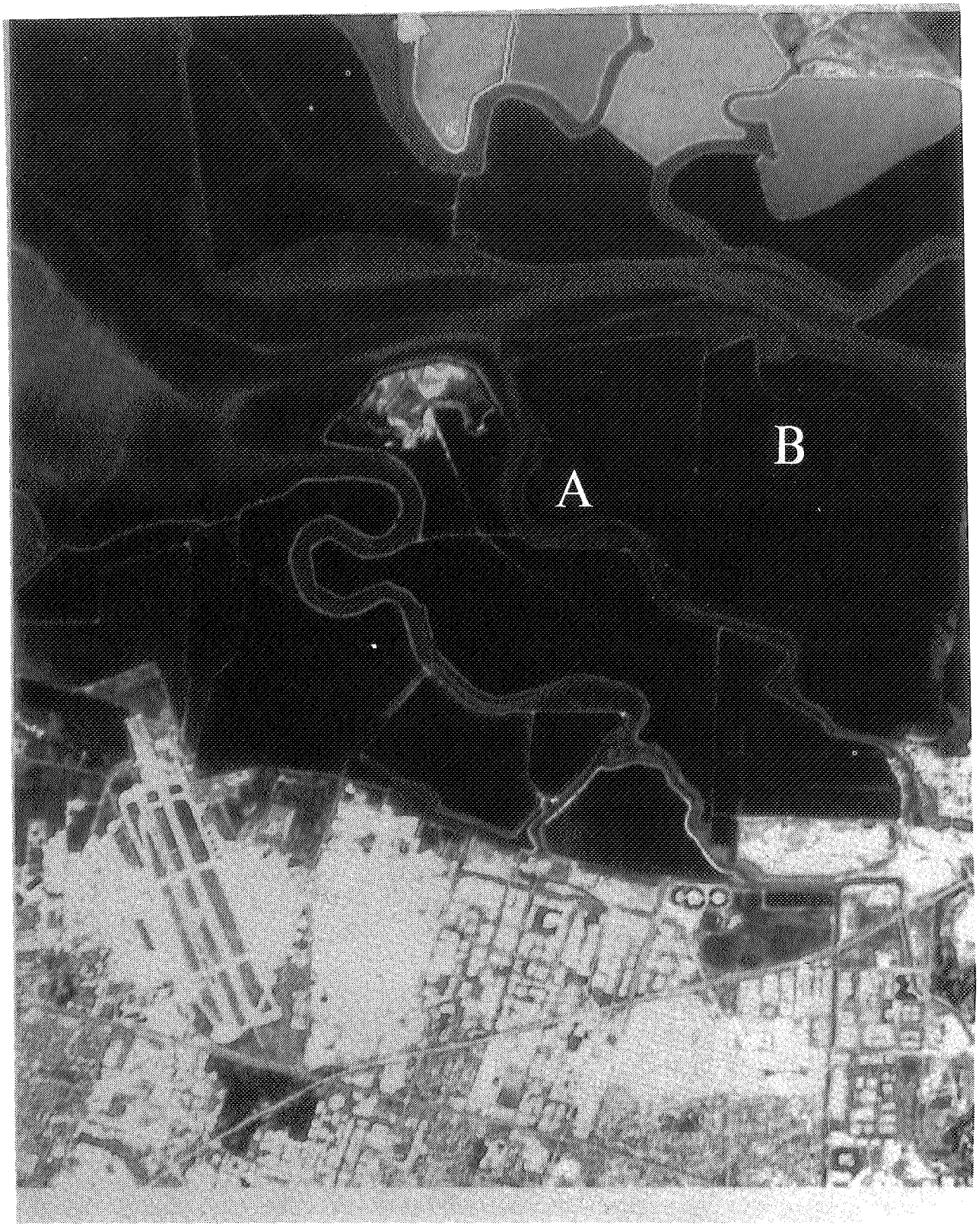

Figure 1. AVIRIS image (single band) of salt ponds near NASA Ames Research Center. Radiance data are from 675.7-684.9 nm (band 30) which covers the red absorbance feature of chlorophyll *a*.

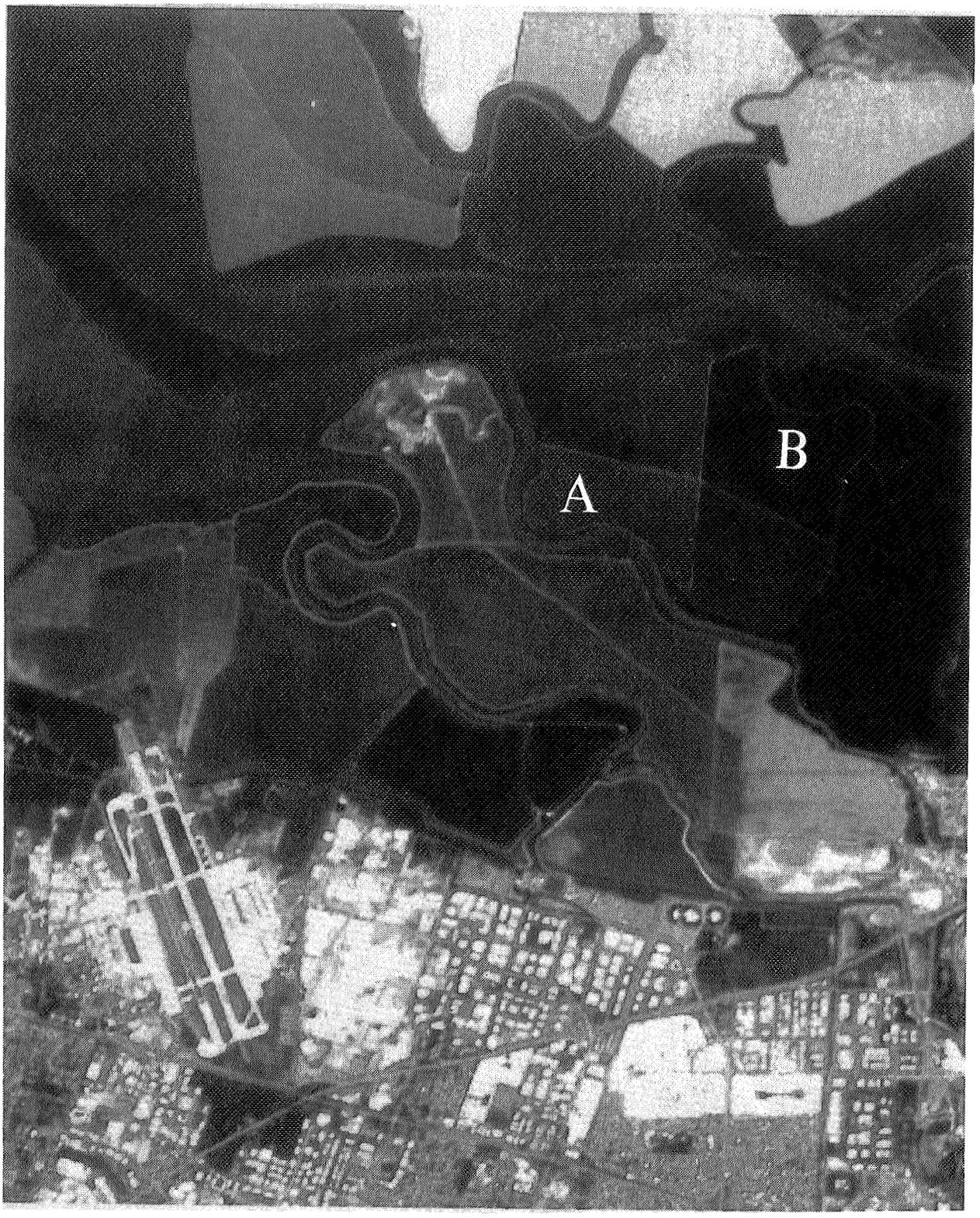

Figure 2. AVIRIS image (single band) of salt ponds near NASA Ames Research Center. Radiance data are from 606.8-616.0 nm (band 23), wavelengths specifically absorbed by phycocyanin.

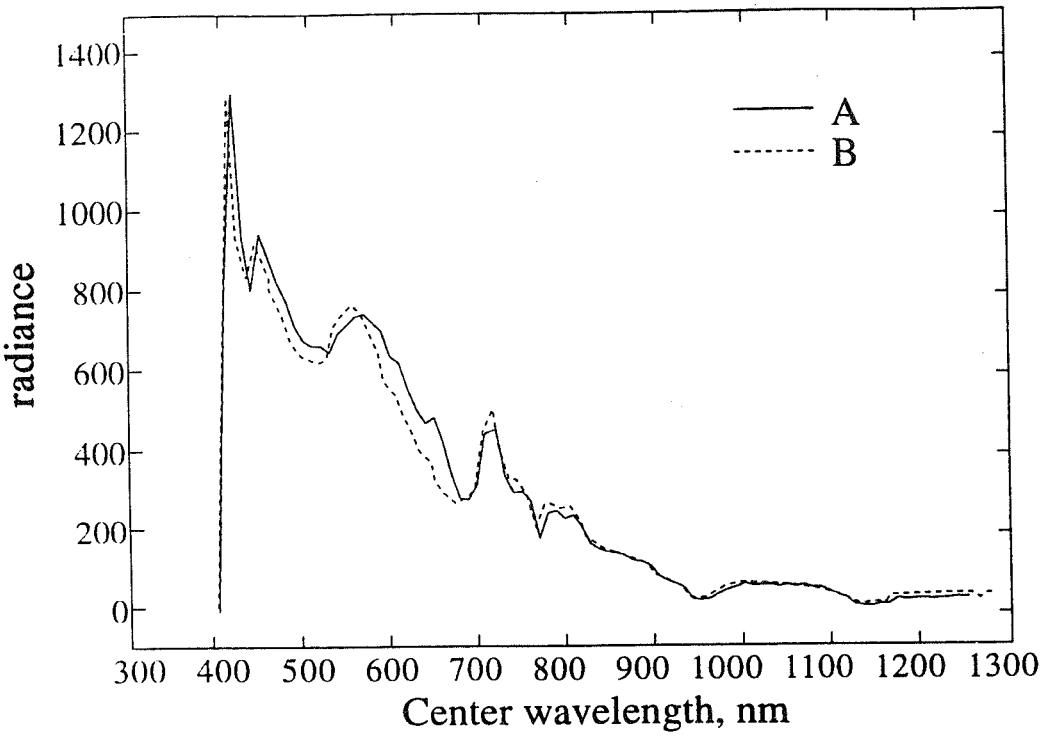

Figure 3. AVIRIS image-derived spectra of ponds A and B shown in Figures 1 and 2.

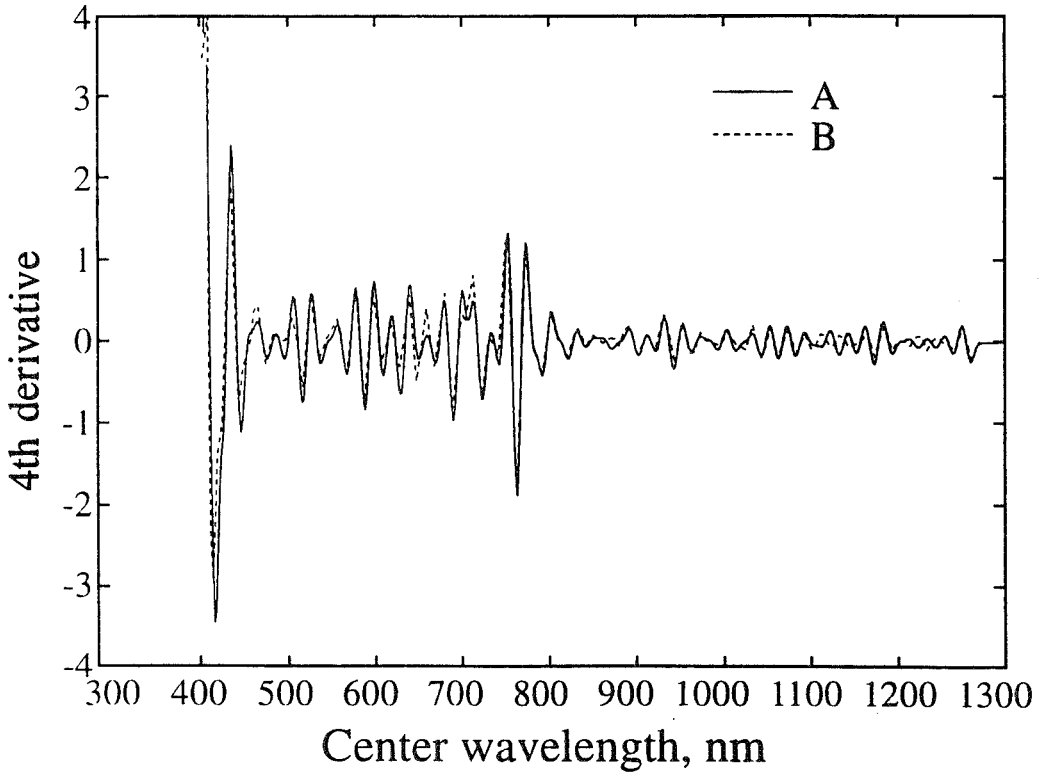

Figure 4. Fourth derivative of AVIRIS spectra shown in Figure 3.

together (spectrally), the fourth derivative must be used (Demetriades-Shah et al., 1990).

The detection of algal accessory pigments to study community structure and population dynamics of algae in aquatic ecosystems by remote sensing has been utilized by a number of investigators (Carder et al, 1993; Dekker, 1992; Richardson et al. 1991, 1994, 1995). These studies have all focused on detection of major groups of algae. Recently, investigators have used a similar approach to investigate algal dynamics at a species level (Bebout and Garcia-Pichel, 1995). In this study, measurements of surface reflectance at wavelengths corresponding to a species specific cyanobacterial accessory pigment (phycoerythrocyanin, λ max at 577 nm) were conducted to document vertical migrations of a population of one cyanobacterial species (*Microcoleus chthonoplastes*) within a mixed population cyanobacterial mat.

The increased signal to noise ratio which has been achieved for AVIRIS in recent years will enhance the capability of this sensor to detect accessory pigments. This will be especially important in less productive waters (as compared to the densely populated salt ponds), but should be possible in aquatic ecosystems such as lakes and shallow water coastal areas with high concentrations of phytoplankton. Research efforts in these areas will require atmospheric correction procedures, which are currently under development by other investigators (see, for example, Carder et al, 1993).

4.0 ACKNOWLEDGEMENTS

We thank Jeff Myers for collaboration, Cheng Jen Liu for spectral processing, and Daniel Buisson for pigment analysis. This research is supported by NASA grant #NAG5-3124.

5.0 REFERENCES

Bebout, B.M. and F. Garcia-Pichel, 1995, "UV B-Induced Vertical Migrations of Cyanobacteria in a Microbial Mat," *Appl. Env. Microbiol.*, vol. 61, pp. 4215-4222.

Bidigare, R.R., J.H. Morrow, and D.A. Kiefer, 1989, "Derivative Analysis of Spectral Absorption by Photosynthetic Pigments in the Western Sargasso Sea," *J. Mar. Res.*, vol. 47, pp. 323-341.

Bjørnland, T., and S. Liaaen-Jensen, 1989, "Distribution Patterns of Carotenoids in Relation to Chromophyte Phylogeny and Systematics," pages 37-60 in J.C. Green, B.S.C. Leadbeater, and W.L. Diver, eds. *The Chromophyte Algae: Problems and Perspectives*, Clarendon Press, Oxford.

Carder, K.L., P. Reinersman, R.F. Chen, F. Muller-Karger, C.O. Davis, and M. Hamilton, 1993, "AVIRIS Calibration and Application in Coastal Oceanic Environments," *Rem. Sens. Env.*, vol. 44, pp. 205-216.

Carder, K.L. and R.G. Steward, 1985, "A Remote-Sensing Reflectance Model of a Red Tide Dinoflagellate off West Florida," *Limnol. Oceanogr.*, vol. 30, pp. 286-298.

Clark, D., 1981, "Phytoplankton Pigment Algorithms for the Nimbus-7 CZCS", pages 227-237, in J.F.R. Gower, ed. *Oceanography from Space*, Plenum, New York.

Dekker, A.G., T.J. Malthus, M.M. Wijnen, and E. Seyhan, 1992, "Remote Sensing as a Tool for Assessing Water Quality in Loosdrecht Lakes," *Hydrobiologia*, vol. 233, pp. 137-159.

Demetriades-Shah, T.H., Steven, M.D., and J.A. Clark, 1990, "High Resolution Derivative Spectra in Remote Sensing," *Rem. Sens. Env.*, vol. 33, pp. 55-64.

Farrand, W.H., and J.C. Harsanyi, 1995, "Discrimination of Poorly Exposed Lithologies in Imaging

Spectrometer Data," *J. Geophys. Res.*, vol. 100, pp. 1565-1578.

Foppen, J.H., 1971, "Tables for the Identification of Carotenoid Pigments," Chromatogr. Rev., vol. 14, pp. 133-298.

Galat, D.L. and J.P. Verdin, 1989, "Patchiness, Collapse and Succession of a Cyanobacterial Bloom Evaluated by Synoptic Sampling and Remote Sensing", *J. Plankt. Res.*, vol. 11, pp. 925-948.

Gieskes, W.W., 1991, "Algal Pigment Fingerprints: Clue to Taxon Specific Abundance, Productivity, and Degradation of Phytoplankton in Seas and Oceans," pages 61-99 in S. Demers, ed. *Particle Analysis in Oceanography*, NATO ASI Series. Vol. G27, Springer-Verlag, Berlin.

Gieskes, W.W. and G.W. Kraay, 1983, "Dominance of Cryptophyceae During the Phytoplankton Spring Bloom in the Central North Sea Detected by HPLC Analysis of Pigments," *Mar. Biol.* vol. 75, pp. 179-185.

Goodin, D.G., L. Han, R.N. Fraser, D.C. Rundquist, W.A. Stebbins, and J.F. Schalles, 1993, "Analysis of Suspended Solids in Water Using Remotely Sensed High Resolution Derivative Spectra," *Photogramm. Eng. and Rem. Sens.*, vol. 59, pp. 505-510.

Hamilton, M.K., C.O. Davis, W.J. Rhea, S.H. Pilorz, and K.L. Carder, 1993, "Estimating Chlorophyll Content and Bathymetry of Lake Tahoe Using AVIRIS Data," *Remote Sensing of Environment*, vol. 44, pp. 217-230.

Leavitt, P.R., S.R. Carpenter, and J.F. Kitchell, 1989, "Whole Lake Experiments: The Annual Record of Fossil Pigments and Zooplankton, *Limnol. Oceanogr.* vol. 34, pp. 700- 717.

Lizotte, M.P. and J.C. Priscu, 1993, "Algal Pigments as Markers for Stratified Phytoplankton Populations in Lake Bonney (Dry Valleys)," *Antarctic J. of the U.S.*, vol. 27, pp. 259-260.

Mantoura, R.F.C., and C.A. Llewellyn, 1983, "The Rapid Determination of Algal Chlorophyll and Carotenoid Pigments and their Breakdown Products in Natural Waters by Reverse-phase High Performance Liquid Chromatography, *Anal. Chim. Acta*, vol. 151, pp. 297-314.

Millie, D.F., H.W. Paerl, and J.P. Hurley, 1993, "Microalgal Pigment Assessments Using High-performance Liquid Chromatography: A Synopsis of Organismal and Ecological Applications," *Can. J. Fish. Aquat. Sci.*, vol. 50, pp. 2513-2527.

Mittenzwey, K.-H., S. Ullrich, A.A. Gitelson, and K.Y. Kondratiev, 1992, "Determination of Chlorophyll *a* of Inland Waters on the Basis of Spectral Reflectance," *Limnol. Oceanogr.*, vol. 37, pp. 147-149.

Morton, A.M., 1975, *Biochemical Spectroscopy*, Wiley and Sons, New York, vol. 1.

Richardson, L.L., 1996, "Remote Sensing of Algal Bloom Dynamics by Detecting Algal Accessory Pigments," *Bioscience*, (in press)

Richardson, L.L., D. Bachoon, V. Ingram-Willey, C. Chee Chow, and K. Weinstock, 1991, "Remote Sensing of the Biological Dynamics of Large-scale Salt Evaporation Ponds," *Proc. Intl. Symp. Rem. Sens. Env.*, pp. 511-623.

Richardson, L.L., D. Buisson and V. Ambrosia, 1995, "Use of Remote Sensing Coupled with Algal Accessory Pigment Data to Study Phytoplankton Bloom Dynamics in Florida Bay," *Proc. Third Them. Conf. Rem. Sens. Mar. and Coast. Env.*, vol. 1, pp. 183-192.

Richardson, L.L., D. Buisson, C.J. Liu, and V. Ambrosia, 1994, "The Detection of Algal Photosynthetic Accessory Pigments Using Airborne Visible-Infrared Imaging Spectrometer (AVIRIS) Spectral Data," *Mar. Tech. Soc. J.*, vol. 28, pp. 10-21.

Rowan, K.S., 1989, *Photosynthetic Pigments of Algae*, Cambridge University Press, Cambridge.

Savitzky, A., and M.J.E. Golay, 1964, "Smoothing and Differentiation of Data by Simplified Least Squares Procedures", *Anal. Chem.*, vol. 36, pp. 1627-1639.

Smith, R.C., and K.S. Baker, 1982, "Oceanic Chlorophyll Concentrations as Determined by Satellite (Nimbus-7 Coastal Zone Color Scanner), *Mar. Biol.*, vol. 66, pp. 269-279.

Soma, Y., T. Imaizumi, K-I. Yagi, and S-I. Kasuga, 1993, "Estimation of Algal Succession in Lake Water using HPLC Analysis of Pigments," *Can. J. Fish. Aquat. Sci.*, vol. 50, pp. 1142-1146.

Wilhelm, C., I. Rudolph, and W. Renner, 1991, "A Quantitative Method Based on HPLC-aided Pigment Analysis to Monitor Structure and Dynamics of the Phytoplankton Assemblage - A Study from Lake Meerfelder (Eifel, Germany)," *Arch. fur Hydrobiol.*, vol. 123, pp. 21-35.

Wright, S.W. and J.D. Shearer, 1984, "Rapid Extraction and High Performance Liquid Chromatography of Chlorophylls and Carotenoids from Marine Phytoplankton," *J. Chromatog.*, vol. 294, pp. 281-295.

MAPPING CHAPARRAL IN THE SANTA MONICA MOUNTAINS USING MULTIPLE SPECTRAL MIXTURE MODELS

Roberts, D.A.[1], Gardner, M.[1], Church, R.[1], Ustin, S.[2], and Scheer, G.[2], and Green, R.O.[1,3]

1. Department of Geography, EH3611, University of California, Santa Barbara, CA 93106
2. Department of Land, Air, and Water Resources, University of California, Santa Barbara, CA 93106
3. Jet Propulsion Laboratory, California Institute of Technology, 4800 Oak Grove Dr., Pasadena, CA 91109

1. INTRODUCTION

California chaparral is one of the most important natural vegetation communities in Southern California, representing a significant source of species diversity and, through a high susceptibility to fire, playing a major role in ecosystem dynamics. Due to steep topographic gradients, harsh edaphic conditions and variable fire histories, chaparral typically forms a complex mosaic of different species dominants and age classes, each with unique successional responses to fire and canopy characteristics (e.g. moisture content, biomass, fuel load) that modify fire susceptibility. The high human cost of fire and intimate mixing along the urban interface combine to modify the natural fire regime as well as provide additional impetus for a better understanding of how to predict fire and its management. Management problems have been further magnified by nearly seventy years of fire suppression and drought related die-back over the last few years resulting in a large accumulation of highly combustible fuels (Radtke et al., 1982; Yool et al., 1985). Chaparral communities in the Santa Monica Mountains exemplify many of the management challenges associated with fire and biodiversity.

A study was initiated in the Santa Monica Mountains to investigate the use of the Airborne Visible/Infrared Imaging Spectrometer (AVIRIS) for providing improved maps of chaparral coupled with direct estimates of canopy attributes (e.g. biomass, leaf area, fuel load). The Santa Monica Mountains are an east-west trending range located approximately 75 kilometers north of Los Angeles extending westward into Ventura County. Within the Santa Monica Mountains a diverse number of ecosystems are located, including four distinct types of chaparral, wetlands, riparian habitats, woodlands, and coastal sage scrub. In this study we focus on mapping three types of chaparral, oak woodlands and grasslands. Chaparral mapped included coastal sage scrub, chamise chaparral and mixed chaparral that consisted predominantly of two species of Ceanothus.

2. METHODS and STUDY SITE

Analysis focused on AVIRIS data collected on October 19, 1994. Two east-west flight lines were collected, consisting of a total of 12 scenes. Results will only be presented for scene 5, centered over Point Dume, California (Fig. 1). Maps of equivalent liquid water thickness, precipitable water vapor and apparent reflectance were generated using an algorithm coupled with the Modtran3 radiative transfer code (Green et al., 1993). Once converted to apparent reflectance, AVIRIS data were modeled as spectral mixtures of field and laboratory measured spectra of soil, non-photosynthetic vegetation (NPV), green leaves and shade (Adams et al., 1993; Roberts et al., 1993). Spectral mixture analysis (SMA) was performed using a complex modeling approach, in which the number of endmembers and types of endmembers were varied on a per-pixel basis (Roberts et al., 1992). This approach has advantages over the simple mixture model because it offers the potential for greater separation of communities through ecosystem unique endmember selection while minimizing fraction errors that typically result from endmember ambiguity or interpixel differences in spectral dimensionality (Sabol et al., 1992).

Reference endmembers were selected from a library of field and laboratory spectra collected during two field campaigns, in June and September 1995 (Ustin et al.,1996). Endmembers were selected using techniques described by Smith et al. (1990) and Adams et al., (1993). These techniques were used to develop suites of candidate endmembers for green vegetation and NPV for each major community in

the study area. A single soil and photometric shade spectrum were selected for simplicity, although community level variability in shade spectra can be significant due to multiple scattering of NIR light (Roberts et al., 1993). Suites of candidate spectra were developed hierarchically, starting with two-endmember models, followed by three endmember models etc. Training areas for each major vegetation type were extracted from the reflectance images and used to guide the development of a candidate library. The final library consisted of 3 leaf spectra, 2 NPV spectra and one each of soil and shade. Candidate leaf spectra for coastal sage scrub, chamise chaparral and mixed chaparral are shown labeled as S24PNL, adfa and Ceme, respectively (Fig. 2). A fourth spectrum consisting of NPV is included on the figure labeled Erci stem (Eriogonum cinereum). The best fit for a leaf in coastal sage scrub was actually an NPV spectrum, reflecting the drought deciduous behavior of many dominants in this community.

Once a candidate library was developed, the library was used as an input into a series of mixture models starting with all reasonable combinations of two-endmember models (leaf-shade, soil-shade, NPV-shade) followed by all possible three endmember models (leaf-NPV-shade) and four endmember models. A total of 14 models were run. Following mixture modeling, a program was developed to select the optimal model for each pixel based on RMS error and spectral fractions. Starting with models with the lowest dimensionality (two-endmember models), each pixel was evaluated based on an RMS threshold of $< 2.5\%$ and the constraint that fractions ranged between -1% and 100%. Once a pixel met these criteria, it was assigned a numeric value equal to the model and removed from the pool. This approach was continued, progressing upwards from models of low-dimensionality to high dimensionality until all models had been evaluated. This resulted in a map consisting of 14 classes, in which class was determined by the number of endmembers in the model and the types that were used. Class maps and fraction images were combined to produce images showing the spectral fractions associated with each green leaf endmember. Fraction maps were then combined with equivalent liquid water maps to produce a final classified image using techniques described by Adams at al. (1995), modified to include liquid water.

3. RESULTS

Using a multiple endmember mixing model, over 95% of the image could be modeled as some combination of 2 to 4 endmembers at an RMS $< 2.5\%$ and with positive fractions. The only unmodeled areas consisted of the city of Malibu and Zuma Beach. In chaparral the dimensionality of individual spectra was remarkably low, with 2-endmember models accounting for 65.9 percent and 3 endmember models accounting for 92.3 percent of the total pixels (Table 1). Although preliminary, based on the field sites and limited field photographs the model appears to have successfully separated chamise chaparral from mixed chaparral and mapped the extent of coastal sage scrub. Near-term objectives are to evaluate map accuracy and refine models based on field observations and aerial photographs. Spring AVIRIS data acquired in 1995 will also be incorporated to study seasonal effects and evaluate any phenological improvements for mapping.

Table 1. Showing the number of pixels modeled using 2, 3 and 4 endmember models. 13,324 of a total 314,368 image pixels were left unmodeled using a combination of the 2, 3, and 4 endmember models. Note, ~10% of the image was ocean, which was selected by the first 2-endmember model, Ceme.

Model Leaf Endmember	2-endmember	3-endmember (includes NPV)	4-endmember (includes soil)	Totals
Ceme	136677	68186	7443	212306
Adfa	9729	12526	2373	24628
Oak (PPNE)	192	699	1067	1958
Zuma (S24PNL)	55286	1497	3	56786
Senesced Grass	2334	X	X	2334
Soil	3032	X	X	3032
Total Unmodeled	107118	24210	**13324**	X
Total Modeled	207250	82908	10886	301044

4. REFERENCES

Adams, J.B., Smith, M.O. and Gillespie, A.R., 1993, Imaging spectroscopy: Interpretation based on spectral mixture analysis, In Pieters, C.M., and Englert, P., eds. Remote Geochemical Analysis: Elemental and Mineralogical Composition 7: 145-166, Cambridge Univ. Press, NY.

Adams, J.B., Sabol, D., Kapos, V., Almeida Filho, R., Roberts, D.A., Smith, M.O., Gillespie, A.R., 1995, Classification of Multispectral Images Based on Fractions of Endmembers: Application to Land-Cover Change in the Brazilian Amazon, *Rem. Sens. Environ.*, 52:137-154.

Green, R.O., Conel, J.E. and Roberts, D.A., 1993, Estimation of Aerosol Optical Depth and Additional Atmospheric Parameters for the Calculation of Apparent Reflectance from Radiance Measured by the Airborne Visible/Infrared Imaging Spectrometer, *Summaries of the 4th Annual JPL Airborne Geoscience Workshop, Oct. 25-29,* Vol. 1. AVIRIS Workshop, Washington D.C., JPL 93-26, Jet Propulsion Laboratory, Pasadena, CA, 73-76.

Radtke, K.W. H., Arndt, A.M., and Wakimoto, R.H., 1982, Fire history of the Santa Monica Mountains, in Proc. Symp. Dynamics and Management of Mediterranean-type Ecosystems. San Diego, CA, USFS General Technical Report PSW-58: 438-443.

Roberts, D.A., Smith, M.O., Sabol, D.E., Adams, J.B. and Ustin, S., 1992, Mapping the Spectral Variability in Photosynthetic and Non-Photosynthetic Vegetation, Soils and Shade using AVIRIS, *Summaries 3rd Annual JPL Airborne Geoscience Workshop: Vol. 1, AVIRIS,* Pasadena, CA. June 1 and 2, 1992, JPL 92-14, Jet Propulsion Laboratory, Pasadena, CA, pp. 38-40.

Roberts, D.A., Adams, J.B., and Smith, M.O., 1993, Discriminating Green Vegetation, Non-Photosynthetic Vegetation and Soils in AVIRIS Data, *Rem. Sens. Environ.*, 44: 2/3 255-270.

Sabol, D.E., Adams, J.B., and Smith, M.O., 1992, Quantitative sub-pixel spectral detection of targets in multispectral images, *J. Geophys. Res.* 97: 2659-2672.

Smith, M.O., Ustin, S.L., Adams, J.B., and Gillespie, A.R., 1990, Vegetation in deserts: I. A regional measure of abundance from muluispectral images, *Remote Sens. Environ.*, 31: 1-26.

Ustin, S.L., Scheer, G., Castañeda, C.M. , Jacquemoud, S., Roberts, D., and Green, R., 1996, Estimating canopy water content of chaparral shrubs using optical methods, *Summaries of the Sixth Annual JPL Airborne Earth Science Workshop, Vol. 1, AVIRIS,* Pasadena, CA, March 4-6, 1996, JPL 96-4, Vol. 1, Jet Propulsion Laboratory, Pasadena, CA, (this volume).

Yool, S.R., Eckhardt, D.W., and Cosentino, M.J., 1985, Describing the brushfire hazard in southern California. *Anal. Assoc. Am. Geograph.* 75: 431-442.

5. ACKNOWLEDGMENTS

Support for this research was provided by a grant from the National Aeronautics and Space Administration, Terrestrial Ecosystems and Biogeochemical Dynamics Branch, NAGW-4626-I, as a subcontract with U.C. Davis. Computer equipment was supplied largely as part of a start-up package at U.C. Santa Barbara in the Department of Geography. A portion of this research was carried out at the Jet Propulsion Laboratory, California Institute of Technology, under a contract with the National Aeronautics and Space Administration.

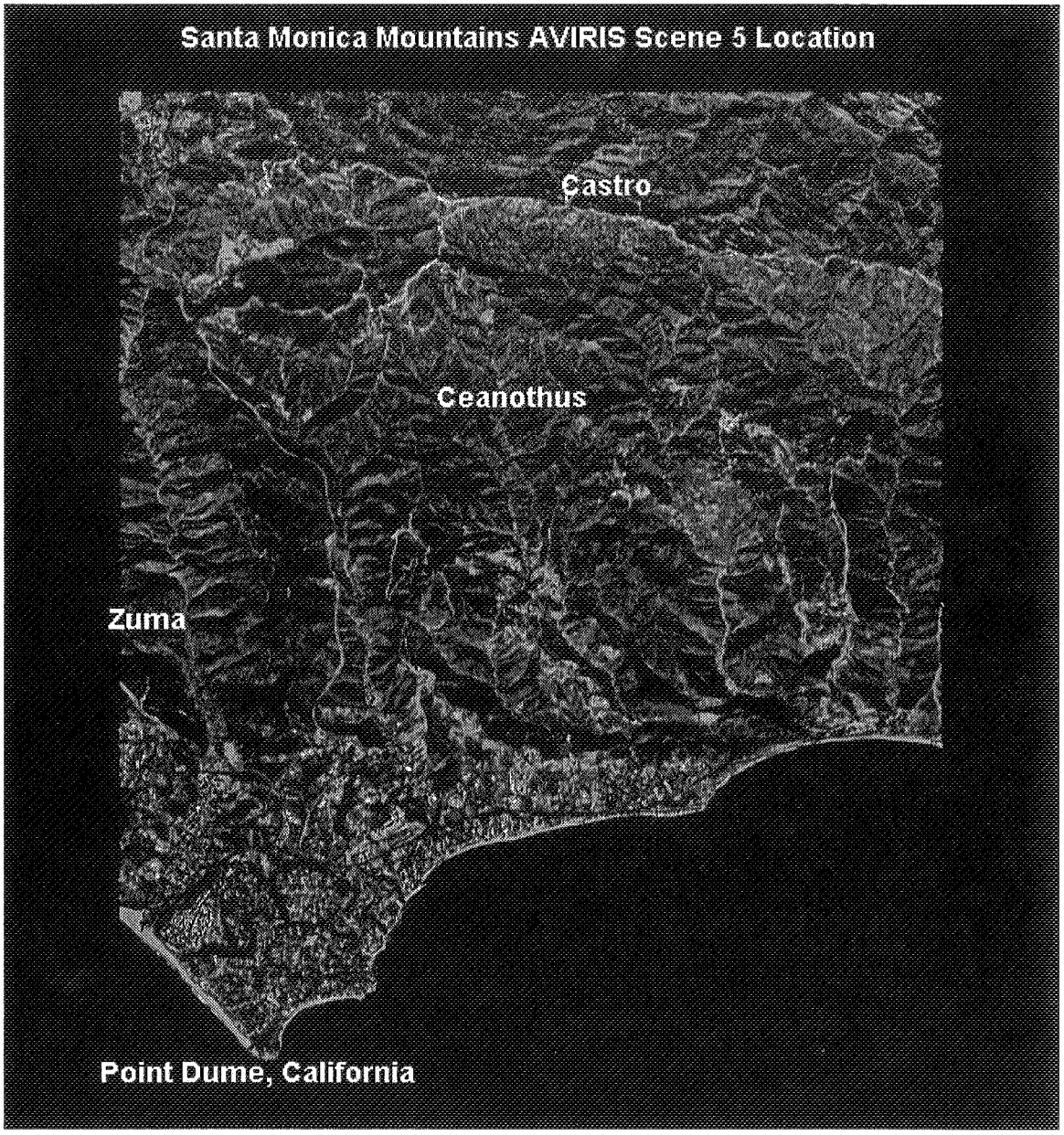

Figure 1. Showing locations of the Chamise chaparral (Castro) and Coastal sage scrub (Zuma) field sites. Ceanothus marks a third site identified to be almost pure Ceanothus from field photographs.

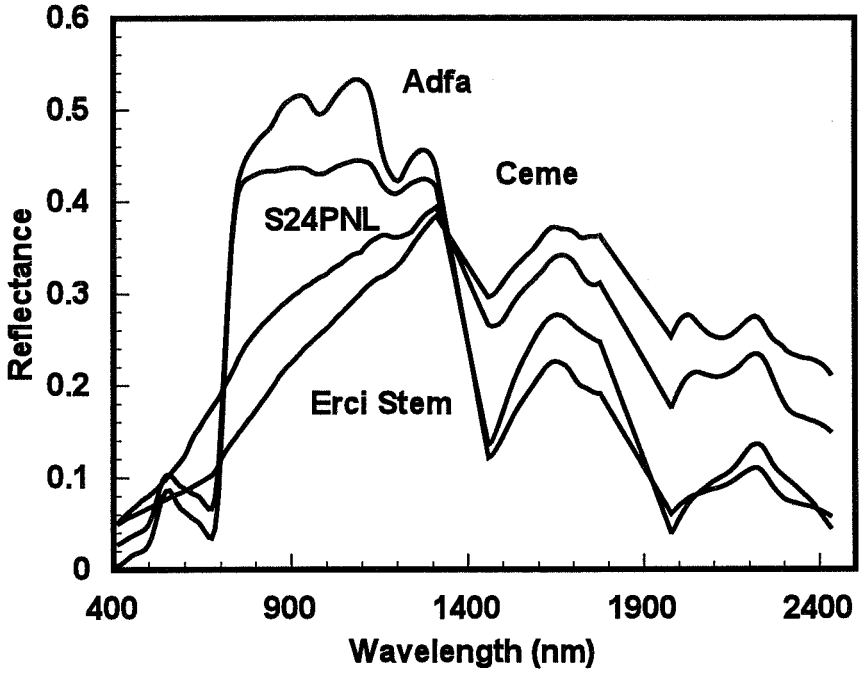

Figure 2. Showing reference endmembers selected for Castro (Adfa = Adenostoma fasciculatum), Ceanothus (Ceme = Ceanothus megacarpus), Zuma (S24PNL = an NPV) and NPV (Erci Stem = Eriogonum cinereum stem).

Page intentionally left blank

S36-43
046100
317388

MONITORING FOREST REGROWTH USING A MULTI-PLATFORM TIME SERIES

[1]Donald E. Sabol Jr., [1]Milton O. Smith, [1]John B. Adams
[1]Alan R. Gillespie, and [2]Compton J. Tucker

[1] Department of Geological Sciences, Campus Box 351310, University of Washington, Seattle, WA 98195-1310
[2] Laboratory for Terrestrial Physics, NASA, Goddard Space Flight Center, Greenbelt, MD 20771

1. INTRODUCTION

Over the past 50 years, the forests of western Washington and Oregon have been extensively harvested for timber. This has resulted in a heterogeneous mosaic of remaining mature forests, clear-cuts, new plantations, and second-growth stands that now occurs in areas that formerly were dominated by extensive old-growth forests and younger forests resulting from fire disturbance (Spies and Franklin, 1988). Traditionally, determination of seral stage and stand condition have been made using aerial photography and spot field observations, a methodology that is not only time- and resource-intensive, but falls short of providing current information on a regional scale. These limitations may be solved, in part, through the use of multispectral images which can cover large areas at spatial resolutions in the order of tens of meters. The use of multiple images comprising a time series potentially can be used to monitor land use (e.g. cutting and replanting), and to observe natural processes such as regeneration, maturation and phenologic change. These processes are more likely to be spectrally observed in a time series composed of images taken during different seasons over a long period of time. Therefore, for many areas, it may be necessary to use a variety of images taken with different imaging systems. A common framework for interpretation is needed that reduces topographic, atmospheric, instrumental, effects as well as differences in lighting geometry between images. The present state of remote-sensing technology in general use does not realize the full potential of the multispectral data in areas of high topographic relief. For example, the primary method for analyzing images of forested landscapes in the Northwest has been with statistical classifiers (e.g. parallelepiped, nearest-neighbor, maximum likelihood, etc.), often applied to uncalibrated multispectral data. Although this approach has produced useful information from individual images in some areas, land-cover classes defined by these techniques typically are not consistent for the same scene imaged under different illumination conditions, especially in the mountainous regions. In addition, it is difficult to correct for atmospheric and instrumental differences between multiple scenes in a time series. In this paper, we present an approach for monitoring forest cutting/regrowth in a semi-mountainous portion of the southern Gifford Pinchot National Forest using a multisensor-time series composed of MSS, TM, and AVIRIS images.

2. METHODS

The time series was composed of five spatially co-registered images: two MSS images (26 June and 30 September 1987, two TM images (7 July 1991 and 31 July 1994), and one AVIRIS image (30 September 1994.). Bands in the 1.4-μm and 1.9-μm water absorption features were not used in analysis of the AVIRIS data, leaving 180 of the original 224 bands. An extension of spectral mixture analysis called Foreground-Background Analysis (FBA) (Smith et al., 1994, 1995) was subsequently applied to these data. Like simple mixing models, the objective of FBA is to obtain quantitative abundance estimates (fractions) of spectral endmembers. However, unlike simple mixing models which typically use three to five endmembers, in FBA a rotation of the spectral data space is found that minimizes the spectral variability within the set of spectra that

represent a sought-after "foreground" material (e.g. green vegetation in this study), and at the same time maximizes the contrast between the foreground set and other materials or shade which are treated as "background." In this study, background included spectral variability from multiple sources, such as subtle atmospheric variations, endmember variability, calibration differences, photometric effects from varying viewing and illumination angles, and multiple scattering. The general set of equations for FBA is:

$$\text{Foreground: } 1 = \sum_{b=1}^{Nb} w_b DN_b + c$$

$$\text{Background: } 0 = \sum_{b=1}^{Nb} w_b DN_b + c$$

where a vector w is defined as a projection in hyperspace of all foreground DNs as 1 and all background DNs as 0. Nb is the number of bands and c is a constant. The vector w and constant c are simultaneously calculated from the above equations using singular-value decomposition. When applied to each of the five data sets, a total of five images, each representing the relative fraction of foreground (green vegetation in this study) in each scene, were produced. From these data the change in the fractions over time for each forest stand was evaluated and compared to U.S. Forest Service cutting/replanting records.

2. RESULTS / DISCUSSION

FBA suppressed topographic effects, and minimized the effects of atmosphere and clouds. An example from the 1994 AVIRIS image is shown in Figure 1. Here, the effectiveness of topographic "removal" can be seen by comparing the 846-μm band, which contains topographic information, to the scaled FBA vegetation fraction image, calculated using 180 of the AVIRIS bands, in which shade has been removed. This removal was effective because in FBA shade can be treated more realistically than in simple mixture models as a range of spectra (Roberts et al., 1991). Shading, shadow, sky-illuminated shadow, bounce-illuminated shadow, and various expressions of vegetation shade all were be grouped as background and "removed" from the image. Because detection of green vegetation was optimized in this application of FBA, the fraction of green vegetation was determined even in areas that were poorly illuminated (e.g. shaded slopes).

Figure 2 shows the change in the fraction of green vegetation over seven years for four representative forest stands. The date of cutting was obtained from U.S. Forest Service records. Forests have a high index (~100) prior to cutting, after which the index drops close to zero. As the cut areas regrow, the index of green vegetation generally increases, although it varies in response to management practices in the area (e.g. burning, thinning, clearing of underbrush).

The distinctive temporal signatures of regrowth and phenologic changes are difficult to determine in this series due to the low temporal resolution. For example, annual images in the series would greatly improve evaluation of regrowth, while determination of phenologic changes would be enhanced with monthly images. However, cutting and general regrowth history can clearly be determined using these images, even in stands that are poorly illuminated due to topography. Our FBA approach shows a vast improvement over our earlier results on a single image where reconstruction of cutting history was reliable only in areas of low relief (Sabol et al., 1995).

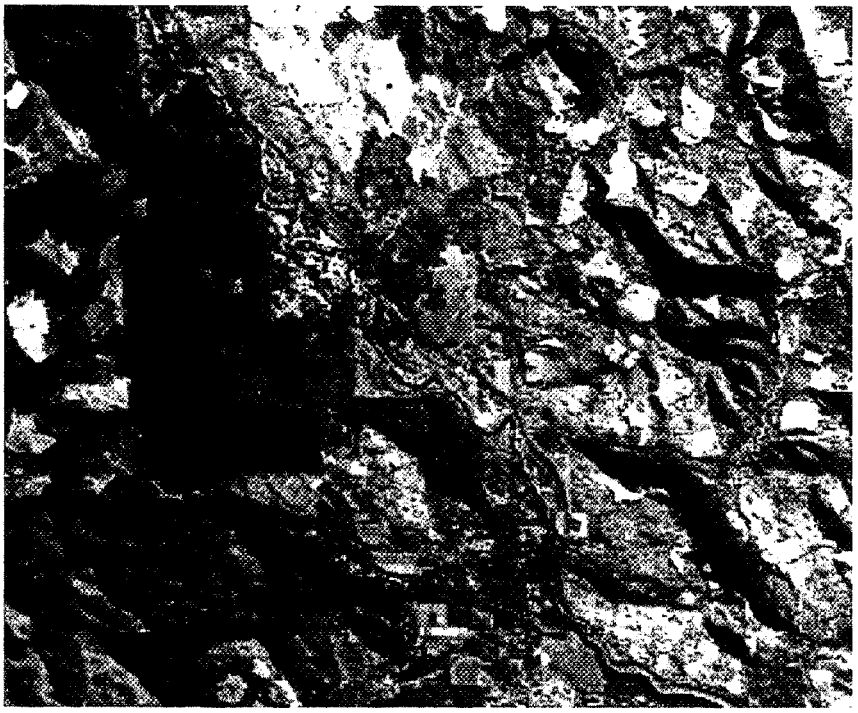

AVIRIS Band Image (848 μm)

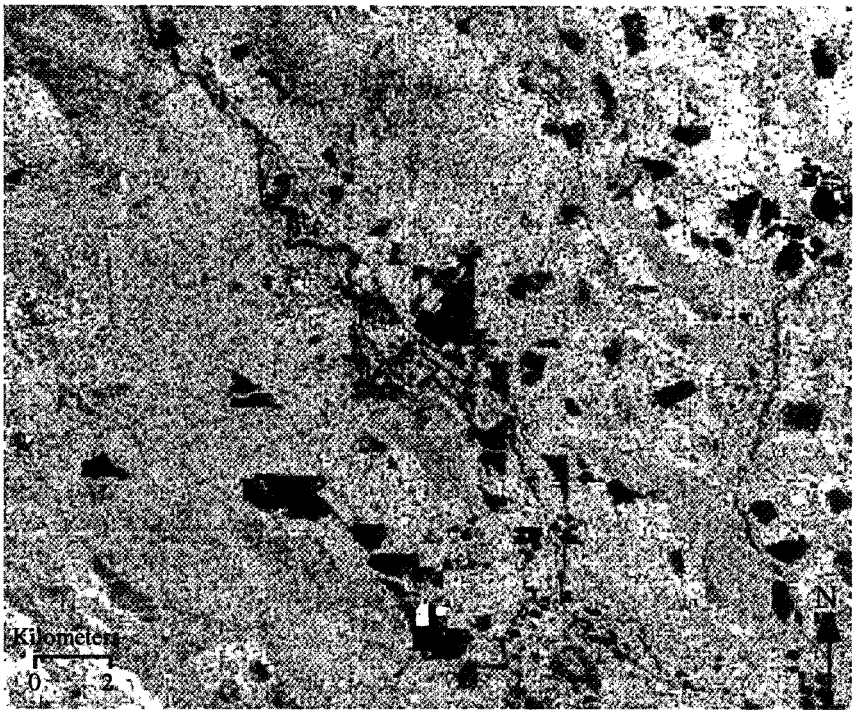

FBA Scaled Vegetation Index Image

Figure 1 - FBA results for an area in the southern Gifford Pinchot National Forest, Washington using AVIRIS (9/30/94) data. Note that the topography is flattened in the scaled vegetation index image (lighter tones indicate a higher abundance of green vegetation).

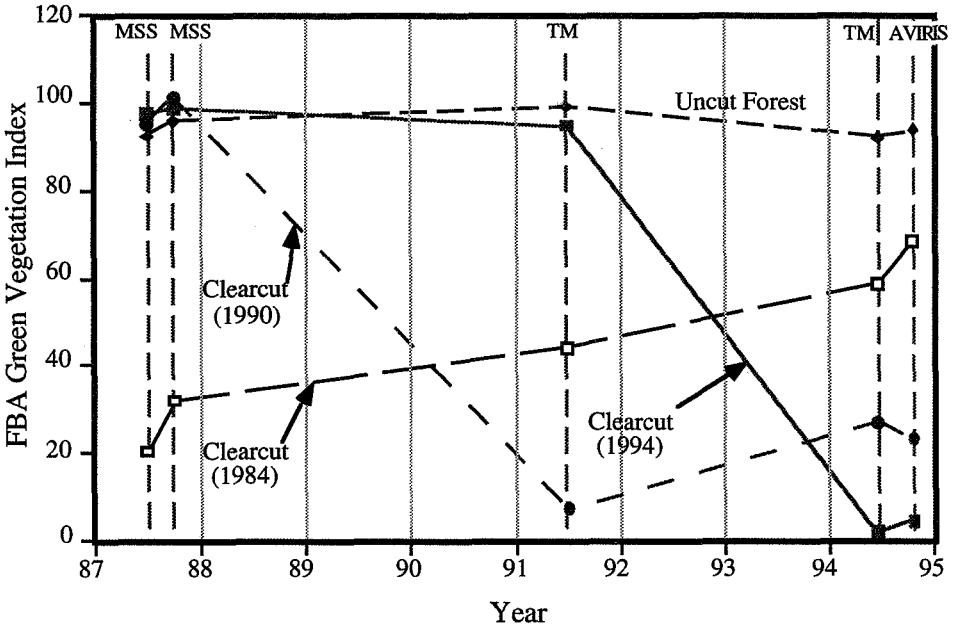

Figure 2 - Change in the FBA vegetation index over time for three clearcuts in the Gifford Pinchot National Forest, Washington. The temporal signature for clearcuts is a rapid decline of vegetation followed by a gradual increase during regrowth.

Because of the low spectral resolution of MSS and TM in the time series and because we have only a single AVIRIS image, we concentrated on optimizing green vegetation for evaluating seral stage instead of a full evaluation of forest endmembers. However, the high spectral resolution of AVIRIS allows estimation of non-photosynthetic vegetation (i.e. bark, stems) (NPV) as an additional parameter for monitoring seral stage and stand health. Sabol et al. (1995) found that detectable fractions of NPV are present in young forests (< 10 years) and may be present in old-growth forests (> 250 years), which may aid in distinguishing old growth stands from other mature forests (100-200 years old). Calibrated AVIRIS spectra from stands of different ages are shown in Figure 3. Downed trees, bark, and branches typically cover the surface of recent cuts. As a result, these sites have a strong NPV component, characterized by absorption features at 2.09 μm (xylan and cellulose) and at 2.13 μm (lignin) (Elvidge, 1987). Within two years, the spectral signature is dominated by invading deciduous bushes and ferns which have a high green vegetation index. In time, replanted coniferous trees become spectrally dominant. The increase of shade/shadow associated with the canopy structure of coniferous forests reduces the overall reflectance of the stand.

3. CONCLUSION

FBA was used to establish a stable framework for evaluation of regrowth history, even when using images taken at different times (different lighting and atmospheric conditions) in mountainous terrain. The stability of this framework in optimizing the detectability of green vegetation allows incorporation of images with low spectral resolution (i.e. Landsat) as well as newer, higher resolution systems (i.e. AVIRIS) into as time series for monitoring forest regrowth.

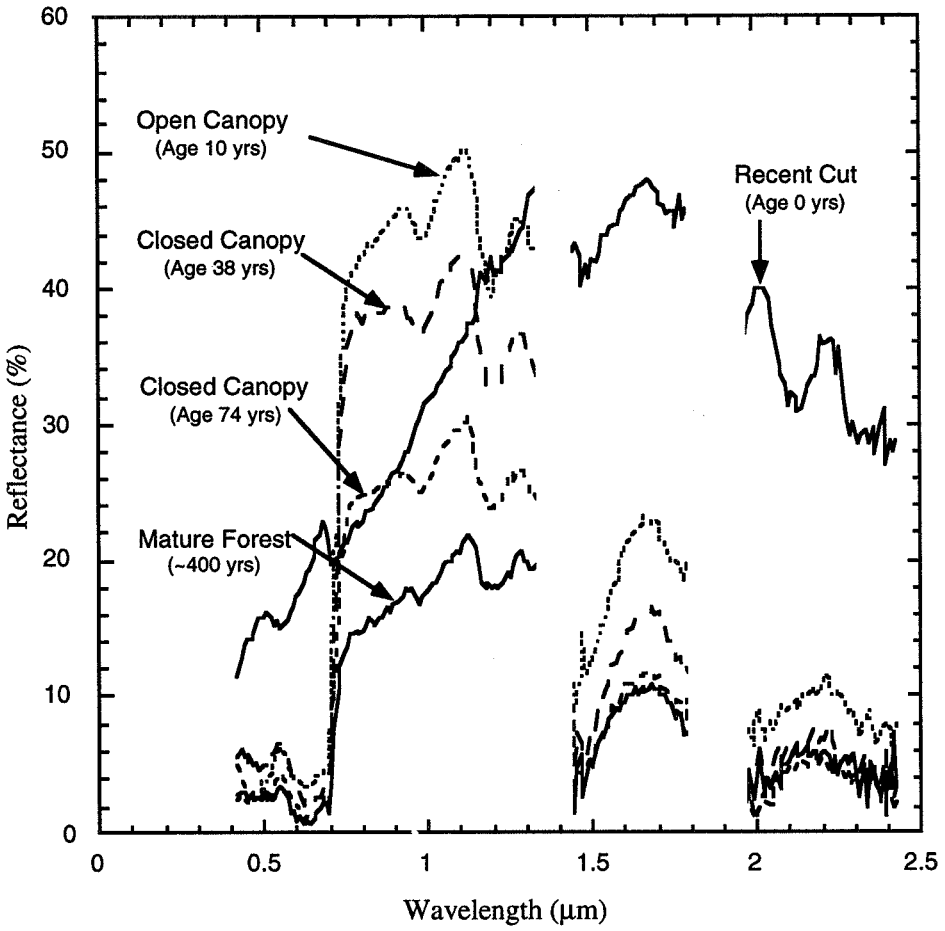

Figure 3 - AVIRIS spectra of different age stands. The surface of the recent cuts are covered with bark, branches and wood scraps resulting in a strong NPV signature (cellulose and lignin absorptions between 2.0-μm and 2.2-μm). Within two years of cutting, brush and ferns invade the area and result in a bright green vegetation signature. As the stand ages, replanted coniferous trees (and the shadows cast by them) gradually dominate.

The low resolution of MSS and TM make spectral separation of NPV and many soils unreliable. Hence, we limited the determination of cutting and replanting history to the changes in the abundance of green vegetation in the scene over time. However, the distinctive absorption features of NPV (cellulose and lignin between 2.0-μm and 2.2-μm) are more detectable using the high resolution of AVIRIS. With the addition of future AVIRIS data of this area to the time series, NPV as well as green vegetation may be used further improve monitoring of cutting, regrowth, and phenology.

4. REFERENCES

Elvidge, C.D., 1987, Reflectance characteristics of dry plant material, In *Proc. 21st Int. Symp. on Remote Sens. Environ.*, Ann Arbor, MI, 26-30 October, 13 pp.

Roberts, D.A., Smith, M.O., Adams, J.B., and Gillespie, A.R., 1991, Leaf spectral types, residuals and canopy shade in an AVIRIS image, In *Proc.. 3rd Airborne Visible/Infrared Imaging Spectrometer (AVIRIS) Workshop (R.O. Green, Ed.), Pasadena, CA, 20-21 May, pp. 43-50.*

Sabol, D.E., Smith, M.O., Adams, J.B., Zukin, J.H., Tucker, C.J., Roberts, D.A., and Gillespie, A.R., 1995, AVIRIS spectral trajectories for forested areas of Gifford Pinchot National Forest, In *Summ. Fifth Ann. JPL Airborne Earth Sci. Workshop, 1. AVIRIS Workshop*, edited by R.O. Green, JPL Publ. 95-1, Jet Propulsion Labratory, Pasadena, CA., Vol. 1., 133-136.

Smith, M.O., Adams, J.B., and Sabol, D.E., 1994, Spectral mixture analysis - new strategies for the analysis of multispectral data, in J. Hill and J. Megier (eds.), *Imaging Spectrometry - a Tool for Environmental Observations*, Brussels and Luxembourg, 125 - 143.

Smith, M.O., Weeks, R., and Gillespie, A., 1995, A strategy to quantify moisture and roughness from SAR images using finite impulse response filters, *Proc. International Symposium of Retrieval of Bio-Geophysical Parameters from SAR Data for Land*, Toulouse, France, October 1995, 10 pp.

Spies, T.A. and Franklin, J.F., 1988. Old growth and forest dynamics in the Douglas-fir region of Oregon and Washington. Natural Areas J. 8:190-201.

S31-47
046101

ATMOSPHERIC PRE-CORRECTED DIFFERENTIAL ABSORPTION TECHNIQUES TO RETRIEVE COLUMNAR WATER VAPOR: APPLICATION TO AVIRIS 91/95 DATA

317390
10P.

Daniel Schläpfer[1], Christoph C. Borel[2], Johannes Keller[3] and Klaus I. Itten[4]

[1] *permanent address: Department of Geography, RSL, University of Zürich, CH-8057 Zürich, Switzerland Phone: +41 1 257 52 49, Fax: +41 1 362 52 27, E-mail: dschlapf@rsl.geogr.unizh.ch*

[2] *Los Alamos National Laboratory, NIS-2, MS C323, Los Alamos, NM 87545, USA*

[3] *Paul Scherrer Institut (PSI), CH-5232 Villigen PSI, Switzerland*

[4] *Remote Sensing Laboratories (RSL), Department of Geography, University of Zürich, CH-8057 Zürich, Switzerland*

1 INTRODUCTION

Water vapor is one of the main forces for weather development as well as for mesoscale air transport processes. The monitoring of water vapor is therefore an important aim in remote sensing of the atmosphere. Current operational systems for water vapor detection use primarily the emission in the thermal infrared (AVHRR, GOES, ATSR, Meteosat) or in the microwave radiation bands (DMSP). The disadvantage of current satellite systems is either a coarse spatial (horizontal) resolution ranging from one to tens of kilometers or a limited insight into the lower atmosphere. Imaging spectrometry on the other hand measures total column water vapor contents at a high spatial horizontal resolution and has therefore the potential of filling these gaps.

The sensors of the AVIRIS instrument are capable of acquiring hyperspectral data in 224 bands located in the visible and near infrared at 10 nm resolution. This data includes the information on constituents of the earth's surface as well as of the atmosphere. The optical measurement of water vapor can be performed using sensor channels located in bands or lines of the absorption spectrum. The AVIRIS sensor has been used to retrieve water vapor and with less accuracy carbon dioxide, oxygen and ozone. To retrieve the water vapor amount, the so called differential absorption technique has been applied (Carrère et al., 1993; Kaufman et al., 1992). The goal of this technique is to eliminate background factors by taking a ratio between channels within the absorption band and others besides the band. Various ratioing methods on the basis of different channels and calculation techniques were developed.

The influence of a trace gas of interest on the radiance at the sensor level is usually simulated by using radiative transfer codes. In this study, the spectral transmittance and radiance are calculated by MODTRAN3 simulations with the new DISORT option (Abreu et al., 1995). The objective of this work is to test the best performing differential absorption techniques for imaging spectrometry of tropospheric water vapor.

2 ATMOSPHERIC PRE-CORRECTION

The radiance at the sensor level L_s can be expressed in a simple form as the sum of the ground reflected radiance L_{gnd} (including direct and path scattered ground reflected radiance) and the backscattered atmospheric radiance L_{atm} not reflected by the ground:

$$L_s(\rho,h) = L_{gnd}(\rho,h) + L_{atm}(h) \quad (1)$$

The second term is not dependent on the ground reflectance ρ but is sensitive to the atmospheric composition, in particular the aerosol amount and the water vapor content, which values depend on the ground altitude h. At low ground reflectance, the atmospheric radiance is the major contributor to the total radiance, whereas at higher reflectance the first term dominates. Erroneous water vapor contents are retrieved, because the second term acts as a ground reflectance independent offset to the first term (Gao and Geotz, 1990a).

For an improved water vapor retrieval it is therefore necessary to perform an atmospheric pre-correction by subtracting an estimate of $L_{atm}(h)$ from the radiometrically calibrated data. The height and channel dependent atmopheric radiance can be estimated by simulating the total radiance at the sensor at zero albedo. It can be shown, that the atmospheric pre-corrected differential absorption method (APDA, see section 3) is insensitive to variations of the ground reflectance, whereas without the atmospheric pre-correction a clear dependency on ground reflectance results. If it is possible to perform a satisfactory atmospheric pre-correction as described, the differential absorption ratio values will only be dependent on an appearant water vapor transmittance. The effects of atmospheric pre-correction, simulated over various surface types and the improvements on water vapor retrieval are shown in detail by Borel and Schläpfer (1996).

3 DIFFERENTIAL ABSORPTION TECHNIQUES

Differential absorption techniques are a practicable way to determine trace gas contents from a spectrum of an absorption band, which is easy to implement at low computing time costs. In general they perform a ratioing between channels within the absorption feature (measurement channels) and channels in its vicinity (reference channels) to detect the relative strength of absorption. Curve fitting techniques (Gao and Goetz, 1990a) are not considered in this study, because of their higher complexity and computing time. Table 1 shows a compilation of the considered techniques.

Method	Abbre-viation	# Meas. channels	# Ref. channels	Source	Remarks
Continuum Interpolated Band Ratio	CIBR	1	2	Bruegge, 1990	common water vapor retrieval technique
Linear Regression Ratio	LIRR	≥1	≥3	Schläpfer, 1995	extended CIBR technique
Atmopheric Pre-corrected Dfferential Absorption technique	APDA	≥1	≥2	new	see paper

Table 1: Differential absorption techniques used in this study.

The reflectance slope can be taken into account by using reference channels on both sides of the absorption band. One measurement channel is ratioed to a linear interpolated value at the same wavelength between two reference channels. The quotient of this 'Continuum Interpolated Band Ratio' technique (CIBR, Bruegge et al., 1990) is calculated as:

$$R_{CIBR} = \frac{L_m}{\omega_{r1} \cdot L_{r1} + \omega_{r2} \cdot L_{r2}} \quad \text{where:} \quad \omega_{r1} = \frac{\lambda_{r2} - \lambda_m}{\lambda_{r2} - \lambda_{r1}} \quad \text{and} \quad \omega_{r2} = \frac{\lambda_m - \lambda_{r1}}{\lambda_{r2} - \lambda_{r1}} \qquad (2)$$

where L_m is the radiance at the measurement channel with its central wavelength λ_m and L_{r1}, L_{r2} are the radiances at the reference channels at the central wavelengths $\lambda_{r1}, \lambda_{r2}$.The sensor's noise is one of the big error sources for a precise trace gas measurement, which is reduced by the consideration of a maximum number of selected channels. A linear regression through the reference channels is used to compute a radiance at the center wavelength of the measurement channels. This Linear Regression Ratio (LIRR) is an extension of the CIBR by more suitable channels.

$$R_{LIRR} = \frac{\overline{L_m}}{LIR\left([\lambda_r],[L_r]\right)\Big|_{\overline{\lambda_m}}} \quad \text{and} \quad R_{APDA} = \frac{\overline{L_m - L_{atm,m}}}{LIR\left([\lambda_r],[L_r - L_{atm,r}]\right)\Big|_{\overline{\lambda_m}}} \qquad (3a, 3b)$$

where $\overline{L_m}$ is the mean of the signal in the measurement channels with the corresponding mean wavelength $\overline{\lambda_m}$. and *LIR([x],[y])* is a linear regression through the defined vectors. When the atmospheric pre-correction is applied by subtracting the atmospheric not ground reflected radiance from the radiance at the sensor, the LIRR becomes an atmospheric pre-corrected differential absorpion technique (APDA, equation 3b). For one measurement channel and two reference channels the equation 3a reduces to the CIBR calculation (eq. 2) and equation 3b reduces to the 3-channel APDA technique, described in Borel and Schläpfer (1996).

4 EVALUATION OF DIFFERENTIAL ABSORPTION TECHNIQUES

4.1. CHANNEL SELECTION

The two channel categories mentioned in section 2 are evaluated using the channel selection procedure proposed by Schläpfer et al. (1995a). Measurement channels are searched within the absorption band because they should be sensitive to variations of the trace gas amount. Furthermore the difference between the signal of the trace gas and the noise must be clearly discernible in these channels and other absorbing atmospheric species must not disturb the signal of the trace gas of interest. A reference channel has to meet two conditions: The signal should not be influenced by any atmospheric species and the effective signal to noise ratio must be as big as possible. The mentioned requirements were expressed as mathematical channel qualifiers for measurement and reference channels by Schläpfer et al. (1995a). One factor, which has to be considered in addition to the mathematical selection procedure is the wavelength distance of the reference channels from their corresponding measurement channels. It has to be minimized to reduce errors due to non-linearity effects of the background radiance.

The channel selection procedure was applied to simulated data corresponding to AVIRIS images from 1991 over Central Switzerland and from 1995 over Camarillo (California). Ranked sets of channels to be used in differential absorption techniques were defined. First analysis showed, that the best suited wavelength region is the 940 nm absorption band. Hence, only channels in its region (from about 850 nm to 1070 nm) were further considered (see table 2). A crucial factor for the channel selection is the total water vapor transmittance, which has to be estimated from an average total columnar water vapor content for each scene. In 1995 the average transmittance was not exactly known from radiosonde data. Therefore the best channels on both sides of the maximal absorption (channels 59 and 64; both in the slope of the absorption feature) were also selected for further evaluations.

	AVIRIS 1991 data	AVIRIS 1995 data
measurement channels	60 (939 nm; σ-band) 61 (949 nm; σ–τ-band)	59 (912 nm; ρ-band) 61 to 64 (932 - 961 nm; σ–τ-band)
reference channels (near the selected meas. channels)	52 to 54 (862 - 881 nm) 66 to 73 (987 - 1065 nm)	54 to 56 (865 - 884 nm) 68 to 70 (999 - 1018 nm)

Table 2: The best performing measurement and reference channels for water vapor measurement, based on the characteristics of 1991 and 1995 AVIRIS data.

4.2 METHOD SELECTION

A good method for the measurement of a trace gas must meet the following requirements: 1) little noise effects due to the statistic error of the single channels, 2) low cross sensitivity to variations of disturbing atmospheric constituents, and 3) insensitivity to changing ground reflectance characteristics. The techniques given in section 3 are applied for various channel combinations and tested regarding the above conditions. Each of the latter is described by a metric value.

For 1991 data a large set of methods were compared by multiplying these values (similar to the channel selection procedure) and by setting single limits for each metric (Schläpfer et al., 1995b). It was found, that the use of more than 3 channels of the best ranked ones reduces the total image noise without losing information. Techniques of higeher complexity like absorption slope analysis or unlinear regressions failed due their high sensitivity to the sensor noise. The APDA(60,61;53,54,66,67,68) method was finally selected for application to the images (Schläpfer et al., 1995b).

For 1995 data a total number of 360 methods was introduced, consisting of APDA and LIRR/CIBR combinations with 4 (respective 2) reference channels and 2 (respective 1) measurement channels. For the test of atmospheric cross sensitivity, MODTRAN3 runs with varying aerosol and water vapor contents were taken as calibration data for the defined methods. All retrieval methods were then applied to radiance data of a spatial image subset. Since it can be assumed, that the water vapor variability over a small flat area is modest, the standard deviation of the processed water vapor ratio values in this image subset is taken as a measure for errors due to the total image noise (= sensor noise + ground reflectance variations).

A limit for the qualifiers was set to get a pre-evaluated set of methods, which had to fulfill the requirements in the best 10 percent of all 360 methods. The percent limit was interactively reduced until less than 10 methods remained. These methods were applied to images and the columnar water vapor content was quantified. Special effects in the water vapor image, like erroneous channels or obvious misquanitfications, leaded to further exclusions and re-evaluation of other methods. The whole method selection process was performed in two major steps after the channel selection: the theoretical pre-evaluation based on simulations, sensor characterisics and image subsets and a practical evaluation, based on effective quantification results, ground truth comparisons and effects in the resulting image.

As expected, the APDA - technique increased the significance of the water vapor signal against the standard deviation in the 100x100 pixel subset, i. e. the background reflectance influences were suppressed. Also the aerosol influence could be slightly reduced by the atmospheric pre-correction. The error induced by aerosols is nearly twice as big for methods with measurement channels in the slope of the band than for those in the center. Therefore the measurement channels in the absorption maximum had to be used, although those in the slope showed better ranking results after the channel selection procedure.

Figure 1 shows six of the best performing methods for 1995 data. The absolute error was obtained by comparing a relatively small water vapor signal with the two error factors 'Aerosols' and 'Total image noise'. The ratioing to the estimated total water vapor amount of about 29.2 kg/m^2 at image base level yielded the percentage of the relative errors. The estimated errors due to an aerosol variation between visibilities of 23 km and 12 km at ground level was between 1.0 and 1.3 kg/m^2; corresponding to a relative error of about 3.5 to 4.5% (see figure 1). The combined background reflectance and sensor noise error, given by the standard deviation within the image subset, is nearly half as big with 2 to 2.5% on the retrieved water vapor amount (this error will increase for larger subsets). The channel combination was defined based on the best performing methods as shown in figure 1. The theoretical total error of the retrieval is estimated to be below 5% (aerosol error + image noise error) on the total water vapor amount out of the above method evaluation, which corresponds to a columnar amount of about ±1.5 kg/m^2.

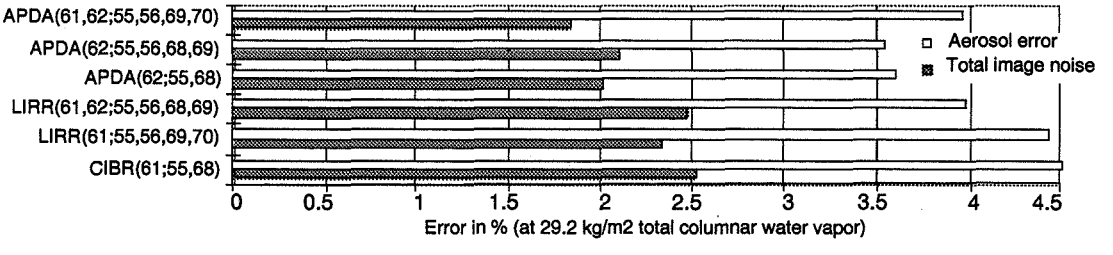

Figure 1: Evaluation results for 1995 AVIRIS data, the water vapor retrieval error is given relative to normal midlatitude summer conditions.

4.3 RELATING RATIO VALUES TO TOTAL COLUMNAR WATER VAPOR

The Differential Absorption technique yields only unquantified ratio values, which have to be transformed to total water vapor amounts. Frouin et al. (1989) and Carrere et al. (1993) used an exponential approach for the relationship of a differential absorption ratio R to its corresponding water vapor amount (PW). For this study it was extended to the equation:

$$R = e^{-\left(\gamma+\alpha(PW)^{\beta}\right)} \qquad \text{solved for the water vapor amount:} \qquad PW = -\left(\frac{\ln(R)+\gamma}{\alpha}\right)^{\frac{1}{\beta}} \qquad (4)$$

The water vapor retrieval procedure for image data follows the following steps: First simulated data in the AVIRIS-channels at various total columnar water vapor contents is obained by MODTRAN3 runs. Then the previously selected, best performing differential absorption technique is applied to the thus simulated radiance at the sensor, what yields a look up table for the relationship between water vapor content and ratio value. The constants α, β and γ of the exponential fitting function (4) are derived from the LUT and used to invert the ratio image to the final retrieved total columnar water vapor distribution image. Typical values for α are 0.12- 0.18, for β 0.65 to 0.80 and for γ -0.05 to 0.4. The procedure can be extended by iterative APDA calculations and by using cubic spline interpolations instead of equation (4) (Borel and Schläpfer, 1996).

5 APPLICATION TO AVIRIS IMAGES

The methodology described in the previous sections was applied to two AVIRIS scenes:

1) Site: Central Switzerland, 'Risch' Date: July 5, 1991 run 6, scene1
2) Site: Santa Monica, 'Camarillo' Date: May 26, 1995 run 8, scene3

5.1 SCENE OVER CENTRAL SWITZERLAND

The selected differential absorption method for 1991 was applied to the AVIRIS'91 scene of Central Switzerland (Meyer, 1994). The '91 data has a five time worse SNR compared with the most recent AVIRIS data. However, this data set is valuable for atmospheric imaging spectrometry because of the extensive simultaneous in-situ measurements of atmospheric trace gases, taken during the Swiss POLLUMET experiment. Various balloon soundings in and near the test region were combined to obtain the actual profile for the date of over flight (5th of July, 1991). The error of these radiosonde measurements is estimated to be within ±10%. Additionally, the spatial distribution of water vapor was measured by in situ flights of an ultra light aircraft.

The above explained correction of the path radiance effect had to be done to diminish the impact of the background albedo. Since the path radiance is dependent on the ground altitude, a height dependent correction had to be applied. The radiance over zero albedo was simulated at different altitudes using MODTRAN3 with the DISORT option. The height information from the corresponding DEM was used to get a height dependent path radiance for each channel and pixel. This term was then subtracted from the radiometric calibrated 1991 AVIRIS-data and the ratio applied to these corrected data.

The water vapor retrieval results of the APDA(60,61;53,54,66,67,68) method are shown in figure 2. The highest concentrations measured near the lake in the image are about 29 kg/m^2 and the mean column near the shore is 28.5 kg/m^2. The integration of the measured water vapor profiles taken from radiosonde data yields a total column of 29.7 kg/m^2 over the lake level (414 m a.s.l.). This small difference of about 5% between radiosonde data and the quantified AVIRIS values is within the error of radiosonde data in general and also within the error range of the retrieval procedure described above.

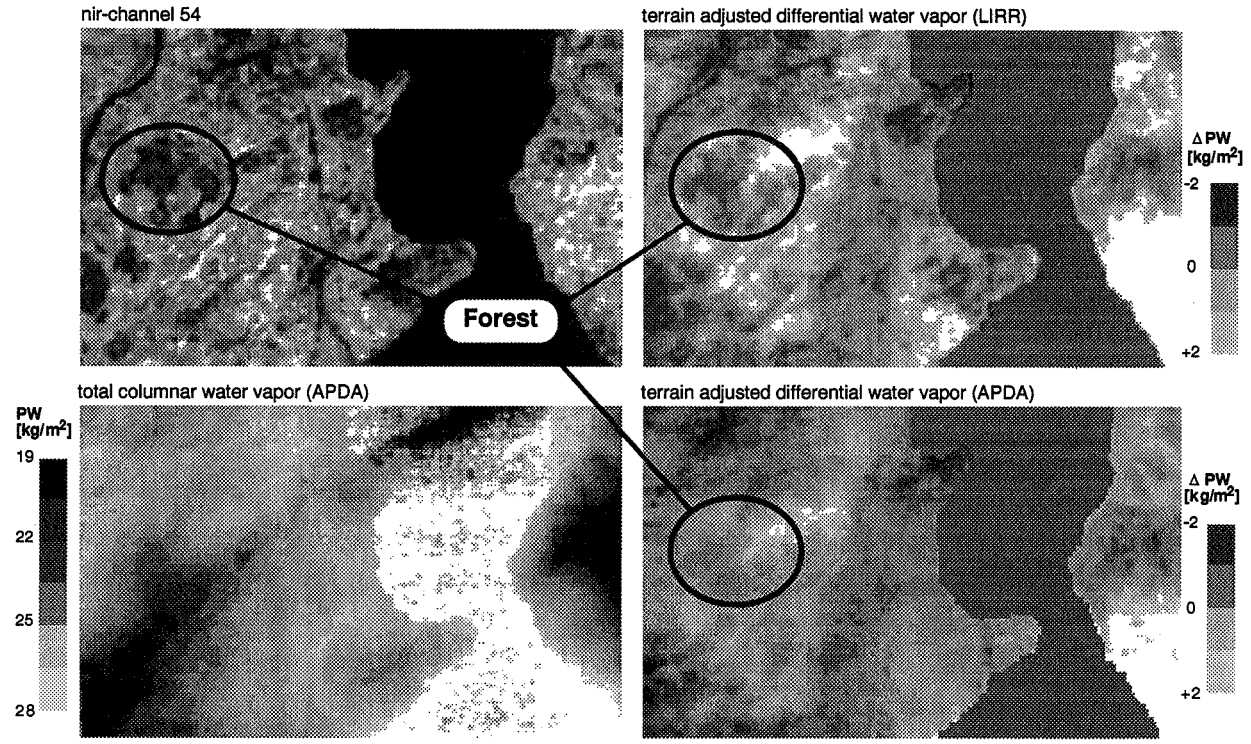

Figure 2: Upper left: raw image (at channel 54, 881 nm); lower left: water vapor retrieval with atmospheric pre-correction; upper right: terrain adjusted differential water vapor distribution without atmospheric pre-correction; lower right: same processing as upper right after height dependent atmospheric pre-correction. All images are smoothed with a filter size of 5x5 pixels. The lake is masked out for the terrain adjusted images.

The spatial water vapor distribution correlates very well with the DTM of the region, because the highest concentrations of water vapor are found in the boundary layer (lower troposphere) with an exponential decrease with height. The difference in terrain height of 540 m produces a decrease of water vapor of about 9 kg/m^2, which is obtained out of the image between the highest and the lowest terrain point (954 m a.s.l to 414 m a.s.l). The same amount is obtained by integrating the radiosonde profile between these height levels, within an error of about 5%.

For the interpretation of water vapor distribution in rugged terrain, the influence of the terrain overrides real spatial changes in water vapor concentrations. This effect of the terrain was reduced by calculating an average 'ideal' water vapor distribution map based on the digital elevation model and the average total columnar water vapor contents at each height level. This water vapor distribution averaged at each height level was then subtracted from the quantified total columnar water vapor distribution. The resulting terrain adjusted differential water vapor maps for LIRR and APDA calculation are shown in figure 2. Obvious underestimations over the relatively dark forests can be observed in the uncorrected image, as already described by Gao and Goetz (1990). If the atmospheric pre-correction is applied, most of these errors caused by variations of the background reflectance disappear, leading to a better estimate of relative water vapor concentrations.

5.2 SCENE OVER CAMARILLO, CALIFORNIA

For the 1995 data the total aerosol content was not known exactly. Therefore L_{atm} determined by MODTRAN3 is not an optimal substitute for $L_{atm,s}$ in $L_s - L_{atm,s}$ of Eq. 3b. Instead, $L_s - f \cdot L_{atm,s}$ was used, where f is determined empirically as the value, which minimizes the standard deviation of the ratio (Eq. 3b) over a subset of the image. This correction factor was used with the APDA technique for the image data as well as for the corresponding

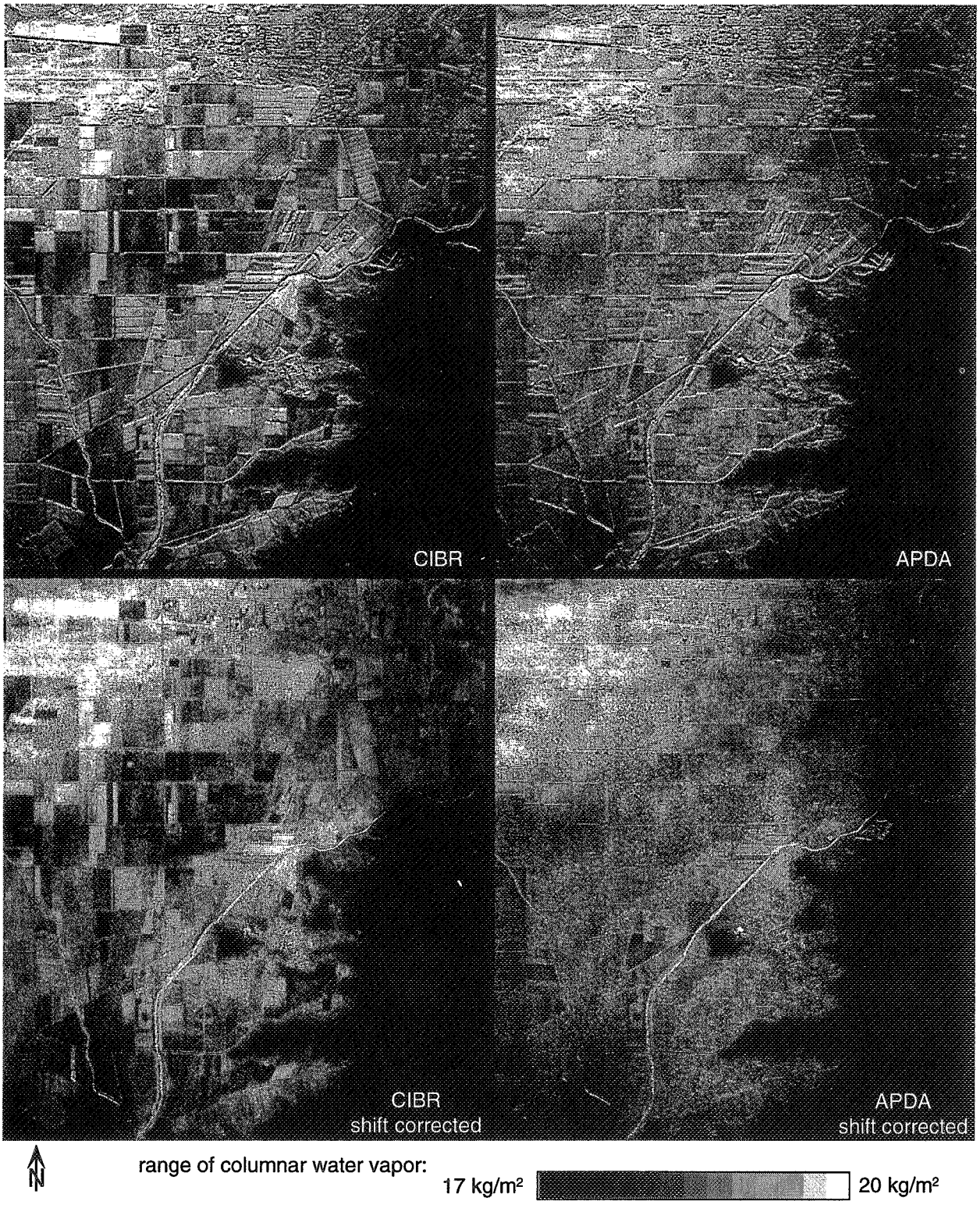

Figure 3: CIBR and APDA(61,62;55,56,68,69) calculation over the 1995 AVIRIS scene at Camarillo (near Oxnard, CA). The images are enhanced to show variations over the plain between Camarillo (northern image border) and Point Mugu (south). The mountain area in the lower right corner appears black, because of the much lower water vapor contents over elevated topography. The four images have not been smoothed.

simulated quantification data. The introduction of that optimization factor is an empirical approach to improve the effect of atmospheric pre-correction, whereas Borel and Schlaepfer (1996) show an iterative approach for the same problem.

The application of the APDA technique on the 1995 data showed the unexpected effects of edge-enhancement along the borders of the agricultural fields (see figure 3, upper images). Since cast shadows in irrigation channels and from plants would not show the observation systematicallity, this must be a sensor inherent effect. According to Chrien (1996) the new AVIRIS focal plane features erroneous amplifiers which cause bright areas bounded by dark areas to appear somewhat delayed. The delay increases with the magnitude of changing signal. Since the reference channels have more than twice the signal of the measurement channels, they were delayed. To correct for this effect, a pixel shifting between single channels was assumed (even before we heard about the AVIRIS hardware problem). A procedure to detect sub-pixel shifts (Varosi, 1994) was run over the channels used in the water vapor retrievel algorithm. This analysis, which maximizes the correlation between the single channels, showed that the used reference channels (# 55,56,68,69,70) were shifted across the flight direction by about 0.15 pixels to the measurement channels (# 61,62), whereas in flight direction nearly no shift was detected. All relevant channels were then reregistered by shifting them by the calculated sub-pixel shifts, using bilinear interpolation. The corrected water vapor images were significantly improved compared to the uncorrected images.

Figure 3 shows the effects of atmospheric pre-correction and pixel shift correction: When doing the traditional differential absorption technique, high impacts of the background characteristics are reported (left). After the atmospheric pre-correction most of this impact disappears, but the borders of the fields seem to be enhanced (upper right). Only a pixel shift correction removes this artifact and shows primary water vapor amounts. (The image at the lower right is not smoothed against the others; the smoother appearance is only due to the applied correction steps!).

The range of the water vapor concentrations is within about 17 to 20 kg/m^2, and even fine variations over the plane between 18 and 19 kg/m^2 can be observed in the shift corrected APDA image. This accuracy can not be achieved with the traditional CIBR-technique, where background effects override the signal of the water vapor. In the final image there are still small ground reflectance caused effects, which show that there is opportunity to improve the water vapor retrieval results by a better atmospheric pre-correction or possibly by using spectral classification techniques.

6 CONCLUSIONS

It was shown that the introduced atmospheric pre-corrected differential absorption (APDA) technique allows to measure spatial water vapor distributions even over flat areas with strong background reflectance variations. In advance a quantitative method of channel selection yielded ranged sets of channels for application in the APDA technique, and a large set of retrieval methods were evaluated using an exclusion and ranking process. This combination of optimized channel selection, method evaluation and the APDA technique made it possible to achieve significant improvement compared to traditional differential absorption techniques.

Applying the radiative transfer code MODTRAN3, the selected methods were calibrated to the total water vapor columns. The retrieval of water vapor over land was possible with an accuracy of about ±5%. The error was attributed to the uncertainty in background reflectance and aerosol concentration in the used atmospheric model. The distribution with terrain height for 1991 data was very similar to the profile measured by radio sondes, although the image was calibrated by the integrated total water vapor column (the slope of the water vapor profile has a negligible effect on the results). Hence, the used methodology has the potential to derive water vapor profiles from the boundary layer, using the digital terrain model.

In future work such profiling methods will be searched and three dimensional modeling of the water vapor field in valleys will be tried. The complementary measurement of water vapor over dark surfaces (like lakes or cast shadow areas) will only be possible with further improvements of the methodology. Such methods will differ essentially from the differential absorption and nonlinear curve fitting techniques. The most promising approaches are the

improvement of the atmospheric pre-correction by introducing an iterative water vapor retrieval process or the application of classification algorithms and spectral databases.

7 ACKNOWLEDGMENTS

The following institutions, foundations and persons are greatly acknowledged: The Swiss National Science Foundation and NASA HQ's Remote Sensing Science Program for the financial support of the project, the AVIRIS group at the JPL Pasadena for providing the AVIRIS-images, Los Alamos National Laboratory (LANL) and the Remote Sensing Laboratories (RSL) for their facilities.

REFERENCES

ABREU L.W., CHETWYND J.H, ANDERSON G.P. and KIMBALL L.M., 1995: *MODTRAN3 Scientific Report.* draft preprint, Geophysics Laboratory, Air Force Command, US Air Force, Hanscom AFB, MA, USA

BERK A., BERNSTEIN L.S., ROBERTSON D.C., 1989: *MODTRAN: A Moderate Resolution Model for LOWTRAN 7.* Geophysics Laboratory, Air Force Command, US Air Force, Hanscom AFB, MA, USA

BRUEGGE C.J., CONEL J.E., MARGOLIS J.S., GREEN R.O., TOON G., CARRÈRE V., HOLM R.G. and HOOVER G., 1990: *In-situ Atmospheric Water-Vapor Retrieval in Support of AVIRIS Validation.*, SPIE Vol. 1298 Imaging Spectroscopy of the Terrestrial Environment, pp 150 - 163

BOREL C.C and SCHLÄPFER D., 1996: *Atmospheric Pre-Corrected Differential Absorption Techniques To Retrieve Columnar Water Vapor: Theory.* Proceedings of the 6th JPL Airborne Earth Science Workshop, JPL, Pasadena (in press)

CARRÈRE V. and CONEL J. E.,1993: *Recovery of Atmopheric Water Vapor Total Column Abundance from Imaging Spectrometer Data Around 940 nm - Sensitivity Analysis and Application to Airborne Visible/ Infrared Imaging Spectrometer (AVIRIS) Data.* Remote Sensing of Environment, Nr. 44 , pp 179 - 204

CHRIEN T.,1995: *personal communication,* mentioned in xxxx.errata-file of AVIRIS data set

FROUIN R., DESCHAMPS P.-Y and LECOMTE P., 1990: *Determination from Space of Atmospheric Total Water Vapor Amounts by Differential Absorption near 940 nm: Theory and Airborne Verification.* Journal of Applied Meteorology, Vol. 29, American Meteorological Society, pp 448 - 459

GAO B.-C., Heidebrecht K.B and GOETZ A.F.H., 1993: *Derivation of Scaled Surface Reflectance from AVIRIS Data,* Remote Sensing of Environment, Nr. 44, New York, pp 165 - 178

GAO B.-C. AND GOETZ A.F.H.,1990a: *Column Atmospheric Water Vapor and Vegetation Liquid Water Retrievals From Airborne Imaging Spectrometer Data,* Journal of Geophysical Research, Vol. 95, No. D4, pp 3549 - 3564

GAO B.-C. AND GOETZ A.F.H.,1990b: *Determination of Total Column Water Vapor in the Atmosphere at High Spatial Resolution from AVIRIS Data Using Spectral Curve Fitting and Band Ratioing Techniques,* SPIE Vol. 1298, Imaging Spectroscopy of the Terrestrial Environment, pp 138 - 149

KAUFMAN Y.J. and GAO B.-C., 1992: *Remote Sensing of Water Vapor in the Near IR from EOS/MODIS.* IEEE Transactions on Geoscience and Remote Sensing, Vol. 30, No. 5, pp 871 - 884

MEYER P., 1994: *A Parametric Approach for the Geocoding of Airborne Visible/Infrared Spectrometer (Aviris) Data in Rugged Terrain.* , Remote Sensing of Environment, Vol. 48, pp 1-25

SCHLÄPFER D., KELLER J. and ITTEN K.I., 1995a: *Imaging Spectrometry of Tropospheric Ozone and Water Vapor.* submitted to EARSeL International Journal 'Advances in Remote Sensing', p 12

SCHLÄPFER D., KELLER J. and ITTEN K.I., 1995b: *Imaging Spectrometry of Tropospheric Ozone: New Methods of Channel Selection,* presented at IGARSS'95, Florence, separatum (not in proceedings), p 3

VAROSI F, 1988-1995: *Varosi's General Purpose IDL Code Library (vlib)* , Mail Code 685, ftp://idlastro.gsfc.nasa.gov /contrib/varosi, NASA/Goddard Space Flight Center, Greenbel MD

VERMOTE E., TANRÉ D., DEUZÉ J.L., HERMAN M. and MORCETTE J.J., 1984: *Second Simulation of the Satellite Signal in the Solar Spectrum.* , 6S User Guide Version 0, NASA-Goddard Space Flight Center, Greenbelt, USA, p 182

Page intentionally left blank

THE HYPERSPECTRAL IMAGER ABOARD THE SSTI's LEWIS SPACECRAFT: A COMPARISON WITH AVIRIS

James K. Sokolowski[1], Kern Witcher[2], Bruce A. Davis[2], Robert O. Green[3]

[1] Lockheed Martin Stennis Operations
Commercial Remote Sensing Program
Building 1210
Stennis Space Center, MS 39529

[2] National Aeronautics and Space Administration
Commercial Remote Sensing Program Office
Building 1100
Stennis Space Center, MS 39529

[3] Jet Propulsion Laboratory
California Institute of Technology
4800 Oak Grove Drive
Pasadena, CA 91109

1. INTRODUCTION

This paper compares the performance and operational parameters of the Hyperspectral Imager (HSI), scheduled for launch aboard the Lewis spacecraft in July 1996, with those of the Airborne Visible/Infrared Imaging Spectrometer (AVIRIS). The HSI is a pushbroom, imaging spectrometer with 30 meter spatial resolution, generating 384 spectral channels over the range 400 to 2500 nm at 5.0 to 6.4 nm resolution for each of its 256 crosstrack pixels. The Lewis spacecraft and the HSI are being built by TRW, Incorporated as part of the Small Spacecraft Technology Initiative (SSTI) initiated by NASA's Office of Space Access and Technology to advance the state of technology and reduce program costs associated with the development and operation of small satellites. The SSTI is also producing the Clark spacecraft being built by CTA, Incorporated, which is scheduled for launch late in the summer of 1996. Clark will carry the high spatial resolution WorldView imager, having 3m panchromatic and 15m multispectral capability, as its primary payload.

Because the SSTI was intended to demonstrate new design and space system qualification methods as well as to promote commercial applications for remotely sensed data, both Lewis and Clark will carry a number of additional payloads and experimental technology demonstrations. Among these payloads are two other imaging spectrometers: the Linear Etalon Imaging Spectrometer Array (LEISA) and the Ultraviolet Cosmic Background (UCB) instrument aboard Lewis. The LEISA is an earth-observing sensor providing 256 spectral bands in the 1000 to 2500 nm region, with roughly 300 meter spatial resolution. The UCB is designed to map the diffuse, ultraviolet cosmic background in the 11.8 to 22.5 eV range. Additional Clark payloads include the Atmospheric Tomography (ATOMS) instrument for determining 3-D atmospheric molecular profiles, the Measurement of Air Pollution from Satellites (μMAPS) sensor for mapping and monitoring atmospheric carbon monoxide profiles, and the X-Ray Spectrometer (XRS) for observing solar flares and cosmic gamma ray bursts over the 1 to 100 keV region.

To augment the list of sensor performance metrics, this paper presents the signal to noise ratios of both the HSI and the AVIRIS for typical observing conditions, outlines plans for standard processing of HSI data, and discusses both data availability and satellite tasking.

2. HSI PERFORMANCE AND OPERATIONAL PARAMETERS

Table 1 compares the performance and operational parameters of the AVIRIS with those of the HSI, which is composed of two focal plane assemblies: the Visible- to Near-Infrared (VNIR) and Short-Wave Infrared (SWIR) spectrometers.

Table 1. Comparison of HSI and AVIRIS System Parameters

Parameter	Lewis/HSI	AVIRIS
Operational Altitude	Circular orbit of 523 ± 10 km altitude, Sun Synchronous (97.5° inclination) 10:50 AM ± 0:20 ascending node.	Nominal 20 km operational altitude.
Positional Accuracy	≈ ± 100 m in X, Y, and Z	≈ ± 100 m in X, Y, and Z
Imaging Attitude	• ± 22° in Roll • ± 0.25° in Pitch • ± 3.8° in Yaw	Nadir pointing only.
Attitude Uncertainties	• ± 8" in Roll (≈2/3 pixel) • ± 25" in Pitch (≈2 pixels) • ± 30" in Yaw (≈1/60 pixel)	• ± 21" in Roll (≈1/10 pixel) • ± 21" in Pitch (≈1/10 pixel) • ± 21" in Yaw (≈1/100 pixel)
Data Collection Rate	One imaging event per working day. Approximately 250 image cubes in the first year of operation.	≈80 cubes per flight day or ≈3,000 cubes per year. This includes 33% downtime for scheduled maintenance.
Radiometric Calibration Plan	• Pre-launch laboratory calibrations • 8 pre-image dark frames • 8 post-image dark frames • 8 post-image white frames at low lamp current • 8 post-image white frames at high lamp current • 1 set of solar frames per week • Periodic, on-orbit calibration verification experiments	• A pre-image sequence of darks, whites, and line frames • A post-image sequence of darks, whites, Lyots, and Line frames • Yearly laboratory calibration • Three operational calibration experiments annually
Radiometric Calibration Accuracy	• ± 5% absolute • ± 2% relative	• ± 4% absolute • ± 2% relative
Data Quantization	12-bit digitization, padded to a two-byte integer	12-bit digitization, padded to a two-byte integer
Spectral Calibration Plan	• Pre-launch calibration • On-orbit verification • Periodic on-orbit monitoring	• Annually in laboratory • ± 1 nm band centers • ± 1 nm band widths full width half max (FWHM)
Spatial Resolution	30m by 30m pixels	20m by 20m nominal pixels
Spatial Size of Data Sets	• 256 cross track pixels • ~1000 along track lines but more in proportion to the fraction of bands *not* acquired	• 614 cross track pixels • 512 along track lines
Spectral Resolution	• VNIR → 5.0 nm FWHM • SWIR → 6.4 nm FWHM	≈10 nm for all spectrometers (A, B, C , and D)
Spectral Sampling	• VNIR → 5.0 nm • SWIR → 6.4 nm	≈10 nm for all spectrometers (A, B, C, and D)
Number of Bands	• VNIR → 128 (400 - 1000 nm) • SWIR → 256 (900 - 2500 nm)	• A → 32 (370 - 680 nm) • B → 64 (670 - 1270 nm) • C → 64 (1250 - 1880 nm) • D → 64 (1880 - 2500 nm)

3. SIGNAL-TO-NOISE RATIOS

Figure 1 compares the signal-to-noise ratios expected from both the HSI and the AVIRIS for a target at 45°N latitude, having a gray albedo of 0.3, an observing geometry with 60° solar zenith angle, using a standard, MODTRAN spring season atmosphere. The signal-to-noise ratios for both VNIR and SWIR are plotted in the 900 nm to 1000 nm region where they overlap.

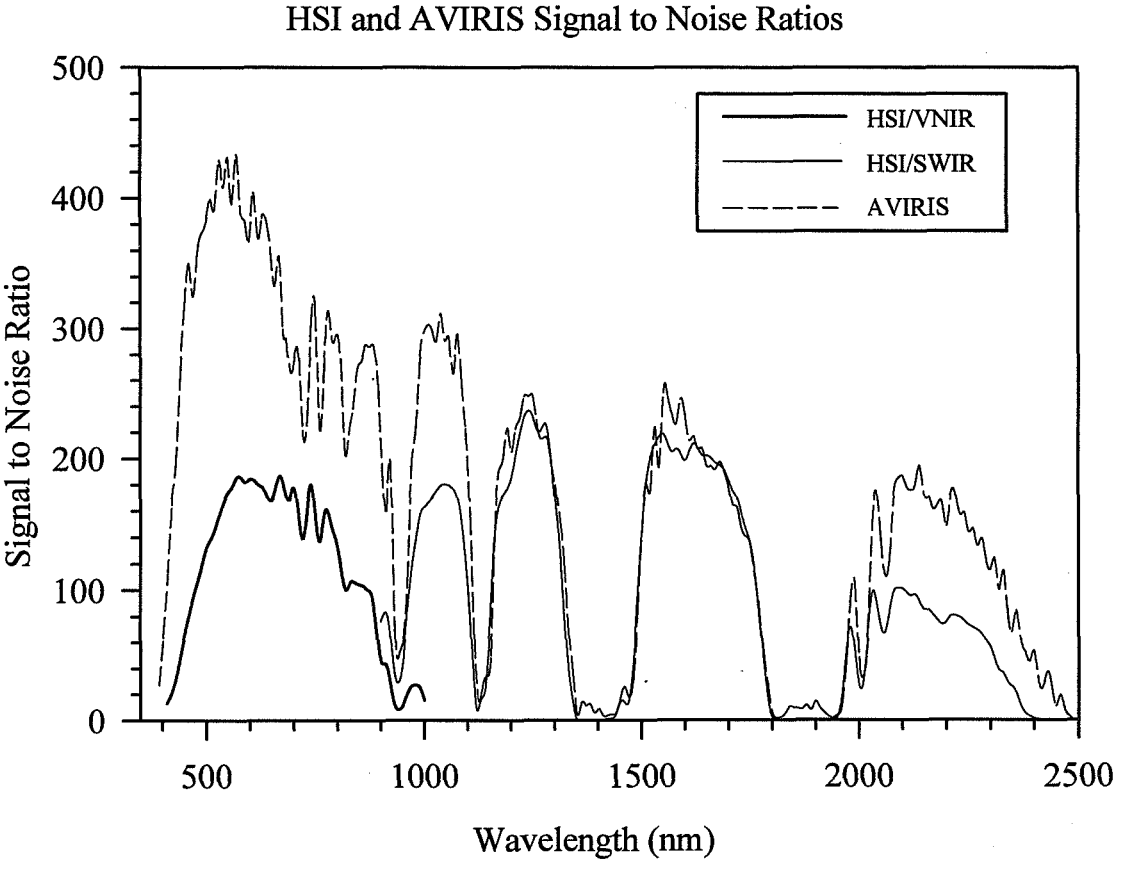

Figure 1. The signal-to-noise ratios expected from both HSI and the AVIRIS for a target at 45° N latitude, having a gray albedo of 0.3, an observing geometry with 60° solar zenith angle, using a standard, MODTRAN spring season atmosphere. The VNIR and SWIR spectral channels have been binned in twos to produce resolutions of 10 nm and 12.8 nm for VNIR and SWIR respectively, comparable with that of the AVIRIS. Both VNIR and SWIR spectra are plotted in the 900 nm to 1000 nm region where they overlap.

4. DATA PROCESSING

The Commercial Remote Sensing Program (CRSP) based at Stennis Space Center (SSC), Mississippi, is developing the Data Processing System (DPS) to derive higher-level data products from level 0 HSI data acquired at the spacecraft. The purpose of the DPS is to optimize the commercial and scientific viability of the Lewis and Clark missions by offering the entire user community standard data products, appropriate to their requirements, for further processing and analysis. The data processing outline of the DPS is 1) radiometric calibration, where signal digital numbers are converted to units of radiance at the spacecraft; 2) atmospheric removal, where molecular absorptions

as well as molecular and aerosol scattering effects are removed, thus converting pixel units to apparent ground reflectance; 3) georeferencing of both VNIR and SWIR spectrometers, where the latitude and longitude of each image pixel center are determined relative to a featureless Earth model (NOTE: there is no data resampling here); 4) the SWIR data are spatially resampled, producing a footprint on step 3's model Earth equivalent to that of VNIR; and 5) the region of spectral overlap between VNIR and SWIR is removed, yielding one complete, apparent reflectance spectrum for each image pixel. The DPS will also perform a number of automated quality assurance (QA) steps and allow for manual QA at every level. All DPS processing will be performed using C++ and IDL codes running in the Windows NT operating system on INTEL-based machines. Processing to level 2 data products and beyond will be accomplished manually by SSC staff for Lewis team members on an as-requested basis.

5. DATA AVAILABILITY

Appropriate data products from the DPS described in section 4 will be made available to all Lewis team partners via the World-Wide-Web-based Mission Data Management System (MDMS). This system will allow team partners to examine all data sets and to download chosen image cubes and associated data structures (*i.e.*, data headers, metadata, parameter blocks, and calibration data structures) directly. Copies of appropriate data within the MDMS will be stored at the EROS Data Center (EDC), where they will be made available to the public following EDC and NASA established pricing guidelines. Generally, there will be no period of exclusivity for SSTI data products, and all SSTI data will be made available immediately following DPS processing. However, data collected in response to national emergencies and for Code S sponsored investigations will retain a one-year period of exclusivity for government use and the Code S experiment team, respectively.

Although subject to change, it appears that the MDMS will contain the following data generated by the DPS for each imaging event: 1) an unprocessed, level 1A cube (prior to step 1 above); 2) a 1G1 cube, which has been converted to georeferenced, apparent reflectances on the ground (processed through step 3 above, NOTE: having undergone no irreversible processing); and 3) a 1R2 cube, containing one complete spectrum per image pixel (processed through step 5 above, NOTE: resulting from both spatial and spectral irreversible processing). Higher-level (data levels 2 and beyond) information products will *not* be made available from within the MDMS environment or at the EDC.

6. LEWIS/HSI TASKING

Current NASA/SSTI data policy is to establish an Experiment Tasking Oversight Group (ETOG), which will review all satellite tasking requests in each of the four basic experiment areas: commercial, science, education, and technology demonstrations. Proposals from current Lewis team partners will be given precedence over those from non-members, who will be required to enter into a Space Act Agreement with NASA, including appropriate experimental results reporting, in order to submit tasking proposals for ETOG consideration. In cooperation with NASA, CRSP, and TRW personnel, the ETOG will generate the tasking priorities among the four general experiment types and establish a coordinated tasking and observation plan. This plan will conform with all existing NASA data policies, including contingencies for national emergencies and natural disasters.

7. ACKNOWLEDGMENTS

Portions of this work were supported by the NASA Office of Space Access and Technology, Commercial Remote Sensing Program Office, under contract number NAS 13-650 at the John C. Stennis Space Center, Mississippi. Some of this work was performed at the Jet Propulsion Laboratory, California Institute of Technology, under a contract with the National Aeronautics and Space Administration.

SURFACE REFLECTANCE RETRIEVAL FROM AVIRIS DATA USING A SIX-DIMENSIONAL LOOK-UP TABLE

K. Staenz[1], D.J. Williams[2], and B. Walker[2]

[1]Canada Centre for Remote Sensing
588 Booth Street, Ottawa, Ontario, Canada K1A 0Y7

[2]MacDonald Dettwiler and Associates Ltd.
13800 Commerce Parkway, Richmond, British Columbia, Canada V6V 2J3

1. INTRODUCTION

Surface reflectance retrieval has become important for quantitative information extraction and multi-temporal and multi-sensor data analysis. The trend related to surface reflectance retrieval in imaging spectrometry is the removal of atmospheric effects with radiative transfer codes in combination with the extraction of atmospheric parameters from the image data themselves (Staenz et al., 1994; Green et al., 1993; Gao et al., 1993; Carrère and Conel, 1992). Unfortunately, such procedures can be very demanding with respect to computation time, especially when data in the gaseous absorption regions are used for subsequent analysis. In order to reduce the run time of these procedures, a look-up table (LUT) based surface reflectance retrieval technique was developed on the Imaging Spectrometer Data Analysis System (ISDAS) (Staenz et al., 1996) of the Canada Centre for Remote Sensing. This paper presents an overview of the LUT generation and subsequent transfer of Airborne Visible/Infrared Imaging Spectrometer (AVIRIS) radiances into surface reflectances.

2. DATA SETS AND DATA PREPARATION

AVIRIS data used for this study were acquired over forested areas in rugged terrain near Canal Flats (scene 1) and near Victoria (scene 2), British Columbia in August of 1990 and 1993, respectively. Available ground reference information relevant to this study includes a digital elevation model (DEM) for scene 1 and reflectance measurements of various targets (asphalt, gravel, soccer field, etc.) and aerosol optical depth for scene 2.

The original DEM of 70 m grid size was resampled to the AVIRIS pixel size (20 m) and then registered to the image cube using the forest cover map. The registration with the nearest neighbour resampling technique resulted in a RMS error of ± 1.50 in the pixel direction and ± 0.95 in the line direction. The map-to-image registration has the advantage of maintaining the radiometric accuracy, which is important for surface reflectance retrieval. Due to the lack of a DEM for scene 2, only point calculations with respect to the retrieval of surface reflectance were carried out for specific targets with terrain elevations extracted from topographic maps.

3. SURFACE REFLECTANCE RETRIEVAL

3.1 Overview

Features of the surface reflectance retrieval procedure include the generation of a linear LUT to provide additive and multiplicative coefficients for removal of scattering and absorption effects, altitude-dependent layering of atmospheric gases and aerosols, scene-based estimation of atmospheric parameters such as water vapour, first-order removal of adjacency effects, Lambertian correction for slope and aspect effects, and choice of exo-atmospheric solar irradiance (E_O) functions from different sources in combination with the different radiative transfer (RT) codes. Available RT codes on ISDAS are M5S (modified version of 5S (Tanré et al., 1990) used at CCRS (Teillet and Santer, 1991)), LOWTRAN7 (Kneizys et al., 1988), or MODTRAN2 (Berk et al.,1989) and MODTRAN3 (Anderson et al., 1995). RT codes can easily be exchanged or added since they share the same user interface. The necessary parameters to run a specific RT code are then automatically extracted from the various input tables. This

surface reflectance retrieval procedure can be applied to individual spectra or entire image cubes in both forward (radiance) as well as backward (reflectance) computation modes. An overview of this procedure is shown in Figure 1 for the retrieval of surface reflectance from AVIRIS data as presented in this paper.

3.2 LUT Computations

In order to generate the LUT, a selected RT code is run for two different flat reflectance spectra ($\rho_1 = 5\%$, $\rho_2 = 60\%$), for a single value or a range of atmospheric water vapour contents (U_{H2O}), optical depths (δ_a), and terrain elevations (z) covering the prevailing atmospheric conditions and the terrain variation. These calculations made on the RT code's wavelength grid (λ_m) are performed at different pixel locations (x) to capture the sensor geometry. Accordingly, a LUT is generated with the following six dimensions:

LUT (λ_m, ρ , x, z, U_{H2O}, δ_a).

The LUTs for both AVIRIS scenes were set up as follows:

LUT (λ_m = 1 cm^{-1} wavelength grid (RT code selected: MODTRAN 2),
ρ_1 and ρ_2,
x: 3 pixel positions (two extreme viewing angles ($\pm 15^\circ$), nadir),
z: 3 terrain elevations (one low and high value to cover range, one in between),
U_{H2O}: 3 water vapour values (one low and high value to cover range, one in between),
δ_a: 1 optical depth).

Accordingly, there are 54 MODTRAN2 runs necessary to generate this LUT, each run taking approximately 7 minutes on a Sun Microsystems SPARC 10/51. This leads to a total computation time of about 6.3 hours. Although the time is quite long, it is much less than running the RT code on a pixel-by-pixel basis. However, the time can be drastically decreased to about 2 minutes if the M5S code (20 cm^{-1} wavelength grid) is used in this LUT configuration. (It should be noted that the performance of MODTRAN2 is superior especially in the gas absorption regions (Staenz et al., 1994)). The input parameters for the MODTRAN2 runs are summarized in Table 1.

The resulting target radiances at the sensor ($L_{g_1}^*$, $L_{g_2}^*$) and the path radiances, ($L_{p_1}^*$, $L_{p_2}^*$) derived from the MODTRAN2 code were then scaled by the spectral ratio of the Green and Gao (1993) E_O function to that which is used in MODTRAN2 (Staenz et al., 1995). Other E_O data sets presently available are those implemented in M5S (Iqbal., 1983), 6S (Vermote et al., 1994), MODTRAN2 (Berk et al., 1989) and MODTRAN3 (Anderson et al., 1994). The next step involved the convolution of the model output radiances with the AVIRIS specific radiance using the relative spectral response profiles for the sensor's spectral bands.

Before converting the AVIRIS radiances into surface reflectances, the LUT was used to estimate the atmospheric water vapour content on a pixel-by-pixel basis from the image data themselves. A non-linear least square-fitting technique similar to those reported by Green et al. (1993) and Gao and Goetz (1990) was applied to the wavelength region covering both the 940 nm and 1030 nm absorption features. Results are shown in Figure 2 for scene 1. It can be seen that the distribution of the water vapour map follows the DEM.

3.3 Surface Reflectance Computation

The LUT was then interpolated to compute the parameters necessary for a conversion of the AVIRIS radiance into the surface reflectance on a pixel-by-pixel basis. The relationship between the reflectance ρ and the MODTRAN2 output radiances L_g^* and L_p^* can be written as (Williams et al., 1992):

$$L_{gi}^* = A \frac{\rho_i}{1 - \rho_i S} \qquad (1)$$

and

$$L_{p_i}^{*} = B \frac{\rho_i}{1 - \rho_i S} + L_a^{*} \quad , \tag{2}$$

where $i = 1, 2$, L_a^{*} is the radiance backscattered by the atmosphere, S is the spherical albedo of the atmosphere, and A and B are coefficients depending on geometric and atmospheric conditions. These equations can be solved for the unknowns A, B, L_a^{*} and S for each set of ($\rho_i, L_{g_i}^{*}, L_{p_i}^{*}$). $L_{g_i}^{*}$ and $L_{p_i}^{*}$ are adjusted for the sensor's viewing condition, atmospheric water vapour content, and terrain elevation on a pixel basis for each spectral band.

Since the radiance (L^{*}) measured by AVIRIS is the sum of equations (1) and (2), the surface reflectance can be calculated as follows:

$$\rho = \frac{L^{*} - L_a^{*}}{A + B + S\left(L^{*} - L_a^{*}\right)} \, . \tag{3}$$

This equation is valid for homogeneous areas, that is if the reflectance of the target in question is the same as the surrounding target reflectance ρ_e. For inhomogeneous areas ($\rho \neq \rho_e$), ρ_e needs to be incorporated into equation (3) by substituting ρ by ρ_e in equation (2) as well as in the denominator of equation (1).

Comparisons of surface reflectances retrieved with the LUT-based procedure and true MODTRAN2 runs show a relative error of ± 1% in the AVIRIS wavelength region.

Figure 3 portrays retrieved surface reflectance spectra of vegetation (conifers, clear cut area, and alpine meadow) extracted from scene 1 using equation (3). An artificial target, asphalt, extracted from scene 2 is shown in Figure 4. Since this target is entirely surrounded by forested areas ($\rho \neq \rho_e$), the adjacency effect caused by this surrounding target was removed (dotted versus dashed curve). It can be seen that this effect is important for wavelengths below 700 nm.

4. CONCLUSIONS

Surface reflectance retrieval from AVIRIS data is presented in this paper. Good results were achieved with the linear LUT-based procedure using MODTRAN2 in combination with the Green and Gao E_o function. For this purpose, a six-dimensional LUT was generated with wavelength, surface reflectance, pixel location, terrain elevation, atmospheric water vapour content, and aerosol optical depth as the dimensions. This procedure has the advantage of using a RT code only for the generation of the LUT, and not on a pixel-by-pixel basis and, therefore, saves computation time. Despite the fact that the RT code is only run for a specific LUT configuration and the linearity of the approach, the retrieved surface reflectances are comparable with results from true RT code runs. Surface reflectance results in the AVIRIS wavelength regions indicate a relative error of ± 1% using MODTRAN2. This procedure is implemented on the Imaging Spectrometer Analysis System (ISDAS), which runs on Sun Microsystems SPARC-10 workstations.

5. ACKNOWLEDGMENTS

The authors are grateful to P.M. Teillet, J.-C. Deguise, and J.-F. Guay of the Canada Centre for Remote Sensing and to J. Cheriyan and M. Budd of MacDonald Dettwiler and Associates for valuable discussions and technical support. Thanks are also due to C. Burke for excellent word processing of this paper.

6. REFERENCES

Anderson G.P., J. Wong, and J.H. Chetwynd, 1995, "MODTRAN3: An Update on Recent Validations Against Airborne High Resolution Interferometer Measurements," Summaries of the Fifth Annual JPL Airborne Earth Science Workshop, JPL Publication 95-1, vol. 1, Pasadena, California, pp. 5-8.

Berk, A., L.S. Berstein, and D.C. Robertson, 1989, "MODTRAN: A Moderate Resolution Model of LOWTRAN7," Final Report, GL-TR-0122, AFGL, Hanscom AFB, Maryland, 42 pages.

Carrère, V., and J.E. Conel, 1992, "Validation of Atmospheric Correction of Airborne Visible/Infrared Imaging Spectrometer (AVIRIS) Radiance Data Based on Radiative Transfer Modeling," Proceedings of the International Symposium on Spectral Sensing Research, vol. 1, pp. 474-487.

Gao, B.-C., and A. F. H. Goetz, 1990, "Column Atmospheric Water Vapour and Vegetation Liquid Water Retrievals From Airborne Imaging Spectrometer Data," Journal of Geophysical Research, vol. 95, no. D4, pp. 3549-3564.

Gao, B.-C., K.B. Heidebrecht, and A.F.H. Goetz, 1993, "Derivation of Scaled Surface Reflectances from AVIRIS Data," Remote Sensing of Environment, vol. 44, pp. 165-178.

Green, R.O., and B.-C. Gao, 1993, "A Proposed Update to the Solar Irradiance Spectrum Used in LOWTRAN and MODTRAN," Summaries of the Fourth Annual JPL Airborne Geoscience Workshop, JPL Publication 93-26, vol. 1, Pasadena California, pp. 81-84.

Green, R.O., J.E. Conel, and D.A. Roberts, 1993 "Estimation of Aerosol Optical Depth and Additional Atmospheric Parameters for the Calculation of Apparent Reflectance From Radiance Measured by the Airborne Visible/Infrared Imaging Spectrometer," Summaries of the Fourth Annual JPL Airborne Geoscience Workshop, JPL Publication 93-26, vol. 1, Pasadena, California, pp. 73-76.

Iqbal., M., 1983, An Introduction to Solar Radiation, Academic Press, New York, 390 pages.

Kneizys, F.X., E.P. Shettle, L.W. Abreu, J.H. Chetwynd, G.P. Anderson, W.O. Gallery, J.E. Selby, and S.A. Clough, 1988, "User's Guide to LOWTRAN7," AFGL-TR-88-0177, Environmental Research Papers, No. 1010, Air Force Geophysics Laboratory, Hanscom AFB, Bedford, Maryland, 137 pages.

Staenz, K., D.J. Williams, G. Fedosejevs, and P.M. Teillet, 1994, "Surface Reflectance Retrieval from Imaging Spectrometer Data Using Three Atmospheric Codes," Proceedings of SPIE's International Symposium on Recent Advances in Remote Sensing and Hyperspectral Remote Sensing, vol. 2318, Rome, Italy, pp. 17-28.

Staenz, K., D.J. Williams, G. Fedosejevs, and P.M. Teillet, 1995, "Impact of Differences in the Solar Irradiance Spectrum on Surface Reflectance Retrieval with Different Radiative Transfer Codes", Summaries of the Fifth Annual JPL Airborne Earth Sciences Workshop, JPL Publications 95-1, vol. 1, Pasadena, California, pp.153-156.

Staenz, K., B. Walker, and J. Schwarz, 1996, "An Image Analysis System Designed for Information Extraction from Hyperspectral Data," Proceedings of the XVIII International Congress for Photogammetry and Remote Sensing, Vienna, Austria (in preparation).

Tanré, D., C. Deroo, P. Duhaut, M. Herman, J.J. Morcrette, J. Perbos, and P.Y. Deschamps, 1990, "Description of a Computer Code to Simulate the Satellite Signal in the Solar Spectrum: The 5S Code," International Journal of Remote Sensing, vol. 11, no. 4, pp. 659-668.

Teillet, P.M., and R.P. Santer, 1991, "Terrain Elevation and Sensor Altitude Dependence in a Semi-Analytical Atmospheric Code," Canadian Journal of Remote Sensing, vol. 17, no. 1, pp. 36-44.

Vermote, E., D. Tanré, J. L. Deuzé, M. Herman, and J. J. Morcrette, 1994, "Second Simulation of the Satellite Signal in the Solar Spectrum (6S)", 6S User's Guide Version 6.0, NASA-GSFC, Greenbelt, Maryland, 134 pages.

Williams, D.J., A. Royer, N.T. O'Neill, S. Achal, and G. Weale, 1992, "Reflectance Extraction From CASI Spectra Using Radiative Transfer Simulations and a Rooftop Radiance Collector", Canadian Journal of Remote Sensing, vol. 18, no. 4, pp. 251-261.

Table 1. Input Parameters for the MODTRAN2 Runs

Parameter	Scene 1	Scene 2
Atmospheric model	Mid-latitude summer	Mid-latitude summer
Aerosol model	Continental	Continental
Date of overflight	August 2, 1990	August 29, 1993
Solar zenith angle	35.9°	46.9°
Solar azimuth angle	179°	218°
Sensor zenith angle	variable	variable
Sensor azimuth angle	variable	variable
Terrain elevation	variable	variable
Sensor altitude above sea level	19.850 km	19.360 km
Water vapour content	variable	variable
Horizontal visibility or Aerosol optical depth	50 km -	- 0.121 (measured)

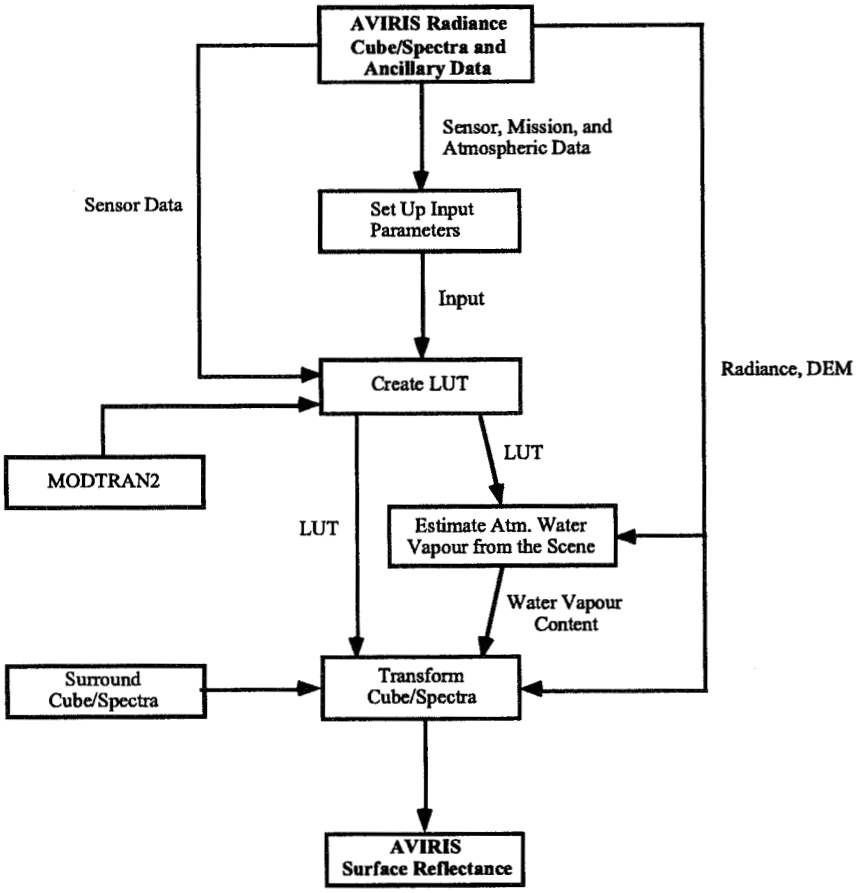

Figure 1: Layout of the LUT-based procedure for retrieval of surface reflectance from AVIRIS data.

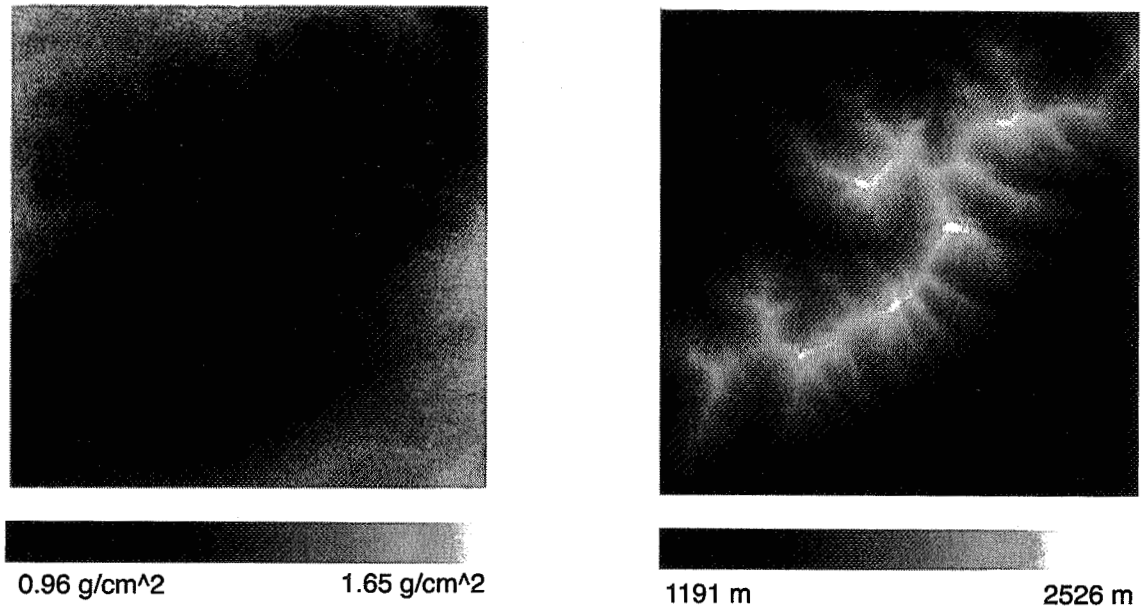

Figure 2: Distribution of the atmospheric water vapour content (left) extracted from AVIRIS scene 1. The DEM is shown on the right for the same area as a comparison.

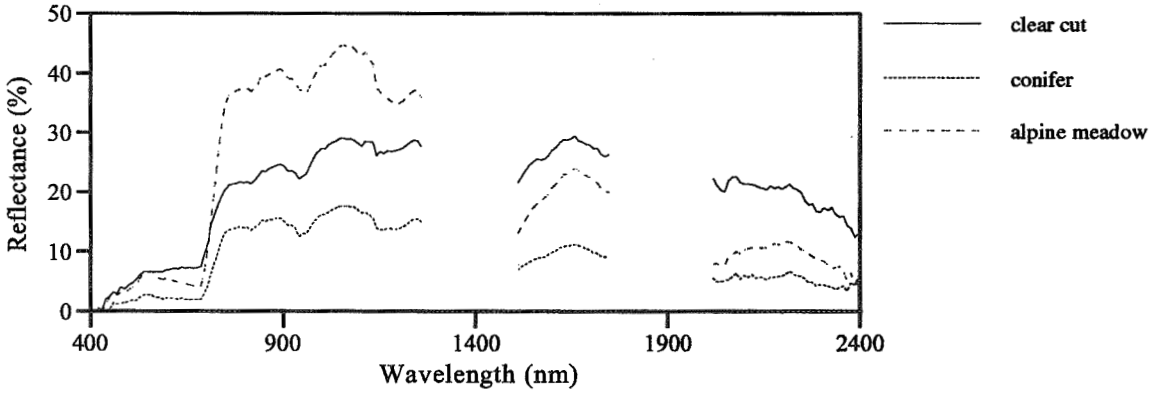

Figure 3: Surface reflectance spectra of different vegetation targets retrieved with the LUT-based approach using MODTRAN2 and the Green and Gao E_o function. Data are extracted from AVIRIS scene 1.

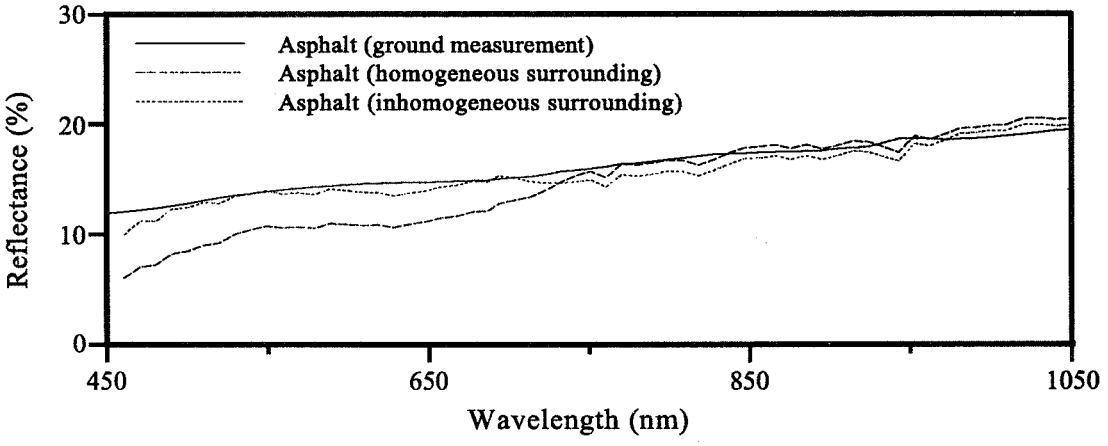

Figure 4: Surface reflectance spectra of asphalt retrieved from AVIRIS scene 2 and from ground-based measurements (solid curve) acquired with a MARK V spectroradiometer. The dashed and dotted curves represent data with homogeneous ($\rho = \rho_e$) and inhomogeneous surrounding terrain ($\rho \neq \rho_e$), respectively. ρ is the reflectance of the target in question and ρ_e is the reflectance of the surrounding targets.

Page intentionally left blank

S34-43
046104

Mapping Acid-Generating Minerals at the California Gulch Superfund Site in Leadville, Colorado using Imaging Spectroscopy

Gregg A. Swayze, Roger N. Clark, Ronald M. Pearson*, and K. Eric Livo

U.S. Geological Survey, Box 25046 MS964 DFC Denver, CO 80225

*U.S. Bureau of Reclamation, P.O. Box 25007 D-8321 DFC, Denver, CO 80225

Introduction

The Leadville mining district, located at an elevation of 3000 m in the Central Colorado Rockies, has been mined for gold, silver, lead and zinc for over 100 years. This activity has resulted in waste rock and tailings, rich in pyrite and other sulfides, being dispersed over a 30 km^2 area including the city of Leadville. Oxidation of these sulfides releases lead, arsenic, cadmium, silver, and zinc into snowmelt and thunderstorm runoff, which drains into the Arkansas River, a main source of water for Front Range urban centers and agricultural communities. The U.S. Environmental Protection Agency (EPA), U.S. Bureau of Reclamation (USBR), contractors, and responsible parties are remediating the mined areas to curtail further releases of heavy metals into various drainage tributaries of the Arkansas River. The USBRs' current work is directed toward characterizing and pinpointing localized sources of acid mine drainage and contamination from waste rock piles found throughout an area of 900 hectares.

Method

The sulfide oxidation process is biologically driven along complex chemical pathways with feedback reactions that enhance the speed and magnitude of oxidation (Nordstrom, 1982). Release of heavy metals is facilitated by sulfide oxidation, since many of the sulfides contain the heavy metals (e.g. Pb, As, Cd, Ag, and Zn). The oxidation-weathering process produces low pH water in which the heavy metals dissolve as aqueous phases that are then transported by runoff into nearby streams. Secondary minerals such as jarosite, ferrihydrite, schwertmannite, goethite, and hematite are formed by sulfide oxidation or precipitation from metal-rich water. These secondary minerals are Fe-rich and usually hydroxyl-bearing, making it possible to identify them from their unique spectral signatures. As the pH of the stream water increases, from dilution with higher pH sources, the secondary minerals precipitate out as streambed coatings. Because the heavy metals can substitute for Fe, they are also precipitated from solution as constituents of secondary minerals or as contaminants adsorbed onto the surfaces of the secondary minerals (Smith and Macalady, 1991; Alpers et al., 1994). Subsequent pulses of low pH water may dissolve the secondary minerals and remobilize the heavy metals and transfer them downstream.

The sulfide mineral pyrite is a primary source of acid drainage. Because direct spectral detection of pyrite is hampered by its low reflectance level, its broad Fe-absorption,

and usual opaque coating of oxidation products, pyrite can only be detected when it is locally concentrated. However, our study shows that pyrite weathers first to copiapite, a mixed Fe^{2+}-Fe^{3+}-sulfate, and then to jarosite, and eventually to hematite or goethite (Table 1), forming a sequence where the degree of oxidation and weathering is indicated by the species of secondary mineral that forms. Therefore, an indirect way to find oxidizing pyrite is to look for areas where the secondary minerals grade through the oxidation-weathering sequence (e.g. those areas with copiapite or jarosite surrounded by goethite or hematite). Quite fortuitously, the presence of heavy metals and low pH associated with the mine waste prevent the growth of vegetation over most waste piles leaving them exposed.

Table 1. Pyrite and Secondary Minerals

Pyrite	FeS_2 *
Copiapite	$Fe^{2+}Fe^{3+}(SO_4)_6(OH)_2 \cdot 20H_2O$
Jarosite	$(Na,K)Fe^{3+}{}_3(SO_4)_2(OH)_6$
Goethite	α-FeO(OH)
Hematite	α-Fe_2O_3

* Formulas from Fleisher (1980)

The size of the Leadville mining district and presence of spectrally detectable secondary minerals from the pyrite oxidation-weathering process makes imaging spectroscopic analysis effective for locating those minerals related to the acid mine drainage sources. AVIRIS data was collected over Leadville on July 27, 1995 as part of the NASA SIR-C Data Integration Project (lead by F. Kruse). Data were calibrated from radiance to reflectance in two stages: 1) removal of solar flux, atmospheric absorption, and path radiance using the ATREM program (Gao et al., 1992), and 2) further corrections of the ATREM reflectance data using ground reflectance targets. One of the additional corrections was needed because ATREM overcorrected the AVIRIS scene's path radiance. We derived this correction by first extracting an average spectrum from the ATREM cube over fir trees in a shaded ravine, and then dividing this into a fir tree spectrum from our library. Next we used the low points in this spectral ratio to cubic spline a new curve which was then added back into the ATREM data cube to compensate for the overcorrection. Since the terrain around Leadville is heavily vegetated we used the Sugarloaf earthen-fill dam as our high reflectance ground calibration target. The dam surface consists of granite boulders and smaller fragments of metamorphic gneiss piled to form an irregular surface dipping uniformly away from the reservoir. Because of the heterogeneity of this site, a portable field spectrometer was used to record 300 reflectance spectra, each of a 0.4 meter diameter roving spot of the dam surface, relative to a spectralon standard. These spectra were averaged and then used to derive a multiplier which was applied to the ATREM cube to removed the remaining artifacts. Given the heterogenous composition of the dam's surface and the need to produce a correction relatively free of noise (to preserve the high S/N of the AVIRIS data), use of a portable field spectrometer was critical to producing the final AVIRIS reflectance calibration.

Calibrated AVIRIS reflectance data was spectroscopically mapped using the Tricorder

algorithm (Clark et al., 1995; Clark et al., in prep.). Tricorder is an expert system which is capable of simultaneously analyzing spectra of solids, liquids, and gases. It can preprocess data, then do an initial analysis, and from this decide on a number of alternate analysis paths. Tricorder's primary subroutine is a least-square shape-matching algorithm which compares spectra of unknown materials to hundreds of reference library spectra and picks the best spectral match. This subroutine uses thresholds on band depth, fit, and continuum slope to help constrain the spectral matching. The spectral library used to map AVIRIS Leadville data contains reference spectra of the individual secondary minerals and some mixtures of these, along with 160 spectra of other materials. Because the visible to 1.0-μm spectral region is dominated by electronic absorptions due to transition metals, including Fe, and because the 2 to 2.5-μm region is dominated by molecular vibrational absorptions, maps of the dominant materials in each spectral region were produced for the Leadville AVIRIS scene.

Results

Examination of the electronic-absorption map shows the waste piles as having small zones of jarosite surrounded by jarosite-goethite zones, in turn surrounded by goethite and hematite zones. Field checks of these oxidation-weathering zones with a portable spectrometer and hand lens indicates that the jarosite zones are pyrite- rich. Coarse pyrite weathers more slowly than fine pyrite and enough had survived weathering that it was mapped in the Oregon Gulch tailings. At the Apache pile, concentrations of finer grained pyrite (used as a pigment to color beer bottles), had an oxidation coating of copiapite which was also identified and mapped. Reprocessed tailings in the Stray Horse Gulch waste piles mapped as hematite, providing a way to aerially separate these materials from the goethite-rich waste rock. Areas surrounding the site of an old smelter spectrally mapped as an amorphous Fe-hydroxide. Field investigation in these areas showed rocks coated with a grayish-coating of the condensed arsenic-rich effluent from the smelter smoke stacks.

Examination of the vibrational absorption map shows that the waste piles abruptly change composition from Na-montmorillonitic to kaolinite-sericitic alteration across a series of interconnected NW-trending graben faults. Since mineralization was hosted in limestones on both sides of the fault, the differences in alteration may be related to changes in the chemistry and temperature of the hydrothermal fluids or the composition of the waste rock. These spectrally observed compositional differences may, nevertheless, fingerprint waste rock piles as originating from specific mines or ore bodies. At present, no clear relationship can be drawn between the distribution of clays and the location of acid drainage point-sources.

Conclusions

The mineral maps created from AVIRIS data are being used to guide USBR's investigation, characterization, and remediation efforts for the EPA at the California Gulch Superfund (NPL) Site. Based on the pattern of secondary oxidation-weathering minerals that form above pyrite-rich waste rock and tailings, a map of the electronic absorption spectral region can be used to locate potential sources of acid mine drainage. Those areas covered by jarosite and jarosite-goethite mine-waste are believed to have a high acid generating capacity and are surface point-sources for acid water and heavy metals. Areas covered by goethite and hematite can still contain heavy metals (adsorbed on or as components of the secondary minerals) but they will not be mobile in the absence of low pH water, normally found in the

jarosite-rich areas. It is possible that the minerals at the surface of the waste piles and tailings may not reflect the pile's composition at depth. Depending on the amount of precipitation and level of the groundwater table, unoxidized sulfides may be mantled by a layer of non-acid generating secondary minerals. In these cases, surficial mineral maps will not show the acid-generating capacity of the waste rock and tailings beneath the surface. In most instances, we believe that these oxidation rinds will prevent water from penetrating to the sulfides, and in effect, isolate them from the aqueous environment. As part of our ongoing investigation, we plan to correlate surface mineralogy with soil metal-concentration and pH information from drill cores and geoelectrical profiling, to better address this possibility.

Significant cost savings in investigation and remediation design have already been realized using AVIRIS data at this National Priority List Site.

References

Clark, R.N., and G.A. Swayze, 1995, Mapping minerals, amorphous materials, environmental materials, vegetation, water, ice, and snow, and other materials: The USGS Tricorder Algorithm: *Summaries of the Fifth Annual JPL Airborne Earth Science Workshop*, January 23-26, (ed.) R.O. Green, Jet Proplusion Laboratory Publication 95-1, p. 39-40.

Clark, R.N., G.A. Swayze, and T. V.V. King, in prep., Imaging spectroscopy: a new tool for identifying and mapping materials: minerals, amorphous materials, environmental and man-made materials, vegetation species, health and water content, water, ice, snow, and atmospheric gases: the USGS Tricorder algorithm: to be submitted to *Science*.

Alpers, C.N., D.W. Blowes, D.K. Nordstrom, and J.L. Jambor, 1994, Secondary minerals and acid mine-water chemistry: *The Environmental Geochemistry of Sulfide Mine-Wastes, Short Course Handbook,* (eds.) D.W. Blowes and J.L. Jambor, vol. 2, Waterloo, Ontario, Canada, Mineralogical Association of Canada, May 1994, p. 247-270.

Fleischer, M., 1980, *Glossary of Mineral Species,* Mineralogic Record, Tucson, Arizona, 192 p.

Gao, B.C., K.B. Heidebrecht, and A.F.H. Goetz, 1992, ATmospheric REMoval Program (ATREM) User's Guide, version 1.1, Center for the Study of Earth from Space document, University of Colorado, 24 p.

Nordstrom, D.K., 1982, Aqueous pyrite oxidation and the consequent formation of secondary iron minerals: in *Acid Sulfate Weathering*, eds J.S. Kittrick et al., Soil Society of America, p. 37-56.

Smith, K.S., and D.L. Macalady, 1991, Water/sediment partitioning of trace elements in a stream receiving acid-mine drainage: Second International Conference on the Abatement of Acidic Drainage, NEDEM, Montreal, Canada, Sept. 16-18., p. 435-450.

Estimating Canopy Water Content of Chaparral Shrubs using Optical Methods

Submitted by
Susan L. Ustin[1], George Scheer[1], Claudia M. Castaneda[1], Stephane Jacquemoud[1], Dar Roberts[2] and Robert O. Green[3]

[1]Department of Land, Air, and Water Resources, University of California, Davis, CA 95616, USA
[2]Department of Geography, University of California, Santa Barbara, CA 93106, USA
[3]Jet Propulsion Laboratory, California Institute of Technology, M.S. 306-438, Pasadena, CA 91109-8099, USA

California chaparral ecosystems are exceptionally fire adapted and typically are subject to wildfire at decadal to century frequencies. The hot dry Mediterranean climate summers and the chaparral communities of the Santa Monica Mountains make wildfire one of the most serious economic and life-threatening natural disasters faced by the region. Additionally, the steep fire-burned hillsides are subject to erosion, slumpage, and mud slides during the winter rains. The Santa Monica Mountain Zone (SMMZ) is a 104,000 ha east-west trending range with 607 m of vertical relief and located in the center of the greater Los Angeles region. A series of fires in the fall of 1993 burned from Simi Valley to Santa Monica within a few hours. Developing techniques to monitor fire hazard and predict the spread of fire is of major concern to the region. One key factor in the susceptibility to fire is the water content of the vegetation canopy. The development of imaging spectrometry and remote sensing techniques may constitute a tool to provide this information.

At least four distinct chaparral communities exist in the mountains which are found in a complex spatial mosaic across this range. These species exhibit different sensitivities to fire and responses to post-fire because of differences in their growth patterns, density, biomass and litter accumulations, and water contents. These shrub communities are known as chamise chaparral (often nearly pure stands of *Adenostoma fasciculatum*). *Ceanothus* chaparral is typically mid-successional and is dominated by one or more species of *Ceanothus* (California lilac). Broadleaf chaparral, which is generally the most diverse, is often composed of several shrub species. Lastly, the coastal region may be dominated by Coastal sage (*Salvia*) species. This latter community tends to maintain the highest foliar density and is greenest to the eye.

We obtained spectral measurements in the field (ASD-2500nm range) and the lab (CARY 5E) on the dominant chaparral species at canopy and leaf scales and compared these to estimates of water content in concurrently acquired AVIRIS images in June and October, 1995 to examine how well variation in canopy water contents can be estimated using optical sensors. Measurements were made at three sites, Zuma Ridge, Castro Crest and Encino Reservoir, which were chosen as representative of the dominant communities and presenting plants of the major species in different stages of growth (Table 1). The three sites are Zuma Ridge, a coastal site with young sage and mixed chaparral vegetation, Castro Crest, a mountain site with medium above ground biomass accumulation and mixed chaparral vegetation, and Encino Reservoir, an inland site on the eastern edge of the reservoir with old growth *Ceanothus* vegetation, with high biomass chaparral shrubs, 3 to 4 meters tall. The Forest Service Fire Lab and the Los Angeles County Fire District harvested above ground canopy biomass from 15 5m x 5m plots. Total plot biomass was weighed in the field. A subsample of the biomass was measured for water content, leaf mass and stem mass (in different stem size categories) for the June data acquisition. The ASD spectrometer was mounted on a bucket truck and above canopy spectra were acquired at the three sites. Water content was estimated for the canopy within the field of view of the ASD. The following species were recorded at these sites:

Table 1. Species found at the three sites.

Zuma: MALA, ARCA, SALE, ERAR
Castro: ADFA, CEOL, ARGL
Encino: CEME, and DRY GRASS

Acronym	Latin name	Family	Common name
MALA	Rhus laurina	Anacardiaceae	Laurel Sumac
ARCA	Artemisia californica	Asteraceae	Coastal Sagebrush
SALE	Salvia leucophylla	Lamiaceae	Purple Sage
ERAR	Eriogonum cinereum	Polygonaceae	Ashy Leaf Buckwheat
ADFA	Adenostoma fasciculatum	Rosaceae	Chamise, Greasewood
CEOL	Ceanothus oliganthus	Rhamnaceae	Hairy-leaf Ceanothus
ARGL	Arctostaphylos glandulosa	Ericaceae	Eastwood Manzanita
CEME	Ceanothus megacarpus	Rhamnaceae	Big Pod Ceanothus

Methods

Field Radiometric Data

For all three sites, seven above canopy locations were chosen and measured from the bucket truck for the radiometric measurements. Species, canopy height, and spectrometer height were recorded. A Spectralon panel was mounted on a tripod attached to the bucket and adjusted normal to the ground using a leveling device taped to the corner of the standard for calibrating to surface reflectance. Corrections for Spectralon were post-processed to produce absolute 100% reflectance.

Laboratory Radiometric Data

For most of the species, both leaf reflectance and transmittance were measured in the lab on a CARY 5E spectrophotometer with a 150mm Labsphere Integrating sphere with a Spectralon surface. The wavelengths range from 400 nm to 2500 nm with an interval of 2 nm. We acquired reflectance spectra for all the species; for ADFA and ARCA which have needle-like leaves, the transmittance could not be measured so only the infinite reflectance of an optically thick sample was obtained.

Laboratory biophysical Measurements

Some samples of fresh leaves, stems and flowers were collected in the field to calculate water content. For large plant leaves, the fresh weight of 3.46 cm^2 disks was measured, which were cut using a cork borer and immediately weighed using a portable electronic balance; for small leaves, we weighed entire blades, the area of which was later measured using a Canon Video Visualizer RE-650 camera and a digitizer. The stems and flowers of some plants were also processed. All the samples were dried at 70°C for four days before dry weights were measured. Assuming that FW is the fresh weight, DW the dry weight, and S the leaf area, water content (WC) was calculated, as were the equivalent water thickness (EWT), the leaf specific weight (LSW) and the specific leaf area (SLA) which is the reciprocal of the leaf specific weight:

$$WC = \frac{FW - DW}{FW} \qquad EWT = \frac{FW - DW}{S} \qquad LSW = \frac{1}{SLA} = \frac{DW}{S}$$

WC is the water mass over fresh mass, EWT and LSW are respectively the water and dry matter masses per unit leaf area, expressed in $g.cm^{-2}$; in consequence, the SLA is provided in $cm^2.g^{-1}$.

Data Analysis

Three methods for estimating canopy water content were applied to the laboratory and field data sets. The first method applied a modified version of the PROSPECT model (Jacquemoud et al., 1996), which predicts several leaf chemistry variables including water thickness from the reflectance data. The second method used a continuum removal technique to fit a curve to the water absorption feature (Clark and Roush, 1984). The third method used a new technique, termed by Smith et al. (1994) Foreground/Background Analysis (FBA). In a modified form described by Pinzon et al. (1995, 1996), FBA relates optical properties to canopy biochemical concentrations in three steps. First, the Gram-Schmidt orthogonalization procedure was used to extract the bands that explain most of the spectral variation for water absorption. Second, the samples were stratified into different reflectance ranges by defining an FBA vector that permits their hierarchical classification. Finally, FBA was used to find new vectors that best relate leaf reflectance to water content. These results from each of these methods were compared for accuracy of the assessment and all three methods gave reasonably good predictions at the leaf and canopy levels. The significance of differences among the methods will be discussed. The methods were then applied to the calibrated AVIRIS datasets from June 1995 and spatial estimates of above ground canopy water contents were obtained.

Table 2. Leaf biophysical measurements predicted by the PROSPECT model. Leaf thickness, pigment content and water content are estimated from 40 fresh leaves measured in the CARY spectrophotometer from this experiment.

Variable	Unit	Range	Mean	Std. Dev.
leaf thickness	mm	86.4-780.0	194.5	114.9
SLA	cm2 g-1	73.9-535.3	224.6	93.4
Water Content	%Fresh Wt.	44.9-92.4	66.4	11.0
Water Concentration	g cm-2	0.0046-0.0405		
Chlorophyll α	µg cm-2	12.8-64.2	36.9	11.4
Chlorophyll β	µg cm-2	3.7-21.3	11.7	3.8
Carotenes	µg cm-2	3.7-19.4	10.5	3.6
Cellulose	%Dry Wt.	9.1-37.2	19.7	6.4
Cellulose	g cm-2	0.00031-0.00545		
Hemicellulose	% Dry Wt.	0.3-38.8	15.2	10.0
	g cm-2	0.00002-0.00332		
Lignin	% Dry Wt.	1.1-27.5	10.2	6.4
	g cm-2	0.00003-0.00305		
Protein	% Dry Wt.	7.4-36.8	20.0	7.0
	g cm-2	0.00048-0.00172		
Starch	% Dry Wt.	0.0-10.0	2.0	2.1
	g cm-2	0.0000-0.00098		
Total Carbon	% Dry Wt.	38.5-52.3	47.4	2.9
	g cm-2	0.00079-0.00665		
Total Nitrogen	% Dry Wt.	1.2-5.9	3.4	1.1
	g cm-2	0.00009-0.00033		

An example of the results of the PROSPECT model run is shown in Figure 1a for one randomly selected leaf from the dataset. The predicted and measured liquid water estimates for 40 leaf samples measured on the CARY spectrophotometer in the lab are shown in Figure 1b. A summary of the predicted foliar biochemical composition from the CARY laboratory spectra for the 40 leaf samples is shown in Table 2. The results of the three leaf and canopy spectral analysis methods were compared to equivalent path leaf water thickness estimates obtained from the atmospheric calibration of AVIRIS data obtained using the method of Green et al. (1995). These results were also compared to the field measured canopy water content and biomass data provided by the Forest Service. Results support the use of AVIRIS image analysis techniques for estimating spatial variation in water content.

References

Clark, R.N., and Roush, T.L., 1984, Reflectance spectroscopy: Quantitative analysis techniques for remote sensing applications. J. Geophysical Research 89: (B7) 6329-6340.

Green, R.O., Conel, J.E., and Roberts, D.A., 1995, "Measurement of atmospheric water vapor, leaf liquid water and reflectance with AVIRIS in the Boreal Ecosystem-Atmosphere Study: Initial Results," In Summaries of the 5th Ann. JPL Airborne Earth Science Workshop, R.O. Green, editor. JPL 95-1: 87-90. Pasadena, CA.

Jacquemoud, S., Ustin, S.L., Verdebout, J., Schmuck, G., Andreoli, G. and Hosgood, B., 1996, "Estimating leaf biochemistry using the PROSPECT leaf optical properties model," *Remote Sensing of Environment*, in press.

Pinzon, J.E., Ustin, S.L., Hart, Q.J., Jacquemoud, S., and Smith, M.O., 1995, "Using foreground/background analysis to determine leaf and canopy chemistry," In Summaries of the 5th Ann. JPL Airborne Earth Science Workshop, R.O. Green, editor. JPL 95-1: 129-132. Pasadena, CA.

Pinzon, J.E., Ustin, S.L., Castaneda, C., and Smith, M.O., 1996, "Investigation of Leaf Biochemistry by Hierarchical Foreground/Background Analysis," manuscript, to be submitted to *IEEE Transactions on Geoscience and Remote Sensing*.

Smith, M., Roberts, D., Hill, J., Mehl, W., Hosgood, B., Verdebout, J., Schmuck, G., Koechler, C. and Adams, J., 1994, "A new approach to quantifying abundances of materials in multispectral images," IGARSS '94, Pasadena, CA, Aug. 8-12, 1994, 3 p.

Figure 1a (left) shows the fit between the measured leaf reflectance and transmission using the revised PROSPECT model. Figure 1b (right) shows the predicted and measured liquid water estimates ($g.cm^{-2}$) for 40 leaf samples of various chaparral shrub species that were measured on the CARY spectrophotometer.

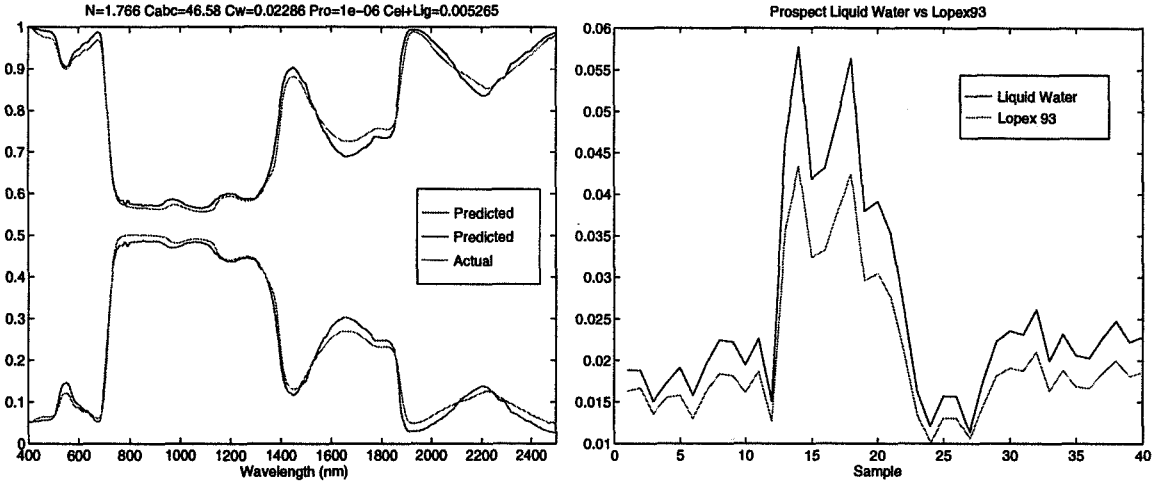

Acknowledgements

This research was funded by National Aeronautics and Space Administration grant NAGW-4626-I. A portion of the research described in this paper was performed at the Jet Propulsion Laboratory, California Institute of Technology, under a contract from the National Aeronautics and Space Administration.

REPORT DOCUMENTATION PAGE

Form Approved
OMB No. 0704-0188

1. AGENCY USE ONLY (Leave blank)	2. REPORT DATE	3. REPORT TYPE AND DATES COVERED
	March 4, 1996	Final

4. TITLE AND SUBTITLE

Summaries of the Sixth Annual JPL Airborne Earth Science Workshop, March 4-8, 1996. Volume 1. AVIRIS Workshop.

5. FUNDING NUMBERS

RF4 BP-453-97-02-00-00

6. AUTHOR(S)

Robert O. Green, Editor

7. PERFORMING ORGANIZATION NAME(S) AND ADDRESS(ES)

JET PROPULSION LABORATORY
California Institute of Technology
4800 Oak Grove Drive
Pasadena, California 91109

8. PERFORMING ORGANIZATION REPORT NUMBER

JPL Publication 96-4, Volume 1

9. SPONSORING/MONITORING AGENCY NAME(S) AND ADDRESS(ES)

NATIONAL AERONAUTICS AND SPACE ADMINISTRATION
Washington, D. C., 20546

10. SPONSORING/MONITORING AGENCY REPORT NUMBER

11. SUPPLEMENTARY NOTES

12a. DISTRIBUTION/AVAILABILITY STATEMENT

Unclassified/Unlimited

12b. DISTRIBUTION CODE

13. ABSTRACT (Maximum 200 words)

This publication contains the summaries for the Sixth Annual JPL Airborne Earth Science Workshop, held in Pasadena, California, on March 4-8, 1996. The main workshop is divided into two smaller workshops as follows:

- o The Airborne Visible/Infrared Imaging Spectrometer (AVIRIS) workshop, on March 4-6. The summaries for this workshop appear in Volume 1.
- o The Airborne Synthetic Aperture Radar (AIRSAR) workshop, on March 6-8. The summaries for this workshop appear in Volume 2.

14. SUBJECT TERMS

1. Infrared and ultraviolet detection
2. Geosciences and Oceanography (general) 3. Geology and mineralogy 4. Hydrology and limnology

15. NUMBER OF PAGES

246

16. PRICE CODE

17. SECURITY CLASSIFICATION OF REPORT	18. SECURITY CLASSIFICATION OF THIS PAGE	19. SECURITY CLASSIFICATION OF ABSTRACT	20. LIMITATION OF ABSTRACT
Unclassified	Unclassified	Unclassified	